Diffusion Limited Planetesimal Formation

Why Asteroid and Kuiper-belt Objects Share a Characteristic Size

Andreas Schreiber

2018

Dissertation

submitted to the

Combined Faculties of the Natural Sciences and Mathematics

of the Ruperto-Carola-University of Heidelberg. Germany

for the degree of

Doctor of Natural Sciences

Put forward by

Andreas Schreiber

born in Langenhagen, Germany

Oral examination: 18th of May, 2018

Diffusion Limited Planetesimal Formation

Why asteroid and Kuiper-belt objects share a characteristic size

Referees:

Apl. Prof. Dr. Hubert Klahr

Prof. Dr. Cornelis P. Dullemond

Abstract

Planets are surprisingly abundant in our own solar system, but also in extrasolar systems. It is striking to find no explanation for them, as dust in protoplanetary disks was found to not outgrow metres in size. The growth barrier of dust to km-sized planetesimals thus states a missing link onto their formation mechanisms. It is evident for planetesimals to have been present in the early solar system, as their remnants prowl the solar system today in the form of asteroids, Kuiper belt objects, and comets. Of them, many were found to be pristine, giving a hint on what once populated the early solar nebula. Studying the sizes of these pristine objects revealed for all of them a characteristic diameter of 100 km. It is stunning to find this feature independent of distance from the Sun in most pristine object families, hence this feature has to be an imprint of their formation mechanism. This thesis derives a formation criterion for planetesimals out of particle cloud collapse within protoplanetary disks. The found mechanism is capable of reproducing the characteristic sizes of these pristine objects, as it is to first order independent of radial distance from the star. By comparing collapse timescale with turbulent particle diffusion timescale, a minimum size criterion for a dust cloud to collapse is found and investigated. Naturally, dust cloud collapse happens at high dust-to-gas ratios, thus the *streaming instability* is a good candidate for this turbulent process. Hence, the streaming instability is studied in 2-d and 3-d simulations at dust-to-gas ratios well above unity and on typical collapse length scales. This study found a new instability, namely the *azimuthal streaming instability*. It operates in the radial-azimuthal plane and has characteristics similar to the streaming instability, thus its name. Subsequent collapse simulations in 2-d and 3-d proved the *diffusion limited planetesimal formation* to produce planetesimals right at the expected 100 km diameter. It is the conclusion of this thesis to have shown a fundamental concept to be applied in future studies on planetesimals. It has the prospect to make verifiable predictions which can proof this mechanism to have shaped the solar system as we see it today.

Zusammenfassung

Planeten gibt es nicht nur in unserem Sonnensystem, sondern auch überraschend häufig in extrasolaren Planetensystemen. Bis heute konnte jedoch der Planetenentstehungsprozess nicht final nachvollzogen werden, da Staub in protoplanetaren Scheiben nicht über eine Größe von Metern hinauswachsen kann. Die dynamischen Prozesse, die km-große Planetesimale entstehen lassen, können als *Missing Link* der Planetenentstehung verstanden werden. Es gilt als erwiesen, dass diese Objekte in großer Anzahl im frühen Sonnensystem vorhanden gewesen sein müssen. Noch heute streifen übrig gebliebene Planetesimale in der Form von Asteroiden, Kuipergürtel-Objekten und Kometen durch unser Sonnensystem. Viele von ihnen noch heute in ihrer ursprünglichen Form und geben einen Einblick in die frühe Phase unseres Sonnensystems. Die Größenverteilungen der meisten dieser Objektfamilien zeigt jedoch unabhängig von der Entfernung zur Sonne eine feste charakteristische Größe von 100 km, was daher ein Merkmal aus ihrem Entstehungsprozess sein muss. In dieser Dissertation wird ein Entstehungskriterium für Planetesimale aus dem Kollaps einer Partikelwolke innerhalb einer protoplanetaren Scheibe hergeleitet. Der gefundene Mechanismus ist in erster Ordnung unabhängig von der Distanz zum zentralen Stern und daher erstmals in der Lage die charakteristische Größe von den heute beobachteten Planetesimalen zu reproduzieren. Durch den Vergleich von Kollapszeit mit turbulenter Diffusionszeit, konnte ein minimales Größenkriterium für eine Partikelwolke gefunden werden. Da der zu erwartende Kollaps bei hohen Staubkonzentrationen stattfindet, ist die *Streaming Instabilität* der beste Kandidat für den stärksten turbulenten Prozess. Daher untersucht diese Dissertation in 2-D und 3-D Simulationen diese Instabilität bei Staubkonzentrationen weit über eins hinaus und auf dem für Kollaps typischen Längenskalen. In dieser Studie wurde eine neue Staub-Gas-Instabilität gefunden, die *azimutale Streaming Instabilität*. Sie ist in der radial-azimutalen Ebene anzutreffen und ähnlich zur Streaming Instabilität. Weiter konnte in 2-D und 3-D Kollaps-Simulationen das hergeleitete *diffusionslimitierte Planetesimal-Entstehungskriterium* erfolgreich verifiziert und die Entstehung von 100 km-großen Planetesimalen vorhergesagt werden. Es ist das Ergebnis dieser Doktorarbeit ein neuen Mechanismus der Planetesimalentstehung identifiziert und verifiziert zu haben. Das Entstehungskriterium ist in der Lage überprüfbare Vorhersagen an unser Sonnensystem zu stellen und wird hoffentlich in der Zukunft Beweis finden, die belegen, dass dieser Prozess unser heute beobachtetes Sonnensystem geprägt hat.

For my father.

Contents

Acronyms

ALMA	Atacama Large Millimeter/submillimeter Array
aSI	azimuthal Streaming Instability
ISM	Intersellar Medium
KBO	Kuiper Belt Object
MMSN	Minimum Mass Solar Nebula
MRI	Magneto-Rotational Instability
NEOs	Near Earth Objects
PPD	Protoplanetary Disk
RDI	Resonant Drag Instability
rms	Root-Mean-Square
SGI	Secular Gravitational Instability
SI	Streaming Instability
TNO	trans-Neptunian object
TSC	Triangluar Shaped Cloud

Symbols

Symbol	Definition	Description
t		time
$\mathbf{u}$, $\mathbf{v}$		gas and dust velocity vector
σ	$\sigma = \sqrt{\frac{1}{N}\sum_i^N (v_i - \bar{v})^2}$	velocity dispersion: rms-velocity
ζ	$\zeta = \sqrt{\frac{1}{N}\sum_i^N (v_i - u(x_i))^2}$	drift velocity between particle and gas
T_{orb}, Ω	$T_{\text{orb}} = 2\pi/\Omega$	orbital period and frequency
c_{s}		speed of sound
η	$\Delta v_\varphi = \eta v_{\text{K}}$	pressure gradient parameter: Sub-Keplerianess
St	$\mathsf{St} = \tau_{\text{s}}\Omega$	Stokes number: dimensionless particle friction
Sc	$\mathsf{Sc} = \alpha/\delta_x$	Schmidt number: ratio of momentum and material transport
δ, D	$\delta = D/Hc_{\text{s}}$	(dimensionless) diffusion coefficient
α	α	α-turbulence: disk viscosity
H	$H = c_{\text{s}}/\Omega$	gas disk scale height
H_{d}	$\mathsf{H}_{\text{d}} = \sqrt{\frac{\alpha}{\Omega\tau_{\text{s}}}}$	dust disk scale height
ε, ε_{max}, ε_0	$\varepsilon = \rho_{\text{d}}/\rho_{\text{g}}$	dust-to-gas density ratio (maximum/initial)
τ_{ff}		free-fall timescale
τ_{c}		cloud contraction timescale, includes friction
τ_{s}		stopping timescale via friction
τ_{coll}		collision timescale
τ_{D}	$\tau_{\text{D}} = r^2/D$	diffusion time
τ_{shear}	$\tau_{\text{shear}} = 2/3\Omega^{-1}$	Keplerian shear timescale
N_{par}		number of particles
$\circ$		symbol for global values (simulation domain wide)
$\square$		symbol for local values (per simulation grid cell)
ρ_{Roche}	$\rho_{\text{Roche}} = 12M/\pi R^3$	Roche density
ρ_{Hill}	$\rho_{\text{Hill}} = 9M/4\pi R^3$	Hill density
ρ_{g}		gas density
ρ_{d}		dust particle density
ρ_0, $\rho_{\text{d},0}$, $\rho_{\text{g},0}$		initial mean (dust/gas) density
ρ_{c}	$\rho_{\text{c}} \equiv \rho_{\text{Hill}}$	critical density that is triggering cloud collapse
$\rho_\bullet$		solid body density
l_{c}, r_{c}	$r_{\text{c}} = l_{\text{c}}/2$	critical length scale and radius of a particle cloud
τ_{corr}	$\tau_{\text{corr}} = \sigma^2/D$	correlation timescale: $\sim$ eddy turn-over time
l_{corr}	$l_{\text{corr}} = \sigma/D$	correlation length scale: $\sim$ eddy size
L		simulation domain size
a_{c}		planetesimal diameter
$R_\odot$, $\rho_\odot$, $M_\odot$		stellar parameters
λ_{free}		mean free path
$\hat{G}$		self-gravity parameter (simulation)

1 Introduction

Earth, as the planet we live on, defines for us what we call a *wanderer in the sky*. Besides the Sun, the Moon, and the stars, bright on the night sky the unaided human eye can observe five planets. By enhancing our capacity to glimpse into the dark night sky, human kind found a total of eight planets orbiting our sun. Most of them have their own moons, see Fig. 1.1, Jupiter for example has dozens of them. Interestingly, there is no sharp size-cutoff between planets and moons. Thus, the category of *dwarf planets* was introduced to deal with moon-sized objects on a stellar orbit, similar to a planet. Dwarf planets are sufficiently massive to have a spherical shape, but they are not massive enough to clear their orbit free of other objects of similar size. Examples are Ceres and Pluto, both smaller than our moon. This can also be seen in Fig. 1.2, which shows solar system objects smaller than 10 000 km in size. Actually, if the criterion for being a planet would be simply defined by being a spherical object orbiting the sun, one would end up with hundreds of objects that would fall into this category. Also, the future for discovering such objects is bright, as thousands more objects are expected to be present in the outer part of our solar system[1]. They are only waiting for us to be found.

Then, there are asteroids, which are meters to kilometres sized (icy) dust balls, in planetology sometimes informally called *rubble piles*. Most of them have a suprising low density of around $2\,\mathrm{g/cm^3}$, some asteroids even have densities lower than water, but most of them are far from being a solid *rock*. This tells us that

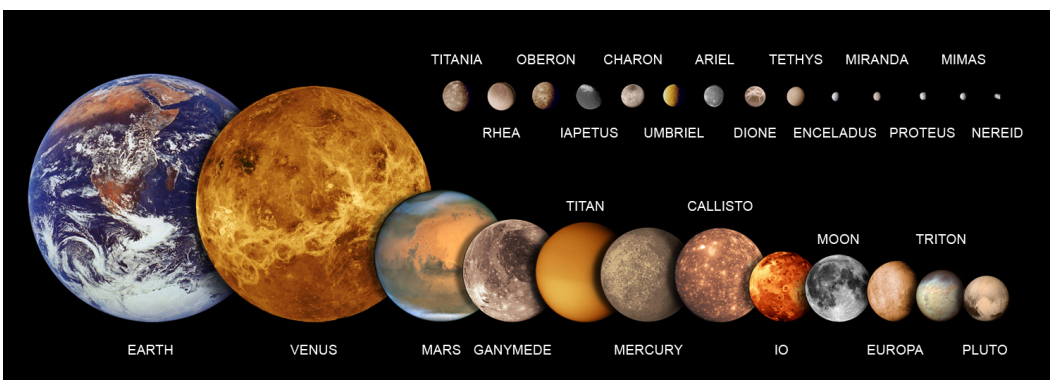

Figure 1.1: Relative sizes of the 25 Solar System objects smaller than Earth. For example, Mars with 6792 km in diameter is of similar syste as Ganymede, with its 5268 km diameter. Mainly, these objects are moons, but they compare in size with some of the main planets and dwarf planets, such as Pluto and Charon. The objects Eris, Haumea, Makemake, Sedna, Ceres, 2007 OR10, 2002 TC302, 2007 JJ43 are missing this overview graphic, as well as some more objects smaller than Tethys, but larger than Nereid, are missing. Notably this includes Vesta, Pallas, Quaoar and Orcus. *Source: Montage by tony_g100 for Wikimedia. Data from NASA / JPL, JHUAPL/SwRI, SSI, and UCLA / MPS / DLR / IDA.*

[1] http://pluto.jhuapl.edu/News-Center/PI-Perspectives.php?page=piPerspective_08_24_2012

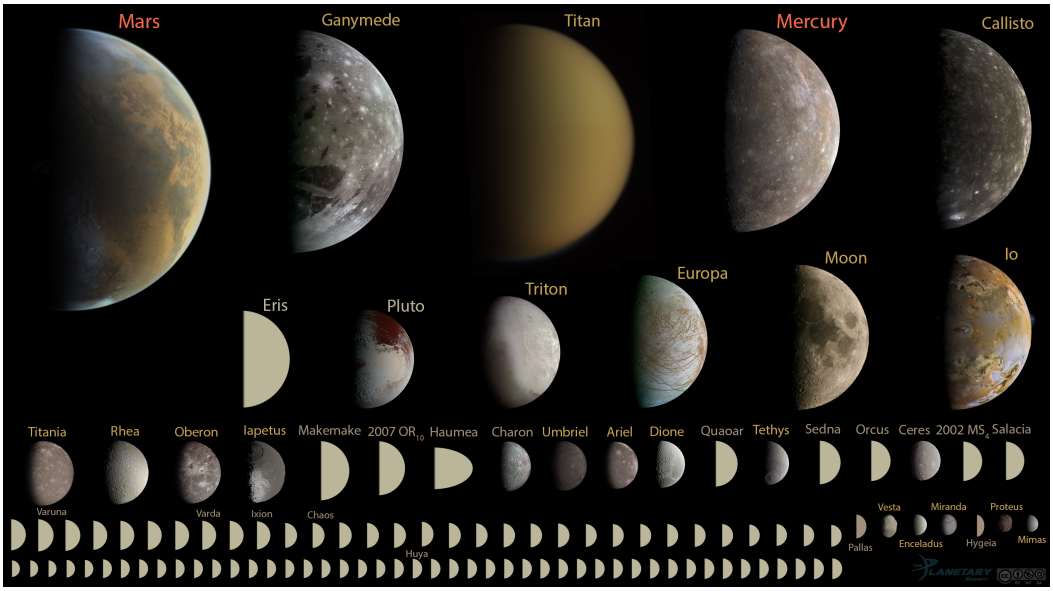

Figure 1.2: Every known spherical object in the solar system under 10 000 km in diameter, to scale. For comparison, the smallest objcets are of several 100 km in diameter. The asteroid Vesta (2.36 AU) has mean diameter of 516 km and is together with Pallas (2.77 AU) one of the two largest objects in the asteroid main belt. Varuna on the other hand is an object in the Kuiper belt (42.95 AU) and has a similar size of 668 km. On the size of Mars and below, there are two planets, 19 moons, 2 asteroids and over 87 *trans-Neptunian object* (TNO) discovered so far. Objects that are too large for an asteroid, but too small for a planet, are called dwarf planets. For example Ceres (2.77 AU) is 963 km in size, and Pluto (39.48 AU) is the largest dwarf planet with 2374 km in diameter. *Source: Montage by Emily Lakdawalla. Data from NASA / JPL, JHUAPL/SwRI, SSI, and UCLA / MPS / DLR / IDA, processed by Gordan Ugarkovic, Ted Stryk, Bjorn Jonsson, Roman Tkachenko, and Emily Lakdawalla.*

these objects did not undergo a melting process. So, neither heating from collisions nor the radioactive decay of isotopes was heating the object sufficiently to melt and segregate it. The collisions they experienced did not even significantly compress them. Consequently, they must consist right out of the material that was available at the time when our solar system was in its making, and when the planets were forming. They are the left-over material that was not incorporated into larger celestial bodies.

The asteroids in our solar system come in very different families and in different locations. The asteroids close to Earth are called *Near Earth Objects* (NEOs). 17 653 of them have been identified yet[2]. They are the type of asteroid that occasionally impact on Earth, but also on Mars or the Moon. Some of them are even right the rocky material that, after an asteroid impact, was catapulted away from the Moon or Mars surface into space, and that millions of years later hits Earth, bringing these material to us to study. Half of the NEOs are over 100 m in size, more than 800 of them are even larger than one kilometre. Their orbits are found to be stable for only a few million years (Morbidelli et al., 2002), as they get eliminated by planetary perturbations, leading either to a collision with the Sun or a planet, or, they get ejected from the inner solar system. The origin of these NEOs are thought to be in the asteroid belt, as resonances with Juipter sends them ultimately into the inner solar system. The reason for only small NEOs to undergo this process, comes from the Yarkosvski effect (Yarkovsky, 1901), as it brings small asteroids from the main belt into the Jupiter resonances in the first place. The Yarkovsky effect[3] describes a net force that arises from anisotropic thermal emission of a rotating body that is heated on one side, by the Sun, and is cooled on the other side. This effect is specially strong for small objects below a few kilometres.

[2] https://cneos.jpl.nasa.gov/stats/totals.html
[3] The Yarkovsky effect should not be confused with the YORP effect that initially brings objects into a rotational state.

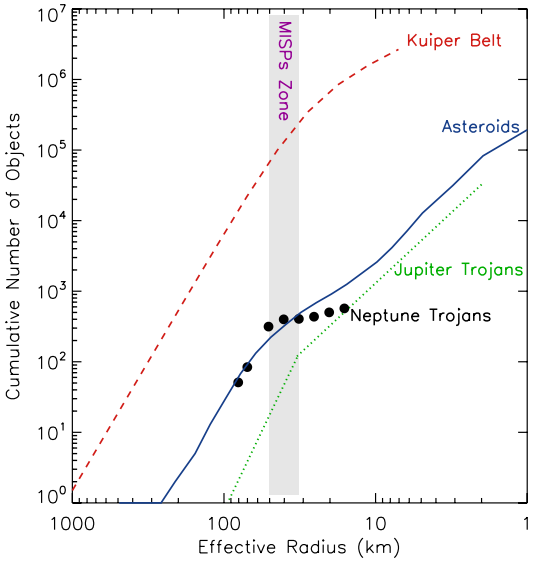

Figure 1.3: Cumulative object radius distributions of KBOs, main belt asteroids, Jupiter Trojans and Neptune Trojans. They all share the common characteristic of having a change in slope around 100 km in diameter. Below this size lies a zone where smaller objects are missing, in the diagram marked by the grey vertical bar. It is seen as an imprint of the asteroid and KBO formation mechanism that produced them. For this diagram, both the Jupiter Trojans and Neptune Trojans families, at Lagrangian points L4 and L5, are taken into account. The Neptune Trojans data stems from Sheppard & Trujillo (2010), the Jupiter Trojans data from Jewitt et al. (2000), the KBOs data from Fuentes & Holman (2008) and Fuentes & Holman (2008), and the asteroid main data from Jedicke et al. (2002) and Bottke et al. (2005). Beware that plotted on the x-axis is object radius, not diameter, i.e. the plateau starts at a diameter of ≈ 100 km! *Source: Sheppard & Trujillo (2010). Big thanks for providing this figure.*

Most of the asteroids in our solar system are found to reside in condensed rings, namely the *asteroid main belt* between 2 and 3.4 AU, and in the *Kuiper belt* between 30 and 50 AU. One typically speaks of asteroids when talking over objects of the main belt. Objects in the Kuiper belt are called *Kuiper Belt Objects* (KBOs), sometimes they are also called *trans-Neptunian object* (TNO). They are both large asteroid reservoirs in terms of mass and number, i.e. the Kuiper belt contains ~ 0.01 to $0.1 M_{\oplus}$ of material. Still, they are much less dense than what one would expect from SciFi movies, as the average distance between two asteroid belt objects is eight times the Earth-Moon distance. The object number density in the asteroid belt is higher than in the Kuiper belt, and also the orbital timescale is shorter. Hence, the collisional evolution in the Kuiper belt is less advanced as in the asteroid belt and the KBOs largely remained pristine.

Surprisingly, both of these object families have something very important in common. They share a knee in the cumulative size distribution, i.e. they have the same shape and an identical location for their size cut-off, as shown in Fig. 1.3, though their total object number is different. This characteristic is found as a change in the slope of the cumulative size distribution. This distribution is getting flatter for objects smaller than 100 km in diameter, indicating that there are almost none of the smaller sized objects below that characteristic size. The plateau goes down to a diameter of 10 km or even lower, where then collisional fragments are found and the plateau ends. Thus, in each family, most of the mass and most of the kilometre-sized objects present, resides in around 100 km sized objects. This is seen by many people in the field of planet formation as an imprint of the formation mechanism that produced these asteroids and KBOs. It lead Morbidelli et al. (2009) to the statement of: *Asteroids were born big.* Interestingly, this characteristic size of 100 km objects is also found for the Trojans of Jupiter and Neptune, see Fig. 1.3. The Trojans are asteroids that are trapped in the dynamically stables points leading before and trailing the planets position on its orbit, which are called the Lagrangian points, i.e. point L4 (leading on the orbit) and L5 (trailing on the

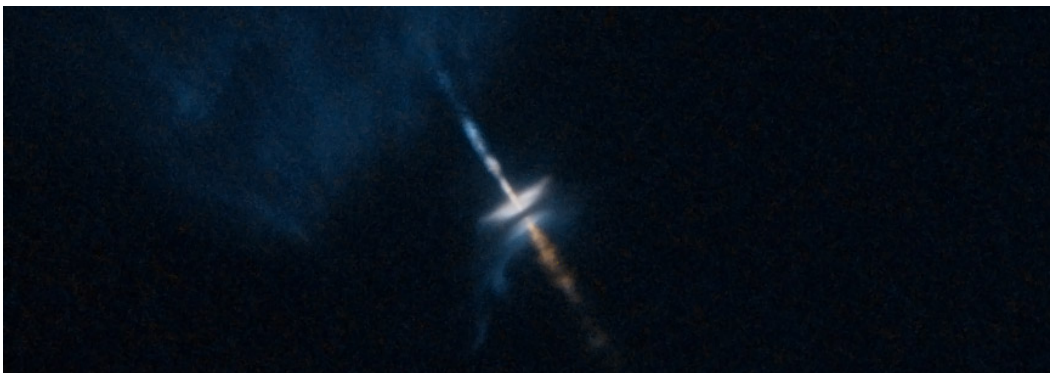

Figure 1.4: This picture of *V1213 Tauri* and its associated *Herbig-Haro 30*, taken with the broad wavelength *Wide Field Planetary Camera 2* of the *NASA/ESA Hubble Space Telescope* in 1995. It shows not only a beautiful PPD but also jets (*Herbig Haro* objects). Jets are tracers of accretion of material, here from the disk onto the star. They transport angular momentum that otherwise would oppose the accretion due to angular momentum conservation, and thus have a high velocity. One also clearly sees the widening of the disk to its outer parts, this is called disk flaring. The state of this star-disk systems is similar to our solar system 4.5 million years ago. *Source: NASA HST, Wolf Pack (Geckzilla.com)*

orbit). In the course of this thesis, an explanation of the mechanisms behind this size distribution feature is presented and validated in numerical simulations, as it is a direction result from gravitational particle cloud collapse (Johansen et al., 2006c, 2007; Cuzzi et al., 2008) as the asteroid and KBO formation mechanism (Safronov, 1972; Morbidelli et al., 2009; Goldreich & Ward, 1973).

A historical view

All these places in our solar system, but also in other stellar systems, are very special in the universe. Not only because human kind came into existence on one of them, but also on a more general perspective. They are regions of the universe that are very rich in metals. Typically, in the interstellar medium the values of solids compare to the values gas, which is mainly hydrogen and helium, by one to one-hundred. The reason is that solids are composed of higher elements which did not got formed by the big bang 13.8 billion years ago, but are formed within stars, super novas, and neutron star mergers that happened rather recently in the universe. The formation of our solar system happened ~ 4.5 billion years ago, what is known from lead isotopic dating measurements of calcium-aluminium rich inclusions (CAis) in asteroids (Amelin et al., 2002). The mechanisms behind planet formation must consequently be very efficient in concentrating these rare materials up to a level where they are bound by their own gravitational attraction. But, one needs to understand that the exact path from small dust grains from the *Intersellar Medium* (ISM), as we find them in star forming regions, to finally asteroids and massive planets, is not fully understood and remains a topic of ongoing research. It is most certain that paradigm shifts will occur in near future.

Following Whipple (1964), the first works in this field of research go down to Kant (1755) who believed that planets could have formed from gas and dust clouds that were orbiting the Sun at a certain point in history. He also came up with the theory of first having small dust grains that by mutual collisions stick and grow up to a point where the whole cloud becomes unstable under its own gravity. A similar approach was formulated by Laplace & Young (1821), not for clouds but for condensed rings which form out of the primordial gas-dust nebula that should have had surrounded our Sun in early times. Hence, the shape of this nebula must have had the shape of a thin disk, he concluded. He found this to also explain, why all planets in our solar system lie in the same plane of motion.

These ideas were brought into the modern age by Weizsäcker (1946), who concluded that turbulent viscosity, meaning the transport of material by underlying turbulence, would separate the nebula into a core, which later becomes the Sun, containing most of the mass, and a disk containing most of the angular momentum. He suspected vortices to emerge within this PPD that further concentrate material up to the point

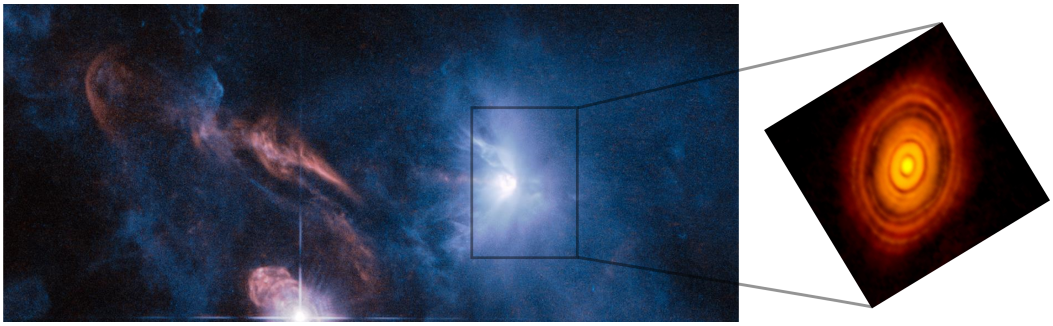

Figure 1.5: Observation of the *HL Tau* system at a distance of ≈ 140 pc in Taurus constellation. On the left, the system as seen with the *Hubble space telescope*. On the right the same system but observed with the ALMA radio telescope at 1.3 mm in the long baseline configuration. ALMA observes the thermal emission of the dust grains. The clear ring structure of the dust that was observed by the gas-dust envelope of the system for the Hubble Space Telescope, could be revealed by the ALMA radio band observation. It is suspected that these rings come either from dust concentrations by pressure anomalies in the system, or that they are carved out by planets. The latter would mean that planet formation is an extreme fast process and the age of the system indicates that the this explanation is hardly true. *Source: ALMA Partnership et al. (2015)*

where self-gravity brings them to collapse directly into a gravitationally bound object. Another milestone in the understanding of the solar system, and in general planet formation, was laid by Safronov (1972) (original Russian publication from 1969), who developed many dynamical models that describe the growth from µm-sized dust gains in gaseous disks up to planets, which are still widely used today. As a good start for new readers in the field of planet formation, the summary by Youdin & Kenyon (2013) is recommended.

Observations of protoplanetary disks

Today, from direct observation, we know of the existence of circumstellar disk material around young stellar objects. The first observational evidence came actually from unresolved star-disk systems, by finding an additional bump of the spectral energy distribution in the long-wavelength regime that could only be explained by an accretion of material onto the host star. With the emergence of the *Hubble Space Telescope* (HST) and very sensitive ground based optical telescopes with high-performance adaptive optic systems, such as the *Very Large Telescope* (VLT), direct observations of disks around young stars became possible, see Fig. 1.4. By that technical advancement, the field of planet formation got shifted from a mainly theoretical field, with very little evidence from our own solar system, to a field that additionally is driven by observations.

PPDs are found especially in star forming regions. They are initially embedded into large molecular clouds out of gas and dust, which get denser towards their star forming cores. This hinders infrared observations and astronomers were in need of a high-resolution radio telescope that could unravel the mechanics within PPDs. In 2013, such a telescope was taken into service. The *Atacama Large Millimeter/submillimeter Array* (ALMA) with its 66 radio antennae measures the thermal emission of the dust directly from the disk interior. ALMA delivered stunning images of PPD sub-structures, such as rings, see right side of Fig. 1.5, non-axisymmetric dust concentrations, and spirals.

A main discussion in the research field is now to find ways to distinguish these disk features by their origin. Which features arise from hydrodynamical effects? Which come from planets that already reside in the disk? Yet, from current observations this cannot be told, as the scales of planet formation remain unresolved. This is why the field of planet formation stays driven by mainly theoretical research, such as the work on planet formation in this thesis.

Overview of the theoretical understanding of planet formation

The focus of this work lies on the growth from micrometer-sized dust grains to the very first kilometer-sized objects. These objects are thought to be the building blocks of planets and are called planetesimals (Weidenschilling & Cuzzi, 1993; Johansen et al., 2014). These objects are needed to have existed at some

point, otherwise the formation of planets and of planetary cores, i.e. the seeds that evolve into gas and ice giant planets, gets impossible, as growth via *dust accretion* seems to be rather inefficient (Ormel, 2017). For example, 10^7 planetesimals with 100 km diameter are needed to form an Earth-sized object. Ten times more mass is needed to form a gas giant core. Reaching these masses solely by dust grain accretion onto a single planetesimal would take many PPDs lifetimes (1 - 10 Myr). Moreover, today we still find such primordial objects in our solar system. But, the formation mechanism of planetesimals is still unclear. This thesis contributes to the understanding of this missing link of planet formation.

The missing link arises from the fact that dust grains inside of PPDs cannot outgrow sub-meter sizes. This is often called *meter-size barrier*, though the largest grain size depends on the radial distance from the star and underlying disk structure, and can be already emerge at mm grain sizes. This growth barrier is a twofold growth barrier. First, particles in the outer part of a PPD start to radially drift inwards faster than they can outgrow drift, leading to a depletion of particles above millimetre. Then, in the inner part of a PPD, the particles relative velocities are found to be higher than the fragmentation velocity and often undergo bouncing (Güttler et al., 2010). This leads to primary destructive particle-particle collisions instead of grain growth.

So far, only two pathways to overcome the growth barriers have been proposed. One way suggests that dust grains could grow extraordinary fluffy and thus surpass this barrier by being massive on one hand, but with low frictional coupling to the gas on the other hand. Thus, drift is strongly reduced and the drift barrier can be surpassed. The fragmentation barrier in the inner disk is surpassed in this model by assuming the collisions to happen at low relative velocities and fluffiness supporting growth. This path of building planetesimals is highly sensitive to many parameters of the PPD, e.g. gas turbulence, and at its best only works within 7 AU, see Kataoka et al. (2013). A second path is stated by Windmark et al. (2012), who estimated the likelihood for a few *lucky winner* particles to reach planetesimal size, as they benefit from the mass transfer in particle-particle collision.

This thesis follows the second path, which states direct formation of planetesimals from small grains via the gravitational collapse of heavily loaded particle clouds (Safronov, 1972). It comes with uncertainties too, as these particle clouds have to form inside of a PPD in the first place. But many mechanisms where found in past years that support this idea, e.g. dust trapping at ice lines, in zonal gas flows, or in vortices. No matter how, the PPD will be assumed to be able to concentrate dust to a sufficient amount, to allow for dust cloud collapse. Once a particle cloud approaches its collapse, certain parameters will be fulfilled, such as dust-to-gas ratio above unity and the particle size can be assumed to be comparably large. This boarder of stability is the situation where the analysis of the particle dynamics and particle cloud collapse within this thesis starts. For that, no specific nature of the dust concentrating mechanism has to be assumed.

Outline of this thesis

The goal of this thesis is to derive a dynamical threshold criterion for a dust particle cloud inside of a PPD to undergo gravitational collapse to a planetesimal, and to characterize the planetesimals formed thereby. The used canonical criterion for cloud collapse is that a cloud has to have a density large enough for its internal gravitational binding to be stronger than the Keplerian shear and stronger than tidal forces. This critical internal density is called *Hill density* and will be introduced in Sec. 3.1.5. In this thesis, a refined criterion is presented that takes the particle turbulent dynamic as well as the particle cloud contraction time into account. Thus, newly derived criterion demands to know the underlying turbulent particle diffusion strength to be expected for such a cloud collapse situation. The *Streaming Instability* (SI), which is a turbulent dust-gas instability acting at dust-to-gas density ratios around and above unity, is found to be a strong source of particle turbulence right on the scales of the collapsing dust cloud. Consequently, in this thesis the SI is investigated in a large parameter study of numerical simulations in 2-d and 3-d. For two different particles sizes, this parameter study sweeps through dust-to-gas ratios from $\varepsilon_0 = 0.1$ up to 1000. In 2-d the radial-azimuthal simulations of this study a new instability was found that is similar to the SI and called *azimuthal Streaming Instability* (aSI). The measured diffusion values can be used to estimate a minimum particle cloud size that allows for cloud collapse to happen. This analytical diffusion limited collapse criterion is then verified in 2-d and 3-d simulations. An additional project investigates aSI-activity in zonal flows, as the SI is often stated to not operate in such pressure bumps. The thesis is structured as follows.

Chapter 2 introduces the gas and the dust as the major ingredients of PPDs. For both, the governing equations are derived, as well as typical PPD parameters, such as the disk gas pressure scale height. For both ingredients the equations of motion is transformed into the shearing sheet approximation. This is a approximative coordinate system allowing for local calculations of the dust and gas dynamics. The coordinate system itself is mimicking an orbital rotation with Keplerian velocity around a central star. Next in this chapter, the particle frictional interaction with the gas is introduced and its consequences on dust and gas dynamics are discussed. The Nakagawa equilibrium solutions for dust and gas are derived, which state an equation for the collective radial dust drift. Also, the SI as major source of particle diffusion in the form of turbulence, is introduced. Lastly, known mechanisms that can trap dust into a local region of a PPD are discussed. They are ultimately needed in PPDs to trigger the SI and cloud collapse.

Chapter 3 presents an analytical study on when a particle cloud is gravitationally unstable. Starting out from the *Jeans criterion* from star formation, different instability criteria for PPDs are derived, such as *Roche* and *Hill* stability. Also, the collapse time for a particle cloud that includes friction is derived. As friction will not allow for clouds to collapse on a free-fall timescale but on a contract timescale at terminal velocity. As most of the simulations performed for this thesis are 2-d simulations, the analytical equivalence of spherical and cylindrical collapse is shown. Finally, the main collapse criterion is derived by setting collapse timescale and diffusion timescale equal. It is derived a second time by solving the dispersion relation for this case. Based on expected solar system values, the criterion is then used to estimate typical planetesimal sizes.

Chapter 4 introduces the used numerical code, which is the PencilCode. Code units are discussed as well as the implementation of the shearing box coordinate system. As for the collapse simulations the self-gravity module of the PencilCode had to be turned on, the gravitational constant in code units is derived. It is a parameter that expresses the total mass in code units and hence needs to be set to Hill density for most of the performed simulations.

Chapter 5 presents the numerical results of the study on the aSIand SI in 2-d radial-azimuthal, 2-d radial-vertical and 3-d simulations. In order to study the pure form of the aSI/SI, stellar gravity and self-gravity is excluded. Particle and gas turbulent strength are investigated and additional parameters for describing the present turbulent instability are discussed. From the measured particle diffusion the corresponding critical length scales for particle cloud collapse are derived, which directly can be used in future research projects. An additional resolution study is performed to ensure the convergence of the results. Lastly, additional simulations with aSI-activity in an artificial zonal flow are presented.

Chapter 6 gives a summary over the results from an 3-d equivalent study on the SI. Turbulent diffusivities are measured an critical collapse length scales derived, that can directly be used in future research projects.

Chapter 7 finally investigates the diffusion limited collapse criterion that has been derived in Chapter 3. It uses two sets of numerical 2-d experiments and one different setup for a 3-d experiment. The 2-d experiments test the validity of the length scale criterion by altering the simulation domain size around the critical length scale. As will be seen, only simulations with a larger domain size do collapse. This shows the correctness of the derived collapse criterion. An additional investigation of this collapse criterion was performed by altering the pressure gradient strength. The properties of the produced planetesimals are recorded and analysed. Lastly, an additional study on cloud collapse in 3-d simulations did not only confirm the collapse criterion, but also showed that strong radial diffusion is sufficiently preventing a collapse. It is not the vertical diffusion that drives collapse in these simulations. If these simulation outcomes are directly applicable to reality is still an open question.

Chapter 8 summarizes the results and discusses them in the context of solar system observations. Possible future experiments and investigations are outlined that state the next steps towards fully understanding the formation of planetesimals in our solar system and in extra-solar systems.

2 Theory of Dust and Gas in Protoplanetary Disks

This chapter introduces the two main players in the context of planet formation in PPDs: gas and dust. PPDs are mainly located in star forming regions where temperatures are around 10 to 20 Kelvin above absolute zero. The material in the gas phase is mainly hydrogen and helium. Every higher element is typically called *metals* by astronomers. The metallicity Z is defined by $Z = (M_{\text{metal}}/M_{\text{total}})$ and typical values for the ISM are found to be $Z \approx 0.01$, see Ansdell et al. (2016).

In PPDs, these metals are found to be condensed out into the form of fluffy dust grains. These grains are µm to cm agglomerates made out of silicates and ices. The mass ratio, at which gas and dust components appear in PPDs, is also called metallicity and assumed to be typically equal to the value of the ISM. Meaning, in PPDs there is expected to be 100 times more mass in the gas than in the dust. This ratio does not come from observational measurements of PPDs as these still lack a full understanding of the observed quantity. A reason for disk observations being difficult comes right from the fact that they mainly consist out of Hydrogen and Helium, both cannot be directly observed. The dust-gas ratio of PPDs can thus only be estimated by indirect measurements. For example by taking the metallicity of stars, e.g. our Sun has a metallicity of $Z_{\odot} = 0.0134$, or by using the values known for the ISM. It is thus certain that the average metallicity of a PPD will be at a similar value. The recent publications that try to determine the dust-to-gas ratio in PPD surveys use the C/O-ratio and find actually values above ≈ 0.01, see Ansdell et al. (2016). As direct consequence emerges the fact that the planetesimal formation mechanism must somehow have the ability to collect enough dust to enhance its concentration locally by orders of magnitude.

In order to understand the dynamics of gas and dust, and in order to investigate planetesimal formation mechanisms, this chapter derives the leading equations for both components. Starting with introducing the internal properties of the gas, i.e. its thermodynamical state and the global pressure gradient, the gas dynamics are calculated using Euler and continuity equations in a local frame of reference. This coordinate system is set to orbit with Keplerian velocity around the central star. It is called *shearing box*, since the Keplerian shear is linearised around its origin. The equations of the dust are then very similar to the gas, since its major difference lies in the fact that the dust is not feeling the gas pressure gradient due to the grains high internal density. But, dust has its own characteristics, such as the dust particle size that is determining the strength of the mutual interplay with the gas via friction. It will be shown that this friction leads to an equilibrium state in which dust is drifting inwards and gas outwards, herein referred to as *Nakagawa drift*, see Nakagawa et al. (1986). The chapter closes with a discussion of possible ways to capture dust locally in non-equilibrium flow features, such as vortices that are capable of enhancing dust concentration locally up to values that trigger gravitational collapse of the trapped particle cloud.

2.1 Gas dynamics

The gas in a PPD has internal properties that dust is lacking, such as a pressure P that comes from the gas temperature T. Since the internal dust particle density is much larger than the gas density, the resulting force from the gas pressure is neglectable. From the inner part, close to the star, the temperature is decreasing towards the outer part of the disk. Hence, a gradient in pressure is acting in radial inward direction. The pressure is supporting the gas radially against stellar gravity, together with the centrifugal force from the circular orbit motion. The structure of this section follows this line of thought. It ends with a transformation

into a local coordinate system that is co-moving on an Keplerian orbit. This allows to follow the gas dynamics without taking care of the central star and large scale, i.e. global, disk dynamics.

2.1.1 Equation of state and adiabatic index

This thesis focuses on local approximations of a PPD and thus one can assume the gas to be isothermal locally, meaning the gas has a constant temperature $T = \text{const.}$ and hence the sound speed c_s is a constant, too. The equation of state is obtained from the ideal gas equation:

$$P = P(\rho) = \underbrace{\frac{k_\text{B} T}{\mu}}_{c_\text{s}^2 = \text{const.}} \rho, \tag{2.1}$$

with molar mass μ and gas density ρ. For this local approximation, and the later presented simulations that are performed in a local disk approximation, one wants to study the evolution of gas density over time. Hence, the gas pressure gradient get rewritten into

$$\frac{\mathrm{d}P}{\mathrm{d}r} = \frac{\mathrm{d}P}{\mathrm{d}\rho}\frac{\mathrm{d}\rho}{\mathrm{d}r}.$$

By using the ideal gas equation (Eq. (2.1)), one can write the radial change in gas pressure as a change in gas density multiplied by the local pressure:

$$\frac{\mathrm{d}P}{\mathrm{d}r} = \frac{P}{\rho}\frac{\mathrm{d}\rho}{\mathrm{d}r} = P\frac{\mathrm{d}\ln\rho}{\mathrm{d}r}.$$

Multiplying this with ρ^{-1} leads to an equation with isothermal sound speed inside:

$$\frac{1}{\rho}\frac{\mathrm{d}P}{\mathrm{d}r} = \underbrace{\frac{P}{\rho}}_{c_\text{s}^2}\frac{\mathrm{d}\ln\rho}{\mathrm{d}r}. \tag{2.2}$$

If one instead is interested in the adiabatic form of this equation, one can consider an adiabatic sound speed together with an adiabatic index γ. The sound speed is known as $c_{\text{s,ad}}^2 = \gamma\frac{P}{\rho}$, with $\gamma = c_p/c_V$, i.e. $\gamma = 5/3$ for a mono-atomic ideal gas, such as helium, or $\gamma = 7/5$ for molecular hydrogen. Plugging

$$\frac{P}{\rho} = \frac{c_{\text{s,ad}}^2}{\gamma}$$

into Eq. (2.2) gives

$$\boxed{\frac{1}{\rho}\frac{\mathrm{d}P}{\mathrm{d}r} = \frac{1}{\gamma}c_{\text{s,ad}}^2\frac{\partial\ln\rho}{\partial r}} \tag{2.3}$$

In this equation, one can see what happens if one assumes isothermal sound speed with $\gamma = 1$. This equation is used for all the following numerical experiments and in general throughout this thesis.

2.1.2 Gas disk pressure scale-height

PPDs do cool significantly fast via their large surface area. This makes them rather small in their vertical extent (D'Alessio et al., 1998). Still, they are vertically stabilized by a pressure gradient on a pressure scale height H, which arises from the increasing gas density towards the disk mid-plane. In a steady state, the vertical gravity must then be equal to the vertical pressure gradient $\rho_\text{g}^{-1}\partial P/\partial z$. The vertical gravity comes mainly from the central star, as typical PPD models use disk masses of $m_\text{disk} \approx 0.01 M_\star$. See Andrews et al. (2013) for further reading, as they suggest a typical disk mass to be 0.6 % of the stellar mass. So the disk self-gravity contribution is negligible in first order approximations. The gravitational pull from the star $g_\star$

on a gas parcel at a distance r from the star and height z over the mid-plane, with $z \ll r$, is then

$$g_{\star,z} = g_\star \sin\theta = \frac{GM_\star}{r^2+z^2} \cdot \frac{z}{\sqrt{r^2+z^2}} \simeq \frac{GM_\star z}{r^3}, \tag{2.4}$$

where $\tan\theta = z/r$. From this, one gets the Keplerian angular frequency

$$\boxed{\Omega = \sqrt{\frac{GM_\star}{r^3}}} \tag{2.5}$$

Following the assumption of an isothermal disk, i.e. taking the equation for the gas pressure from Eq. (2.1), and setting the pressure gradient equal to the vertical gravitational force, one gets

$$c_s^2 \frac{\mathrm{d}\rho_g}{\mathrm{d}z} = -\Omega^2 z. \tag{2.6}$$

This can be solved by simple integration to

$$\rho_g(z,r) = \rho_{g,0}(r) \exp\left(-\frac{z^2}{2H(r)^2}\right), \tag{2.7}$$

where the vertical gas disk scale height is introduced by defining

$$\boxed{H(r) \coloneqq c_s(r)/\Omega.} \tag{2.8}$$

Parametrizing the sound speed via $c_s(r) \sim r^{-\beta_s}$ and one gets a disk aspect ratio of $h(r) \sim r^{-\beta_s+1/2}$. A disk with a constant aspect ratio has $\beta_s = 1/2$, while a flared disk has a larger outer disk aspect ratio, thus $\beta_s < 1/2$. Simple PPD models assume no disk flaring, hence a fixed ratio between gas disk scale-height $H(r)$ and radius r. This is expressed as a fixed *disk aspect ratio* via:

$$\boxed{h = \frac{H}{r} \approx \text{const.}} \tag{2.9}$$

Consequently, a disk with a typical aspect ratio of $h \approx 0.04$ (Hayashi, 1981) has a circumference of $U = 2\pi/hH \approx 157H$, a value that later will be compared to, when a local coordinate system for the numerical experiments is introduced.

Of course, there are more complex PPD models. Some take the ice lines of volatiles into account. They mark the radial distance at which water, or other volatile elements, are no longer solid but gaseous. By being outside of the water ice line, the dust grains are of silicate-ice mixture and therefore have an enhanced stickiness. In comparison, the CO ice line though it produces observational features, does not enhance the stickiness. A special model for our solar system is the *Minimum Mass Solar Nebula* (MMSN) model from Weidenschilling (1977) and Hayashi (1981). In the MMSN model the initial mass distribution in the solar nebula is estimated, from which planets, moons and asteroids have formed. One gains by that a lower threshold for the mass distribution of the early solar system. For this estimate, one takes all planets, together with their moons, as well as the asteroid and Kuiper belt, and then distributes their mass over half the distance to the respective next object. However, the actual original solar nebular is expected to have had a few times more mass than what is observed today. With surface density

$$\Sigma(r) = \int_{-\infty}^{\infty} \rho_g(z,r)$$

the MMSN model can be approximated by

$$\Sigma(r) = 1700\,\mathrm{g/cm^2} \left(\frac{r}{\mathrm{AU}}\right)^{-3/2}.$$

The slop of the MMSN is found to be steeper than in observed PPDs (Andrews et al., 2010) and steeper than what is found in viscously evolving disks (Armitage, 2015), hence one should use this model rather as a reference then as a prescription of a PPD.

2.1.3 Global pressure gradient

An object on a circular in the solar system of today moves around the Sun with Keplerian orbital speed of

$$\boxed{v_\mathrm{K} = \Omega r\,,} \tag{2.10}$$

with distance to the central star r and orbital frequency Ω.

A main feature of a protoplanetary disk now is its high gas content, leading to a different equilibrium state in which the gas is not travelling with Keplerian orbital speed but instead slower. This comes from its intrinsic, radially inward pointing gradient in the gas density and hence existing gas pressure gradient. The change in orbital velocity then depends on the strength of this additional force from the pressure, as it is stabilising now the gas together with the orbital centrifugal force, see Adachi et al. (1976) and Weidenschilling & Davis (1985).

In a gas free 1-d case, in radial direction, the gravitational acceleration is

$$g = \frac{GM_\star}{r^2} = \Omega^2 r = \frac{v_\mathrm{K}^2}{r}\,.$$

The additional acceleration g' due to the force from the gas pressure gradient, adds to the gas velocity via:

$$g' \coloneqq -\frac{1}{\rho_\mathrm{g}}\frac{\partial P}{\partial r}$$

Consequently, the gas is in hydrostatic equilibrium under the condition of

$$\frac{u(r)^2}{r} = \frac{v_\mathrm{K}^2}{r} + g'\cdot r \quad\Leftrightarrow\quad u(r) = v_\mathrm{K}\cdot\sqrt{1+\frac{g'\cdot r}{v_\mathrm{K}^2}} \overset{g'\ll g}{\approx} v_\mathrm{K} + \frac{g'\cdot r}{2v_\mathrm{K}^2}v_\mathrm{K}\,.$$

This can be expressed as deviation from the original Keplerian orbital velocity via

$$\boxed{\Delta u = v_\mathrm{K} - u = v_\mathrm{K} - v_\mathrm{K} - \frac{g'r}{2v_\mathrm{K}^2}v_\mathrm{K} = -\frac{g'}{2g}v_\mathrm{K}} \tag{2.11}$$

Using the conditions for an isothermal disk, of $P = c_\mathrm{s}^2\rho$ and $H = c_\mathrm{s}/\Omega$, this can be well parametrized in the often used beta-parameter $\beta_{\ln(\rho)}$ via

$$g' = -\frac{1}{\rho}\frac{\partial P}{\partial r} = -\frac{c_\mathrm{s}^2}{\rho}\frac{\partial \rho}{\partial r} = -c_\mathrm{s}^2\frac{\partial \ln\rho}{\partial r} = -\frac{Hc_\mathrm{s}\Omega}{r}\frac{\partial \ln\rho}{\partial \ln r} =: -\beta_{\ln(\rho)}c_\mathrm{s}\Omega\,.$$

One can also use the disk aspect ratio $h = H/r$ in order to become an even shorter expression for $\beta_{\ln(\rho)}$:

$$\beta_{\ln(\rho)} = -h\frac{\partial \ln\rho}{\partial \ln r}\,. \tag{2.12}$$

With $\beta_{\ln(\rho)}$, the acceleration from the pressure gradient becomes

$$\boxed{g' = -c_\mathrm{s}\Omega\beta_{\ln(\rho)}\,.} \tag{2.13}$$

Now, defining the sub-Keplerianess η of the gas velocity u as a factor between Keplerian velocity and its

deviation from it, via

$$u_\varphi = v_\mathrm{K}(1-\eta)\,, \tag{2.14}$$

one finds $\eta = -\frac{g'}{2g}$. Consequently,

$$\eta = \frac{g'}{2g} = \frac{-\frac{1}{\rho}\frac{\partial P}{\partial r}}{2\Omega^2 r} = -\frac{c_\mathrm{s}\Omega\beta_{\ln(\rho)}}{2\Omega^2 r} = -\frac{c_\mathrm{s}}{2\Omega r}\beta_{\ln(\rho)} \tag{2.15}$$

and η gets a rather compact form of

$$\eta = -\frac{1}{2}\frac{H}{R}\beta_{\ln(\rho)}\,, \tag{2.16}$$

or with $v_\mathrm{K} = \Omega r$ and $c_\mathrm{s} = H\Omega$, this can also be written as

$$\eta = -\frac{1}{2}\beta_{\ln(\rho)}\frac{c_\mathrm{s}}{v_\mathrm{K}}\,.$$

Typically, the orbital velocity at a distance of $r = 1\,\mathrm{AU}$ around a star with mass $M_\star = M_\odot$ is about $32\,\mathrm{km/s}$. With a PPD typical value for $\eta \approx 10^{-3}$, the gas orbits at $1\,\mathrm{AU}$ with a velocity of

$$u_\varphi = (1-\eta)\,v_\mathrm{K} \approx 31.968\,\frac{\mathrm{km}}{\mathrm{s}} \approx 114\,\frac{\mathrm{km}}{\mathrm{h}}\,.$$

This velocity difference might look insignificant, but the resulting radial particle drift due to friction with the gas, challenges the planet formation community now for decades. As will be seen in the following of this chapter, once particles grow to a size where they decouple from the gas, they try to move with the full Keplerian speed, hence radial drift of the particles and the gas, as well as turbulent dynamics arise.

2.1.4 Viscous stress

A canonical prescription of turbulent gas transport inside of PPDs is the α-model. It was introduced for the use in black hole accretion disks by Shakura & Sunyaev (1973) and describes the accretion rate from turbulent viscosity. It got also a widely used prescription of turbulent angular momentum transport in all kind of astrophysical accretion disks. In general, α is a parameter that measures viscous stress originating from gas turbulence and magnetic fields that couple onto the ionized part of the gas. Sometimes, α is determined from observationally measuring accretion rates. But, a certain α-value does not state anything on the largest turbulent eddy scale or on the appearing turbulent velocity (Cuzzi et al., 2001).

Per definition, the α-value scales the turbulent viscosity, see Shakura & Sunyaev (1973). Lin & Papaloizou (1980) and Pringle (1981) introduced a splitting of the α-parameter onto a turbulent velocity component and a turbulent length scale, i.e. eddy size, via

$$\nu = \alpha^s c_\mathrm{s} \cdot \alpha^{1-s}\mathrm{H}\,.$$

Here, s is the free parameter that controls the splitting into the two fractions of turbulent velocity and eddy length scale. A low s value state the turbulent eddies to be small but quickly turning, a high value would mean to have large, slowly turning eddies. Thus, this parameter will be between $0 \leq s \leq 1$, as turbulent eddies will not turn over faster than sound speed, as this would rise shocks, and will not be larger than the disc scale height. Following the estimations by Cuzzi et al. (2001), this parameter is assumed to be $s = 1/2$ in PPDs. In their paper, they assume the largest eddies within PPDs are only allowed if they have a Rossby number of $R_\mathrm{O} = 1$. This ensures that all turbulence is 3-d and isotropic, and hence a Kolmogorov cascade via vortex stretching is allowed. The Rossby number for a turbulent eddy in a PPD can be expressed via

$$R_\mathrm{O} \simeq \frac{u}{\Omega_0 l} = \frac{\omega}{\Omega_0}\,,$$

with Ω_0 the disk orbital frequency, and $\omega \simeq u/l$ the largest eddy frequency. The argument in Cuzzi et al. (2001) is that an eddy with $\omega < \Omega_0$ cannot follow a Kolmogorov cascade. Hence, in a PPD, the largest turbulent eddy that cascades to smaller scales has to satisfy $R_\mathrm{O} \geq 1$. The assumption herein made, is that the eddy resides then on the largest scale for a given α, which means $R_\mathrm{O} = 1$.

One can do now the following ansatz:

$$u = \alpha^s c_\mathrm{s} \qquad \text{and} \qquad l = \alpha^{1-s} \mathrm{H}. \tag{2.17}$$

By combining this ansatz with the Kolmogorov cascade (Kolmogorov, 1991) for turbulence in gas, which states for a turbulent cascade the energy transfer rate to be a scale-invariant:

$$\underbrace{u^2}_{\text{specific energy}} \cdot \underbrace{u/l}_{\text{dissipation time}} = \frac{u^3}{l} = \text{energy transfer rate} = \text{const.}$$

And by using the assumptions of being in a point, where $R_\mathrm{O} = 1$, one gets

$$R_\mathrm{O} = 1 = \frac{\alpha^s c_\mathrm{s}}{\Omega_0 \alpha^{1-s} \mathrm{H}} = \alpha^{2s-1} \quad \forall\ \alpha \qquad \Rightarrow s = 1/2$$

Under this assumption, the α-turbulence in a PPD distribute equally into the largest eddy size and highest turbulent velocity. Moreover, since the slope of a line in the u-l diagram for R_0 is with $u \sim l$ steeper than for the Kolmogorov cascade, with $u \sim l^{1/3}$, the turbulent cascade of an turbulent eddy in a PPD will probably always loose energy into the disk. Hence, the gas turbulence could be weaker on smaller scales than what is expected from this extrapolation in α down to smaller scales.

From the above, one can state a definition for the measurement of α in simulations via

$$\boxed{\alpha = \nu/(c_\mathrm{s} H)\,,} \tag{2.18}$$

where to calculate ν the Reynolds stress component $A_{r\varphi}$ is typically used. Canonical values for α in PPDs are found from simulations of turbulent instabilities, i.e. the *Magneto-Rotational Instability* (MRI) (Balbus & Hawley, 1991), the vertical shear instability (Nelson et al., 2013; Flock et al., 2017), also called Goldreich-Schubert Fricke instability, or the convective overstability (Klahr & Bodenheimer, 2003; Lyra & Klahr, 2010; Raettig et al., 2013; Klahr & Hubbard, 2014). They are mostly around $\alpha = 10^{-4}$ to 10^{-3}. Lately also observational upper limits on α were tried to be measured, see Teague et al. (2016), Flaherty et al. (2016), and Flaherty et al. (2017).

2.1.5 Equation of motion in the shearing sheet approximation

The dynamics of gas in a PPD are described by momentum equation, which is an Euler equation with different terms for the individual physical processes that induce momentum:

$$\underbrace{\frac{\mathrm{d}\vec{u}}{\mathrm{d}t}}_{(1)} + \underbrace{(\vec{u}\nabla)\,\vec{u}}_{(2)} = \underbrace{-\frac{1}{\rho}\nabla P}_{(3)} + \underbrace{\frac{1}{\rho}\vec{J}\times\vec{B}}_{(4)} \underbrace{-\frac{1}{\tau_\mathrm{s}}(\vec{u}-\vec{v})}_{(5)} \underbrace{-\nabla\Phi}_{(6)} + \text{other forces} \tag{2.19}$$

This equation describes the change over time of the velocity field of a fluid (1): It changes due to advection (2), and other physical processes that are described on the right hand. These are the gas pressure (3) (see Sec. 2.1.3), magnetic fields that couple onto a charge current (4), friction with particles that have a velocity $\vec{v}$ and a friction coefficient of τ_s^{-1} (5) (see Sec. 2.2.1), and gravity (6). But, many other terms might enter this equation. Term (4) will be dropped in the following as no magnetic fields are discussed.

The shearing sheet coordinate system

For this thesis, scales $L \ll H$ are of interest, where H is the pressure scale height. These scales L are so small that a numerical computation in the form of a global disk, covering the whole PPD is not feasible.

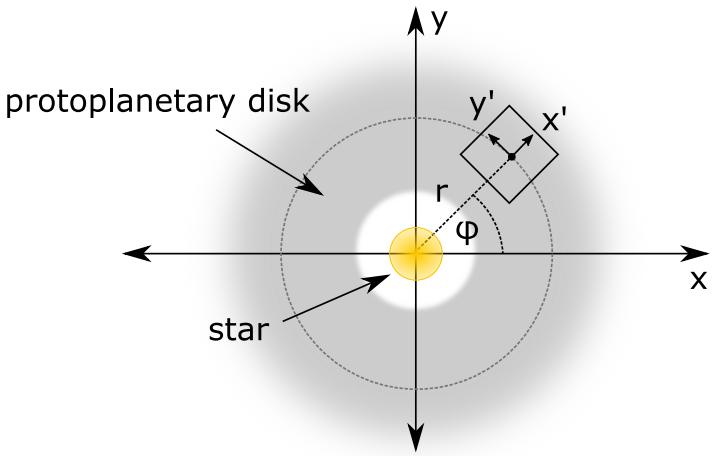

Figure 2.1: Since protoplanetary disks are relatively flat, they are often described in cylindrical coordinate systems to omit vertical gravity. But, cylindrical coordinate systems are global and once one is interested in the micro-physics that is happening on the scales of a percent of a disk scale height H, one cannot use a global coordinate system anymore. Hence the *shearing sheet*, or *shearing box*, coordinate system was introduced. In this drawing it is the primed system with coordinates x' and y'. It is a coordinate system that orbits around the star with the Keplerian velocity at its origin. Hence, unity vectors in $\hat{\varphi}$ transform into $\hat{y}$ of the primed system. Consequent, the Keplerian shear has to be linearised in the shearing sheet coordinate system. In order to have the radial boundary condition periodic, one include a shear periodic boundary condition that adjusts the azimuthal velocity when surpassing the radial boundary.

Comparing the scales of interest with the circumference of a disk, see Eq. (2.9), shows that these scales are six orders of magnitude smaller than the full azimuthal extent of a disk. Moreover, if one is interested in investigating the local micro-physics of gas, and later including dust, a local approximation is needed. This is done by changing from the global Cartesian coordinate system, into a local Cartesian coordinate system at a distance R_0 from the central star that itself orbits around the central star with Keplerian velocity $v_\mathrm{K}(R_0)$. Linearising the local shear that arises due to the Keplerian rotation is sufficient to mimic the dynamics of a co-rotating system, without having that intrinsic rotation explicitly calculated. As assumed by the linearisation, this local coordinate system will only allow for scales that are much smaller than R_0, in order to hold the approximation of being local and able to linearise, see below. This type of coordinate system is called *shearing sheet*, or *shearing box* coordinate system.

The goal of this section is to derive the equations of motion for such a shearing sheet coordinate system. The derivation starts from Eq. (2.19), but the coordinate transformations will only affect the left hand side terms, i.e. the time derivative (1) and the advection term (2). This is only partly true, since also the gravitational potential will change, as shown later in this section. Since a PPD is a rotating system that transformation will introduce Coriolis forces. Fig. 2.1 shows the three needed coordinate systems:

(a) the Cartesian coordinate system around the star, with axis (x, y, z)

(b) the cylindrical coordinate system around the star, with axis (r, φ, z)

(c) the local Cartesian coordinate system that orbits the central star in a distance R_0, with axis (x', y').

Linearising the Keplerian shear

But first, the Keplerian shear needs to be linearised around R_0. For this, a Taylor expansion of Eq. (2.5) around R_0 at the point $p = R_0 + \Delta r$ can be done, which leads to

$$T_N\Omega(R_0;p) = \sum_{n=0}^{N} \frac{f^{(n)}(p)}{n!}(x-p)^n \approx \Omega_0 + \Omega'(r=R_0)\cdot(\cancel{R_0} + \Delta r - \cancel{R_0}) = \Omega_0\left[1 - \frac{3}{2}\frac{\Delta r}{R_0}\right],$$

where $\Omega_0 = \Omega(R_0)$. Using the primed radial coordinate, Δr becomes x', and by using $v = \Omega R_0$ the orbital velocity becomes its linearised form

$$v = \Omega_0 \left(1 - \frac{3}{2}\frac{x'}{R_0}\right) R_0 = \Omega_0 R_0 - \frac{3}{2}\Omega_0 x' \,.$$

Thus, the linearised Keplerian shear velocity is approximated in the co-rotation frame as

$$\boxed{v_{\text{shear}} = -\tfrac{3}{2}\Omega_0 x' \,.} \tag{2.20}$$

Transforming the advection term (2) into the shearing sheet coordinate system

As stated, the terms (1) and (2) can be dealt with separately. Starting with the advection term (2) is recommended, as this one is easier to transform. In the following the Einstein index notation is used, where there is an unwritten but existing sum over all indices that appear twice. Hence, term (2) is $(\vec{u}\nabla)\,\vec{u} = u_i \partial_i u_j$. This now is getting transformed into the primed Cartesian coordinate system via

$$u \quad \rightarrow \quad u' + u'_0 = u' - \frac{3}{2}\Omega_0 x' \hat{y}' \,,$$

where $\nabla' \equiv \nabla$ since $x' \ll R$ and $y' \ll R$. Thus, (2) becomes

$$u_i \partial_i u_j = \left[\left(\vec{u}' + \vec{u}'_0\right)\right]\left(\vec{u}' + \vec{u}'_0\right) = \underbrace{\left[\left(\vec{u}' + \vec{u}'_0\right)\nabla'\right]\vec{u}'}_{\text{(2a)}} + \underbrace{\left[\left(\vec{u}' + \vec{u}'_0\right)\nabla'\right]\vec{u}'_0}_{\text{(2b)}}$$

with

$$\text{(2a)} = \left(u_i + u_0\right)\partial_i u_j = u_i \partial_i u_j + u_{0,i}\partial_i u_j = \left(\vec{u}'\nabla'\right)\vec{u}' + u_{0,y}\frac{\partial \vec{u}'}{\partial y'}$$

$$\text{(2b)} = \left(u_i + u_{0,y}\delta_{iy} y\right)\partial_i u_{0,y}\delta_{jy} = u_i \partial_i u_{0,y}\delta_{jy} + u_{0,y}\delta_{iy}\partial_i u_{0,y}\delta_{jy} = \hat{y}'\left(-\frac{3}{2}\Omega_0 u_x\right) + \underbrace{u_{0,y}\partial_y u_{0,y}}_{=0}$$

The last term in (2b) is zero, since the Keplerian shear velocity changes only in the radial direction, but not in the azimuthal direction, see Eq. (2.20). Reassembling both terms, (2) from Eq. (2.19) becomes

$$(2) = \left(\vec{u}'\nabla'\right)\vec{u}' + u'_{0,y}\frac{\partial \vec{u}'}{\partial y'} - \frac{3}{2}\Omega u'_x \hat{y}'$$

Transforming velocity time derivative (1) into the shearing sheet coordinate system

In order to rewrite term (1) of the momentum equation, one has to express $\frac{\mathrm{d}\vec{u}}{\mathrm{d}t}$ in polar coordinates. In contrast to the Nabla operator, now the time derivative of the velocity field introduces on one hand the shear advection and on the other hand the Coriolis forces. Thus, one has to take care of the time derivative of the unit vectors of the coordinate system and it is a good choice to do this carefully:

$$\frac{\mathrm{d}\vec{u}}{\mathrm{d}t} = \frac{\mathrm{d}}{\mathrm{d}t}\left(\dot{r}\hat{r} + r\dot{\varphi}\hat{\varphi}\right) = \ddot{r}\hat{r} + \dot{r}\dot{\varphi}\hat{\varphi} + \dot{r}\dot{\varphi}\hat{\varphi} + r\dot{\varphi}\frac{\mathrm{d}\hat{\varphi}}{\mathrm{d}t} \tag{2.21}$$

From $\hat{\varphi} = (-\sin\varphi, \cos\varphi, 0)^{\mathsf{T}}$ follows

$$\frac{\mathrm{d}\hat{\varphi}}{\mathrm{d}t} = -\cos\varphi\dot{\varphi}\hat{x} - \sin\varphi\dot{\varphi}\hat{y} = -\dot{\varphi}\hat{r}$$

and Eq. (2.21) becomes

$$\frac{\mathrm{d}\vec{u}}{\mathrm{d}t} = \frac{\partial \vec{u}}{\partial t} + \underbrace{2\dot{r}\dot{\varphi}\hat{\varphi} - r\dot{\varphi}^2\hat{r}}_{(\triangle)}\,.$$

The right term $(\triangle)$ has now to be transformed into the primed coordinate system via

$$x' = r - R_0, \qquad y' = R_0\left(\varphi - \varphi_0 - \Omega_0 t\right), \qquad z' = z, \qquad \text{and} \qquad t' = t\,. \tag{2.22}$$

Using this transformation, one gets the following table that translates the expressions within $(\triangle)$:

$$\hat{\varphi} = \hat{y}' \qquad\qquad \dot{\varphi} = \Omega_0 + \frac{1}{R_0}\underbrace{\frac{\partial y'}{\partial t}}_{\dot{y}'} = \Omega_0 + \frac{1}{R_0}u_y'$$

$$\hat{r} = \hat{x}' \qquad\qquad r = R_0 + x'$$

$$\dot{r} = \dot{x}' = u_x' \qquad\qquad \varphi = \frac{y'}{R_0} + \varphi_0 + \Omega_0 t$$

Hence, the term $(\triangle)$ becomes

$$\begin{aligned}(\triangle) &= 2\dot{x}'\left(\Omega_0 + \frac{1}{R_0}u_y'\right)\hat{y} - \underbrace{\left(x' + R_0\right)}_{x' \ll R_0}\left(\Omega_0 + \frac{1}{R_0}u_y'\right)^2\hat{x} \\ &= 2u_x'\Omega_0\hat{y} + \underbrace{2u_x'u_y'\hat{y}}_{\approx 0} - R_0\left[\Omega_0^2 + \frac{2\Omega_0 u_y'}{R_0} + \left(\frac{u_y'}{R_0}\right)^2\right]\hat{x} \\ &= 2u_x'\Omega_0\hat{y} - R_0\Omega_0^2\hat{x} - 2\Omega_0 u_y'\hat{x}\,.\end{aligned}$$

Transformed momentum equation

Putting everything together, and renaming the primed system to unprimed, i.e. switching into the primes system as our new coordinate system, the momentum equation becomes

$$\frac{\partial \vec{u}}{\partial t} + \left(\vec{u}\nabla\right)\vec{u} + u_{0,y}\frac{\partial \vec{u}}{\partial y} - \vec{f}\left(\vec{u}\right) - \underbrace{R_0\Omega_0^2\hat{x}}_{(*)} = -\frac{1}{\rho}\nabla P + \ldots \tag{2.23}$$

with Coriolis forces

$$\vec{f}\left(\vec{u}\right) = \begin{pmatrix} 2\Omega_0 u_y \\ -\frac{1}{2}\Omega_0 u_x \\ 0 \end{pmatrix}. \tag{2.24}$$

The term with the $(*)$ is a constant in this equation which represents the equilibrium velocity profile $R_0\Omega_0^2 = -\frac{\partial \Phi}{\partial r}\,|_{r=R_0}$ that is introduced in the coordinate transformation. This can be dropped on the arrival in the primed coordinate system, as it is part of the global gravitational potential. It can be found by approximating the gravitational force of a point mass $M_\star$ in radial direction to first order, and evaluating this force at $x = 0$:

$$g_{\star,x} = -\frac{GM_\star}{\left(R_0 + x\right)^2} = -\frac{GM_\star}{R_0^2}\frac{1}{1 + 2\frac{x}{R_0} + \frac{x^2}{R_0^2}} \approx -\frac{GM_\star}{R_0^2}\left(1 - 2\frac{x}{R_0}\right)$$

The final momentum equation of the fluid reads in the shearing sheet coordinate system as

$$\boxed{\frac{\partial \vec{u}}{\partial t} + \left(\vec{u}\nabla\right)\vec{u} + u_{0,y}\frac{\partial \vec{u}}{\partial y'} - f\left(\vec{u}\right) = -\frac{1}{\rho}\nabla P - \frac{1}{\tau_\mathrm{s}}\left(\vec{u} - \vec{v}\right) - \nabla\Phi' + \ldots} \tag{2.25}$$

where Φ' now is the change in the gravitational potential from the potential of the central star as point mass. The dots represent additional momenta that act on the fluid, for example coupling of magnetic fields or molecular viscosity. And the same can be done for the continuity equation, leading to:

$$\frac{\partial \rho_g}{\partial t} = -u_{0,y} \frac{\partial \rho_g}{\partial y} - \nabla \left(\rho_g \vec{u} \right) \tag{2.26}$$

Together, these equations give a good approximation of the gas evolution in a local patch of a PPD. In the continuity equation, the first term on the right hand side is again the advection of density by the Keplerian shear flow, the latter two terms come from transforming the original $\nabla \left(\rho_g \vec{u} \right)$ term likewise as done with the equation of motion.

As a consequence of the coordinate transformation, the gas movement, including pressure support and Keplerian shear, in the shearing frame changed from Eq. (2.14) to

$$u_\varphi(x) = -\frac{3}{2}\Omega x - v_K \eta = -\frac{3}{2}\Omega x + \frac{1}{2}\beta_{\ln(\rho)} c_s \,.$$

2.2 Dust dynamics

The dynamics of the dust are very similar to the one of the gas, but without the effect of the gas pressure. The Euler equation is identical to Eq. (2.25), but without term (3),

$$\frac{\partial \vec{v}}{\partial t} + (\vec{v}\nabla)\,\vec{v} + u_{0,y} \frac{\partial \vec{v}}{\partial y'} - \vec{f}(\vec{v}) = -\frac{1}{\tau_s}(\vec{v} - \vec{u}) - \nabla \Phi' + \ldots \,, \tag{2.27}$$

where Φ' again is the change in the gravitational potential, from the potential of the central star as point mass. Here, $\vec{f}$ is again the Coriolis force, see Eq. (2.24). And the continuity equation reads:

$$\frac{\partial \rho_d}{\partial t} = -u_{0,y} \frac{\partial \rho_d}{\partial y} - \nabla \left(\rho_d \vec{v} \right) \tag{2.28}$$

Though the equations of motion are merely similar, introducing dust into a coupled system changes the dynamics of both components tremendously. Friction couples two systems that have different natural azimuthal velocities. The dust wants to orbit with Keplerian velocity v_K whereas the pressure supported gas tries to orbit with $(1-\eta)v_K$, or ηv_K in the primed system. The section introduces the friction timescale τ_s, with its canonical representation in dimensionless Stokes number St, and deals with the consequence of dust inward drift.

As stated earlier, the interaction of dust and gas happens via the friction force, i.e. (5) in Eq. (2.19). This friction introduces interesting dynamics into the system. This section will thus also discuss the most important effects: The relative drift of dust and gas that can be derived by solving for an equilibrium solution of the two components by treating them as homogeneous fluids. The *Streaming Instability* (SI) is a linear (Youdin & Goodman, 2004; Youdin & Johansen, 2007) and non-linear (Johansen & Youdin, 2007) instability of the dust-gas mixture. It arises once the dust-to-gas density ratio

$$\varepsilon = \frac{\rho_d}{\rho_g} = \frac{Z}{1-Z} \overset{Z \ll 1}{\approx} Z$$

reaches unity, where Z is in the beginning of this chapter defined (local) metallicity. Often Z is also used to describe the disk column metallicity, i.e. the ratio of dust and gas in an infinitely extended cylinder in vertical direction. From the latter, one cannot derive the mid-plane dust-to-gas ratio, since it gets a function of H, and dust scale height $\mathrm{H_d}$.

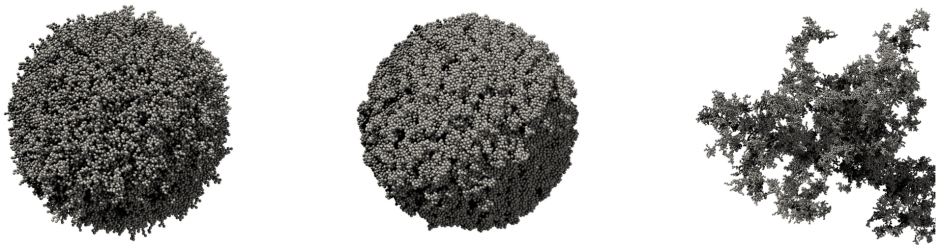

Figure 2.2: Computer model of compact and fluffy dust aggregates. They consist of 10^4 to 10^5 monomers and have a diameter of 100 µm. Dust grains can be compact (center) or fluffy (right). It is still unclear, what the optimal shape of dust grains in PPDs is, but they will tend to have a combination of both, being fluffy but not to fragile (left). They can grow by mutual sticking only as long as relative velocities are below $\lesssim 1\,\mathrm{m/s}$, see Seizinger & Kley (2013). *Source: Seizinger et al. (2013)*

2.2.1 Particle friction and Stokes number

Dust particles and icy aggregates can have complicated shapes and properties. Visit Dominik & Tielens (1997), Paszun & Dominik (2009), Seizinger et al. (2013), and Wada et al. (2013) for further reading. Though they might share an identical mass m and size a, they can have different filling factors, sometimes called fluffiness, and they might be far from an ideal spherical shape, see Fig. 2.2. Describing the interaction with an underlying gas flow would seem complicated, if not the physical description of a particle interacting with a gas flow via a friction force comes to rescue. In the herein considered cases, the friction forces are proportional to the velocity difference, times a constant:

$$\vec{f}_{\mathrm{drag}} = -A\,(\vec{v} - \vec{u})$$

The constant A is a parametrized strength of the frictional coupling. A feather and a bowling ball have different constants, as a feather easily gets affected by air currents, the bowling ball does not. This constant has the units of s^{-1} and thus one calls A^{-1} the *friction time* τ_{s} and writes

$$\boxed{\vec{f}_{\mathrm{drag}} = -\tfrac{1}{\tau_{\mathrm{s}}}\,(\vec{v} - \vec{u})\,.} \tag{2.29}$$

The friction time is often also called *stopping time*, since it resembles the time a particle needs to adjust to the underlying flow. From this, the stopping length l_{s} can be derived as

$$l_{\mathrm{s}} = \int_0^\infty \mathrm{d}t\,(\vec{v}(t) - \vec{u}) = v_0 \int_0^\infty \mathrm{d}t e^{-t/\tau_{\mathrm{s}}} = v_0 \tau_{\mathrm{s}}\,,$$

where v_0 is the absolute value of the velocity difference between dust and gas.

A picture to have in mind is throwing a ball while being underwater. If the ball is small, i.e. a tennis ball, the ball will within a few seconds lose its initial velocity due to friction with the water and instead will follow the flow of the water current. If the ball is large, i.e. a bowling ball, the ball will not be affected much by the water current and instead follow its trajectory until gravity takes over and it sinks to the ground. This gedanken experiment can also be done in PPDs, where tiny dust particles might couple to the sub-Keplerian gas flow within a fraction of an orbital timescale, or where a planetesimal will basically never adjust to the gas flow.

Though Eq. (2.29) is correct, for the dust within a PPD the friction time in the two extreme cases from the gedanken experiment has to be calculated differently. In the first case, the particle radius a is smaller than the mean-free-path λ_{free} and the particle is in the *Epstein* drag regime, which is the regime where particle and gas can both be treated as particles. If the particle size is larger than the mean-free-path, the particle is in the *Stokes* drag regime, which is the fluid regime where a large particle is embedded into the

gas, described as a fluid, see Epstein (1924) and Stokes (1851). The friction times are

$$\tau_{\mathrm{s}} = \begin{cases} \tau_{\mathrm{s}}^{(\mathrm{Ep})} = \dfrac{3m}{4\rho_{\mathrm{g}} v_{\mathrm{th}} A_{\mathrm{p}}}, & \text{for } a \leq \dfrac{9}{4}\lambda_{\mathrm{free}} \quad \text{(Epstein)} \\ \tau_{\mathrm{s}}^{(\mathrm{St})} = \dfrac{4a}{9\lambda_{\mathrm{free}}} \cdot \tau_{\mathrm{s}}^{(\mathrm{Ep})}, & \text{for } a > \dfrac{9}{4}\lambda_{\mathrm{free}} \quad \text{(Stokes)} \end{cases}$$

where A_{p} is the particle surface area and $v_{\mathrm{th}} = \sqrt{8/\pi} c_{\mathrm{s}}$ the mean thermal velocity of the gas molecules. The mean-free-path within a PPD can be approximated via

$$\lambda_{\mathrm{free}} \simeq \frac{m_g}{\sigma_{\mathrm{mol}} \rho_{\mathrm{g}}},$$

following Okuzumi et al. (2012), which is valid as long as the particle background is not moving. With the geometrical collisional cross section of the hydrogen gas molecules of $\sigma_{\mathrm{mol}} \approx 2 \cdot 10^{-15} \mathrm{cm}^3$, this leads to a mean-free-path of

$$\boxed{\lambda_{\mathrm{free}}(r) = 120\,\mathrm{cm} \left(\frac{r}{5\,\mathrm{AU}}\right)^{11/4} \left(\frac{152\,\mathrm{g/cm^3}}{\rho_{\mathrm{g}}(r)}\right)} \tag{2.30}$$

in the mid-plane. So, it is of order of meters and consequently most of the dust particles will be in the Epstein regime! Further, assuming the particles can be described as being spherical, the stopping time in the Epstein regime can be expressed via

$$\tau_{\mathrm{s}}^{(\mathrm{Ep})} = \frac{\rho_{\bullet} a}{\rho_{\mathrm{g}} v_{\mathrm{th}}}.$$

Typically, the stopping time is normalized by the characteristic timescale $1/\Omega$, i.e. normalized on orbital timescales. The stems from the radial drift of particles which scales via $v_r \sim \tau_{\mathrm{s}}\Omega$. The emerging dimensionless quantity is the *Stokes number*

$$\boxed{\mathrm{St} \coloneqq \tau_{\mathrm{s}}\Omega\,.} \tag{2.31}$$

The Stokes number will be used throughout this thesis. Note that it is defined independently from the underlying drag regime, i.e. it is a valid quantity in both, Epstein and Stokes drag regime, or any other drag regime. The Stokes number is hence a description of how long a particle takes to couple to the gas, in terms of orbits.

2.2.2 Collective drift: Nakagawa solution for dust and gas

Nakagawa et al. (1986) and Weidenschilling, Stuart J. (1987) found that dust and gas in a PPD have an equilibrium solution that surprisingly determines the fate of the dust to be doomed. The result is a steady inward drift of larger particles that is much faster transporting dust radially inwards than it can grow by collisions.

Starting from the equations of motion for a homogeneous gas and dust, means one can drop advection terms. The equations for the gas velocity $\vec{u}$ and the dust velocity $\vec{v}$ are

$$\frac{\mathrm{d}\vec{u}}{\mathrm{d}t} = -A\rho_{\mathrm{d}}(\vec{u} - \vec{v}) - \frac{GM_\star}{r^3}\vec{r} - \frac{1}{\rho_{\mathrm{g}}}\nabla P \tag{2.32}$$

and

$$\frac{\mathrm{d}\vec{v}}{\mathrm{d}t} = -A\rho_{\mathrm{g}}(\vec{v} - \vec{u}) - \frac{GM_\star}{r^3}\vec{r} - \underbrace{\frac{1}{\rho_{\bullet}}\nabla P}_{\simeq 0}\,. \tag{2.33}$$

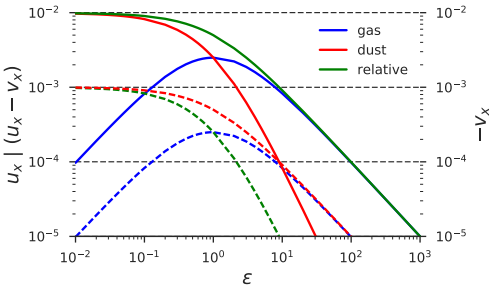

(a) Radial gas velocity and radial drift $u_x - v_x$ are positive. Radial dust velocity is negative (inwards).

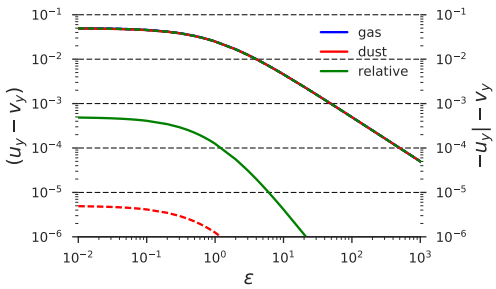

(b) Azimuthal dust and gas velocities are both negative. Relative drift $u_y - v_y$ is positive.

Figure 2.3: Radial (left) and azimuthal velocities (right) of dust (red) and gas (blue), and their relative velocity (green), as calculated from the Nakagawa solution in Eq. (2.36) and Eq. (2.37). Plotted for $\mathrm{St} = 0.1$ (solid) and $\mathrm{St} = 0.01$ (dashed) particles, with $\eta = 0.005$, and $c_\mathrm{s} = 1$. The radial gas velocity is positive (outwards, left y-axis), whereas the dust and the relative velocity are negative (inwards, right y-axis). The absolute values of azimuthal dust and gas velocity are almost identical and sub-Keplerian (negative). The maximum relative azimuthal velocity is 10^{-3} for $\mathrm{St} = 0.1$ and 10^{-5} for $\mathrm{St} = 0.01$. Even for $\varepsilon = 1000$ the relative azimuthal velocity deviates from the Keplerian velocity by 0.1 % in both components, dust and gas.

In these equations, the acceleration by the gas pressure gradient onto the dust particles can be neglected as their internal density $\rho_\bullet$ is orders of magnitude larger than ρ_g. The coefficient A is the drag coefficient that is different for the Stokes and the Epstein regime, see Sec. 2.2.1:

$$A = \begin{cases} \dfrac{c_\mathrm{s}}{\rho_\bullet R} & R \lesssim \dfrac{9}{4}\lambda_\mathrm{free} \qquad \text{(Epstein)} \\ \dfrac{3 c_\mathrm{s} \lambda_\mathrm{free}}{2\rho_\bullet R^2} & R > \dfrac{9}{4}\lambda_\mathrm{free} \qquad \text{(Stokes for } \mathrm{Re} \geq 1) \end{cases} \tag{2.34}$$

The Eq. (2.32) and Eq. (2.33) are in Cartesian coordinates and need to be rewritten in polar coordinates and then linearised in velocity, similar to Sec. 2.1.5. The cylindrical coordinates are $\vec{r} = r\,(\cos\varphi, \sin\varphi)^\mathsf{T}$ with

$$\frac{\mathrm{d}\vec{r}}{\mathrm{d}t} = \dot{r}\hat{r} + r\dot{\varphi}\hat{\varphi}$$

The z-component is found to be zero in the equilibrium solution, which is clear since there is no reason for vertical motions. The radial and azimuthal velocity components can be treated separately.

Radial dust velocity component

Starting with the radial dust component, it reads

$$\begin{aligned} \frac{\mathrm{d}}{\mathrm{d}t} v_r = \frac{\mathrm{d}}{\mathrm{d}t}\left(\vec{v}\hat{r}\right) &= \left(\frac{\mathrm{d}\vec{v}}{\mathrm{d}t}\right)\hat{r} + \vec{v}\dot{\hat{r}} = \left(\frac{\mathrm{d}\vec{v}}{\mathrm{d}t}\right)\hat{r} + \left(\dot{\varphi}\hat{\varphi}\right)\cdot\left(r\dot{\varphi}\hat{\varphi} + \dot{r}\hat{r}\right) \\ &= -A\rho_\mathrm{g}\left(v_r - u_r\right) - \underbrace{\frac{GM}{r^3}}_{\Omega^2 r} r + \underbrace{\left(r\dot{\varphi}\hat{\varphi}\right)\left(\dot{\varphi}\hat{\varphi}\right)}_{r\dot{\varphi}^2 = \frac{v_\varphi^2}{r}} + \underbrace{\left(\dot{r}\hat{r}\right)\left(\dot{\varphi}\hat{\varphi}\right)}_{=0} \\ &= -A\rho_\mathrm{g}\left(v_r - u_r\right) - \Omega^2 r + \frac{v_\varphi^2}{r} \end{aligned}$$

Now, one can transform the velocities to be expressed as relative to the Keplerian orbital velocity $\vec{v}_{\rm K} = r\Omega\hat{\varphi}$. For the gas and dust velocities this yields, respectively:

$$\vec{U} = \vec{u} - \vec{v}_{\rm K} \qquad \text{and} \qquad \vec{V} = \vec{v} - \vec{v}_{\rm K}\,.$$

Consequently, with $v_{\rm K} = \vec{v}_{\rm K}\hat{\varphi}$, the equation of radial motion component for the dust gets

$$\frac{\mathrm{d}}{\mathrm{d}t}v_r = -A\rho_{\rm g}\left(V_r - U_r\right) - \Omega^2 r + \frac{\left(V_\varphi - v_{\rm K}\right)^2}{r}$$

where

$$\frac{\left(V_\varphi - v_{\rm K}\right)^2}{r} = \frac{1}{r}\left(\underbrace{V_\varphi^2}_{\approx 0} + 2V_\varphi r\Omega + r^2\Omega^2\right) = 2V_\varphi\Omega + r\Omega^2\,,$$

where $V_\varphi^2 = (\eta v_{\rm K})^2 \approx 0$. Thus,

$$\frac{\mathrm{d}}{\mathrm{d}t}v_r = -A\rho_{\rm g}\left(V_r - U_r\right) + 2\Omega V_\varphi\,.$$

Azimuthal dust velocity component

One can do a similar derivation for the azimuthal velocity component of the dust:

$$\begin{aligned}\frac{\mathrm{d}}{\mathrm{d}t}v_\varphi &= \left(\frac{\mathrm{d}}{\mathrm{d}t}\vec{v}\right)\hat{\varphi} + \vec{v}\dot{\hat{\varphi}} = \frac{\mathrm{d}\vec{v}}{\mathrm{d}t}\hat{\varphi} + \vec{v}\cdot\left(-\dot{\varphi}\hat{r}\right) = -A\rho_{\rm g}\left(v_\varphi - u_\varphi\right) - \underbrace{\left(r\dot{\varphi}\hat{\varphi} + \dot{r}\hat{r}\right)\dot{\varphi}\hat{r}}_{\dot{r}\dot{\varphi} = \frac{v_\varphi v_r}{r}} \\ &= -A\rho_{\rm g}\left(V_\varphi - U_\varphi\right) - \frac{\left(V_\varphi + r\Omega\right)V_r}{r} = -A\rho_{\rm g}\left(V_\varphi - U_\varphi\right) - \underbrace{\frac{V_\varphi V_r}{r}}_{\approx 0} + \Omega V_r\end{aligned}$$

Where the term $1/r$ is small since the distance r is very large. This leads to

$$\frac{\mathrm{d}}{\mathrm{d}t}v_\varphi \approx -A\rho_{\rm g}\left(V_\varphi - U_\varphi\right) - \Omega V_r\,.$$

The gas velocity components

A similar procedure for the equation of motion for the gas leads to

$$\frac{\mathrm{d}}{\mathrm{d}t}u_r = -A\rho_{\rm d}\left(U_r - V_r\right) + 2\Omega U_\varphi - \frac{1}{\rho_{\rm g}}\frac{\partial P}{\partial r}\,,$$

for the radial velocity. Now the last term is the additional gas pressure. The azimuthal reads

$$\frac{\mathrm{d}}{\mathrm{d}t}u_\varphi = -A\rho_{\rm d}\left(U_\varphi - V_\varphi\right) - \Omega U_r\,.$$

The Nakagawa drift

Nakagawa et al. (1986) and Weidenschilling, Stuart J. (1987) showed that in these derived solutions of the four velocities components a steady state solution exists. It can be found by using $\partial/\partial t \equiv 0$, and by assuming homogeneous dust and gas densities. Which means the dust-to-gas ratio is fixed. The original solution is

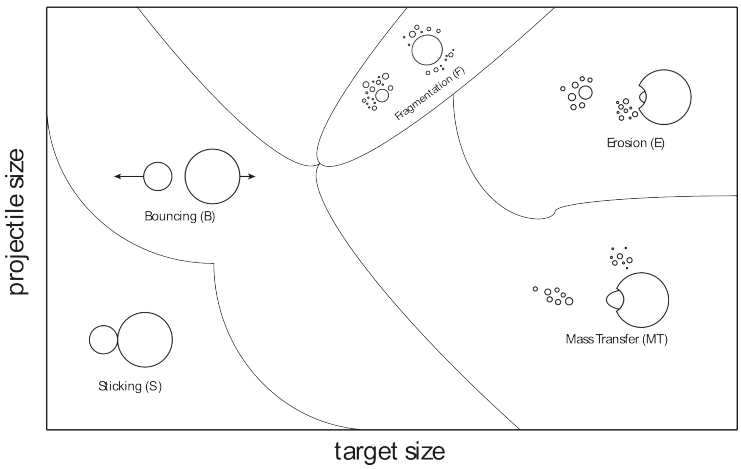

Figure 2.4: Collisional outcome for mutual silicate grain collisions. Schematic plot of the analysis from in Güttler et al. (2010) and Windmark et al. (2012). For the MMSN at 1 AU particle sizes above a few cm can hardly be achieved. Though, beyond the ice line, water ice could improve the ability of grains to stick (Gundlach & Blum, 2015; Lorek et al., 2016) (CO^2 in contrast has sticking properties that compare rather to silicates, see Musiolik et al. (2016)), this is not enough to have grains surpass the fragmentation barrier. Still, if some would do, they will end up at the drift barrier, see Fig. 2.5. *Source: Windmark et al. (2012)*

this set of four equations:

$$U_r = \frac{\rho_\mathrm{d}}{\rho_\mathrm{g}+\rho_\mathrm{d}} \frac{2D\Omega}{D^2+\Omega^2} \eta v_\mathrm{K} \qquad U_\varphi = \left(\frac{\rho_\mathrm{d}}{\rho_\mathrm{g}+\rho_\mathrm{d}} \frac{D^2}{D^2+\Omega^2} - 1 \right) \eta v_\mathrm{K}$$

$$V_r = -\frac{\rho_\mathrm{g}}{\rho_\mathrm{g}+\rho_\mathrm{d}} \frac{2D\Omega}{D^2+\Omega^2} \eta v_\mathrm{K} \qquad V_\varphi = \frac{\rho_\mathrm{g}}{\rho_\mathrm{g}+\rho_\mathrm{d}} \frac{D^2}{D^2+\Omega^2} \eta v_\mathrm{K}$$

With the simplifiction of $D = A\left(\rho_\mathrm{g}+\rho_\mathrm{d}\right)$, and η is the parametrized deviation from the Keplerian velocity, see Eq. (2.16).

These set of solutions can be further simplified by using the dust-to-gas ratio $\varepsilon = \rho_\mathrm{d}/\rho_\mathrm{g}$ and expressing the particle drag coefficient A via the Stokes number:

$$\mathrm{St} = \tau_\mathrm{s}\Omega = \frac{\rho_\bullet a}{\rho_\mathrm{g} v_\mathrm{th}}\Omega = \frac{\Omega}{\rho_\mathrm{g} A}\,.$$

Using in this equation the formulation of the Epstein drag coefficient of

$$A = \frac{v_\mathrm{th}}{\rho_\mathrm{g} a}\,,$$

with particle size a and thermal speed, which is typically the sound speed $v_\mathrm{th} \equiv c_\mathrm{s}$. From this, the radial drift of the gas becomes:

$$\frac{U_r}{\eta v_\mathrm{K}} = \frac{\rho_\mathrm{d}}{\rho_\mathrm{g}+\rho_\mathrm{d}} \frac{2D\Omega}{D^2+\Omega^2} - 1 = \frac{\varepsilon}{\varepsilon+1} \frac{2\Omega^2(\varepsilon+1)}{\mathrm{St}^2\left(\frac{\Omega^2}{\mathrm{St}^2}(\varepsilon+1)^2+\Omega^2\right)}$$

This can be simplified by using

$$\lambda := \frac{1}{(1+\varepsilon^2)+\mathrm{St}^2}\,. \tag{2.35}$$

The simplified version of the Nakagawa drift is then

$$\frac{U_r}{\eta v_\mathrm{K}} = 2\varepsilon \mathrm{St}\lambda\,.$$

Doing this steps for both components of the gas and the dust velocity, leads to a short writing of the set of equations as:

$$\boxed{\frac{U_r}{\eta v_\mathrm{K}} = 2\varepsilon\mathrm{St}\lambda \qquad \text{and} \qquad \frac{U_\varphi}{\eta v_\mathrm{K}} = -\left(1+\varepsilon+\mathrm{St}^2\right)\lambda \qquad \text{(Gas)}} \tag{2.36}$$

$$\boxed{\frac{V_r}{\eta v_\mathrm{K}} = -2\mathrm{St}\lambda \qquad \text{and} \qquad \frac{V_\varphi}{\eta v_\mathrm{K}} = -\left(\varepsilon+1\right)\lambda \qquad \text{(Dust)}} \tag{2.37}$$

The difference of dust and gas velocity is the relative Nakagawa drift, herein this thesis used and defined in its absolute value:

$$\boxed{\zeta_\mathrm{Nakagawa} \coloneqq |\vec{v}-\vec{u}| = \sqrt{\left(V_r-U_r\right)^2+\left(V_\varphi-U_\varphi\right)^2}} \tag{2.38}$$

2.2.3 The drift and fragmentation barrier

If dust and gas are in their velocity equilibrium state, the Nakagawa solutions showed for this case how the dust steadily drifts inwards while gas is transported outwards, see also Whipple (1972). The reason for the drift is a centrifugal deficiency of the dust. As particle Stokes numbers are low, the dust adjusts to the local gas velocity via friction in less than one orbit. But, the dust can not maintain this sub-Keplerian orbital velocity because it is not stabilized by the force from the gas pressure gradient. It hence lacks a compensation for the lower centrifugal force and the particle feels a net inward force. When it moves inward, it has to readjust to the now even lower gas velocity via momentum transport onto the gas, thus the dust gives momentum to the gas. Thus, as consequence from momentum conservation, the gas has to move outwards. But, this does not implicate a gas depleted inner disk. Since the gas pressure scale height is larger than the dust disk scale height, the gas can easily get replenished by the upper parts of the disk its atmosphere. For the dust, the drift states a problem, since in an isolated disk it cannot be replenished from outwards. The dust thus radially drifts into the star and no planets do form. Which cannot be as we have strong evidence for their existence. The expected drift velocities peak at a value of 100 m/s for dust particle of 100 cm in size. Taking smaller dust as an example, in a MMSN a 10 cm particle would drift 100 AU in only 30 000 years, see Brauer et al. (2008).

But, there is a second problem with the dust growth that comes from particle-particle collisions. These high drift velocities, and also the expected *Root-Mean-Square* (rms)-velocities of cm-sized dust leads to a stall in dust growth when they collide. Fig. 2.4 shows the outcome of these collisions. Here, schematically shown is the collisional outcome for pure silicate dust grains. A more detailed review can be found, e.g., in Birnstiel et al. (2016). Only small dust grains can stick. Further increasing the particle sizes leads to bouncing (Zsom, A.; Ormel, C. W.; Güttler, C.; Blum, J.; Dullemond, 2010), erosion and fragmentation, see Brauer et al. (2008) and Birnstiel et al. (2009). The only path through this fragmentation barrier lies in the possibility of small grains hitting a larger grain and the latter then is able to grow via mass transfer. Still, this process only works as long as only a few large grains exist, and if the small-grain on large-grain scenario stays the dominant collision mode. If instead if larger grains exist, they will destroy themselves by mutual collisions. In the end this scenario of growth via mass transfer is unlikely, since no process is known that reduces the supply on larger grains to a level that a few of them are able to surpass the fragmentation barrier via mass transfer.

This can be best seen in the results of a numerical dust evolution model from Birnstiel et al. (2012), as shown in Fig. 2.5. This dust evolution model incorporates the growth of dust via sticking, dust fragmentation due to collisions, where the relative velocities take the drift velocity and the particle rms-velocities into account and the radial drift. The dust rms-velocity comes from gas turbulence, where in the shown model the gas

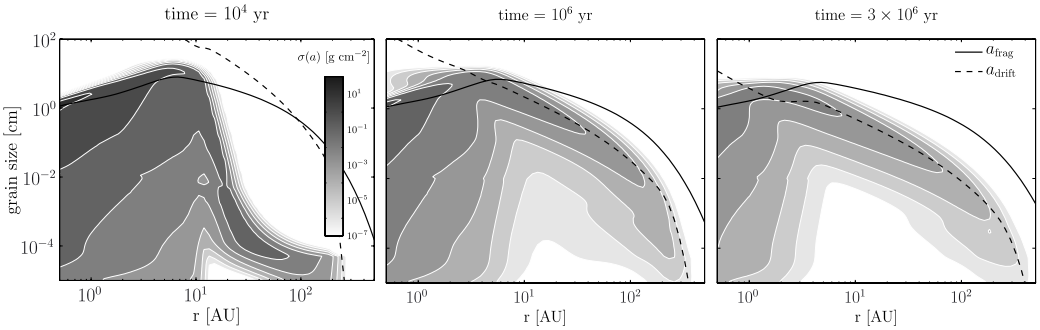

Figure 2.5: Dust evolution model from Birnstiel et al. (2012) that incorporates the growth of dust via sticking, dust fragmentation due to collisions from relative velocities and the radial dust drift. It shows that growth gets stalled by two barriers, the fragmentation barrier (solid line) and the drift barrier (dashed). The three pictures show the temporal evolution of the dust surface density for an initial smooth disk of small dust particles. The disk has a gas turbulence level of $\alpha = 10^{-3}$, see Sec. 2.1.4. In the first picture, the dust could grow more easily in the denser inner disk, but the growth is stalled by the fragmentation barrier. Later times bring the drift barrier down, as the dust density depletes, since growth takes longer. The outer disk consequently gets drift limited. In this model, no planetesimals form and all the dust vanishes into the central star. *Source: Birnstiel et al. (2012)*

turbulence has a level of $\alpha = 10^{-3}$, see Sec. 2.1.4. The results show that growth gets stalled by two growth barriers: The fragmentation barrier (solid line) and the drift barrier (dashed). The three pictures show the temporal evolution of the dust surface density for an initial smooth disk of small dust particles. In the first picture, the dust could grow fast in the denser inner disk, but the growth gets stalled by the fragmentation barrier. Later times bring the drift barrier down, as the dust density depletes. This comes from the fact that with less dust the time needed to grow becomes longer. The outer disk consequently gets earlier drift limited. In this model, no planetesimals from direct grow form and all the dust vanishes into the central star. If one would add planetesimal formation by adding a unspecified collapse mechanism, this process would represent an additional sink for the dust density and consequently the dust growth gets drift limited already at earlier times throughout the whole disk.

2.2.4 The streaming instability and its azimuthal counterpart

A second consequence from the difference in particle and gas velocity arises once inhomogeneities in the dust-to-gas ratio are considered. The Nakagawa solution for the gas (Eq. (2.36)) and for the dust (Eq. (2.37)) both scale with ε. Consequently, the solution for the velocities changes, if a perturbation in ε is introduced. A patch with a slightly higher dust concentration will drift slower and dust from underdense regions can fall into this patch from the radial outward direction. This is then even further enhancing the locally higher dust concentration making this patch even drift less and would be a run away process if not non-linearities come into play.

The linear instability was first endeavoured in Youdin & Goodman (2004) and a simplified version of the equations can be found in Jacquet et al. (2011). They named it the *Streaming Instability* (SI), and found it by solving the dispersion relation for this problem in r-z direction, i.e. the azimuthal symmetry is assumed. The found instability does not require self-gravity or stellar gravity to act. Already in pure hydrodynamical dust-gas calculations, see Youdin & Johansen (2007), the instability can act quite strongly. The growth timescales of this instability are found to be faster than the radial drift timescales. Thus, Youdin & Goodman (2004) suggested that the SI might be the trigger for planetesimal formation, as it can significantly concentrate dust locally and this maybe even up to values that trigger collapse. However, the latter has never been fully proven, though claims are out there, i.e. from Johansen et al. (2015) or Simon et al. (2016). The open question in their work is whether the collapse comes from SI alone or is assisted by stellar gravity together with extremely high dust-to-gas ratios.

In the works of Johansen & Youdin (2007), and every work that followed, the SI is not considered as

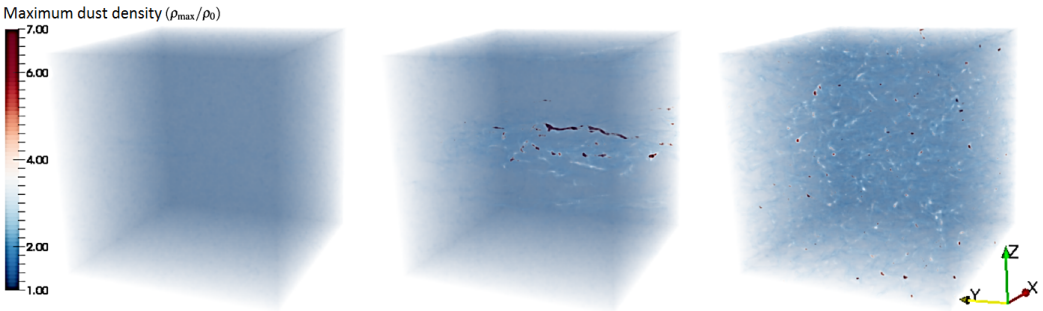

Figure 2.6: Time evolution of the 3-d SI with $\varepsilon_0 = 1$ and $\mathrm{St} = 0.1$. Initial dust density distribution is homogeneous, but then SI modes emerge from noise perturbations in the dust and gas densities. The shown simulation domain size is $L = 0.1\,\mathrm{H}$. The maximum dust density fluctuations reached in a single grid cell is ≈ 10. The last snapshot (right) shows the SI to populate the full simulation domain when saturated.

a linear instability anymore, as they find the non-linear phase to drive the dust dynamics in particle-gas simulations. The non-linear phase of the SI comes with additional strong turbulence in the dust particle field, see Fig. 2.7b. This turbulence stalls the maximum dust concentration at values of $\varepsilon_{\mathrm{max}}/\varepsilon_0 \approx 10$, where ε_0 is the initial mean dust-to-gas ratio. In Johansen & Youdin (2007), the non-linear SI is found to occur for particles with $\mathrm{St} = 0.1$ and 1.0, at dust-to-gas ratios above unity. The SI is found to work the best for marginally coupled particles of around $\mathrm{St} \approx 0.1 \ldots 1$. But, the instability can be found for Stokes numbers as low as $\mathrm{St} = 10^{-3}$, see Yang et al. (2016), and up to $\mathrm{St} = 4$, as found by Carrera et al. (2015).

So far, in basically all the published work, the SI has been considered in either 3-d simulations or in 2-d simulations, where the 2-d simulations only covered the r-z plane. No analysis has been done on the SI in radial azimuthal direction, besides a first prove of its existence in Raettig et al. (2015). The reason is, it was believed from the solution of the dispersion relation (Youdin & Goodman, 2004) that the SI is an instability acting in radial-vertical direction only.

In Chapter 5 of this thesis the results from the performed numerical study on the SI in the r-φ plane found in fact a very similar non-linear instability. The found instability shows a mode pattern and parameters very similar to the SI. Since the equivalence of this new-found instability to the SI is not analytically proven, it is named *azimuthal Streaming Instability* (aSI). Note that in the following the term SI is sometimes also used for the aSI, since the physical implication from both instability as equal. A sample for the aSI, in comparison with the SI is shown in Fig. 2.7.

After the work of Johansen & Youdin (2007), no further investigations into the pure SI has been performed, until recently in Squire & Hopkins (2017); Squire & Hopkins (2017) the SI was becoming part of a more general family of instabilities, the *resonant drag instabilities*. From the works that followed Johansen & Youdin (2007) they all included stellar gravity and self-gravity. Out of them, the work of Bai & Stone (2010a) is notable, as they found the SI to be the particular instability that prevents the dust settling to the disk mid-plane, where before the Kelvin-Helmholtz instability was believed to do so.

The mentioned parameter study from Chapter 5 investigates a parameter space of $\varepsilon = 0.1$ up to $\varepsilon = 1000$, on scales of $L = 0.1\,\mathrm{H}$ down to $0.001\,\mathrm{H}$, for $\mathrm{St} = 0.1$ and $\mathrm{St} = 0.01$ particles. For the whole parameter space, the SI growth rates were calculated. They are shown in Fig. 2.8 and Fig. 2.9, for the two Stokes numbers respectively. The growth rate s in this plot is the expression for

$$s = \Im(\omega)\,,$$

for the SI amplitude $\sim \exp\left(\mathrm{i}\vec{k}\vec{x} - \mathrm{i}\omega t\right)$. It can be seen that at dust-to-gas ratios well above unity, the SI does not die out. The fastest growing modes are found to shift towards smaller wavelengths, but most of the k_x-k_z wavenumber space gets populated with SI modes. For comparison, the domain sizes of the simulation translate into $\log_{10}(k_x \eta r)$ of 0.5, 1.5, and 2.5, respectively. This concludes that the aSI should not be found for $\mathrm{St} = 0.1$ and $\varepsilon = 0.1$, but still the SI should show active modes, specially in vertical direction. As can be

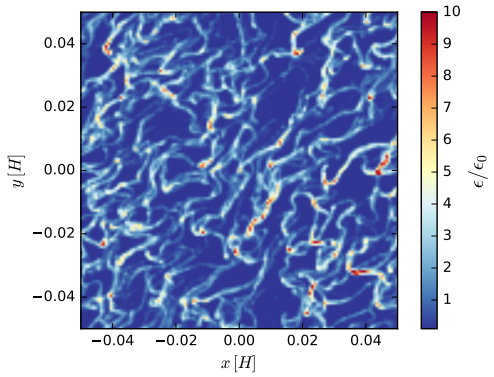

(a) aSI in r-φ plane at 128^2 resolution.

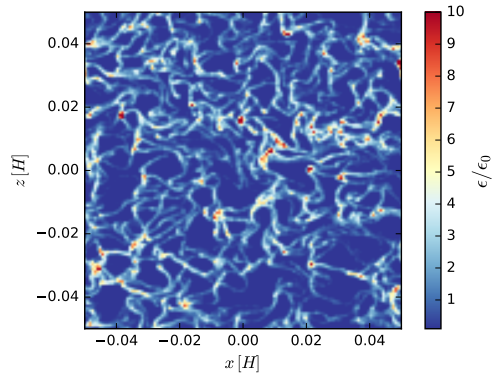

(b) SI in r-z plane at 128^2 resolution.

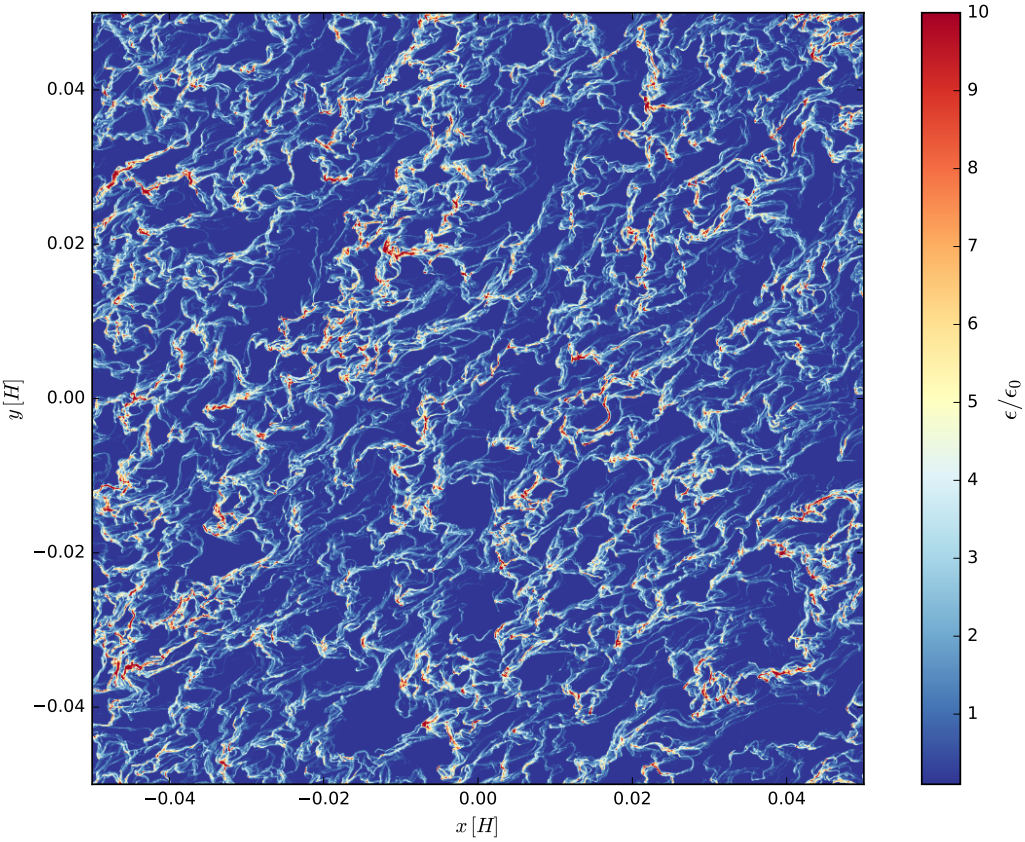

(c) aSI in r-φ plane at 1260^2 resolution.

Figure 2.7: Examples for the saturated non-linear SI from gravity-free simulations of $\mathrm{St} = 0.1$ particles. Plotted is the local dust-to-gas ratio that was initially set homogeneously with $\varepsilon = 1$. The two snapshots (top) are from low resolution 2-d simulations with $N^2 = 128^2$. The left is set up in the r-φ plane and thus shows the aSI. The right is set up in the r-z plane and thus shows the SI. The simulations in the lower figure is identical to the one of the top-left, but with almost ten times higher resolution. Interesting to note, the SI and the aSI both look very similar. The difference in the mode pattern arises from the additional Keplerian shear which stretches and tilts the aSI-modes in azimuthal direction. The higher resolution allows for aSI-modes with higher wavenumber and thus the mode pattern looks similar but is also refined.

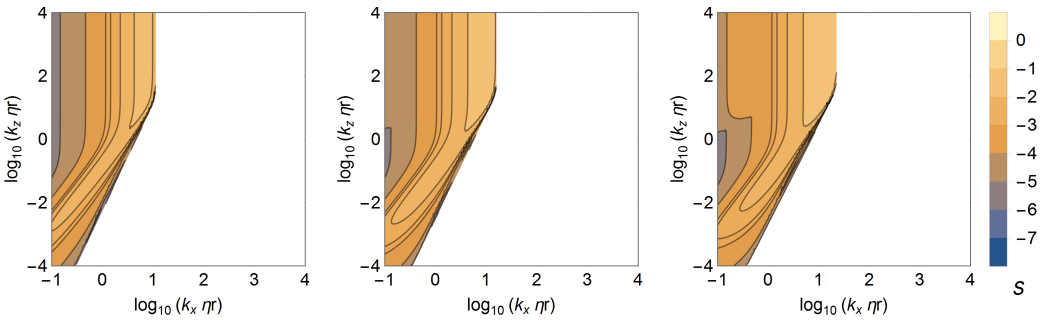

(a) $\tau_s = 0.1$ - $\varepsilon = 0.1$ **(b)** $\tau_s = 0.1$ - $\varepsilon = 0.3$ **(c)** $\tau_s = 0.1$ - $\varepsilon = 0.5$

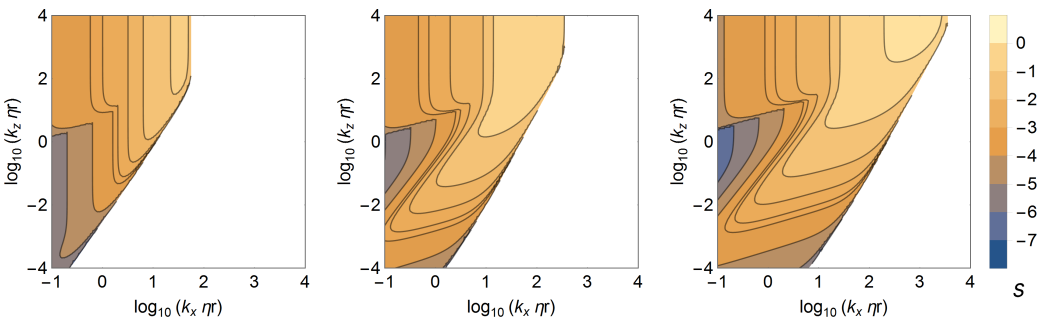

(d) $\tau_s = 0.1$ - $\varepsilon = 1.0$ **(e)** $\tau_s = 0.1$ - $\varepsilon = 3.$ **(f)** $\tau_s = 0.1$ - $\varepsilon = 10.$

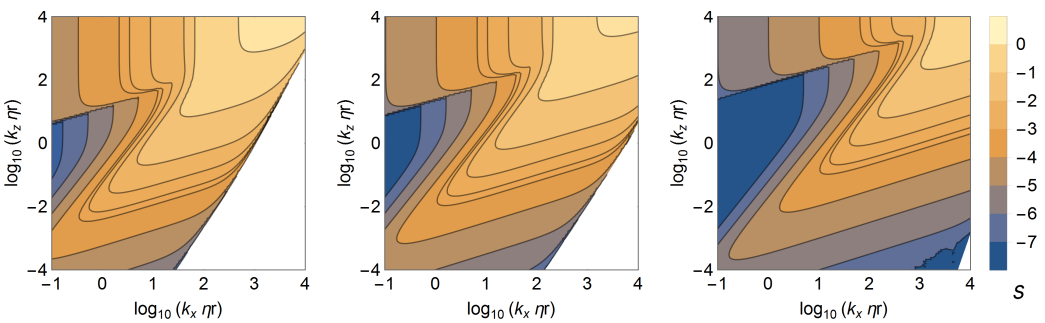

(g) $\tau_s = 0.1$ - $\varepsilon = 30.$ **(h)** $\tau_s = 0.1$ - $\varepsilon = 100.$ **(i)** $\tau_s = 0.1$ - $\varepsilon = 1000.$

Figure 2.8: Logarithmic growth rate s (colour) for the SI for $\mathbf{St} = 0.1$ particles. Calculation based on Squire & Hopkins (2017).

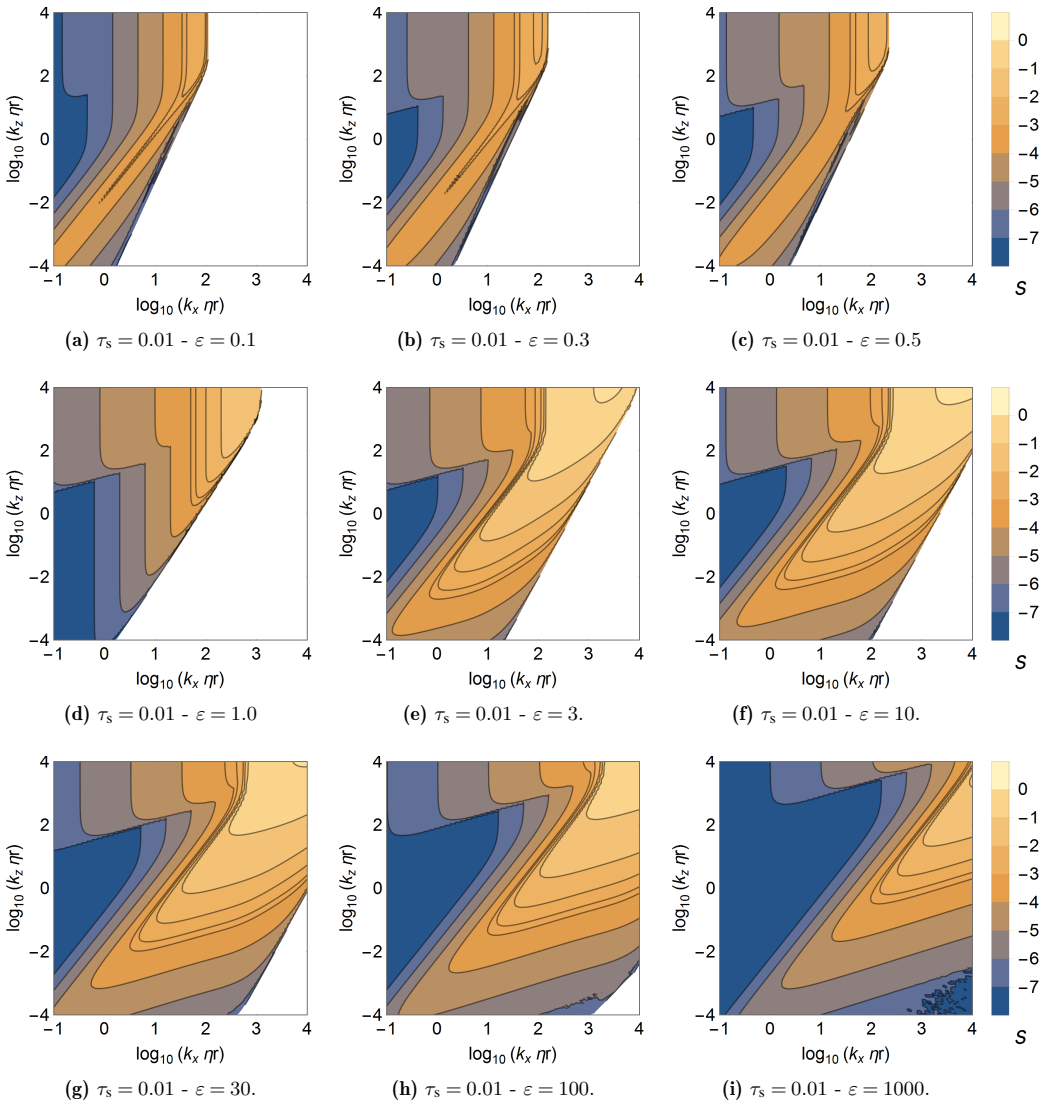

(a) $\tau_s = 0.01$ - $\varepsilon = 0.1$ **(b)** $\tau_s = 0.01$ - $\varepsilon = 0.3$ **(c)** $\tau_s = 0.01$ - $\varepsilon = 0.5$

(d) $\tau_s = 0.01$ - $\varepsilon = 1.0$ **(e)** $\tau_s = 0.01$ - $\varepsilon = 3.$ **(f)** $\tau_s = 0.01$ - $\varepsilon = 10.$

(g) $\tau_s = 0.01$ - $\varepsilon = 30.$ **(h)** $\tau_s = 0.01$ - $\varepsilon = 100.$ **(i)** $\tau_s = 0.01$ - $\varepsilon = 1000.$

Figure 2.9: Logarithmic growth rate s (colour) for the SI for $\mathbf{St} = 0.01$ particles. Calculation based on Squire & Hopkins (2017).

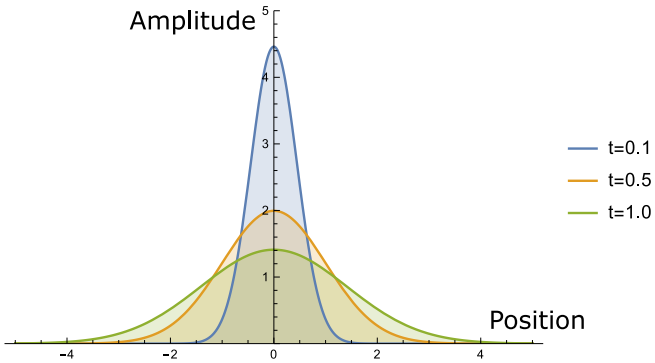

Figure 2.10: The solution (Eq. (2.41)) of the diffusion equation (Eq. (2.40)) for three different time steps. The diffusion coefficient in this sample is $D = 1$ and the initial number of particles is $N_\mathrm{p} = 5$. Over time the initial peak spreads out by the underlying diffusion, but the Gaussian shape is maintained.

seen in Fig. 5.2 this is right the numerical finding. In contrast, for $\mathrm{St} = 0.01$ and at the same dust-to-gas ratio, the numerical simulations confirm that both, SI and aSI modes are active. Additional simulations of the SI in 3-d simulations are performed that show mode patterns as in Fig. 2.6. Since in 2-d the particles can actually surround gas parcels, and thus the gas must stream through these dust particle filaments, in 3-d the gas can flow above such a dust filament. The consequence is that the SI can be weaker in 3-d, in terms of ability to concentrate dust and in terms of particle turbulence strength.

2.2.5 Turbulent particle diffusion

The non-linear SI is a turbulent instability of the dust together with the gas, though the gas densities and velocities only change by one percent at maximum, the dust is strongly affected. The dust velocities get strongly turbulent as the back-reaction onto the gas is changing due to local dust fluctuations. These dust density fluctuations itself are only stable for a short time and continuously form and vanish.

As mentioned in the introduction, the measurement of this particle turbulence in terms of particle diffusion, is a main topic of this thesis. The measurement is discussed in the following. The derivation follows the lecture of *Prof. Dr. Martin Keller* from the *TU Dresden* and of *Prof. Dr. Karl-Heinz Gericke* from the *TU Braunschweig*.

Diffusion equation and coefficient

The physical problem of describing the thermal conduction through a rod, the dispersion of a gas in another gas, and the movement of micro-organism, they all have in common that these processes show the same behaviour, they are spreading in the direction of the negative gradient of that quantity. This process is called diffusion. In order to simplify things, herein the derivation of the diffusion is restricted to one dimension: x. Diffusion has two main properties, one is the conservation of the total of the quantity, the other is the flow from a large concentration of that quantity, to a lower concentration.

By looking at the rate J at which a quantity q is flowing from x_0 to $x_0 + \Delta x$, one can try to understand this phenomenon. Since the total of the quantity is conserved, one can write

$$\frac{\partial}{\partial t} \int_{x_0}^{x_0+\Delta x} q\,(t,x)\,\mathrm{d}x = J\,(t,x_0) - J\,(t,x_0+\Delta x)\,.$$

Dividing this equation by Δx and taking the limit of $\Delta x \to 0$ gives directly the equation of conservation for the quantity q:

$$\frac{\partial}{\partial t} q\,(t,x) = -\frac{\partial}{\partial x} J\,(t,x) \tag{2.39}$$

As the process is diffusion, one knows that the rate $J(t,x)$ is determined by the spatial change in concentration $u(t,x)$. Hence, the diffusion rate has to be a function of that concentration gradient, i.e.

$$J(t,x) = F\left(\frac{\partial}{\partial x} q(t,x)\right),$$

i.e. a constant concentration results in no diffusion $F(0) = 0$. Since the flow of the concentration happens from the higher to the lower concentration, one can do a linear ansatz, which is also called *Fick's first law*:

$$J(t,x) = -D\frac{\partial q}{\partial x}(t,x),$$

where the mobility D is introduced that is scaling the ability of a concentration to flow along a infinitesimal small distance. Plugging this into Eq. (2.39) leads to *Fick's second law*, the diffusion equation:

$$\boxed{\frac{\partial q}{\partial t} = D\frac{\partial^2 q}{\partial x^2}} \tag{2.40}$$

This differential equation is an equation of second order in space and first order in time. To solve it, one needs to state two spatial (initial) conditions and one temporal condition. Assuming particles in a turbulent fluid, at $t = 0$ all N_p particles are at $x = 0$ and within a $\mathrm{d}x$ of space. The following ansatz is a valid solution of this equation:

$$q(t,x) = \alpha t^{-1/2} \exp\left(-\frac{x^2}{4Dt}\right),$$

where α is a parameter that expresses the number of particles, as will be seen in the following. Now, for $t \to 0$ its $q(t = 0, x) = 0$ for all x, except $q(t = 0, x = 0) = \infty$. Since all N_p particle are initially at the same spot. Using the conservation of total number of particles, leads to

$$N_\mathrm{p} = \int_{-\infty}^{\infty} q(t,x)\,\mathrm{d}x = \alpha \int_{-\infty}^{\infty} t^{-1/2} \exp\left(-\frac{x^2}{4Dt}\right)\mathrm{d}x = 2\alpha(\pi D)^{1/2}.$$

Solving for α and plugging it into the ansatz leads to

$$q(t,x) = N_\mathrm{p}\sqrt{\frac{1}{4\pi Dt}} \exp\left(-\frac{x^2}{4Dt}\right). \tag{2.41}$$

In Fig. 2.10 shown, is an example for the time evolution of this solution for the diffusion problem.

Looking on a single particle out of this ensemble, one can ask for the probability if a particle has travelled a distance x after a time t. Let this probability be $p(x)\,\mathrm{d}x$. It describes the probability of a particle to be in the interval x to $\mathrm{d}x$. One can get this probability from the fraction of particles within this interval and the total number of particles.

$$p(x)\,\mathrm{d}x = \frac{u(x,t)\,\mathrm{d}x}{N_\mathrm{p}} = \sqrt{\frac{1}{4\pi Dt}} \exp\left(-\frac{x^2}{4Dt}\right)\mathrm{d}x$$

Using this, one can ask for the mean squared distance after a time t: $\langle x^2 \rangle$. Beware that $\langle x \rangle = 0$ from the ansatz of all particles being at $x = 0$ in the beginning. Then

$$\langle x^2 \rangle = \int_{-\infty}^{\infty} x^2 p(x)\,\mathrm{d}x$$

has to be solved. The computation is not trivial, and the result is

$$\langle x^2 \rangle = 2Dt.$$

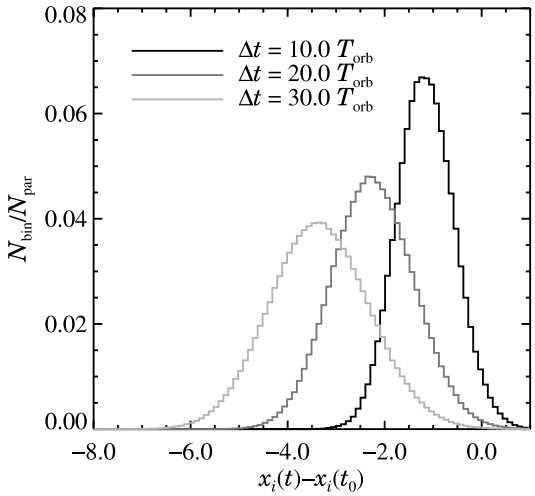

Figure 2.11: Histogram of the radial travel distance for a group of particles from a SI simulation. The travel distance is the distance a particle has surpassed, measured from its initial position $x_i(t=0)$. The curve centre moves inward due to the net radial particle drift from the Nakagawa solution. It is further spreading due to turbulent diffusion acting as a random walk equivalent. As consequence, the Gaussian width increases with the square root of time. The Gaussian distribution of this measure is found to be slightly platykurtic, or flat tailed, due to the fraction of particles that experience a decreased diffusion as being in one of the more massive particle clumps. *Source: Johansen & Youdin (2007).*

This could already be seen from Eq. (2.41), since a Gaussian has a function of $y \sim \exp\left(-\frac{1}{2}\frac{x^2}{\sigma}\right)$ and for a Gaussian one finds directly: $\langle x^2 \rangle \equiv \sigma = 2Dt$.

Particle diffusion: δ

For dust particles in PPDs, one has to deal with the particle concentration in a gas. Since the gas density can be assumed to be constant, see Sec. 7.4.2, the differential equation (Eq. (2.40)) transforms into an equation for the dust density $\rho_{\rm d}$, as

$$\dot{\rho_{\rm d}} = D\nabla^2 \rho_{\rm d}\,.$$

A solution for the 1-d case is known from above, but this solution is for all particles initially at the same position and a constant diffusion coefficient D. Still, with that solution, the particles will reach a mean square distance of

$$\left\langle x_i\,(t)^2 \right\rangle_i = \sigma = 2Dt$$

after a time t.

In order to technically use this solution, one can use the assumption of a constant diffusion coefficient. Then, one has not to track the absolute particle position $x_i(t)$, but their position relative to the individual initial position $x_i(t) - x_i(t_0)$. Consequently, σ is the root-mean-square of the travel distance, or as in Fig. 2.11, the width of a travel distance histogram. The equation than can be read as

$$\boxed{D = \frac{1}{2}\frac{\partial \sigma^2}{\partial t}\,.} \tag{2.42}$$

So, the diffusion coefficient can be obtained from the time derivative of the root-mean-square travel distance. Beware, that herein this equation the factor 1/2 is introduced in order to compensate the factor 2 from the

solution of Fick's second law, compare with Eq. (3.35).

The diffusivities D can also be expressed in disk units, of orbits Ω and sound speed c_s, as a dimensionless quantity:

$$\delta = \frac{D}{c_s^2/\Omega}\,. \tag{2.43}$$

As will be shown in Chapter 4, these units are right the code units of the PencilCode. In the following analysis of the performed simulations, the diffusion is measured by tracking the position of a sample of at least 10^4 super-particles and measuring their travel distance over time, compare with Johansen & Youdin (2007). Note that in a shearing box only radial and vertical diffusivity can be measured by this method since shearing motions dominate in azimuthal direction.

2.2.6 Dust trapping and planetesimal formation

The scientific community discusses two major ways that allow planetesimals to form. One is direct growth from µm to km. The authors of this idea claim that the dust can undergo the growth barriers, namely drift and fragmentation barrier, see Sec. 2.2.3, by growing in a very fluffy fashion (Kataoka et al., 2013). Another states that some particles are lucky and surpass the meter-size barrier by gaining mass from mass transfering collisions only (Windmark et al., 2012). By that the dust stays at a comparable low Stokes number, though its mass increases, see Fig. 1 in Okuzumi et al. (2012). The third way, as followed in this thesis, expects planetesimals to form via gravitational collapse of a dust heavy particle cloud. The formation of planetesimals would then be comparable to the formation of stars. As a stability formation criterion is known for stars, a similar criterion should exist for particle clouds that collapse to planetesimals. This diffusion limited collapse criterion will be investigated in the following Chapter 3.

The fluffy growth scenario is hampered by the need of fine-tuning the parameters of turbulence in the PPD. The works by Kataoka et al. (2013) showed that under the right conditions planetesimals could from fluffy growth within $R \leq 7\,\mathrm{AU}$. Where the final compactification comes from gas ram pressure, self-gravity and internal heating. But, they do not take collisional erosion into account (Krijt et al., 2014, 2015). In contrast, the gravitational collapse can only happen in a situation where the dust volume density is significantly higher than the gas density. Since the dust concentration within a PPD is typically assumed to be $Z = 0.01$, ways to enhance the dust have to be found. The good thing is that planets in extra-solar systems where found to be rather abundant. This means nature must have a robust way to form planetesimals to explain this observation.

The dust cloud collapse scenario can be separated into two regimes as well. One is the global enhancement of the dust concentration by reducing the amount of gas, the second is the local trapping of dust in *particle traps* (Whipple, 1972; Lucas & Ackbar, 1983; Klahr & Lin, 2000; Haghighipour & Boss, 2003; Fromang & Nelson, 2005). The triggering of gravitational collapse by the reduction of disk gas mass, and hence increase in disk metallicity, is found need a dust concentration of around $Z = 0.02$. Only then particle clumps where found to form, see Johansen et al. (2015), Carrera et al. (2015), and Yang et al. (2016). Considered situations where this can happen, is late phase disk evaporation, when the PPD dissolves and only the dust remains (Carrera et al., 2017), or when gas giant planets deplete the gas disk. The first situation might be an explanation for asteroids and comets, but both are not a good explanation for planets and gas giants itself. The seeds of planets demand to form early, else there is no time to grow and accrete gas. If not the current understanding of disk physics is completely off, the way to form such dust concentration has to come from local particle trapping. Several approaches on this where done in the past years.

Raettig et al. (2015) investigated trapping in anticyclonic *vortices* (Barge & Sommeria, 1995). Vortices are shown to form on multiple ways, for example vertical convection cells (Klahr & Henning, 1997; Klahr & Hubbard, 2014; Lyra, 2014) or the baroclinic instability (Klahr & Bodenheimer, 2003; Klahr, 2004). Raettig et al. (2015) found in local shearing box simulations the particle concentration to increase up to four orders in magnitude, and even found evidence of SI activity inside these dust concentrations. The work by Johansen et al. (2007), Johansen et al. (2009), and Dittrich et al. (2013) found a azimuthally extended rings, called *zonal flows* (Whipple, 1964; Klahr & Lin, 2000), to also trap particles efficiently, and even showed planetesimal formation therein. Zonal flows represent radial pressure bumps that can trap particles since particles seek the point of highest pressure, see Whipple (1972). They can emerge in different ways, one

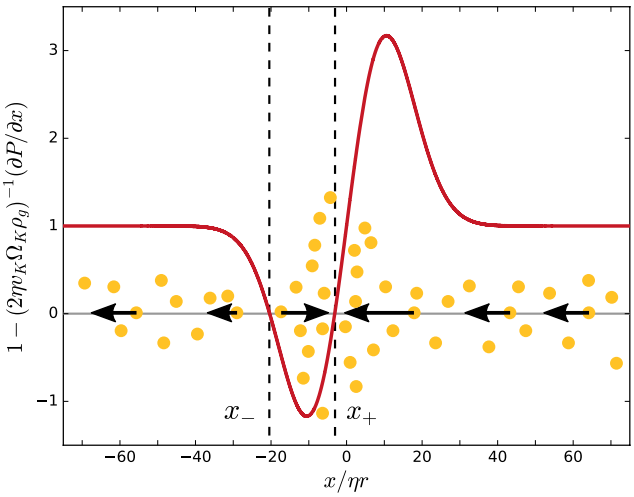

Figure 2.12: Schematic view on an axisymmetric pressure bump that is capable of trapping particles (Whipple, 1972). This type of gas flow feature is typically referred to as *zonal flow*, as it is an axisymmetric gas flow perturbation. The y-axis shows the pressure gradient, see Sec. 2.1.3, the x-axis the radial distance from the trapping location (x_+), normalised to the global pressure gradient η. An locally increased gas pressure slows the particle drift down. If the gas pressure gradient vanishes, i.e. reaching the horizontal grey line in this plot, particles can get trapped where the gas velocity is right at Keplerian speed. If the pressure bump is even stronger, it forms a region where particle start to drift outwards (between x_- and x_+). The point x_- is not a particle trap, as this is an unstable equilibrium point. As can be seen, the slope in pressure gradient is much higher in the vicinity of the zonal flow than on the global disk scale. Hence, if dust-to-gas ratios around unity are reached, the SI might be even more violent within a zonal flow. *Figure based on Onishi & Sekiya (2017)*

is from magnetic coupling onto the disk gas (Kato et al., 2009). Zonal flows might explain the dust rings observed in recent ALMA observations, see Fig. 1.5. They arise from magnetic coupling of the ionised gas disk onto the stellar magnetic field. They act efficient in increasing the dust density by up to four orders of magnitude, too.

Different approaches on dust trapping take static disk features, like the inner disk rim, inner edge of a turbulence-dead zone (Lyra et al., 2008; Drążkowska et al., 2013), gaps carved by other planets (Lyra et al., 2009; van der Marel et al., 2013), or the ice lines of volatiles. In the inner of an ice line, i.e. water ice line, the volatiles evaporate but can get transported radially outwards, so they re-condensate on grains right at the ice line (Stammler et al., 2017). This could also trigger planetesimal formation (Schoonenberg & Ormel, 2017) by increasing the locally increasing the dust concentration. Another perspective for dust concentration are high-pressure regions between turbulent eddies on the smallest scale of the Kolmogorov cascade (Sec. 3.3.4), see Cuzzi et al. (2001), Cuzzi et al. (2008), and Johansen et al. (2014). Some discussed mechanism work only in strongly turbulent disks, with a turbulent α-values above 10^{-3}, and by that are less likely to be the dominant mode of planetesimal formation.

There might be not *the one and only way* to form planetesimals. It might be a combination of may interlinking processes or different processes being active at different times. The hope is to better understand these processes in the future, and maybe even find more. If one is lucky, the planetesimals that are found today in the solar system have imprints from their formation mechanism and one day we are able to distinguish solar system objects by their formation time and path. One distinctive feature could be the asteroid size. As shown in the following chapter, it is the turbulent particle diffusion that determines the lowest planetesimal size. In the future, also the compositional structure of a planetesimal (Jansson et al., 2014) will become important to study.

Chapter 2

3 Gravitational Instability of a Particle Cloud

In the following of this chapter, the stability of self-gravitating particle clouds in PPDs is analytically investigated. Thus, the chapter has two main components, that in the end merge into the diffusion limited collapse criterion. The components are:

i) The two canonical used instability criteria are the *Roche stability* and the *Hill stability* criterion. The first was calculated in the 19th century by Édouard Roche, who investigated the stability of loosely bound material in the vicinity of larger bodies, such as the breakup of comets close to the Sun. A good example is the breakup of Shoemaker-Levy 9 while approaching Jupiter in 1994, see Fig. 3.1. Based on the work of Édouard Roche, George William Hill calculated the dynamical stability of a testmass around a smaller body in a rotating frame. This is typically interpreted as a spherical volume around a minor body, e.g. around Earth, in which a small body, e.g. the Moon, stays bound to it. Being outside of this sphere of influence, the gravitational attraction onto the small body is dominated by a major body, i.e. the Sun. Points on the surface of this sphere show little net acceleration forces. Characteristic points of these are the Lagrangian points. The Lagrangian Points L1 and L2 are often used for positing satellites therein. The Lagrangian points L3 and L4 are trailing and leading points of stability on the orbit of the respective minor body. In L3 and L4 of Jupiter an asteroid reservoir resides that objects are called *Jupiter Trojans*. The *Hill sphere* is sometimes also called after its origin *Roche lobe*, after its origin. Both criteria state that stability is granted as long as mutual gravitational interaction within a particle cloud is stronger than the gravitational gradient, exerted by a larger mass outside of the body of interest, which is in our case a particle cloud, see Sec. 3.1.4 and following. The Hill stability differs from the Roche criterion by demanding an orbital motion of the particle cloud around a central mass. The thereby induced additional centrifugal force further stabilises the particle cloud by reducing the gravitational gradient across the cloud. A Roche criterion that neglects

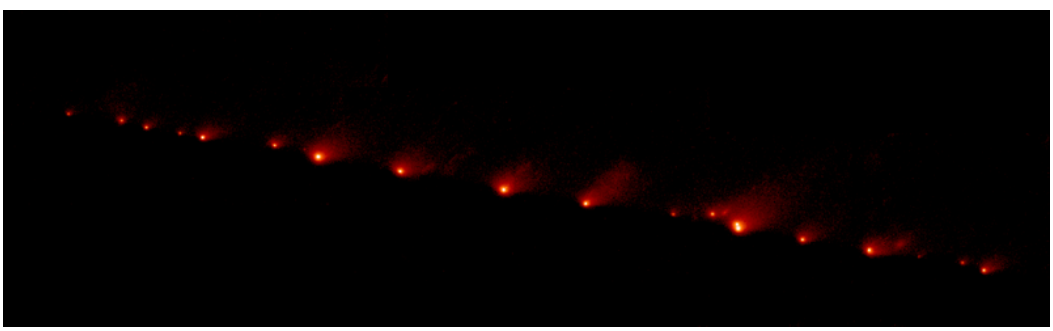

Figure 3.1: Breakup of comet Shoemaker-Levy 9 when it approached Jupiter in 1993. This comet can be taken as a good example where the tidal forces of Jupiter where stronger than the internal binding. Since the internal binding of a comet is rather loose, they are also called *rubble piles*. For Shoemaker-Levy 9 the internal density has been calculated to a surprisingly high value of $\rho = 5\,\mathrm{g/c^3m}$ (Asphaug & Benz, 1996). *Source: NASA/ESA, H. Weaver and E. Smith (STScI).*

an orbital motion is obviously an insufficient criterion for particle cloud stability analysis in PPDs. Also, the Hill criterion might be invalid in a PPD as these disks contain a non-negligible amount of gas interacting via drag with the particles. Therefore, the Hill criterion might be used as an approximation as long as drag forces can be neglected, see Sec. 3.2.

ii) If a particle cloud is allowed to collapse depends not only on the Keplerian shear and tidal forces. It also depends on the dynamical state the particles have at the moment of collapse. Obviously, a too high particle rms-velocity will ballistically disperse a particle cloud faster than it collapses. The same is true for underlying turbulent diffusion (Shariff, Karim and Cuzzi, Jeffrey N., 2015) that resides in the particle-gas mixture. Such a turbulent scenario was briefly discussed in Shariff, Karim and Cuzzi, Jeffrey N. (2015). This work will go into more depth and show the turbulent diffusion to state a threshold on particle cloud collapse. By stating the particle diffusion timescale to be as long as the gravitational collapse time a criterion on cloud stability will be found by the end of this chapter.

The derivation of the final diffusion limited collapse criterion is based on the co-author paper Klahr & Schreiber (2015) and Klahr et al. (2018). In both papers, I independently set up, tested, performed and evaluated the numerical experiment. I also extensively contributed to the theory and the paper writing.

3.1 Stability criterion

In Sec. 3.3 a stability criterion for a particle cloud will be derived, which follows a similar idea as the collapse of an interstellar cloud to a star, see Fig. 3.2. Before this can be done, this chapter will introduce the basic concepts of gas and dust stability analysis. The section starts with the case of a basic star formation criterion, the *Jeans criterion* by Jeans (1902). It asks, if the gas pressure from the internal temperature is stronger than the cloud its own self-gravity. Only if gravity is stronger, a star can form from collapse. Else, the cloud either has to cool in order to shrink any further, or gets dispersed, not forming a star.

As described in points i) and ii) from above, a collapsing cloud has not only to be internally stable against tidal forces and Keplerian shear, i.e. Hill stable, but also particle rms velocity and diffusion has to be low. Comparing with star formation, the diffusion takes the part of the internal pressure, but now it is a question

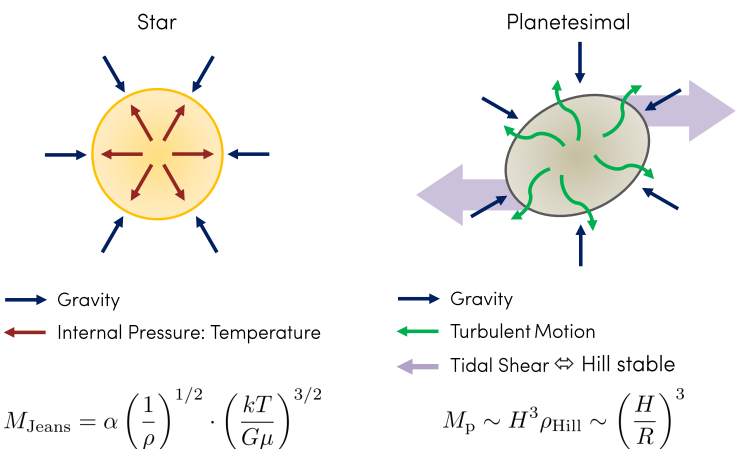

Figure 3.2: The situation of a collapsing dust particle cloud to a planetesimal is very similar to the case of a interstellar cloud that tries to collapse into a star. Internal pressure as the obstacle in the stellar case translate into turbulent particle diffusion for planetesimal formation. This changes the picture form a force balance into a picture of dynamical timescale balance. Additionally, the Keplerian shear and stellar tidal forces pull on the particle cloud, and so the cloud has to overcome both of these effects. The shear stability is generally assumed to be reached at Hill density. In order to deal with the turbulent diffusion, herein this work the collapse timescale is set equal to the diffusion timescale. This directly gives a length scale criterion similar to the Jeans length, but for planetesimal formation in PPDs.

of timescales rather than competing forces. Meaning, collapse can only occur if the collapse is faster than turbulent diffusion.

In the following different stability criteria investigated are, starting with the Jeans criterion (Sec. 3.1.1), over the Toomre instability that describes collapse of gas clouds in PPDs (Sec. 3.1.2), secular gravitational instabilty (Sec. 3.1.3), describing a mode of instability in dust rings, and the section is ending with the Roche (Sec. 3.1.4) and the Hill stability criteria (Sec. 3.1.5). The following derivations of the Jeans criterion and of the free-fall timescale follows *Susanne Höfners* (*Uppsala University*) lecture notes[4]. The author gratefully thanks her for providing this at open access and for inspiring the herein derived criterion for particle cloud stability and collapse times.

3.1.1 Star formation in a nutshell

The subject of consideration is a gas cloud that has formed within a gas filament inside of a galaxy. This gas cloud is about to collapse into a star. For a given homogeneous density ρ and temperature $T = PV/nR$, the gravitational stability of this gas cloud is investigated. Assuming spherical symmetry, the problem reduces to a one dimensional analysis.

The dynamics are descriped by the equation of continuity

$$\frac{\partial \rho}{\partial t} + \frac{\partial}{\partial x}(\rho u) = 0 \tag{3.1}$$

and the 1-d equation of motion

$$\frac{\partial}{\partial t}(\rho u) + \frac{\partial}{\partial x}\left(\rho u^2\right) = -\frac{\partial P}{\partial x} - \rho \frac{\partial \Phi}{\partial x}, \tag{3.2}$$

with u the radial gas velocity and Φ the gravitational potential of the gas cloud. The latter is given by Poisson's equation for self-gravity:

$$\frac{\partial^2 \Phi}{\partial x^2} = 4\pi G \rho. \tag{3.3}$$

Assuming the gas to be in isothermal equilibrium holds as long as the gas can cool faster than it heats up due to compression from the collapse, i.e. as long as the gas is not getting optically thick and cooling by radiation remains efficient. Being isothermal is indeed justified in most astrophysical processes as the timescales for thermal adjustment are short compared with the timescales of dynamical changes in the system. Hence, the barotropic equation of state can be used, as in Eq. (2.1), i.e.

$$P = c_\mathrm{s}^2 \rho,$$

with isothermal sound speed c_s.

Initially, the gas cloud shall have a constant density ρ_int and internal gas pressure P_0, and be at rest $u_0 = 0$. Now, considering a small perturbation in the form of $\exp[\mathrm{i}(kx + \omega t)]$. One can express the change (primed) in density, pressure, potential, and consequently gas velocity as

$$\rho = \rho_\mathrm{int} + \rho', \quad P = P_0 + P', \quad \Phi = \Phi_0 + \Phi', \quad u = u',$$

were the unperturbed quantities have a 0 as index. The perturbation are considered of being small and isothermal: $P' = c_\mathrm{s}^2 \rho'$, with c_s remains unchanged, i.e. cooling is fast.

Inserting this perturbation into the equations Eq. (3.1) - Eq. (3.3), one obtains three equations that

[4] http://www.astro.uu.se/~hoefner/astro/teach/apd_files/apd_collapse.pdf

describe the dynamics of the induced perturbation. First, the equation of continuity:

$$\underbrace{\frac{\partial \rho_{\text{int}}}{\partial t}}_{=0} + \frac{\partial \rho'}{\partial t} + \rho_{\text{int}} \frac{\partial u'}{\partial x} + \frac{\partial}{\partial x} \underbrace{\left(\rho' u'\right)}_{\approx 0} = 0 \tag{3.4}$$

$$\frac{\partial \rho'}{\partial t} + \rho_{\text{int}} \frac{\partial u'}{\partial x} = 0 \tag{3.5}$$

Here, time derivatives of the constant initial values cancel, as well as the products of two perturbations, since both are already individually considered to be very small, and so also their derivatives are small. Second, the equation of motion:

$$\frac{\partial}{\partial t}\left(\left(\rho_{\text{int}} + \rho'\right) u'\right) + \frac{\partial}{\partial x}\left(\left(\rho_{\text{int}} + \rho'\right) \underbrace{u' u'}_{\approx 0}\right) = -\frac{\partial \left(P_0 + P'\right)}{\partial x} - \left(\rho_{\text{int}} + \rho'\right) \frac{\partial \left(\Phi_0 + \Phi'\right)}{\partial x} \tag{3.6}$$

$$\frac{\partial u'}{\partial t} = -\frac{c_{\text{s}}^2}{\rho_{\text{int}}} \frac{\partial \rho'}{\partial x} - \frac{\partial \Phi'}{\partial x} \tag{3.7}$$

Third, the Poisson's equation for the perturbation can be separated from the initial potential Φ_0 to

$$\frac{\partial^2 \Phi'}{\partial x^2} = 4\pi G \rho' \,. \tag{3.8}$$

Assuming a solution of the form $\exp\left[\mathrm{i}\left(kx + \omega t\right)\right]$ exists to all these perturbed quantities, the set of these homogeneous linear equations can be solved in Fourier space, since the derivatives transform in Fourier space into

$$\frac{\partial}{\partial x} \equiv \mathrm{i}k \qquad \text{and} \qquad \frac{\partial}{\partial t} \equiv \mathrm{i}\omega \,.$$

This leads to

$$\begin{bmatrix} \omega & k\rho_{\text{int}} & 0 \\ \frac{c_{\text{s}}^2 k}{\rho_{\text{int}}} & \omega & k \\ 4\pi G & 0 & k^2 \end{bmatrix} \cdot \begin{pmatrix} \rho' \\ u' \\ \Phi' \end{pmatrix} = \begin{pmatrix} 0 \\ 0 \\ 0 \end{pmatrix} .$$

This set of equations can only have a non-trivial solution if the determinant, which is right the *dispersion relation*, is zero:

$$\omega^2 = c_{\text{s}}^2 k^2 - 4\pi G \rho_{\text{int}} \tag{3.9}$$

This dispersion relation has two different solutions. One, if ω is real, and another one if it is imaginary. If ω is a real number, then the solution is an oscillation around a given amplitude, i.e. $\exp\left(i\omega t\right)$. If it is an imaginary number, the perturbation is unstable, i.e. $\exp\left(-\Im\left(\omega\right) t\right)$. If the solution for ω is unstable, it is either unstable in form of a decreasing amplitude (damping) or in form of an increasing amplitude (growth). Consequently, to get the gas cloud to be unstable, ω^2 needs to be negative, i.e. $k^2 c_{\text{s}}^2 - 4\pi G \rho_{\text{int}} < 0$ and thus wavenumbers smaller than

$$k_{\text{Jeans}} = \sqrt{\frac{4\pi G \rho_{\text{int}}}{c_{\text{s}}^2}} \,,$$

get unstable. Which is expressed in wavelength

$$\lambda_{\text{Jeans}} = \left(\frac{\pi}{G \rho_{\text{int}}}\right)^{1/2} c_{\text{s}} \,.$$

So, perturbations with $\lambda > \lambda_{\text{Jeans}}$ are unstable. This is called the Jeans criterion for star formation.

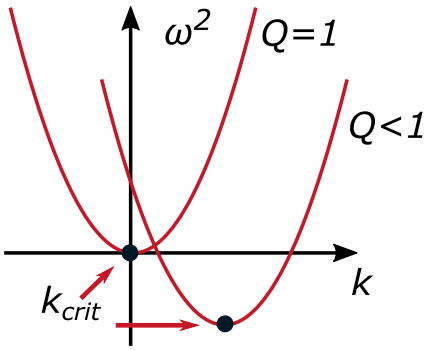

Figure 3.3: Growth modes of an instability have $w^2 < 0$. For Toorme values $Q < 1$ there are many unstable wavenumbers, but the one at its minimum is the most unstable wavelength with k_{crit}.

3.1.2 Toomre stability of a gas disk

Taking the derivation of the Jeans criterion as a basis for stability analysis, one can derive a similar criterion for a gas cloud in a PPD that includes Keplerian shear. Following the analysis as above, the determinant of equations that describe a fluid in a shearing box, see Sec. 2.1.5, is

$$\omega^2 = \underbrace{c_s^2 k^2}_{\text{pressure}} \underbrace{-2\pi G\Sigma|k|}_{\text{gravity}} + \underbrace{\Omega^2}_{\text{shear}} . \tag{3.10}$$

Here, a thin disk approximation has been used, which translates a volume density ρ into a column density Σ via

$$\Sigma(r) := \int_{-\infty}^{\infty} \rho_g(r,z)\,\mathrm{d}z .$$

In this stability analysis, a growing mode needs to satisfy $\omega^2 < 0$, meaning ω needs to be imaginary. One can also ask for the most unstable wavelength k_{crit}, i.e. the maximum/minimum of ω^2 via

$$0 \overset{!}{=} \frac{\partial \omega^2}{\partial k} = 2c_s^2 k_{\text{crit}} - 2\pi G\Sigma \quad \Rightarrow k_{\text{crit}} = \frac{\pi G\Sigma}{c_s^2}$$

and combine this with Eq. (3.10) yielding

$$\omega^2 = -\frac{(\pi G\Sigma)^2}{c_s^2} + \Omega^2 \overset{!}{<} 0,$$

which has to be less than zero in order to give an imaginary ω. Solving this, an instability criterion is found, the so called *Toomre instability criterion*. It is usually expressed in the form of

$$\boxed{Q := \frac{\Omega c_s}{\pi G\Sigma} \overset{!}{<} 1}, \tag{3.11}$$

where Q is the Toomre parameter. It represents the ratio of Keplerian shear together with temperature over self-gravity. If self-gravity is stronger than both other effects, the collapse of a pure gas cloud in a PPD is possible. The gas disk surface densities Σ needed in order to trigger this Toomre collapse are very large (Kuiper, 1951). It is still unclear if Toomre instability plays a major role in planet formation, see Baehr & Klahr (2015). But, if Toomre instability occurs, the planets that would form would be of the order of several Jupiter masses, and thus are reaching into the realm of brown dwarfs and stars.

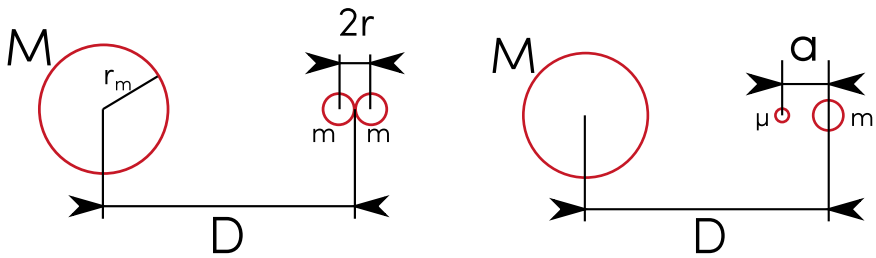

(a) Roche criterion **(b)** Hill criterion

Figure 3.4: The Roche criterion (left) is a criterion on internal stability. It can be simplified for two masses m that are held together only by their mutual gravitational attraction. Breakup of this system can only occur, if an external force is stronger than their binding forces. In the Roche criterion, the force that tries to disrupt them, is the gravitational force gradient from a larger mass M. If this force gradient is stronger, the two smaller masses separate from each other, i.e. the objects breaks up. The Hill criterion (right) is a similar criterion. It looks for the boundedness of a test mass μ onto a smaller mass m, in the vicinity of a larger mass M. The Hill analysis assumes the smaller mass to have an orbital motion around the larger mass, which is not the case in the Roche criterion. The Roche criterion can be used for the situation of an asteroid, or comet, that approaches a planet and one is interested in the point of breakup of this object. The Hill analysis leads to a Hill sphere, which is the sphere of zero acceleration around the mass m. Everything inside this sphere is bound, under the assumption of not having escape velocity or other perturbations occurring. From the Hill analysis result the Lagrangian points of a planet. These are points of stability along the star-planet axis, but also in front and behind the planet on its orbit. They are favoured for the positioning of satellites, but also the Trojans are found in the Lagrangian points (Emery et al., 2015).

3.1.3 Secular gravitational instability of dust

The *Secular Gravitational Instability* (SGI) (Youdin, 2011; Takeuchi & Ida, 2012) is a Toomre-like criterion, but for dust rings in PPDs. Doing a similar analysis for the dust, one can drop the pressure term $c_s^2 k^2$. The assumption of particles to be initially at rest, $v_0 = 0$, gives as result that there is no fastest growing mode, since the dispersion relation is now a monotonic function in k. Meaning, everything with

$$-2\pi G\Sigma\,|k| + \Omega^2 < 1$$

is unstable. This can be reformulated to derive a critical dust surface density Σ_{crit} for an annulus with diameter λ at distance R from a star with mass $M_\star$:

$$\Sigma_{\text{crit}} = \frac{\lambda}{4\pi^2}\frac{M_\star}{R^3}. \tag{3.12}$$

The result scales with ring width λ. So for a wider ring a higher density is needed to have it collapse. But, making the ring smaller, arbitrary small densities can collapse into small rings. It has to be kept in mind that particle rms velocities and turbulent diffusion will destroy the small rings, stating a lower limit for the SGI.

This SGI is a slowly growing gravitational instability with comparable slow growth rates. Takahashi & Inutsuka (2014) found for a solar mass star at a distance of 100 AU a most unstable wavelength of around 13 AU and a growth timescale around $2 \cdot 10^4$ yrs. Latter & Rosca (2016) found that SGI is only allowed for very low gas turbulence values, i.e. in terms of paramterized turbulent viscosity of $\alpha < 10^{-4}$, see Sec. 2.1.4.

Still, it cannot be ruled out that in a locally low turbulent disk, i.e. in a so called *turbulent dead zone* (Gammie, 1996; Turner & Drake, 2009), low dense particle rings can form from SGI and trigger collapse, if enough time is given. On might visit the review paper Chiang & Youdin (2010) for further reading.

3.1.4 Roche stability

Compared with Toomre and SGI, the Roche and Hill stability criterion are both not based on perturbation theory, but on force equilibrium. Assuming two spheres with identical mass m which are only bound by

their mutual gravitational force, see Fig. 3.4. They are getting disrupted by tidal forces, if their mutual gravitational force f_m is weaker than the differential gravitational force ΔF_M, exerted from the larger central object, e.g. a star, with mass M:

$$\text{stable} \Leftrightarrow \Delta F_M \leq 2 f_m .$$

This leads to an equation of critical stability if all net forces sum up to zero:

$$0 = \frac{Gmm}{(2r)^2} - \left[\frac{GMm}{(D-r)^2} - \frac{GMm}{(D+r)^2} \right]$$

Using $M \gg m$ and $D \gg r$, this can be simplified to

$$0 \approx \frac{m}{M}\frac{1}{4r^2} - \frac{r}{D^2}\left[\frac{4\frac{r}{D}}{1+2\frac{r}{D}-2\frac{r}{D}+4\frac{r^2}{D^2}} \right] \approx \frac{m}{M}\frac{1}{4r^2} - \frac{r}{D^2}\left[4\frac{r}{D}\right].$$

Reformulating to $m/M = 16r^3/D^3$ gives a relation for the necessary distance to keep the spheres bound together as

$$D_{\text{crit}} = r \cdot \sqrt[3]{\frac{16M}{m}} \approx 2.5r \cdot \sqrt[3]{\frac{M}{m}}.$$

This can be further reformulated in order to derive a critical densities of a dust sphere. The critical density is then

$$\rho_{\text{c}} = \rho_m = \frac{3m}{4\pi r^3}.$$

Using the Roche criterion from above gives the so called *Roche density*:

$$\boxed{\rho_{\text{Roche}} = \tfrac{12}{\pi}\tfrac{M}{D^3} \approx 3.82\tfrac{M}{D^3}} \tag{3.13}$$

3.1.5 Hill stability

The Hill stability criterion is a dynamical criterion. It is very similar to the Roche criterion, see Fig. 3.4. Since both analyse, for Roche and Hill, are done in 1-d, the dynamics narrows down to the additional centrifugal force by the orbital motion in the Hill criterion. Everything within the Hill sphere of the mass m, or Hill radius in the 1-d case, is gravitationally bound to it. Everything outside is bound to the larger, primary object, with mass M, e.g. the central star. Asking for the Hill sphere is equivalent to asking for a 'zero-acceleration' sphere. It is the surface at which a rigidly bound test mass μ will not get accelerated. Rigidly bound means the centrifugal forces of m and μ are set to be equal. One can write that centrifugal forces on m are in equilibrium with the gravitational pull from M:

$$m\Omega_m^2 D = \frac{GmM}{D^2} \qquad \Rightarrow \qquad \Omega_m = \frac{GM}{D^3} \overset{!}{\approx} \Omega_\mu .$$

The forces acting on μ are $F_\mu = \sum_i F_i = 0$ and thus

$$\begin{aligned}
0 &\overset{!}{=} -F_{\text{grav},M} + F_{\text{grav},m} + F_{\text{centrifugal}} \\
&= -\frac{GM\mu}{(D-a)^2} + \frac{Gm\mu}{a^2} + \mu\Omega_\mu^2 (D+a) = -\frac{1}{(D-a)^2} + \frac{1}{a^2}\frac{m}{M} + \frac{D-a}{D^3} \\
&= -1 + \frac{(D-a)^2}{a^2}\frac{m}{M} + \frac{(D-a)^3}{D^3} \\
&= -1 + \frac{D^2-2Da+a^2}{a^2}\frac{m}{M} + \frac{D^3-3D^2a+3Da^2-a^3}{D^3}.
\end{aligned}$$

Again, going for the limit of $D \gg a$ leads to $(D+a)^2 \approx D^2$. Further using $D^2 \gg D \cdot a$ simplifies the equation to

$$\frac{3a^3}{D^3} = \frac{m}{M}.$$

Solving for the minimal stable distance of the μ-m-system to M, gives

$$D_{\text{crit}} = a \cdot \sqrt[3]{\frac{3M}{m}} \approx 1.44a \cdot \sqrt[3]{\frac{M}{m}}. \tag{3.14}$$

For the critical density of a particle cloud, one assumes m to be the center of mass of this cloud, e.g. a sphere of particles with $m = \sum_i \mu_i$, and thus $m = \rho \frac{4}{3}\pi a^3$. The critical density of the particle cloud m is then

$$\rho_{\text{Hill}} = \frac{m}{\frac{4}{3}\pi a^3} = \frac{9}{4\pi}\frac{M}{D^3} \approx 0.72\frac{M}{D^3}. \tag{3.15}$$

The derived critical density value is smaller than the Roche density by a factor of 5. This is because the bound rotation of the whole particle cloud around its host star gives an additional stabilising effect to it. Sekiya (1983) defines his critical density for an axisymmetric 3-d annulus of particles and finds a value of

$$\rho_{\text{Sekiya}} = 0.62\frac{M}{R^3}, \tag{3.16}$$

which is in fact very close to the presented 1-d derivation.

This density of a particle sphere can now be used as a first approximation for the stability of the system. It is derived in a 1-d case and clearly some effects are missing, such as friction with the underlying gas disk. But still, as will be shown within this work, the derived criterion works surprisingly well when it comes down to predicting planetesimal formation via cloud collapse.

3.2 Collapse time

Having a criterion for stability against Keplerian shear and tidal forces is not enough to ensure planetesimal formation by cloud collapse. Collapse takes its time, especially when it comes to particles with small Stokes numbers, see Sec. 2.2.1. This collapse time then might be longer than the time a particle cloud needs to disperse from intrinsic rms-velocities or turbulence. Also, secondary effects, such as cloud erosion by gas ram pressure, might prevent a final collapse.

3.2.1 Classical collapse time

To find out, what this collapse timescale τ_c is, one can assume the collapse to happen at free-fall velocity, i.e. $\tau_c = \tau_{\text{ff}}$. A particle at distance r from the center of mass, with cloud mass $m = \frac{4\pi}{3}R_0^3\rho_{\text{int}}$, has an acceleration and velocity of

$$\ddot{r}(t) = -\frac{Gm}{r(t)^2} \qquad \text{and} \qquad \dot{r}(t) = v(r(t)).$$

Using these two equations yields

$$\ddot{r} = \frac{\mathrm{d}}{\mathrm{d}t}\left(\frac{\mathrm{d}r}{\mathrm{d}t}\right) = \frac{\mathrm{d}}{\mathrm{d}t}(v(r(t))) = \frac{\mathrm{d}r}{\mathrm{d}t}\frac{\mathrm{d}v}{\mathrm{d}r} = v\frac{\mathrm{d}}{\mathrm{d}r}v = \frac{1}{2}\frac{\mathrm{d}(v^2)}{\mathrm{d}r},$$

that can be plugged into the equation of motion from above as

$$\frac{1}{2}\mathrm{d}(v^2) = -\frac{Gm}{r^2}\mathrm{d}r.$$

This equation can be integrated and the solution is, by using out that $r(t=0)=R_0$ and $v(t=0)=0$:

$$v=\sqrt{2Gm\left(\frac{1}{r}-\frac{1}{R_0}\right)}.$$

Using $v=\dot{r}$, this can be rewritten under the substitute of $\kappa=r/R_0$ and $\mathrm{d}\kappa=\mathrm{d}r/R_0$, giving

$$\mathrm{d}t=-\left(\frac{2Gm}{R_0^3}\right)^{-1/2}\frac{\mathrm{d}\kappa}{\left(\kappa^{-1}-1\right)^{1/2}}=-\left(\frac{8\pi G\rho_{\mathrm{int}}}{3}\right)^{-1/2}\left(\frac{\kappa}{1-\kappa}\right)^{1/2}\mathrm{d}\kappa.$$

The integration of this equation will directly give the free-fall time τ_{ff}. The boundaries of this integration are the beginning of collapse, where $\kappa=1$, and the end of the collapse, where $\kappa=0$:

$$\tau_{\mathrm{ff}}=-\left(\frac{8\pi G\rho_{\mathrm{int}}}{3}\right)^{-1/2}\int_{\kappa=1}^{0}\mathrm{d}\kappa\left(\frac{\kappa}{1-\kappa}\right)^{1/2}.$$

The integral in κ can be calculated by making another substitution of $\kappa=\sin^2(\phi)$. Thus the integral becomes, with $\mathrm{d}\kappa=\mathrm{d}\phi 2\sin\phi\cos\phi$:

$$\int_1^0\mathrm{d}\kappa\left(\frac{\kappa}{1-\kappa}\right)^{1/2}=\int_{\pi/2}^{0}\mathrm{d}\phi 2\sin^2\phi=2\left[\frac{1}{2}\left(\phi-\sin\phi\cos\phi\right)\right]_{\phi=\pi/2}^{0}=-\frac{\pi}{2}.$$

Leading to a free-fall timescale of

$$\boxed{\tau_{\mathrm{ff}}=\left(\frac{3\pi}{32G\rho_{\mathrm{int}}}\right)^{1/2}} \tag{3.17}$$

that only depends on the cloud density, but not on the actual size of the dust cloud. Inserting the Hill density from Eq. (3.15), this leads to a collapse time of $\tau_{\mathrm{ff}}(\rho=\rho_{\mathrm{Hill}})\approx 0.1T_{\mathrm{orb}}$.

3.2.2 Contraction time for frictional particles

Once taking into account that the cloud particles undergo friction with the gas while collapsing, the collapse will take longer than the free-fall time τ_{ff}. This new cloud collapse timescale is the contraction time $\tau_{\mathrm{c}}=\tau_{\mathrm{c}}(\mathrm{St},\rho_{\mathrm{int}})$. It is now not only a function of cloud density, but also of particle size, i.e. more specific, the Stokes number from Eq. (2.31).

In the following, it is assumed that the collapse happens at terminal velocity and the gas is assumed to be incompressible, i.e. the gas density is constant throughout the collapse.

The assumption of collapse to be at terminal velocity means that stopping time τ_{s} by particle-gas friction is shorter than the free-fall time (Cuzzi et al., 2008). Being at terminal velocity means that the velocity of a cloud particle can be expressed via

$$v_{\mathrm{t}}(r(t))=-\tau_{\mathrm{s}}\frac{mG}{r^2(t)}. \tag{3.18}$$

With m the total mass of the cloud. During the collapse, the stopping time does not depend on r, since ρ_{g} is assumed to stay roughly constant, see Sec. 7.4.2. The new frictional *contraction time* τ_{c} can be calculated from this equation via integration of Eq. (3.18):

$$r(t)=\sqrt[3]{r_0^3-3G\tau_{\mathrm{s}}mt}\quad\overset{r(\tau_{\mathrm{c}})=0}{\Rightarrow}\quad\tau_{\mathrm{c}}=\frac{r_0^3}{3G\tau_{\mathrm{s}}m} \tag{3.19}$$

Where the collapse starts at $t=0$. Hence, a spherical clump of size r_0 and mass density ρ_{int} is expected to

collapse within a collapse time

$$\tau_c = \frac{1}{4G\pi\tau_s\rho_{int}}. \tag{3.20}$$

Now, this can be expressed in terms of free-fall time. Combining both terms for long (Eq. (3.17)) and short stopping times (Eq. (3.20)) gives an approximation of the collapse time for marginally coupled particles as

$$\boxed{\tau_c = \tau_{ff}\left(1 + \frac{8\tau_{ff}}{3\pi^2\tau_s}\right).} \tag{3.21}$$

This approximation gives good results in the limit of tightly coupled and loosely coupled particles, but might be a factor ~ 2 off when it comes to marginally coupled particles, compare with Fig. 3.5.

For the case of a cloud at Hill density, i.e. plugging Eq. (3.15) into Eq. (3.21), one finds a radius independent limit for particles with Stokes number smaller that a critical value of

$$\mathrm{St}_{crit} = \frac{8}{3\pi^2}\tau_{ff}\Omega = 0.172. \tag{3.22}$$

For this approximation in density and Stokes number, the cloud contraction time becomes

$$\tau_c = \frac{1}{9\mathrm{St}}\Omega^{-1}. \tag{3.23}$$

Numerical verification of the contraction time

A comparison of the analytical approximation for the collapse time with a numerical value from a Leap Frog approach on the differential equation for frictional collapse, i.e.

$$\partial_t v = -\frac{Gm}{r^2} - \frac{v}{\tau_s}, \tag{3.24}$$

gives as result Fig. 3.5. Here the collapse times are plotted as expressed in free-fall time for Stokes numbers ranging from $\mathrm{St} = 0.001$ to 10. Comparing this result with the approximation from Eq. (3.23) gives good agreement up to particles with $\mathrm{St} = 0.1$.

3.2.3 Equality of spherical, cylindrical and plane parallel collapse time

Within this thesis, results from simulations on particle cloud collapse will be presented. Most of them are 2-d, due to the strong increase in computation time when going to 3-d. So, one might guess that the contraction time from Eq. (3.21) is acutally different, when dealing with 2-d simulations. In a 2-d simulation, a sphere becomes a vertical cylinder, since the vertical dimension is a single grid cell which vertical extend is a full domain size. In order to verify that the collapse calculations from above are also valid for a cylindrical collapse, the collapse time of an infinitely extended cylinder to a line has to be calculated, and compared with the collapse time of a sphere to a point.

It might be surprising that comparing the collapse of a cylinder with a sphere leads to exact the same collapse time, though the collapse motion is different. Starting with the same ansatz as in Sec. 3.2, a different expression for the gravitational acceleration g of a cylinder of length L, radius R_0 and density ρ_{int}, is needed. The calculation will be done for a cylinder of length L, but later the transition for $L \to \infty$ will be done.

The gravitational acceleration g of a homogeneous cylinder one can get in two different ways. One, solving the Poisson equation $\Delta\Phi = 4\pi G\rho$ and using $g/m = -\nabla\Phi$. Or by using the Gauss law for

$$\oint_S \mathrm{d}A\vec{g}\cdot\vec{n} = -4\pi Gm$$

and integrating over a cylindrical surface around the cylinder. Both ways are equivalent, since the Poisson equation can be derived from the Gauss law.

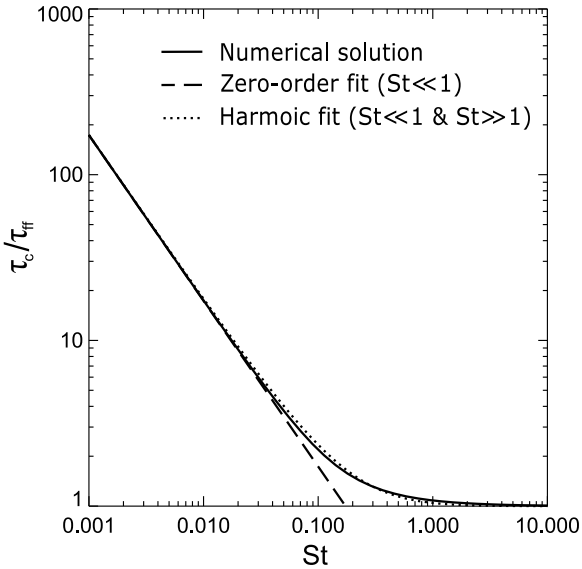

Figure 3.5: Contraction time τ_c for a dust cloud at Hill density in units of free-fall time τ_{ff}, as a function of the particle Stokes number. The dotted line is the full expression from Eq. (3.21) for the contraction time that is combining the solutions for large and small particles. The analytic approximation for the solution for small Stokes number particles from Eq. (3.23) is plotted as a dashed line. The solid line results from numerical Leap Frog integration of Eq. (3.24). As can be seen, the analytic solution holds quiet well, and the approximation for small particles should only be used for $\mathrm{St} \leq 0.1$.

Derivation via potential

The first way to calculate the equation of motions from the Poisson equation needs further knowledge of the problem, hence one can assume $\Delta\Phi(\rho > R_0) \equiv 0$ and $\Delta\Phi(\rho \leq R_0) \equiv 4\pi G\rho_{\mathrm{int}}$. Since the cylinder is symmetric and infinitely extended, the potential will not depend on φ and z, so $\Phi(r, \varphi, z) = \Phi(r)$. Further simplification are for the Laplace operator in cylindrical coordinates

$$\Delta f = \frac{1}{r}\frac{\partial}{\partial r}\left(r\frac{\partial f}{\partial r}\right) + \frac{1}{r^2}\cancelto{0}{\frac{\partial^2 f}{\partial \varphi^2}} + \cancelto{0}{\frac{\partial^2 f}{\partial z^2}}.$$

Solving the Poisson equation for $r \leq R_0$ leads to

$$\frac{1}{r}\frac{\partial}{\partial r}\left(r\frac{\partial \Phi}{\partial r}\right) = 4\pi G\rho_{\mathrm{int}} \quad \Rightarrow \quad r\frac{\partial \Phi}{\partial r} = 2\pi G\rho_{\mathrm{int}} r^2 + \mathrm{const.}$$

Solving for the potential leads to

$$\Phi(r \leq R_0) = \pi G\rho_{\mathrm{int}} r^2 + \underbrace{\ln(r) - \mathrm{const.}}_{\text{asym.}}\cancelto{0}{\,.}$$

Where the last term can be dropped, since the potential needs to be symmetric for positive and negative r. The potential is then

$$\boxed{\Phi(r \leq R_0) = \pi G\rho_{\mathrm{int}} r^2} \tag{3.25}$$

for the inner of the cylinder.

For the outer part known is $\Delta\Phi(r > R_0) = 0$, consequently

$$[r(\partial_r\Phi)]_{r\geq R_0} = \text{const.} \quad \forall r \geq R_0, \text{ so choose } r = R_0\,.$$

Solving this equation directly leads to

$$\text{const.} = R_0(\partial_r\Phi) = 2\pi G\rho_{\text{int}}R_0^2 \stackrel{!}{=} r\frac{\partial\Phi}{\partial r} \quad \forall r \geq R_0$$

This now can be solved by integrating radially from R_0 to r via

$$\begin{aligned}\Phi(r) &= \Phi(R_0) + \int_{R_0}^{r} \mathrm{d}r'\, 2\pi G\rho_{\text{int}}R_0^2\frac{1}{r'} \\ &= \Phi(R_0) + 2\pi G\rho_{\text{int}}R_0^2(\ln(r) - \ln(R))\,.\end{aligned}$$

where one can use the solution for the inner cylinder and get

$$\boxed{\Phi(r) = \pi G\rho_{\text{int}}R_0^2[1 + 2(\ln r - \ln R_0)]\,.} \tag{3.26}$$

The resulting force is:

$$\boxed{\frac{F}{m} = -\nabla\Phi = \begin{cases} -2\pi G\rho_{\text{int}}r & r \leq R_0, \text{ inner} \\ -2\pi G\rho_{\text{int}}R_0^2/r & r > R_0, \text{ outer}\end{cases}} \tag{3.27}$$

Derivation via Gauss law

This result can be derived in a shorter number of steps by using the Gauss law:

$$\oint_S \mathrm{d}A\vec{g}\cdot\vec{n} = -4\pi Gm \tag{3.28}$$

Here, S is the surface on which the gravitational force is to be calculated and $\vec{n}$ the normal vector on S. Since the cylinder is assumed to be infinitely extended, there is no interest in the end-caps of the cylinder. Though if the end-caps would matter, one would find $\vec{g}\cdot\vec{n} = 0$ as long as $\vec{g} \sim \hat{r}$, and so they do not contribute to the overall integral. Along the curved surface of S the vector $\vec{g}$ is anti-parallel to $\vec{n}$, i.e. $\vec{g}\cdot\vec{n} = -g$. Bringing this constant outside of the integral leads to

$$-g\oint_S \mathrm{d}A = -4\pi Gm\,.$$

Performing this integral over the cylinder surface becomes

$$-2\pi rLg = 4\pi Gm\,,$$

here with m being the mass enclosed by the surfance S. With an infinitely extended cylinder, one cannot use a total mass but has to use a line density $\lambda = m/L$ for a line segment of length L. With this segments mass λL, this is giving

$$-2\pi rLg = 4\pi G\lambda L\,.$$

Reformulating for the g, one finds the gravitational pull to be

$$\boxed{g = -\tfrac{2G\lambda}{r}\,.} \tag{3.29}$$

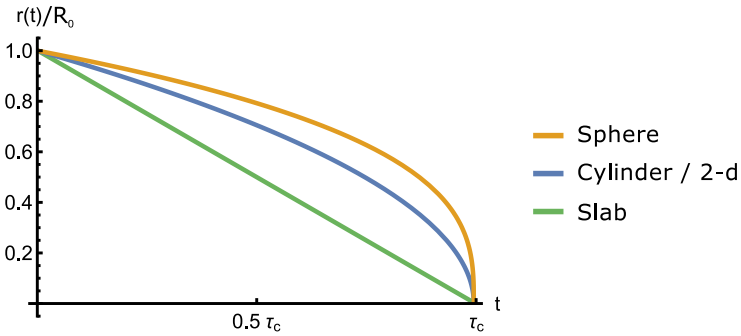

Figure 3.6: Comparison of the free-fall trajectory of a spherical distribution of particles and a cylindrical distribution. The initial radius of both is set to $r_0 = 1$. The cylinder has an infinite extend in z. The cylinder collapses faster in the beginning, but the spherical collapse catches up towards the end, so both situations have the same collapse time τ_{coll}.

One can directly identify the linear mass density to be $\lambda = \pi \rho_{\text{int}} R_0^2$ and gets the same result as in Eq. (3.27).

2-d planar collapse of a circle

At this point, it is interesting to note that the collapse in 2-d gives a almost identical result. The Gauss integral from Eq. (3.28) can be applied onto a 2-d circle and gives

$$\left(4\pi r^2 \hat{r}\right) \cdot (g\hat{r}) = -4\pi G m \,.$$

Solving for the gravitational force g gives a result similar to Eq. (3.29), of

$$\boxed{g = -\frac{2Gm}{r}} \tag{3.30}$$

Collapse time of a cylinder

Going back to the ansatz for a collapsing spherical cloud, one can again assume the collapse of a cylinder to happen at terminal velocity and thus

$$v_{\text{t}}(r) = -\tau_{\text{s}} g = -\tau_{\text{s}} \frac{2\lambda_0 G}{r\,(t)} \,. \tag{3.31}$$

Integrating this equation in time leads to an equation of motion for the collapsing cylinder and a contraction time:

$$r(t) = \sqrt{R_0^2 - 4\pi G \tau_{\text{s}} \lambda_0 t} \quad \overset{r(\tau_{\text{c}})=0}{\Rightarrow} \quad \tau_{\text{c}} = \frac{R_0^2}{4G\tau_{\text{s}}\lambda_0} \tag{3.32}$$

Hence, a cylinder of size R_0 and mass density ρ_{int} is expected to collapse within a collapse time that is identical to the collapse time of a sphere:

$$\boxed{\tau_{\text{c}} = \frac{1}{4\pi\tau_{\text{s}}\rho_0 G} \equiv \tau_{\text{c,sphere}} \,.} \tag{3.33}$$

This is shown in Fig. 3.6 for a sphere and a cylinder with identical intial radius R_0. The cylinder is collapsing faster in the beginning of the collapse. At around half the collapse time, the collapse of a sphere speeds up and both geometries have an identical overall collapse time.

Plane parallel collapse

For a slab with infinite extend in x and y direction and height R_0, the gravitational pull is independent of hight above the slab. It reads

$$g_z = 4\pi L_z \rho_{\text{Hill}} G\,.$$

Thus, the collapse of a slab happens linear over time, see Fig. 3.6. Calculating the collapse time of such a slab, again at terminal velocity, yields

$$\tau_{\text{c},slab} = \frac{1}{4\pi\tau_\text{s}\rho_0 G} = \tau_{\text{c,sphere}}\,. \tag{3.34}$$

Hence, also the collapse time of a slab is identical to the one of a sphere.

3.3 The length scale criterion on dust cloud collapse

In order to formulate a comprehensive collapse criterion that is incorporating the above outlined criteria on Keplerian shear stability and short collapse time, one further needs to quantify the collapse opposing effects, which are of diffusing nature. It will be found that only a clump of a specific diameter of $l_\text{c} = 2r_\text{c}$ or larger can contract against any sort of underlying turbulent particle diffusion D.

3.3.1 The critical length scale

The idea that leads to a critical length scale criterion is by comparing the time a spherical particle cloud needs to collapse with the time a turbulent diffusion process needs to disperse the cloud, i.e. the time it takes a diffusion of strength D to surpass a distance r_c. This is also why the equality of the cylindrical and the spherical collapse time is important, as derived in the previous section. The simulations that are presented in the following Chapter 7 are 2-d simulations that mimic cylindrical and not spherical collapse.

Considering small particles with $\text{St} \ll 1$ which fall at their terminal velocity. The free-fall timescale is known from equation Eq. (3.33). The diffusion timescale stems from Fick's second law of diffusion,

$$\dot{\rho} = D\nabla^2\rho\,.$$

Here, this equation is used as a description of density diffusion, where normally it is concentration diffusion, i.e. the ratio of two mass densities. But, since the gas density is in first order constant throughout the collapse phase, as will be shown in the simulation results in Sec. 7.4.2, this equation holds. From this equation, a solution for the spreading of a perturbation can be found in the form of

$$\left\langle r^2(t)\right\rangle_x = Dt\,. \tag{3.35}$$

In this equation, D is defined as in Eq. (2.42). The typical expression of Eq. (3.35), e.g. from Einstein (1905), has an additional factor of 2, that is incorporated into the diffusion coefficient D.

This equation can be reformulated in the form of a *diffusion timescale* τ_D. This timescale is a measure for the time a particle needs to surpass a distance r_c by a diffusion process of strength D. The diffusion timescale reads

$$\boxed{\tau_\text{D} = \tfrac{r_\text{c}^2}{D}\,.} \tag{3.36}$$

In order to use this timescale in the analysis of PPDs, it can be rewritten into a dimensionless diffusion via

$$\delta = \frac{D}{c_\text{s} H}\,. \tag{3.37}$$

This translates the Ansatz $\tau_c \stackrel{!}{=} \tau_D$ into:

$$\frac{r_c^3}{3\tau_s m G} = \frac{1}{4\pi\tau_s \rho_{int} G} \stackrel{!}{=} \frac{r_c^2}{D} = \frac{r_c^2}{\delta H c_s} \tag{3.38}$$

Where $m = 4/3\pi r_c^3 \rho_{int}$ is the bulk mass of the spherical cloud with critical radius r_c. By expressing the internal cloud density in terms of multiplies f of Hill density ρ_{Hill}, one gains further flexibility by scaling the critical cloud density,

$$\boxed{\rho_{int} = f \cdot \rho_{Hill} = \frac{9f}{4\pi}\frac{M}{R^3}\,.} \tag{3.39}$$

Though shear stability is a primary condition for planetesimal formation via gravitational collapse, it is not necessarily reached right at Hill density, since Hill density neglects the influence of gas and friction on the collapse. By introducing f, one is in no need to exactly specify this 'real' critical density ρ_c, in order to derive a critical length scale, but the critical length scale is scalable for different critical densities.

With this density, Eq. (3.38) can be solved for the cloud size right at the border of stability in both, critical density and turbulent diffusion (Shariff, Karim and Cuzzi, Jeffrey N., 2015). The critical cloud diameter is

$$\boxed{l_c = \frac{2}{3}\sqrt{\frac{\delta}{f \cdot \mathrm{St}}}\mathrm{H}\,.} \tag{3.40}$$

This expression is called the *diffusion limited collapse criterion* and was first derived by *H. Klahr* in 2015 and first published in Klahr & Schreiber (2015). Note that this criterion is valid for all f *as long as* for the individual situation the condition for shear and tidal stability is given. For example, a particle cloud at Roche density would have a parameter $f \approx 5.3$ and a cloud at quarter of Hill density $f = 0.25$. Such a cloud at Roche density is clearly shear stable, but would probably have already collapsed at an earlier, lower density. A cloud at a quarter of Hill density is not shear stable in the first place, thus the criterion cannot be used.

The diffusion limited collapse criterion is further investigated in Chapter 7. Therein, numerical experiments are performed that show actually $f \approx 1$ is indeed a sufficient value and gas influence can be neglected to first order.

3.3.2 Stability analysis via solving the dispersion relation

A different approach to a critical length scale criterion can be performed, by doing a linear stability analysis of the problem in a local shearing sheet model (Goldreich & Lynden-Bell, 1965) and deriving a stability criterion from the dispersion relation. This is following a mixed case of Goldreich & Ward (1973) and Safronov (1972), similar yet not identical to the SGI, see Ward (2000).

Being only interested in radial and azimuthal length scales that are on the order or smaller than the particle scale height

$$\mathrm{H_d} = \sqrt{\alpha/\Omega\tau_s}\,,$$

which expression is only valid for small particles, one has to consider the dust clouds in terms of 3-d dust volume densities ρ_d. A treatment of the dust as surface density Σ_d is not sufficient. Consequently, a razor thin approximation cannot be made. The gravitational potential can be modelled as acting on plane waves in the Wentzel-Kramers-Brillouin (WKB) approximation $\sim e^{i(k_r r + \omega t)}$, i.e. gravitational potential $\Phi' = 4\pi G\rho'/k^2$ has to be taken, rather than $\Phi' = 2\pi G\Sigma'/|k|$ (Safronov, 1972).

In contrast to the SGI of a dust layer, in the case of dust cloud stability only the wavelengths λ smaller than the vertical extent are of interest. In the herein investigated case for the final collapse phase of a spherical cloud to a planetesimal, which is found in 3-d simulations (Johansen et al., 2007), the amplitudes of radial and vertical wavenumbers will be on the same order. This leads to a treatment of gravity that is the same as applied in the numerical simulations with the PencilCode, see Sec. 4.4.

The ansatz is the equations describing the evolution of the dust density, and the two dust velocity com-

ponents. To the equations here added are terms describing the frictional coupling between dust and gas (1), see Ward (1976), Ward (2000), Coradini et al. (1981), and Youdin (2005), and turbulent dust density diffusion (2) (Binney et al., 2009).

$$\frac{1}{\rho_\mathrm{d}}\frac{\partial \rho_\mathrm{d}'}{\partial t} + \frac{\partial v_r'}{\partial r} = \underbrace{\frac{D}{\rho_\mathrm{d}}\frac{\partial^2 \rho_\mathrm{d}'}{\partial^2 r}}_{(2)} \tag{3.41}$$

$$\frac{\partial v_r'}{\partial t} - 2\Omega v_\phi' = -\frac{\partial \Phi'}{\partial r} - \underbrace{\frac{v_r'}{\tau_\mathrm{s}}}_{(1)} \tag{3.42}$$

$$\frac{\partial v_\phi'}{\partial t} - \frac{\kappa^2}{2\Omega} v_r' = 0 \tag{3.43}$$

A pressure term for the dust, i.e. $-\frac{c^2}{\rho_\mathrm{d}}\frac{\partial \rho_\mathrm{d}}{\partial r}$, can be ignored, because effects of a velocity dispersion for the dust are treated in the diffusivity D (Shariff & Cuzzi, 2011). Further ignored is the effect of azimuthal friction $-v_\phi'/\tau_\mathrm{s}$, by assuming to be already in the dust dominated regime, i.e. dust-to-gas ratio being larger than unity and hence the gas follows the particle dynamics. Still, friction in the radial velocity expression is maintained, because here the gas cannot follow the collapse of the particles because the gas is incompressible.

A limiting case is gained for very long coupling times and zero diffusivity. In this limit one receives the dispersion relation as

$$\omega^2 = \Omega^2 - 4\pi G \rho_\mathrm{d}\,. \tag{3.44}$$

This dispersion relation defines the minimum density needed to have a dust ring radially contracting from self-gravity against the acting Coriolis force:

$$\rho_\mathrm{c} > \frac{1}{4\pi}\frac{M_\star}{R^3} \tag{3.45}$$

This density is by a factor of 9 smaller than the Hill density as defined in Eq. (3.15), because Keplerian shear has no influence on axis-symmetric ring collapse.

The full non-axissymmetric dispersion relation, but without diffusion and friction, is

$$\omega^2 = \Omega^2 - 4\pi G\rho_\mathrm{d} + i6\pi G \frac{k_x k_y}{k^2}\frac{\Omega}{\omega}\,. \tag{3.46}$$

Where k_x is now a function of time, because a plane wave Ansatz is subject to shear. This gets clear when imagining a line of tracer particles that is laid out in radial direction. This line will tilt due to the Keplerian shear, and so do pure radial modes get transformed into azimuthal modes over time. As being interested in collapse, this means one has to limit this down to cases where $|k_x| < k_y$. Thus, the complex term on the right-hand-side can be neglected.

In order to have $|k_x| < |k_y|$ fulfilled for a sufficient long time, the growth of the instability has to be faster than the Keplerian shear is ripping it apart. Thus, the growth rate $-i\omega$ has to be larger than the shear rate that can be determined from $k_x(t) = \frac{3}{2}k_y\Omega t$, which comes from the linearised shear, see Eq. (2.20). Choosing the growth rate to be double the shear rate gives $\omega^2 = -9\Omega^2$. The resulting critical density in that case is

$$\rho_\mathrm{c} > \frac{10}{4\pi}\frac{M}{R^3}\,, \tag{3.47}$$

which is still in good agreement with the Hill density.

Considering diffusion and friction in the dispersion relation for the axis-symmetric, or WBK case, with

$$k = \sqrt{k_x^2 + k_y^2} \approx k_x$$

because of $k_x \gg k_y$, one receives:

$$\omega^3 + \omega^2 \left(-iDk^2 - \frac{i}{\tau_\mathrm{s}} \right) + \omega \left(-\frac{Dk^2}{\tau_\mathrm{s}} + 4G\pi\rho_\mathrm{d} - \Omega^2 \right) + iDk^2\Omega^2 = 0\,. \tag{3.48}$$

The roots of this equations are given by

$$\omega^2 - \frac{Dk^2}{\tau_\mathrm{s}} + 4G\pi\rho_\mathrm{d} - \Omega^2 = 0 \qquad \text{and} \qquad \omega^2 \left(Dk^2 + \frac{1}{\tau_\mathrm{s}} \right) - Dk^2\Omega^2 = 0. \tag{3.49}$$

The second equation finds

$$\omega^2 = \frac{\tau_\mathrm{s} Dk^2}{\tau_\mathrm{s} Dk^2 + 1}\Omega^2, \tag{3.50}$$

which is always leading to positive, i.e. stable solutions for ω^2. The first equation has its roots at

$$-\frac{Dk^2}{\tau_\mathrm{s}} + 4G\pi\rho_\mathrm{d} - \Omega^2 = 0. \tag{3.51}$$

Thus, the critical wavenumber is dependent on the underlying density:

$$k = \sqrt{\frac{\tau_\mathrm{s}}{D}\left(4G\pi\rho_\mathrm{d} - \Omega^2\right)} \tag{3.52}$$

For ρ_c from Eq. (3.15) this is

$$k = \sqrt{8f\frac{\tau_\mathrm{s}}{D}}\Omega, \tag{3.53}$$

or translated into a critical wave length:

$$\boxed{l_\mathrm{c} = \frac{\pi}{\sqrt{2}}\sqrt{\frac{\delta}{f\mathrm{Si}}}H} \tag{3.54}$$

This is almost identical to the timescale derivation in the previous section (Eq. (3.40)) and differs only in a factor of 3.3, which may be attributed to the approximation in the linear regime and the restriction to axis-symmetric modes, i.e. ring collapse. Thus, it only tells us from what minimum wavelength a kind of SGI would start to operate, while neglecting Keplerian shear. The fully turbulent state on the other hand is apparently better described by the timescale criterion based on a non-linear amplitude. As numerical tests will later show, the criterion derived in Eq. (3.40) is in fact the relevant one.

3.3.3 Initial planetesimal size derived from collapse criterion

From this length scale criterion on a spherical particle cloud, one can try to estimate the resulting planetesimal diameter a_c. For this purpose, one can assume the particles within a collapsing cloud of mass $m = m_\mathrm{Hill}$ to get transformed into a spherical planetesimal of mass $m_\mathrm{p} = q \cdot m$. Here, q is the quality of the collapse and describes what fraction of the initial particle cloud gets incorporated into the final planetesimal.

Using this a priori assumption, one can determine the mass of the resulting planetesimal m_p. The cloud is assumed to contract to a solid, spherical body with size a_c and solid density $\rho_\bullet$.

$$m_\mathrm{p} = \frac{4}{3}\pi a_\mathrm{c}^3 \rho_\bullet = q \cdot \frac{4}{3}\pi r_\mathrm{c}^3 f \rho_\mathrm{Hill}\,,$$

see Eq. (3.39), where $r_c = l_c/2$ is the critical cloud radius. The resulting body would then have a diameter of

$$a_c = q \cdot l_c \left(\frac{f \rho_{\text{Hill}}}{\rho_\bullet} \right)^{\frac{1}{3}} = q \cdot \frac{l_c}{R} f^{\frac{1}{3}} R_\odot \left(\frac{3\rho_\odot}{\rho_\bullet} \right)^{\frac{1}{3}} .$$

Hence, the resulting planetesimal size will only depend on the initial particle cloud density via $a_c \sim \rho_{\text{int}}^{-6}$.

Combining this equation with the critical length scale criterion from Eq. (3.40) and expressing a_c in terms of solar radii, one arrives at the relation

$$a_c = f^{-\frac{1}{6}} \sqrt[3]{\frac{8\rho_\odot}{9\rho_\bullet}} \sqrt{\frac{\delta}{St}} \frac{H}{R} R_\odot , \tag{3.55}$$

where the first two terms are of order unity and can be neglected for order of magnitude estimates.

One can do a naive estimate on this, by using best guess solar nebula parameters. For a typical value of the solar nebula thickness $H/R = 0.04$ (Bell et al., 1997; D'Alessio et al., 1998) the radial flux dominating particle size, measured in Stokes number, is $\mathrm{St} = 0.1$, as was found in numerical simulations of the dust evolution in the solar nebula (Birnstiel et al., 2012). Together with a moderate numerically determined diffusivity value of $\delta_z(\mathrm{St} = 0.1) = 2.7 \times 10^{-6}$, taken from 3-d SI simulations of Johansen & Youdin (2007), performed at a dust-to-gas ratio of $\varepsilon = 10$, this results in planetesimals of diameter of

$$a_c = \left(\frac{q}{1.}\right)^{\frac{1}{3}} \left(\frac{1.}{f}\right)^{\frac{1}{6}} \frac{H/R}{0.04} \sqrt{\frac{\delta}{2.7 \cdot 10^{-6}}} \sqrt{\frac{0.1}{\mathrm{St}}} 98\,\mathrm{km}. \tag{3.56}$$

The found planetesimal diameter is comfortably in agreement with the observed characteristic object sizes, i.e. diameter at which the number density peaks, i.e. the cumulative size distribution has a knee in asteroid belt (Bottke et al., 2005), Kuiper belt (Nesvorný et al., 2011; Parker & New Horizons Science Team, 2015), Jupiter Trojans (Jewitt et al., 2000; Emery et al., 2015) and Neptune Trojans (Sheppard & Trujillo, 2010), see Fig. 1.3. Following Delbo et al. (2017), it is also the value at which the center of the likely initially Gaussian size distribution of the initial planetesimals in the asteroid belt lies (Morbidelli et al., 2009). Note that the absolute distance R from the Sun does not directly enter this equation, making planetesimal formation self-similar to first order at all distances from the Sun. Instead, the planetesimals formed depend on the disk aspect ratio $h = H/R$.

This result relies on the assumption of a complete conversion of a dust cloud into a single planetesimal, i.e. $q = 1$. One could also imagine a similar planetesimal formation scenario as for the birth of a multiple stellar system from a single but large turbulent molecular cloud core. In which case more than one planetesimal would form in a binary or even hierarchical system. The in Chapter 7 presented results of collapse simulations of such clouds show actually only a certain percentage of the available material gets converted into a bound clump, suggesting $q \approx 0.1$ - 0.2. Though this efficiency factor q needs to be further studied, with $a_c \sim q^{\frac{1}{3}}$ the resulting planetesimal diameter itself will only change slightly. Also, the other parameters St and δ influence the size of the planetesimals only weakly. Further consequences of this finding can be found in the discussion in Chapter 8.

The used value for the turbulent particle diffusion in Eq. (3.56) comes from measurements of 3-d SI simulations. If a stronger source for particle turbulence is found, this value has to be adjusted accordingly.

3.3.4 Kolmogorov cascade of large scale turbulence as particle diffusion source

Now, one might assume that it is not the turbulent diffusion from the SI that drives the particle diffusion in Eq. (3.40). Instead, it could be the large scale gas turbulence, i.e. α-turbulence in the gas that couples onto the particles. One can try to estimate the actual strength of this gas turbulence on the scales of planetesimal formation, and then compare this value with the value obtained from SI simulations. The following derivation should be taken as a worst-case approximation and not as a guaranteed value, since the Rossby criterion from Cuzzi et al. (2001) from Sec. 2.1.4 might play an additional role. Also the turbulent cascade in the dust-gas mixture might be different. Thus, here assumed is that the turbulent cascade of

pure gas turbulence happens in an environment with a density ρ_g. This turbulence cascades down onto the scales of planetesimal formation and then, on this scale, the turbulent energy gets transferred onto a new fluid that has the combined density of dust and gas, i.e. $\rho_g(1+\varepsilon)$, with ε the dust-to-gas ratio.

A typical value for gas turbulence in a PPD is $\alpha \approx 10^{-3}$, see for example Turner et al. (2014). This values stems from measurements of the turbulent strength of different gas instabilities in pure gas simulations. Hence, these simulations all have in common that they are performed without taking dust into account and cannot give reliable results on turbulent particle diffusion strength. Especially as the herein discussed dust particles are marginally coupled and do a back-reaction onto the gas. This considerations are neglected in (most) α measurements in the literature. The simulations presented in the following chapters to measure the gas turbulence to have a strength of $\alpha < 10^{-4}$ found cases with active SI, compare with Fig. 5.11. But, if one wants to compare this value with the typical value of $\alpha = 10^{-3}$ this takes neither the turbulent Kolmogorov cascade nor the additional dust load of the performed aSI and SI simulations into account.

The Kolmogorov cascade describes the way a turbulent eddy transports energy down onto smaller sized eddies via vortex stretching. This cascade reaches down to smaller sizes until the scale of molecular viscosity is reached and the flow gets laminar. Hence, a turbulence with a certain α-value does not mean this value is identical an all scales. In PPDs, the turbulence of gas is typically parametrized as a turbulent viscosity ($\alpha = \nu c_s \mathrm{H}$). The α parameter can be separated into a gas turbulent velocity u and a characteristic eddy size L_0, as argued by Cuzzi et al. (2001), via

$$u_0 = \sqrt{\alpha_0} c_s \qquad \text{and} \qquad L_0 = \sqrt{\alpha_0} H\,, \tag{3.57}$$

see Sec. 2.1.4. As the α prescription does not state the nature of the turbulence, the turbulence herein will be assumed to be isotropic an on a scale of L_0. This is not necessarily the correct physical situation that is found in all simulations of, i.e. the MRI or the vertical shear instability. In them also large (spiral) waves, or shear waves, do transport angular momentum. But, the following analysis stays with the idea of an isotropic turbulence in order to derive a value comparison for the turbulent viscosity on the scales of planetesimal formation. Still, the derived values for the turbulence at the small scales of planetesimal formation should be seen as a worst case scenario. In any other scenario the velocity u' on the small scales will be lower.

Now, taking the turbulent velocity from Eq. (3.57), and letting it undergo the Kolmogorov cascade for an isotropic turbulence, see Kolmogorov (1991), one finds

$$u^2 \cdot \frac{u}{l} = \frac{u_0^3}{L_0} = C = \text{const.}\,, \tag{3.58}$$

where u^2 is the kinetic energy, u/l the energy dissipation timescale, and the C is the dissipation rate. This rate is constant over all length scales for a Kolmogorov turbulence cascade, until the molecular dissipation scale is reached.

However, this neglects the influence of dust within the dust-gas mixture, as it is the medium in the presented aSI and SI simulations. Hence, the turbulent momentum in the gas has to additionally undergo an energy transfer from pure gas into a mixture of dust and gas, which has to be done in the energy dissipation picture of Kolmogorov. Assumed here is for simplicity that the dust and the gas have the same velocity. This means, the additional load of the dust onto the gas is introduced similar to an enhancement in the gas density, i.e. as if one sets $\mathrm{St} = 0$. This means, the cascade gets feeded with the prescription from Eq. (3.58) and cascades down onto the primed length scales l' of planetesimal formation. Then, on the primed scale, the kinetic energy gets transferred onto a new eddy with $(1+\varepsilon)$ higher mass. In this energy picture, since the density changed from ρ_g to $\rho_\mathrm{g} + \rho_\mathrm{d} = \rho_\mathrm{g}(1+\varepsilon)$, the Kolmogorov cascade of a turbulence α_0 produces a turbulent velocity u' on the scale of l', as

$$C = \frac{u_0^3}{L_0} = \frac{\sqrt{\alpha_0}^3 c_\mathrm{s}^3}{\sqrt{\alpha_0} H} = \alpha_0 c_\mathrm{s}^2 \Omega \overset{!}{=} \frac{u'^3_0}{l'} \overset{!}{=} u'^2 (1+\varepsilon) \cdot \frac{u'}{l'}\,. \tag{3.59}$$

The α-value measured in the presented simulations needs to be compared with a turbulent viscosity ν on the corresponding scales l' of the simulation domain. In order to get this viscosity, one can use the mixing length cascade from Eq. (3.59):

$$\boxed{\nu' = l' u' = \left[\tfrac{l'}{1+\varepsilon} C\right]^{1/3} l' = \left(\tfrac{\alpha_0}{1+\varepsilon}\right)^{1/3} l'^{4/3}\,.} \tag{3.60}$$

This equation now can be used to calculate a turbulent viscosity value that originates from a pure gas turbulence of strength α_0, but cascaded down onto the scales of the aSI and the SI, by taking the dust load into account. The scale l' that one has to use for this comparison is in the best case $\mathrm{d}x$, and in the worst case L_x. The results of this comparison with the measured α in the simulations, is done in Sec. 5.2.

4 Numerical Methods

The simulations presented in the course of this thesis use the open source PencilCode[5], see Brandenburg (2001), Brandenburg & Dobler (2002), Brandenburg (2005), and Youdin & Johansen (2007) for details on the implementation of the specific methods. In general, the PencilCode is a numerical solver. In this work, it is used in form of a finite-difference solver for hydrodynamic problems. It comes with a scheme that uses sixth-order symmetric spatial derivatives and a third-order Runge-Kutta time integrator. The code is written in Fortran-95. It has different modules for different physical problems and for different numerical schemes, such as the implementation of Lagrangian particles and the shearing sheet approximation. It is parallelized via the *message passing interface* (MPI), and runs smoothly on up to a few ten-thousand cores in hydro-only simulations, and a few thousand cores in simulations that also incorporate Lagrangian particles.

Within this thesis, all the presented simulations are performed in the shearing-sheet approximation. This is a Cartesian coordinate system that is co-rotating with the Keplerian orbital frequency Ω at an arbitrary distance R_0 from the star, see Sec. 2.1.5. Arbitrary means that the simulation results are valid independent of the distance from the star, and thus the simulation time and length scales are set in PPD units of H and Ω. In the following, all the code parameters and quantities, e.g. distance, Stokes number, or particle diffusion, are set to be in dimension free disk units as well. The coordinate system (x, y, z) of the shearing box can be identified as (r, φ, z) for small r and φ, see Fig. 2.1 and Fig. 4.1. In the following these notations will be used interchangeably. The boundary conditions of the shearing sheet are periodic in y- and z-direction, and shear-periodic in x-direction. The latter means that the velocities and positions have to be readjusted for a quantity or particle that is transported over the radial boundary condition, see below.

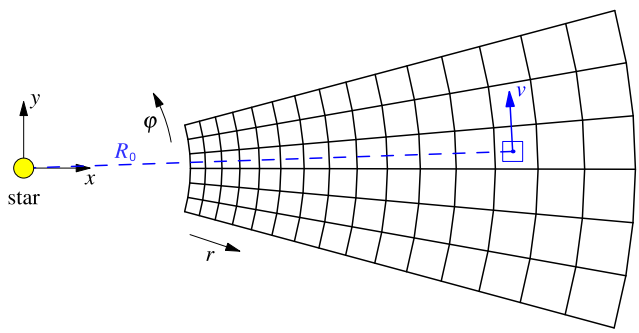

Figure 4.1: The shearing sheet approximation allows to simulate a patch (blue box) out of a protoplanetary disk (black grid). The center of the shearing box has a distance R_0 from the star and moves with Kepler velocity $v_K = \Omega R_0$ around it. This movement is translated by the coordinate transformation and shear linearisation into a linear shearing motion, see Sec. 2.1.5. In this shearing box coordinate system, the center of the domain is at rest. Everything closer to the star ($x < 0$) moves forward in azimuthal direction, everything towards the outside of the domain ($x > 0$) moves backwards. *Illustration by Thomas Müller.*

[5] http://pencil-code.nordita.org/

The particle prescription used in the presented simulations describes the particles as Lagrangian super-particles. Super-particles represent a swarm of identical particles that interact with the gas as a group. Their properties, e.g. density, is smoothed out over the neighbouring grid cells via the *Triangluar Shaped Cloud* (TSC) scheme, see Youdin & Johansen (2007) for details on the implementation in the PencilCode.

4.1 Solving the streaming instability problem in a shearing sheet approximation

The presented simulations solve the momentum equation for the motion of the gas and dust particles on a Cartesian grid in a shearing box approximation, see Goldreich & Lynden-Bell (1965), Balbus & Hawley (1992) and Brandenburg et al. (1995). The gas velocity $\vec{u}$, relative to the Keplerian shear, is evolved via its Euler equation:

$$\frac{\partial \vec{u}}{\partial t} + (\vec{u}\cdot\nabla)\vec{u} + u_{0,y}\frac{\partial \vec{u}}{\partial y} = \left(2\Omega u_y \hat{x} - \frac{1}{2}\Omega u_x \hat{y} + \Omega^2 z \hat{z}\right) - c_s^2 \nabla \ln \rho_\mathrm{g} - 2\Omega\eta\hat{x} - \frac{\varepsilon}{\tau_\mathrm{s}}[\vec{u}-\vec{v}] + \vec{f}_\nu(\vec{u},\rho_\mathrm{g}). \quad (4.1)$$

Its derivation is performed in Sec. 2.1.5. The terms in this equation are as follows. The second and the third terms of the left-hand side are the advection terms, where the third term resembles the advection by the shear flow. On the right-hand side are the terms for the Coriolis force, stellar gravity, the local pressure gradient, with $\nabla P = c_s^2 \nabla\rho$, the global radial pressure gradient from Eq. (2.13), the particle-gas drag interface and the numerical hyper-viscosity term $\vec{f}_\nu$ (VonNeumann & Richtmyer, 1950). The dust-to-gas ratio is defined as volume density ratio of dust and gas, i.e. $\varepsilon = \rho_\mathrm{d}/\rho_\mathrm{g}$. All in the following presented simulations do not include vertical gravity from a central star, hence $\Omega^2 z = 0$. The unperturbed Keplerian orbital velocity in the local Keplerian frame is $u_{0,y} = -\frac{3}{2}\Omega x$, from Eq. (2.20).

The gas density is evolved via the continuity equation:

$$\frac{\partial \rho_\mathrm{g}}{\partial t} + \nabla\cdot(\rho_\mathrm{g}\vec{u}) + u_{0,y}\frac{\partial \rho_\mathrm{g}}{\partial y} = f_\mathrm{D}(\rho_\mathrm{g}).$$

Here, the function $f_\mathrm{D}(\rho_\mathrm{g})$ is the numerical hyper-diffusivity (VonNeumann & Richtmyer, 1950). Together with the numerical hyper-viscosity, they both ensure the stability of the PencilCodeby reducing steep gradients in densities and velocities. The hyper-viscosity is also responsible for the shock viscosity, see PencilCode manual for further reading.

The particles positions are evolved via

$$\frac{\partial \vec{x}}{\partial t} = -\frac{3}{2}\Omega x_\mathrm{p}\hat{y} + \vec{v} + \vec{f}_\mathrm{D}(\rho_\mathrm{d}),$$

with particle radial position x_p and particle velocity $\vec{v}$. The particle velocities are evolved, similar to the gas velocity, via

$$\frac{\partial \vec{v}}{\partial t} + (\vec{v}\cdot\nabla)\vec{v} + u_{0,y}\frac{\partial \vec{v}}{\partial y} = \left(2\Omega v_y \hat{x} - \frac{1}{2}\Omega v_x \hat{y} - \Omega^2 z\hat{z}\right) - \frac{1}{\tau_\mathrm{s}}[\vec{v} - \vec{u}(\vec{x})], \quad (4.2)$$

were again the stellar gravity term is neglected in the calculations, $\Omega^2 z = 0$, which was here added for completeness. In the equation for the dust particles, the global gas pressure gradient is not acting. The reason is the physical density of a particle that is much higher then the gas density and thus the exerted momentum from the gas pressure onto a particle is small.

4.2 Code units, boundary conditions and the shearing sheet implementation

Fig Fig. 4.2 illustrates how the shear periodic boundary for a shearing sheet domain L works. At the initial timestep $t = t_0$ (top), the radial periodicity is similar to a classical periodic boundary condition. But, with

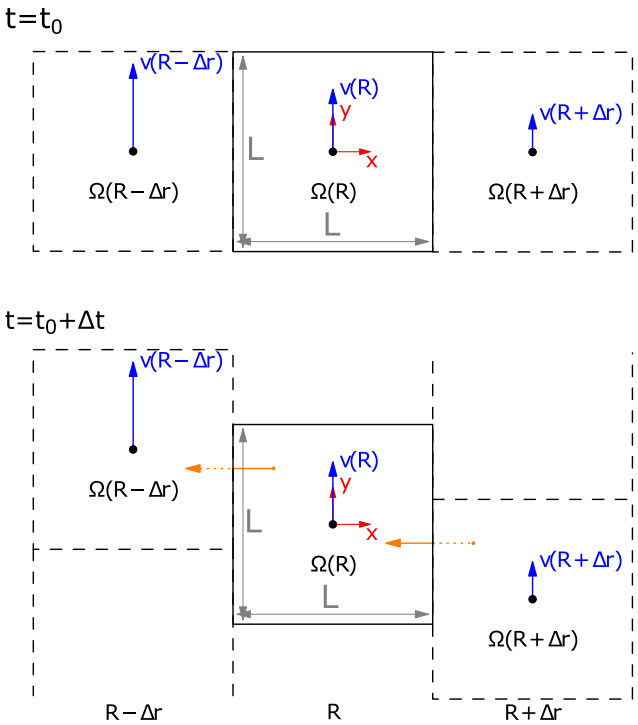

Figure 4.2: Example for the shear periodic boundary condition for a shearing box of L in size. At the initial time step t_0 (top), the radial periodicity is similar to a normal periodic boundary condition. But, with evolving time, the linear shear moves this periodic boundary in azimuthal direction. A particle leaving the radial inner boundary re-enters the simulation domain shifted by the shear-offset, see yellow arrow, and its azimuthal velocity is shear corrected. *Illustration by Thomas Müller.*

evolving time, the linear shear moves this periodic boundary in azimuthal direction. The azimuthal velocity of the radially next inner domain is

$$v_{R-\Delta r} = -\frac{3}{2}\Omega(-L) = \frac{3}{2}\Omega L\,.$$

In order to correct for this shearing bondary condition, a particle that leaves the radial inner boundary at an azimuthal position of $y_{\mathrm{p},-L}$, re-enters the simulation domain on the outer boundary at a position $y_{\mathrm{p},+L}$. This new azimuthal position has to be shifted by the shear-offset of the radially inner box, i.e.

$$y_{\mathrm{p},+L} = y_{\mathrm{p},-L} + \mathrm{mod}\left(\frac{3}{2}\Omega L \cdot t, L\right).$$

The particle azimuthal velocity also has to change by the velocity offset from the inner to the outer boundary, which is also

$$v_{-L} = v_{+L} \underbrace{-\frac{3}{2}\Omega L}_{v_{\mathrm{shear}}}.$$

Of cource, the same, but with different sign, happens to a particle that crosses the outer radial boundary.

4.3 Implementation of the global pressure gradient

A main driver in the investigated dynamics inside of a PPD is the sub-Keplerian velocity of the gas. It is induced by the global gas pressure gradient. Assuming an isothermal disk, the pressure gradient arises from the density gradient via

$$P = \frac{\partial \ln \rho_\mathrm{g}}{\partial \ln r} = r \frac{\partial \ln \rho_\mathrm{g}}{\partial r} = r \left(\nabla \ln \rho_\mathrm{g} \right) \quad \Rightarrow \quad \nabla \ln \rho_\mathrm{g} = \frac{P}{r} \,.$$

As Sec. 2.1.3 showed, this can be reformulate into a sub-Keplerianess parameter η via

$$\eta v_\mathrm{K} = -\frac{1}{2} \left(\frac{\partial \ln \rho_\mathrm{g}}{\partial \ln r} \right) h^2 v_\mathrm{K} \,,$$

where $h = H/R$ is the disk aspect ratio.

For using this pressure gradient in the PencilCode, the pressure gradient has to be normalized to disk units by

$$\eta v_\mathrm{K} = -\underbrace{\frac{1}{2} \left(\frac{\partial \ln \rho_\mathrm{g}}{\partial \ln r} \right)}_{=:\beta_{\ln(\rho)}} h \cdot c_\mathrm{s} \quad \Rightarrow \eta = -\frac{1}{2} \beta_{\ln(\rho)} h \,.$$

Now, the sub-Keplerianess of the gas can be expressed in $\beta_{\ln(\rho)}$, together with the disk aspect ratio h, see Eq. (2.12). The sub-Keplerianess is found by looking at the expression of ηv_K and plugging $v_\mathrm{K} = c_\mathrm{s}/h$ into if. Where the latter expression comes from

$$\frac{c_\mathrm{s}}{v_\mathrm{K}} = \frac{H}{R} \,,$$

which isefl is a combination of Eq. (2.8) and Eq. (2.10).

It follows

$$\eta v_\mathrm{K} = \eta \frac{c_\mathrm{s}}{h} = -\frac{1}{2} \beta_{\ln(\rho)} \frac{c_\mathrm{s}}{\cancel{h}} \cancel{h} = -\frac{1}{2} \beta_{\ln(\rho)} c_\mathrm{s}$$

The herein chosen value for the gas pressure gradient is $\beta_{\ln(\rho)} = -0.1$ to be comparable with Johansen & Youdin (2007). This value translates into $\eta = 0.05 \cdot H/R$, see Sec. 2.16, i.e. $\eta = 0.005$ for $c_\mathrm{s}/v_\mathrm{K} = \mathrm{H}/R = 0.1$.

To conclude, by re-formulating the pressure gradient in terms of a dimension-free sub-Keplerianess $\beta_{\ln(\rho)}$, the sub-Keplerian velocity of the gas becomes independent of a specific disk model. This adds a degree of freedom to the code interpretation. So, by defining the value of $\beta_{\ln(\rho)}$, one does not define a specific disk model in terms of H/R. Hence, the simulation length scales, i.e. herein expressed in disk scale height H, can later in the interpretation changed. Either by choosing a specific value for H/R or by choosing a value for η.

They are all interlinked by this equation:

$$-\frac{1}{2} \beta_{\ln(\rho)} H = \eta R \quad \Rightarrow \quad H = -2 \frac{\eta}{\beta_{\ln(\rho)}} R \,.$$

When studying the source code of the PencilCode, beware of there is also `beta_glnrho_scales` defined in the code, which is set to `beta_glnrho_global*Omega/cs0` for code internal reasons.

4.4 Deriving a gravitational model for the dust density to be at Hill density

The gravitational potential in the code is calculated by solving the dimension-free form of the Poisson equation

$$(H\nabla)^2 \Phi / c_\mathrm{s}^2 = \hat{G} \frac{\rho_\mathrm{d}}{\rho_\mathrm{g}} \tag{4.3}$$

via the Fourier method, see Johansen et al. (2007). Hence, the ansatz for the gravitational potential is

$$\Phi(\vec{x}) = \sum_k \Phi_k \exp\left(\mathrm{i}\vec{k}\cdot\vec{x}\right),$$

with spatial wavenumber $\vec{k}$ and

$$\Phi_k = -4\pi \frac{\hat{G}\tilde{\rho}_k}{\left|\vec{k}\right|^2}.$$

Here, $\tilde{\rho}_k$ is the Fourier amplitude of the density and $\hat{G}$ is the self-gravity parameter in code units.

4.4.1 Justification for neglecting the vertical stellar gravity component

Chapter 7 numerically analyses the gravitational instability of a dust cloud, especially the cloud stability criterion as derived in Sec. 3.3. It might surprise, but the dominating source of gravitational force at work actually is the self-gravity of the dust cloud. The additional contribution by the vertical stellar gravity component can be neglected. This approximation can be confirmed by either looking at the gravitational acceleration on the surface of a sphere with Hill density, or by looking at the gravitational acceleration that is exerted by an infinitely extended slab at Hill density. The slab in this case represents a disk mid-plane at Hill density.

Gravitational acceleration on the surface of a Hill sphere

First, the gravitational acceleration $g_\mathrm{Hill,sphere}$ is calculated on the surface of a Hill sphere with radius z and compared with the stellar gravity component. The stellar gravity is known from Eq. (2.4) as

$$g_\star = \Omega^2 z = z \cdot \frac{GM_\star}{R^3}.$$

The gravitational acceleration by a spherical Hill mass cloud is

$$g_\mathrm{Hill,sphere} = \frac{Gm_\mathrm{Hill}}{z^2} = \frac{3z^3}{z^2}\frac{GM_\star}{R^3} = 3z \cdot \frac{GM_\star}{R^3}.$$

Where the spherical cloud is assumed to be centred around the disk mid-plane. By comparing these two, one can conclude that the gravitational pull of a dust sphere at Hill density is three times stronger than the vertical stellar gravity.

Gravitational acceleration by a disk mid-plane at Hill density

The considered Hill sphere will properly be part of a very dense mid-plane layer of hight z. This mid-plane layer can be guessed to be infinitely extended in radial and azimuthal direction. This dense mid-plane can further be assumed to also be right at Hill density. This assumption on the mid-plane density is the considered case in the following collapse simulations of Chapter 7. One can calculate the gravitational force by approximating the dense mid-plane as an extended slab of thickness z. The gravitational acceleration

can be found via the Gauss integral:

$$\oint \vec{g}_{\text{Hill,slab}} \cdot \mathrm{d}\vec{A} = -4\pi G m$$
$$-2 g_{\text{Hill,slab}} A = -4\pi G \rho_{\text{Hill}} A 2z$$

One finds in this formula the extend of the slab to be incorporated in the surface area A, and this then cancels out, i.e. the extend of the slab is of no importance. The resulting gravitational acceleration is

$$\Rightarrow g_{\text{Hill,slab}} = 2\pi G \frac{9}{4\pi} 2z \frac{M_\star}{R^3} = 9z \frac{GM}{R^3}$$

This means that a particle right above a mid-plane at Hill density will feel a nine times stronger pull from the self-gravity of the disk mid-plane, than from the star.

4.4.2 Gravitation constant for Hill density in code units

The way one can set a simulation to be at Hill density, is by altering the gravitational constant in the code input parameters. Since the coordinate transformation into the shearing frame did already remove the gravitational potential from the star, changing the gravitational constant in the code only affects the self-gravity.

By looking at the Poisson equation in code units, one finds the correct way to alter the gravitational constant in order it to represent a value that sets the total simulation density at its Hill density. This can be achieved by dividing the Poisson equation by a factor of Ω^2 and using the fact that densities in the code are normalized in a way that the mean gas density is $\rho_0 = 1$.

$$\frac{\nabla^2 \Phi}{\Omega^2} = \frac{4\pi G \rho}{\Omega^2} = \frac{4\pi \left(G\rho_0\right)}{\Omega^2} \cdot \frac{\rho}{\rho_0}$$

This is right the Poisson equation expressed in code units. Reformulating it leads to

$$\nabla^2 \hat{\Phi} = 4\pi \hat{G} \hat{\rho} \,. \tag{4.4}$$

The gravitational constant in code units reads

$$\boxed{\hat{G} = G\rho_0/\Omega^2 \,,} \tag{4.5}$$

and the density in code units as

$$\boxed{\hat{\rho} = \rho/\rho_0 \,.} \tag{4.6}$$

Now, Eq. (3.39) can be used to scale the code internal density by means of Hill density, by introducing again the scaling parameter f. Eq. (3.39) can be rewritten into an equation for the gravitational constant, by using $M_\star/R^3 = \Omega^2/G$, such that it reads

$$G = \frac{9f}{4\pi} \frac{\Omega^2}{\rho_{\mathrm{g}} \varepsilon} \,.$$

Plugging this into Eq. (4.5) leads to a gravitational constant in code units of

$$\boxed{\hat{G} = \tfrac{9f}{4\pi\varepsilon} \,,} \tag{4.7}$$

which now expresses densities in terms of Hill density, by scaling it with f, i.e. $f = 1$ is right the condition for the simulation to be at Hill density.

5 Azimuthal and Vertical Streaming Instability on the Scales of Planetesimal Formation

This chapter studied the *Streaming Instability* (SI) in radial-vertical 2.5-d simulations for $\mathrm{St} = 0.1$ and $\mathrm{St} = 0.01$ particles at initial dust-to-gas ratios from $\varepsilon_0 = 0.1$ up to 1000. Here, 2.5-d means radial-vertical simulations that take variations in the azimuthal velocity component into account. Additionally, investigated are 2-d simulations in radial-azimuthal extend of the same initial parameters. The simulations in the radial-azimuthal plane found a very similar instability to the streaming instability. This new instability is named *azimuthal Streaming Instability* (aSI), as this new instability is not proven to be identical to the SI, as known from Youdin & Goodman (2004) and Johansen & Youdin (2007). Before this project has been carried out, the canonical view on the SI saw this instability to only operate in radial-vertical extend, as Youdin & Goodman (2004) only solved the dispersion relation for the SI solely in the radial-vertical plane. The only appearance in the literature of the aSI in 2-d radial-azimuthal simulations is in the work of Raettig et al. (2015), yet, no afford was made in further studying this instability in radial-azimuthal simulations. The here in this chapter presented work can thus be seen as the very first dedicated endeavour into the realm of the aSI. This new instability should actually keep its new name, as it is still unclear if the presented instability identical to the SI.

Before going into the simulation results, the first section of this chapter defines the diagnostic quantities that help to characterize the instabilities, e.g. rms-velocities and correlation length. With this set of tools in hand, Sec. 5.2 then presents the results from four performed *parameter studies*. Two parameter studies were performed for the SI (r-z plane) and two for the aSI (r-φ plane). For each instability, one parameter study performed with $\mathrm{St} = 0.01$, and one with 0.1 particles. Each of these four parameter studies then covered simulations domain sizes of $L = 0.1\,\mathrm{H}$, $0.01\,\mathrm{H}$ and $0.001\,\mathrm{H}$, with a numerical resolution of $N = 128$. As second parameter, the initial dust-to-gas ratios was altered from $\varepsilon_0 = 0.1$ up to 1000. Additionally, a resolution study was performed for the aSI with $\mathrm{St} = 0.1$ particles that additionally investigate the instability in simulations with numerical resolutions of $N = 256$ and $N = 1260$, see Sec. 5.3. The results presented on the 2-d parameter study are from the first author publication Schreiber & Klahr (2018).

In the case of dust trapping in a zonal flow, the aSI/SI has to operate within it a pressure bump if the diffusion limited collapse scenario is correct. This has already been shown numerically in the work by Johansen et al. (2007) and analytically in Auffinger & Laibe (2017), but only for the SI and not for the aSI. Thus, Sec. 5.4 investigates the aSI in an artificial zonal flow. Lastly, also 3-d simulations of the SI were performed. Their results are presented separately in Chapter 6.

5.1 Investigated quantities

A main part of this project is the measurement of the particle diffusivities δ of the SI and the aSI. The measurement method for the particle diffusivity is presented in Sec. 2.2.5. For a better understanding of the SI and aSI properties, further quantities were studied, and these quantities are introduced in the following.

5.1.1 Particle dispersion σ

The dispersion describes which velocity an ensemble of particles is spreading out with. This is not necessarily due to a diffusion process.

Consider a heap of force-free particles, all of them with a different initial velocity. This heap will disperse, i.e. fly apart ballistically. The reason is each particle has its own velocity direction and nothing keeps them bound. The heap is clearly dispersing and not diffusing, since the spreading of the particle is not following the laws that define a diffusion process, see Sec. 2.2.5, i.e. their movement does not compare with a random walk. In order to quantify such a dispersive behaviour, the *Root-Mean-Square* (rms) deviation from mean velocity of the particle heap is measured:

$$\sigma \equiv v_{\mathrm{rms}} = \sqrt{\frac{1}{N_{\mathrm{par}}} \sum_{j=1}^{N_{\mathrm{par}}} \left| \vec{v}_{\mathrm{par},j} - \left\langle \vec{v}_{N_{\mathrm{par}}} \right\rangle_x \right|^2} \tag{5.1}$$

Here, N_{par} is the number of particles in the heap and $\left\langle \vec{v}_{N_{\mathrm{par}}} \right\rangle$ the mean velocity of the particle ensemble. Where the angle bracket is the arithmetic mean value.

In a numerical simulation, this quantity can be derived *globally*, meaning for the whole simulation domain, and *locally*, meaning for a single simulation grid cell. In the following, globally will be indicated by a $\circ$ symbol and locally by a $\square$ symbol.

5.1.2 Correlation time τ_{corr}

Comparing the measurment methods for δ, see Sec. 2.2.5, with σ from above, one sees that the method for estimating δ has the drawback of only being able to give a single value for the whole simulation domain, and not a local diffusivity at a certain spot. The reason is that a constant diffusion coefficient has to be assumed in order to use the time derivative of the rms of the travel distances for measuring the diffusion strength, see Eq. (2.42). Thus, it would be preferable to measure the local particle dispersion $\sigma_\square$ and link it to a local diffusivity $\delta_\square$ via a correlation time:

$$\tau_{\mathrm{corr}} \coloneqq \delta/\sigma^2 \quad \Rightarrow \quad \delta_\square = \tau_{\mathrm{corr}} \sigma_\square^2 \tag{5.2}$$

This is only true under the assumption that τ_{corr} is constant on all turbulent scales for a whole SI-active simulation. Which is not necessarily true on all scales, since the correlation time resembles the turbulent eddy turn-over time.

The correlation time can be derived from assuming the turbulent diffusion to be Fickian process, see Johansen et al. (2006b). Assuming u_k to be the turbulent velocity amplitude on the length scale l_k, over which the turbulent eddy transport D_k is occuring, then $D_k \simeq u_k l_k$. One can approximate $l_k = u_k \tau_k$, with τ_k the eddy turnover time. In this equation, the turbulent velocity can be seen as $\sqrt{u^2}/c_{\mathrm{s}}$, which is right the Mach number. Hence, the diffusion coefficient should scale with σ^2. Averaging over all scales leads to Eq. (5.2), where $\tau_k \equiv \tau_{\mathrm{corr}} = \mathrm{const.}$

5.1.3 Correlation length l_{corr}

One can ask, if the simulations resolve the dominant scales of the turbulent eddies. Thus, the correlation length

$$l_{\mathrm{corr}} = \frac{\delta}{\sigma} \tag{5.3}$$

can be computed, which is a measure for the turbulent eddy size. If l_{corr} is getting smaller than $\mathrm{d}x$ they tend to be not resolved by the simulation grid and eddies larger than the domain size L should not be present as they do not fit inside the simulation domain. It can also be seen as an 'poor mans fourer analysis', giving the most prominent eddies size.

5.1.4 Particle drift ζ

In order to investigate the behaviour of the particles with respect to the underlying gas velocity, one can use the particle drift ζ as rms deviation of the particle velocity v from the gas velocity u at the particle location $\vec{x_i}$, via

$$\zeta = \sqrt{\frac{1}{N_{\text{par}}} \sum_{i=1}^{N_{\text{par}}} |\vec{v}_i - \vec{u}(\vec{x}_i)|^2}, \tag{5.4}$$

with N_{par} the total number of particles within a grid cell or the total number of particles when evaluated globally. This expression should be equal to the Nakagawa drift solution from Eq. (2.38). Again, it can be distinguished between local drift $\zeta_\square$ and global drift $\zeta_\circ$. For the simulation results, the interpolation of the gas velocity at the particle position is done via the TSC method, see Chapter 4.

5.1.5 Viscous stress α

As explained in Sec. 2.1.4, the canonical prescription of turbulent gas transport inside of PPDs is done via the α-turbulence model. In the presented shearing box simulations, it is calculated by setting the Reynolds stress equal to an artificial, equivalent viscous stress, via

$$\langle u_x' u_y' \rangle = \nu \nabla \cdot \vec{u}. \tag{5.5}$$

Here, the perturbation theory notation is used, i.e. perturbations from the mean flow u are marked as primed, u'. The turbulent viscosity ν that originates from turbulent Reynolds stress is canonically written in the form of α viscosity by normalizing them to disk units, via

$$\boxed{\alpha = \nu/(c_s H).} \tag{5.6}$$

Starting from Eq. (22) from Klahr & Bodenheimer (2003), the r-φ Reynolds stress tensor component reads

$$\alpha = A_{r\varphi} = \frac{\langle u_\varphi' (\rho u_r)' \rangle}{\bar{\rho} c_s^2},$$

where the angle brackets and bar represent spatial and time averages. One can further simplify this equation by using

$$\langle u_x' u_y' \rangle = \langle u_x u_y \rangle - \langle u_x \rangle \langle u_y \rangle$$

and $\nabla \vec{u} = -(3/2)\Omega$. Where the latter is again the linearised Keplerian shear approximation, see Eq. (2.20). A new form is obtained as

$$\boxed{\alpha = \frac{-2(\langle u_x u_y \rangle - \langle u_x \rangle \langle u_y \rangle)}{3 c_s^2},} \tag{5.7}$$

where a constant gas density was assumed. A constant gas density is valid, since the measured gas density fluctuations in the presented simulations have at their maximum an amplitude of 10^{-3}. In this equation, the averaging $\langle \cdot \rangle$ is done in space and time.

In this equation now, the present underlying linear gas transport gets subtracted by the second term. In the herein presented SI simulations the linear gas transport arises from the Nakagawa drift solution. Hence, this second term is non-negligible as the Nakagawa gas drift does not contribute to the Reynolds stress tensor, but is part of the unperturbed gas flow.

5.1.6 Schmidt number Sc

Additionally investigate is the *Schmidt number*. It is defined as the ratio of radial momentum transport over radial mass diffusion:

$$\boxed{\mathrm{Sc} = \alpha/\delta_x} \tag{5.8}$$

Here in this analysis the Schmidt number is used to investigate the ratio of gas transport α against particle diffusion δ. Note that some authors assume $\delta \equiv \alpha$, which is only true for tightly coupled particles. As will be seen, this is not true for the SI nor for the aSI.

5.2 2-d parameter study on the streaming instability and its azimuthal counterpart

This first numerical project is a parameter study of the SI and the aSI in 2.5-d/2-d simulations at dust-to-gas ratios well above unity. The SI is known from Youdin & Goodman (2004) as a dust-gas instability in radial-vertical direction. They showed that only one direction, e.g. $k_r \neq 0$ and $k_z = 0$, is insufficient to trigger an instability. The non-linear behaviour of the SI is known from Johansen & Youdin (2007), but only for the radial-vertical extent. Though they performed 3-d simulations, their work did not indicate the SI, or a similar instability, to operate in the radial-azimuthal direction. This presented work is a dedicated investigation to the presence of a SI-type instability in 2-d simulations of radial-azimuthal extent. Indeed, a similar instability is found that previously was only barely known from Raettig et al. (2015). This new instability is named *azimuthal Streaming Instability* (aSI), since there is no clear proof of this new instability to be identical with the classical SI.

The following of this section will deepen the understanding of the numerical SI and aSI in 2-d (r-φ) and 2.5-d (r-z) simulations, respectively. In the future, this performed parameter study can be used to estimate the expected diffusion values from the aSI/SI, which is present during particle cloud collapse. In the following, meant by 2-d simulation is a simulation domain were the vertical direction is only covered by a single grid cell. This grid cell stands for a vertical column with infinite extend, since the boundary condition is periodic in z, though no vertical motions are present. Consequently, modes in vertical direction get completely suppressed. The density in this kind of simulations represent the vertical column density $\Sigma = \rho \cdot L_z$, with simulation box height L_z. For simplicity and consistency, this will also be declared as ρ. In the r-z runs, the vertical direction is well resolved but the azimuthal direction is only resolved by a single grid cell. Meaning, these simulations can be treated as being axisymmetric in azimuthal direction. Still, these kind of simulations considers fluctuations in the azimuthal dust and gas velocity (Johansen & Youdin, 2007; Youdin & Johansen, 2007) as the Keplerian shear is included in the Euler equations for radial-vertical dynamics. This is called 2.5-d, since azimuthal modes get suppressed but the needed azimuthal velocity is included. In this parameter study the following four parameters were altered:

1. Particle size, in terms of Stokes number: $\mathrm{St} = 0.1$ or 0.01
2. Simulation domain extend: either r-φ (2-d) or r-z (2.5-d)
3. Simulation domain size: $L = 0.1\,\mathrm{H}$, $0.01\,\mathrm{H}$, or $0.001\,\mathrm{H}$
4. Initial dust-to-gas ratio: $\varepsilon_0 = 0.1 \ \ldots \ 1000$

The initial dust-to-gas ratio is altered in equidistant manner in log-space, with higher coverage of dust-to-gas ratios below unity. The numerical resolution is $\mathrm{N} = 128$ grid cells in each direction, each cell is initialized with $N_{\mathrm{par}} = 10$ particles in drag-force equilibrium with the gas. This high particle number is needed in order to cover the SI also in regions of low dust density, compare with Johansen & Youdin (2007). Simulations of the SI that include vertical gravity thus can have lower total particle numbers, as they automatically get concentrated into the mid-plane achieving a proper dust resolution. The following of this section presents the results of all four parameter studies as a whole. Afterwards, the results of a resolution study on the aSI in the r-φ plane are shown. A full list of the measured diagnostic quantities for all simulations are found in the appendix, in Tab. D.1 to Tab. D.4.

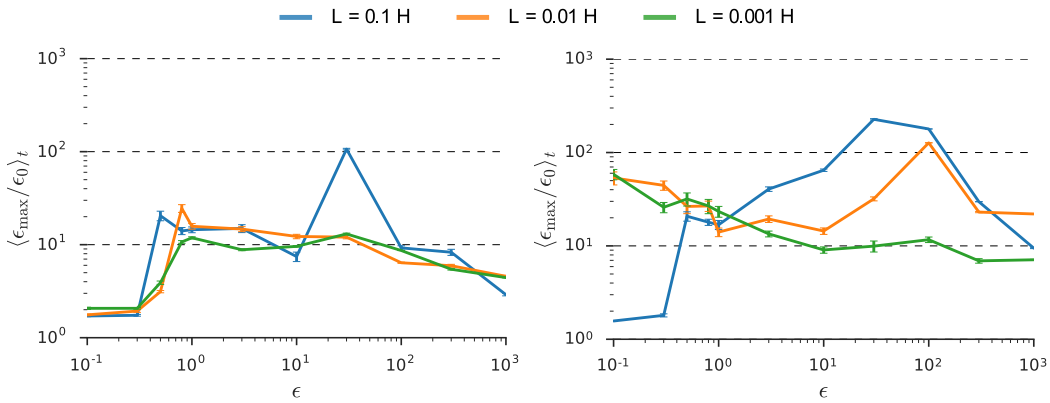

(a) St = 0.1 - r-φ plane

(b) St = 0.1 - r-z plane

(c) St = 0.01 - r-φ plane

(d) St = 0.01 - r-z plane

Figure 5.1: Values of maximum dust density fluctuations and their standard deviation. The simulations with active multi-mode aSI/SI manage to enhance their dust concentration locally to a value of ~ 10. Only in the cases where zonal flows are emerging, e.g. (r-φ, St $= 0.1$,$L = 0.1$ H, $\varepsilon_0 = 30$), or vertical bands, e.g. (r-z, St $= 0.1$,$L = 0.001$ H, $\varepsilon_0 = 1$), further concentrations form that range up to values of $\varepsilon_{max}/\varepsilon_0 \approx 100$. Surprisingly, for St $= 0.01$ the aSI is showing activity also for initial dust-to-gas ratios below $\varepsilon_0 = 1$, see Fig. 5.3. For this Stokes number, no activity could be found in the simulations with the largest domain size (blue curve). On the smallest scales, suprinsingly high dust density fluctuations are found for simulations with initial dust-to-gas ratio below unity that need further investigations.

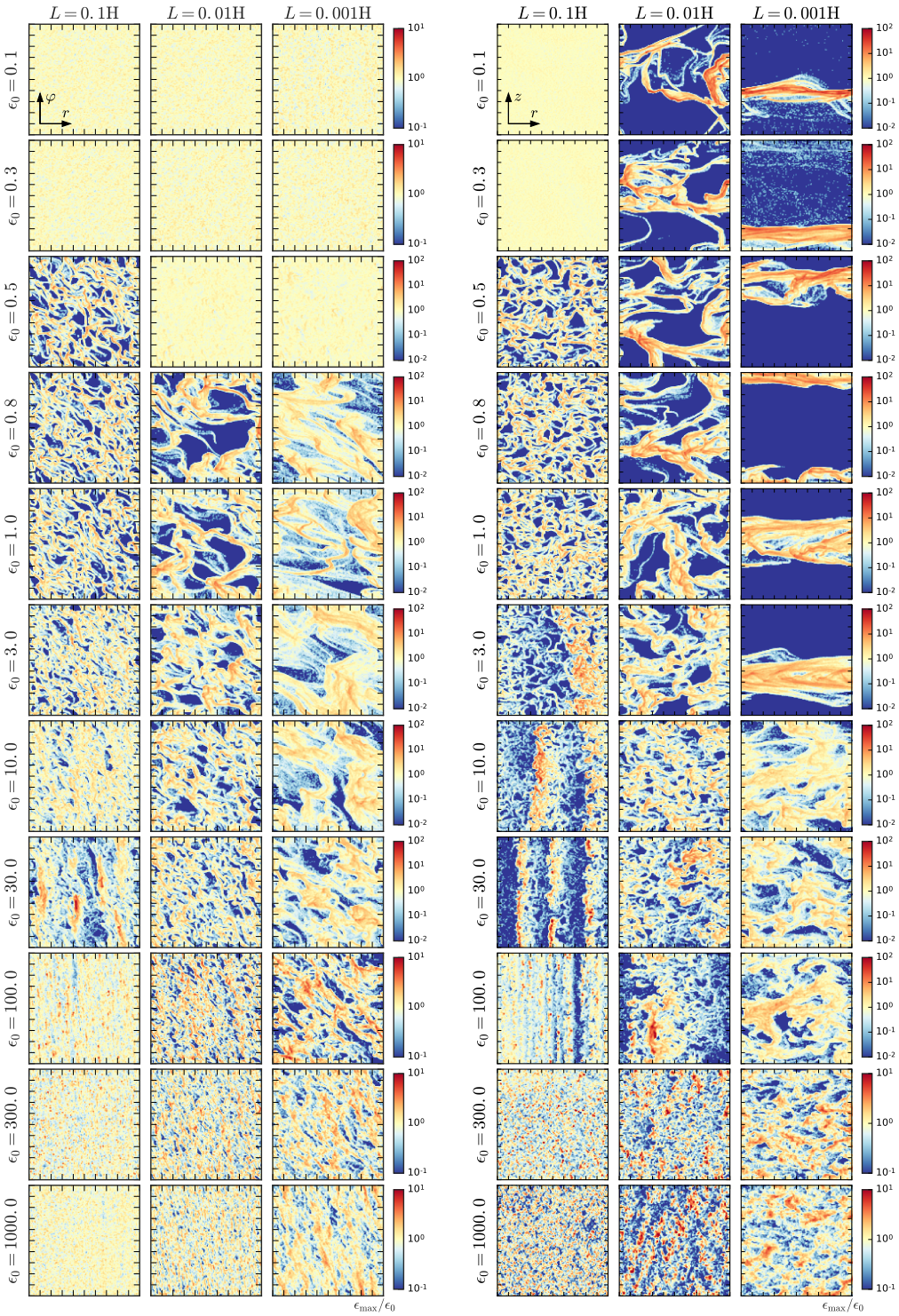

(a) St = 0.1 - r-φ plane

(b) St = 0.1 - r-z plane

Figure 5.2: Last snapshots of the dust-to-gas ratio normalized to ε_0 (yellow). Over-densities are coloured in red, particle voids in blue. Beware of the changing colormap range in the upper and lower ε range. All simulations have the same number of grid cells.

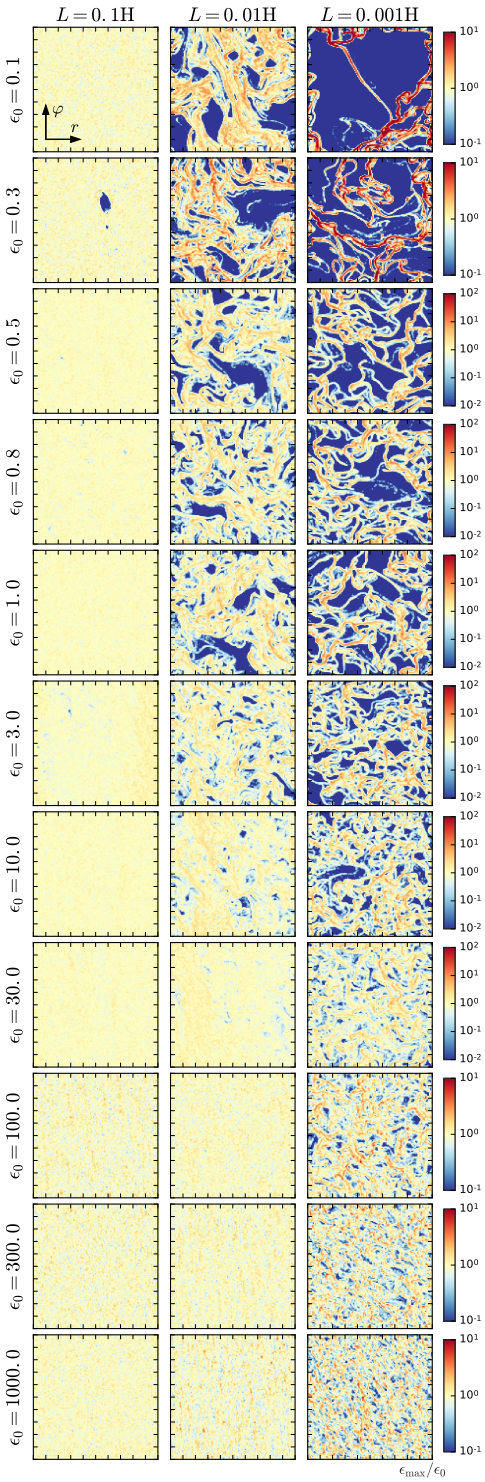

(a) St $= 0.01$ - r-φ plane

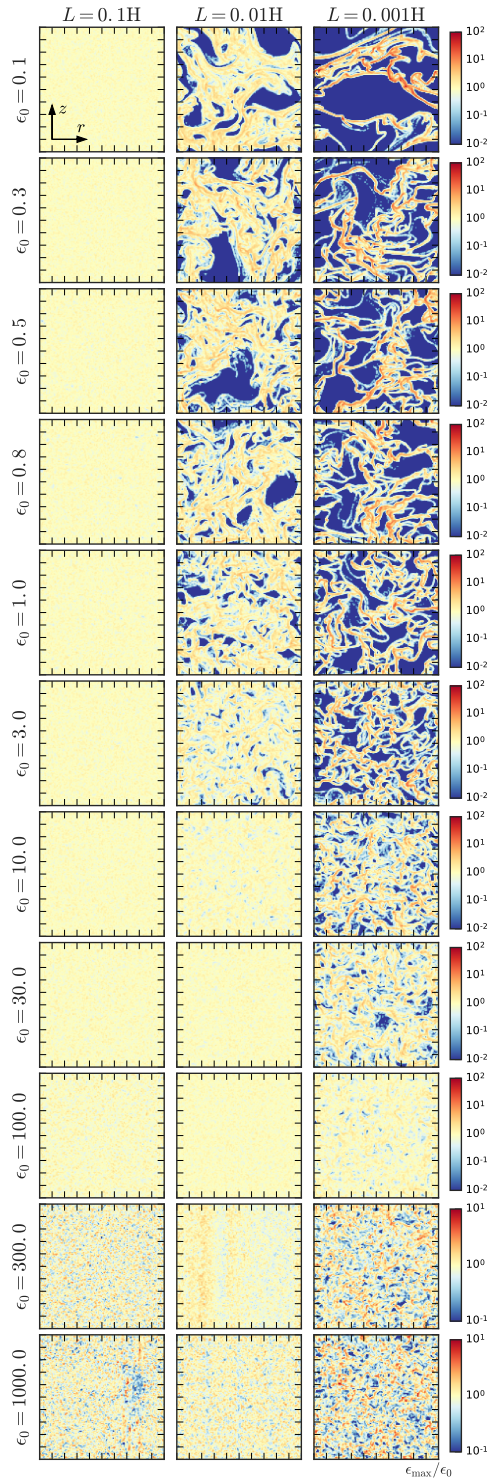

(b) St $= 0.01$ - r-z plane

Figure 5.3: Last snapshots of the dust-to-gas ratio normalized to ε_0 (yellow). Over-densities are coloured in red, particle voids in blue. All simulations have the same number of grid cells. Colour mapping changes for high and low ε_0.

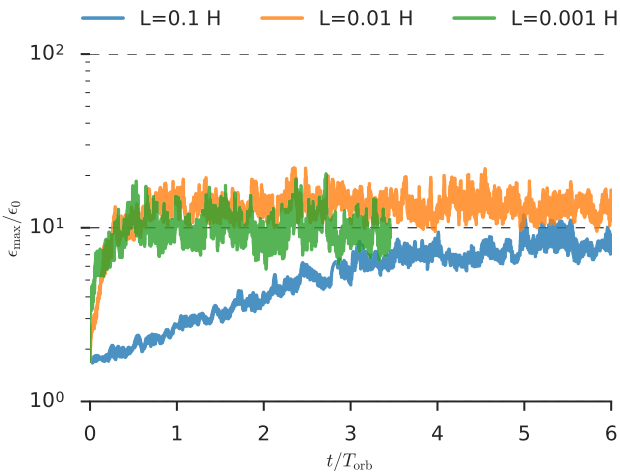

Figure 5.4: Timeseries of the maximum occurring dust-to-gas ratio in the simulations with $\mathrm{St} = 0.1$ and $\varepsilon = 10$ of the r-φ, i.e. the aSI simulations. The time frame in this figure is limited to the growth phase of the aSI. Clearly, the modes grow the fastest on the intermediate (orange) and the smallest (green) scales, as in these runs the maximum dust-to-gas ratio increases to their saturation level within less than one orbit. The measured growth rates can be found in Tab. 5.1.

5.2.1 Dust density fluctuations

The active aSI/SI is enhancing the dust-to-gas ratio locally by having the particle clump together, as they are energetically more stable in a group. This likewise creates particle voids, see Fig. 5.2 and Fig. 5.3. The mutual drag between dust and gas is different for different dust-to-gas ratios, see Eq. (4.1), which leads to growing perturbations that can grow up to a value that triggers a non-linear state with turbulence.

Taking the timeseries of the maximum dust density, $\rho_{\mathrm{d,max}}$, one can calculate the normalized maximum dust-to-gas ratio that is occurring in the simulations as

$$\frac{\varepsilon_{\max}}{\varepsilon_0} = \max\left(\rho_{\mathrm{d}}/\rho_{\mathrm{g}}\right) ,$$

where for simplicity $\rho_{\mathrm{g}} = \rho_0 = \text{const.}$ is assumed, as the variation in this value are found to be insignificant. This maximum value on particle concentration is plotted in Fig. 5.1 together with its standard deviation. In most of the simulations, the dust density is found to get enhanced by a factor of ≈ 10. Only for the special case of zonal flows emerging, e.g. (r-φ, $\mathrm{St} = 0.1$,$L = 0.1\,\mathrm{H}$, $\varepsilon_0 = 30$), the dust enhancement goes up to values of ≈ 100, see Sec. 5.2.9. An additional discussion on the influence of the numerical resolution on the maximum dust-to-gas ratio is done in Sec. 5.3. One should keep in mind that this value is the absolute maximum value and only occurs in a single grid cell. As explained in Chapter 3 a high value is not a guarantee for gravitational collapse and the enhancing of dust is not a run away process that increases with numerical resolution, see Sec. 5.3.

In Fig. 5.1a, one sees that the aSI has an active range from $\varepsilon_0 = 0.8$ till ~ 300. Meaning that the aSI is able to concentrate dust locally significantly higher than the mean dust density value. For $\varepsilon = 1000$, the aSI seems to be dead by having an dust enhancement factor of ≈ 3 on the largest scale. But, on the two smaller scales the aSI remains active, by providing dust density fluctuations up to a value of $\varepsilon_{\max}/\varepsilon_0 \approx 5$. Furthermore, the aSI does has a surprisingly sharp cut off at low dust-to-gas ratios and emerges first on the largest scale (blue line at $\varepsilon = 0.8$), and on the two smaller scales at $\varepsilon = 1$. The saturation level is for $L = 10^{-2}\mathrm{H}$ and $10^{-3}\mathrm{H}$ identical for all ε_0.

The achieved maximum dust-to-gas ratios in the case of pure SI in r-z are very similar to the one of the aSI in r-φ, compare Fig. 5.1b with Fig. 5.1a. But, in the majority of the cases, the simulations are dominated by strong horizontal or vertical modes, see Fig. 5.2b. They do much stronger concentrate particles, similar

to the zonal flow in the r-φ run, mentioned above. Thus, the maximum dust enhancement values in most cases exceed the aSI values. These dominant modes appear in most of the investigated SI-active simulations for $\mathrm{St} = 0.1$ particles. They are a consequence of the chosen simulation domain sizes. This is visible from the row for $\varepsilon_0 = 3$ in Fig. 5.2b, where there is a strong horizontal band in the smallest simulation (right), but a typical non-linear SI mode behaviour in the next larger run (center) without band-like structures. The largest of the three simulations (left) then shows the presence of a strong horizontal mode that looks different again if one goes to even larger domain sizes, see run BC in Fig. 3 in Johansen & Youdin (2007), where there are many vertically aligned particle concentrations, but no clear single mode structure resides.

One can follow this also up with the simulations on the smallest scales, by looking at the green curve in Fig. 5.1b. It shows the emerging of single mode dominated behaviour when following this curve from large (right) to small (left) initial dust-to-gas ratios. This is also true for the largest simulations (blue) where towards higher dust-to-gas ratios vertical modes appear that come along with high particle trapping therein. They range up to values of $\varepsilon_{\mathrm{max}}/\varepsilon_0 \geq 100$. In all the setups, one finds that the many-mode turbulent SI is clearly only capable of enhancing the dust-to-gas ratio only up to the typical value of ≈ 10. It is then the presence of these single horizontal bands (smallest scales) and horizontal modes (largest scales) that induces stronger particle clumping that from the pure SI.

The picture changes for $\mathrm{St} = 0.01$ particles. The maximum dust density fluctuations found for the SI are extremely similar to the ones of the aSI in r-φ. On the largest scales (blue) no aSI and no SI can be found, see Fig. 5.1c. Hence, these simulations can be neglected in the following of this analysis. On the next smaller scale (orange) both instabilities appear up to a value of $\varepsilon_0 \approx 10$. The smallest scale (green) shows surprisingly an activity throughout the whole parameter space, especially including simulations with $\varepsilon_0 \leq 1$. In all the aSI-/SI-active runs, there appear no zonal flows or horizontal bands, as they were found in the simulations with $\mathrm{St} = 0.1$. It is also surprising to find a very high ability to still concentrate dust at the lowest initial dust-to-gas ratio of the study, with values of up to $\varepsilon_{\mathrm{max}}/\varepsilon_0 \approx 60$. In contrast, the aSI and the SI on the intermediate scales both peaks at $\varepsilon_0 = 1$ with a value of $\varepsilon_{\mathrm{max}}/\varepsilon_0 \approx 10$, what is again the aSI/SI typical value. This strong increase on the very smallest scales needs further investigations.

On the intermediate scale (orange), the peak in the maximum dust density fluctuations for the SI is shifted slightly towards lower initial dust-to-gas ratios, to $\varepsilon = 0.5$, where for the r-φ runs it is at $\varepsilon = 1$. This indicates that a higher dust load is needed to trigger the instability if an additional shear is present. On the smallest scales (green) again the parameter space is covered with SI up to a value of $\varepsilon_0 = 100$. Comparing the slope with the ones from Fig. 5.1c for the r-φ runs, the drop in the ability to enhance the dust concentration is slightly steeper in the r-z runs, i.e. for ($L = 0.001\,\mathrm{H}$, $\varepsilon_0 = 100$) the SI is active in the r-φ case, but seems rather inactive in the r-z case.

5.2.2 Growth rates

Fig. 5.4 shows an example for the timeseries of the maximum dust-to-gas ratio, again normalized to its initial mean value, for the aSI simulations with $\mathrm{St} = 0.1$ and $\varepsilon_0 = 10$. The timeseries in this figure is specially shortened to the initial saturation phase, where the SI reaches its typical dust density fluctuation value of ≈ 10. Here, one clearly sees the saturation time to be the fastest on the smaller scales (orange and green). This is a consequence of the fastest growing mode to get smaller with increasing ε, i.e. the wavenumbers get larger. The SI growth rates are analytically calculated and plotted in Fig. 2.8 for $\mathrm{St} = 0.1$ particles, and in Fig. 2.9 for $\mathrm{St} = 0.01$ particles.

From the $\varepsilon_{\mathrm{max}}$ timeseries, the growth rate s can be estimated in units of Ω, by fitting the logistic function, i.e.

$$\varepsilon(t) = A + \frac{B}{1 + \mathrm{e}^{-s(t-t_0)}}$$

to it. The logistic function has an exponential growth for times shorter than the saturation time, i.e. $f(t \ll t_0) \approx A + B\mathrm{e}^{s(t-t_0)}$. Thus, one than can derive from the function fit the growth rate via

$$s = \frac{4}{B}\frac{\mathrm{d}\varepsilon}{\mathrm{d}t}(t = t_0)\,.$$

As expected, the resulting growth rates for the aSI/SI-active simulations depend on the simulation domain

size. They are listed in Tab. 5.1. Simulations with active zonal flows, or vertical bands, show growth rates below 10^{-1}. The horizontal bands in the r-z simulations do not show an imprint on the measured growth rates.

5.2.3 End-state snapshots

For the ε range around unity, the aSI for $\mathrm{St} = 0.1$ particles shows the same behaviour on all scales, i.e. from left to right it appears like a zoom-in, see Fig. 5.2a. In fact, the relevant modes are visually rather similar but identical in the ability to concentrate dust, see Fig. 5.1a. For $\varepsilon_0 > 30$ the aSI slowly vanishes on the largest scale, but remains active on smaller scales. Hence, simulations with an insufficient resolution will suppress these very small but turbulent aSI modes. For $\varepsilon < 1$ a sharp cut-off in aSI activity is found. Any mode activity in this parameter sub-space is found to depend on the underlying hyper-viscosity and -diffusivity, see Sec. 5.2.10.

The SI for $\mathrm{St} = 0.1$ particles shows activity throughout most of the parameter space. It has a rather similar mode pattern as the aSI. Though may simulations are dominated by large vertical bands (zonal flows) and horizontal bands. These cases with a multimode pattern can best be identified in Fig. 5.1b, since for them the maxima in the dust density fluctuations are found to be around $\varepsilon_{\mathrm{max}}/\varepsilon_0 \approx 10$. A value that will be found throughout all aSI and SI simulations when the only the multi-mode instability is active. For $L = 0.1\,\mathrm{H}$ (left column) many of the simulations are dominated by horizontal modes (vertical bands). They start to appear starting from $\varepsilon \geq 3$, with a decreasing wavelength for increasing ε, i.e. more vertical bands appear with higher dust load. The modes here might be similar to the zonal flows observed in the (r-φ, $\mathrm{St} = 0.1$,$L = 0.1\,\mathrm{H}$, $\varepsilon_0 = 30$). But, this remains to be shown. Similar band structures are found on the scale of $L = 0.01\,\mathrm{H}$ (middle column) for runs with $\varepsilon \geq 30$. For $L = 0.001\,\mathrm{H}$, single horizontal bands are found for $\varepsilon \leq 10$. In contrast to the horizontal modes on the large scales, here only a single band appears that gets vertically more compact with smaller ε. In constrast to the vertical bands on the largest scales, no second band emerges on the smallest scales within the parameter range. Also, these dominant horizontal bands do not show up in the next larger simulations with $L = 0.01\,\mathrm{H}$ (center), though particle concentrations increase significantly here as well. This indicates that the SI modes might more strongly concentrate particles at lower dust-to-gas ratios, than what is expected from the $L = 0.1$ simulations. This also needs further investigations.

The simulations with $\mathrm{St} = 0.01$ show in the r-φ and the r-z simulations a very similar pattern. Both, aSI and SI show strong active dust density fluctuations for rather low initial dust-to-gas ratios that even reach below $\varepsilon_0 = 1$. On the intermediate scale (orange) the aSI is strongest around $\varepsilon_0 = 1$ and peaks there at the typical value for the maximum dust density fluctuations of ≈ 10, as did the previous $\mathrm{St} = 0.1$ runs. The aSI on the smallest scales is throughout the whole parameter space actively enhancing the dust-to-gas ratios up to values close and well above 10. The dust density enhancements on this scale even reach up to values close to 100, which also needs further investigations. For the case of the SI on the intermediate scale, the strongest peak in the dust density fluctuation is around $\varepsilon_0 = 0.5$, where for the aSI this peak is at $\varepsilon_0 = 1$. see Fig. 5.1.

	$L = 0.1\,\mathrm{H}$ SI	$L = 0.1\,\mathrm{H}$ aSI	$L = 0.01\,\mathrm{H}$ SI	$L = 0.01\,\mathrm{H}$ aSI	$L = 0.001\,\mathrm{H}$ SI	$L = 0.001\,\mathrm{H}$ aSI
$\mathrm{St} = 0.1$	4e−1	3e−1	8e−1	1	1.5	2
$\mathrm{St} = 0.01$	-	-	5e−1	5e−1	3.0	4.0

Table 5.1: Mean growth rates in units of Ω, for SI and aSI simulation in comparison. They tend to not significantly depend on the intial dust-to-gas ratio ε_0. They are found to be similar for SI and aSI, and also similar for $\mathrm{St} = 0.1$ and 0.01 particles. For $\mathrm{St} = 0.01$ and on the scales of $L = 10^{-1}\mathrm{H}$ no SI/aSI is found and thus no growth rate can be expressed. These values compare well with the maximum growth rate from Fig. 2.8 for $\mathrm{St} = 0.1$ particles, and in Fig. 2.9 for $\mathrm{St} = 0.01$ particles, as they show that the fastest growing SI mode tends to be on scales below $L = 10^{-1}\mathrm{H}$. This suggests that the growth rates of the SI can fairly well be used for the aSI, too.

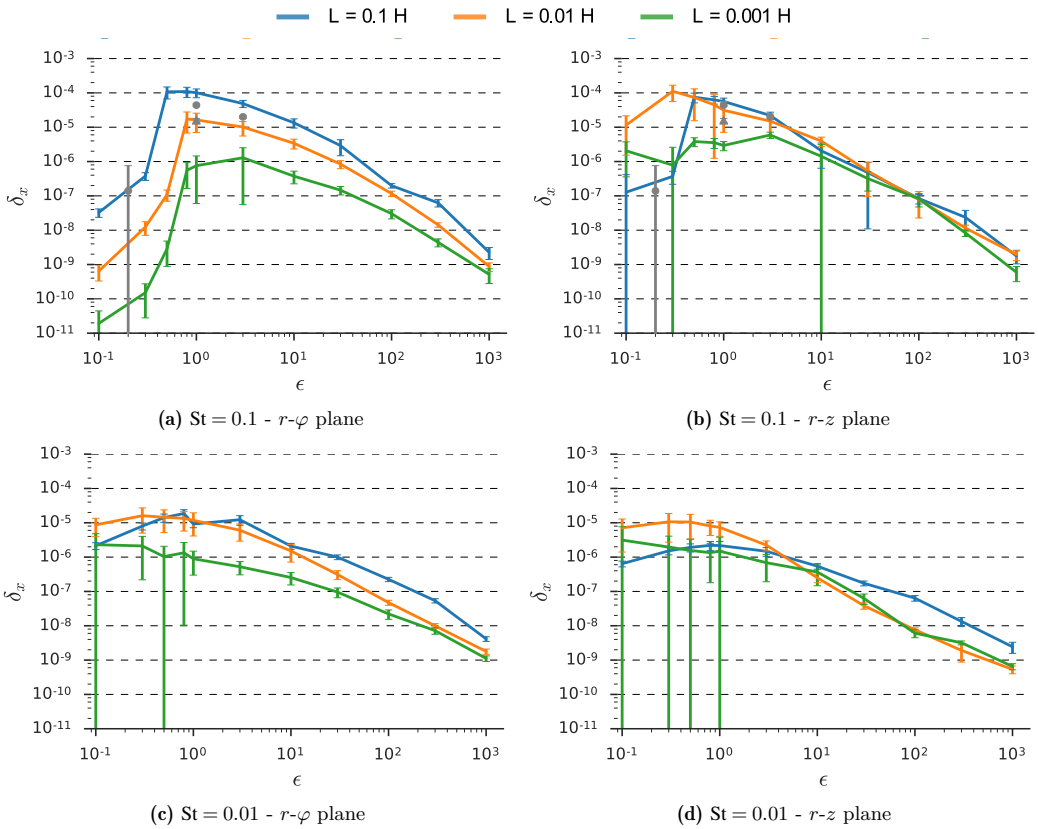

(a) St = 0.1 - r-φ plane

(b) St = 0.1 - r-z plane

(c) St = 0.01 - r-φ plane

(d) St = 0.01 - r-z plane

Figure 5.5: Particle diffusion δ_x estimated by treating the SI as a random walk. For comparison, in grey circles (2D) and triangle (3D) the diffusivities for St = 0.1 particles and $L \geq 2$H from JY07 Tab. 3 are plotted. Diffusion values for St = 0.01 on the scales of $L = 0.1$H are not due to SI or aSI, but residing turbulence from the initial condition, compare with Fig. 5.3a.

5.2.4 Particle diffusion

The particle diffusion is measured by treating the aSI and SI as a random walk-like process and using Eq. (2.42) to measure the diffusion kernel.

Radial diffusion, see Fig. 5.5

When exceeding $\varepsilon = 30$, the diffusivities for the aSI for St = 0.1 particles shows a steeper drop on large scales (blue) than on smaller scales, see Fig. 5.5a. The slope of the radial diffusion for this setup goes with ε^{-2} on the large scales and with ε^{-1} on smaller scales. For comparison plotted in grey circles (2D) and triangle (3D) are the diffusivities from JY07 Tab. 3, for St = 0.1 particles and $L \geq 2$H.

The SI on the same Stokes number shows a radial particle diffusion with a slope between $\delta_x \sim \varepsilon^{-1.1} \ldots \varepsilon^{-1.5}$, see Fig. 5.5b. For comparison plotted in grey circles (2D) and triangle (3D) are the diffusivities for St = 0.1 particles and $L \geq 2$H, from JY07 Tab. 3. Surprisingly, the presence of vertical modes (large boxes, high $\varepsilon_{\max}/\varepsilon_0$) maintains vertical diffusion.

For the smaller Stokes number particles, the slope of the radial diffusion for the aSI goes with $\varepsilon^{-1.5}$ on intermediate scales (orange), and with $\varepsilon^{-1.0}$ on small scales (green). Diffusion values on the largest scales (blue) are not from the aSI, see Fig. 5.3a, but from lasting gas turbulence that is induced by the initialization

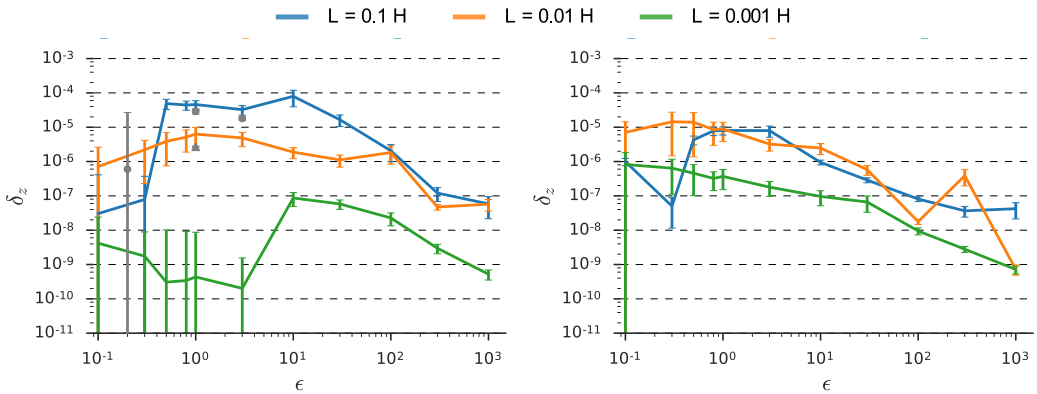

(a) St = 0.1 - r-z plane

(b) St = 0.01 - r-z plane

Figure 5.6: Particle diffusion δ_y estimated by treating the SI as a random walk. For comparison plotted in grey circles (2D) and triangle (3D) are the diffusivities for $\mathrm{St} = 0.1$ particles and $L \geq 2\mathrm{H}$, from JY07 Tab. 3. Diffusion values for $\mathrm{St} = 0.01$ on the scales of $L = 0.1\mathrm{H}$ are not due to SI or aSI, but residing turbulence from the initial condition, compare with Fig. 5.3a.

of the particles in drag force equilibrium. The origin of this gas turbulence is still unclear and needs further investigations. Since no dust fluctuations and no SI modes were found, this is a clear sign that these values must come from different effects.

Very similar values for the radial particle diffusion of the SI for this Stokes number are found. The radial particle diffusion has a $\delta_x \sim \varepsilon^{-2.0}$ slope. The diffusion values on the largest scales (blue) are again not from the SI, see Fig. 5.3a, but stem from the initial particle density noise and resulting rms velocity introduced by the drag force equilibrium between dust and gas.

Vertical diffusion, see Fig. 5.6

Clearly, the measurements for vertical diffusion are only for the SI simulations possible, since in the aSI vertical modes are suppressed. For $\mathrm{St} = 0.1$, the vertical particle diffusion scales with a $\delta_z \sim \varepsilon^{-0.3} \ldots \varepsilon^{-1.5}$ slope, see Fig. 5.6a. For comparison plotted in grey circles (2D) and triangle (3D) are the diffusivities for $\mathrm{St} = 0.1$ particles and $L \geq 2\mathrm{H}$, from JY07 Tab. 3. The presence of vertical modes (large boxes, high $\varepsilon_{\max}/\varepsilon_0$) maintains vertical diffusion, but the presence of a strong horizontal band (small box, low $\varepsilon_{\max}/\varepsilon_0$) shuts down the vertical diffusion but maintains radial diffusion, see above.

For one order of magnitude smaller Stokes number particles, the vertical particle diffusion of the SI has a slope of $\delta_x \sim \varepsilon^{-0.5}$. The diffusion values on the largest scales (blue) are again not from the SI, see Fig. 5.3a, but from the initial particle density noise and resulting rms velocity introduced by the drag force equilibrium between dust and gas.

Comparing radial and vertical diffusion, see Fig. 5.7

A comparison of vertical and radial diffusion is done in Fig. 5.7 for the r-z SI. Vertical diffusion is found to be mostly lower than the radial diffusion, i.e. $\delta_x/\delta_z > 1$. Once vertical modes or horizontal bands appear, the strongest diffusion is in the direction of the corresponding particle concentrating structure. On the intermediate scale, for $\mathrm{St} = 0.01$, the vertical diffusion for the SI active simulations is found to be as strong as the radial diffusion. Once going to smaller scales, the radial diffusion gets stronger again.

5.2.5 Particle dispersion and drift

In Fig. 5.8 plotted are the global and local particle dispersion values (Eq. (5.1)) and in Fig. 5.9 the drift speed (Eq. (5.4)) values.

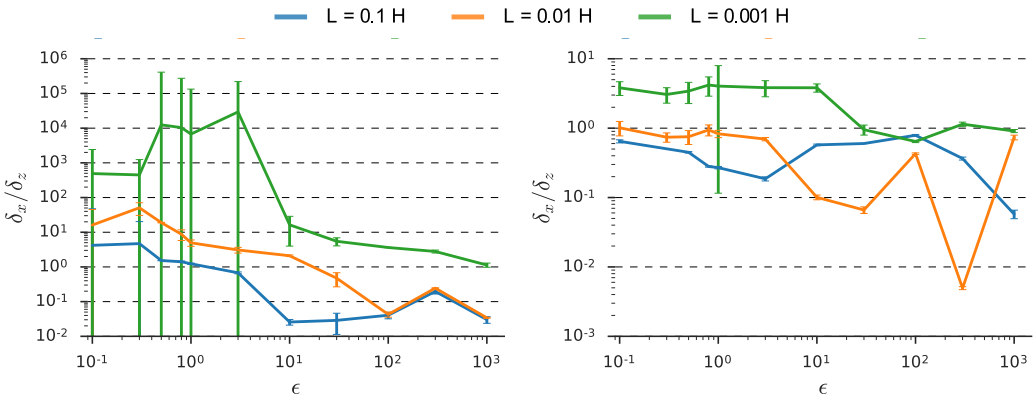

(a) St = 0.1 - r-z plane

(b) St = 0.01 - r-z plane

Figure 5.7: Comparison of radial and vertical particle diffusion from SI runs. Left figure shows the comparison for St = 0.1, and right figure the comparison for St = 0.01. As can be seen, an active SI provides most of the time a stronger radial diffusion than vertical diffusion. The ratio of these two values is larger for the St = 0.1 particles. The blue curve for the smaller Stokes number particles can be ignored, since in these simulations there is not active SI found.

The dispersion in the case of an symmetric unperturbed Keplerian flow in a shearing box approximation is zero. In the case of aSI/SI, the dispersion is a measurement of the appearing turbulent velocity. Fig. 5.8a compares global dispersion $\sigma_\circ$ (colored lines) with local dispersion $\sigma_\square$ (shaded contours), were the local dispersion is calculated for each grid cell with two or more particles inside (grey dots), hence the scatter is large. The plots show $\sigma_\square$ being on average much smaller than $\sigma_\circ$, which is a result of the aSI having large extended modes, whereas grid cell wise the particles behave as a group, only slowly dispersing. For smaller $\varepsilon_\square$-values the dispersion reduces as a result of the particle voids being the less turbulent regions (blue areas in Fig. 5.2a). For larger $\varepsilon_\square$ the particles locally dominate with their momentum over the frictional influence of the gas, consequently particle groups stay longer together. In between the aSI/SI is actively stirring the particles.

Fig. 5.9 shows the particle motion relatively to the gas. This drift speed ζ is found to be nearly identical on local and global scales and only marginally larger than the Nakagawa drift values from the Nakagawa et al. (1986) steady state solution from Eq. (2.38). Note that all particles were initially set to be in local Nakagawa drift equilibrium with the gas. That indicates that the aSI increases the particle drift speed by a factor of ~ 2. But, this value is still up to a factor of 100 times lower than without the frictional feedback.

Furthermore, particles that group together at very high dust-to-gas ratios of $\varepsilon > 100$ do drift one order of magnitude faster than what is predicted by Eq. (5.4). In the simulations, this behaviour is found such that local particle heavy heaps do drift radially inwards with a significantly higher speed than the dust background. This indicates a limit around $\varepsilon = 100$ on the validity of the Nakagawa equations, at least from the presented simulations.

In the r-z case, one finds the particle dispersion and the measured drift speed to have values that compare well to the r-φ simulations. Simulations with non-active SI, here the simulations with larger domain size and with $\varepsilon < 1$ show a strong drop in particle dispersion but not as strong as in the r-φ simulations. The global particle drift $\zeta_\circ$ again agrees well on large and small scales. Slight increases in the drift speed can be found for the simulations with strong radial modes, as they produce zonal flows, e.g., $L = 0.1\,\mathrm{H}$ with $\varepsilon_0 = 10$ to 100 and $L = 0.01\,\mathrm{H}$ with $\varepsilon_0 = 100$.

For simulations with St = 0.01, the dispersion magnitude again follows the slope of the Nakagawa solution for particle drift (dashed line). But now, since the aSI is active, also for $\varepsilon_0 \leq 1$, the global dispersion values on the intermediate and smallest scales do actually continues to follow the Nakagawa solution, whereas for St = 0.1 one observes a knee at around $\varepsilon = 1$.

The particle drift in Fig. 5.9c again shows a perfect agreement between local and global drift values. For

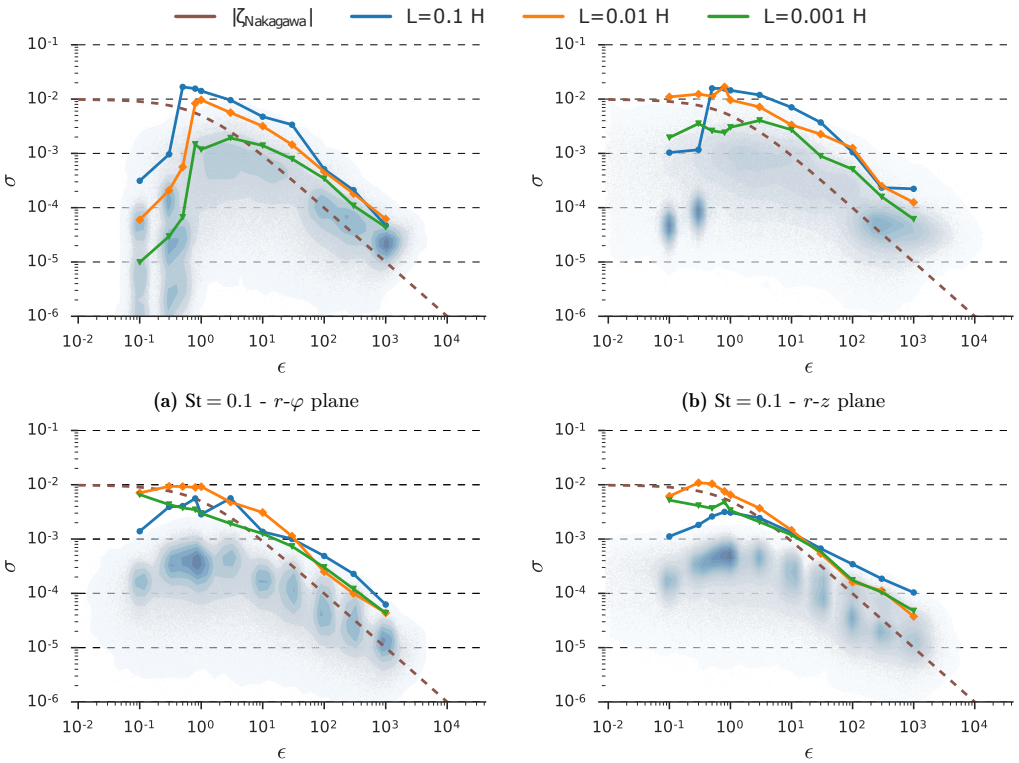

(a) St = 0.1 - r-φ plane

(b) St = 0.1 - r-z plane

(c) St = 0.01 - r-φ plane

(d) St = 0.01 - r-z plane

Figure 5.8: Global dispersion $\sigma_\circ$ (lines) and local dispersion $\sigma_\square$ (contour). Blue, orange and green lines show the individual global values. The local, i.e. grid cell wise, values for all simulations combined are shown in shaded contours. As reference in dashed is shown the absolute magnitude of the Nakagawa drift speed from Eq. (2.38). The dispersion values all seem to follow the curve of the Nakagawa drift. Once the aSI or SI breaks down, the measured rms-velocities drop. The blue lines for St = 0.01 can be ignored, since the measured velocity is not from the aSI or SI, respectively.

this Stokes number, one finds the drift values to even be closer to the predicted value from Eq. (2.38). In the blue contours that represent $\zeta_\square$, the horizontal bars in this plot indicate the drift velocity to depend rather on the mean dust-to-gas ratio, which is equal to ε_0, and does not follow the expected value from the Nakagawa drift solution. The particle dispersion for the r-z simulation with St = 0.01, shown in Fig. 5.8d, is almost identical to the dispersion that is found for the r-φ case. This again shows that for this lower Stokes number the aSI and the SI are to a high degree similar.

5.2.6 Correlation time and correlation length

The correlation time represents a measure for the characteristic turbulent eddy turnover time. It can be used to link the turbulent rms-velocity with the particle diffusion, see Sec. 5.1.2. The eddy size can be approximated by the correlation length, see Sec. 5.1.3, which is measured by the ratio of particle diffusion and particle rms-velocity.

Correlation time: eddy turnover time

Assuming a correlation between δ_x and $\sigma_\circ$ via τ_{corr}, as stated in Eq. (5.2), for aSI-active runs, one finds for St = 0.1 and r-φ a typical correlation time of $\tau_{\text{corr}} \approx 0.3\Omega^{-1}$. For this value only runs were considered with

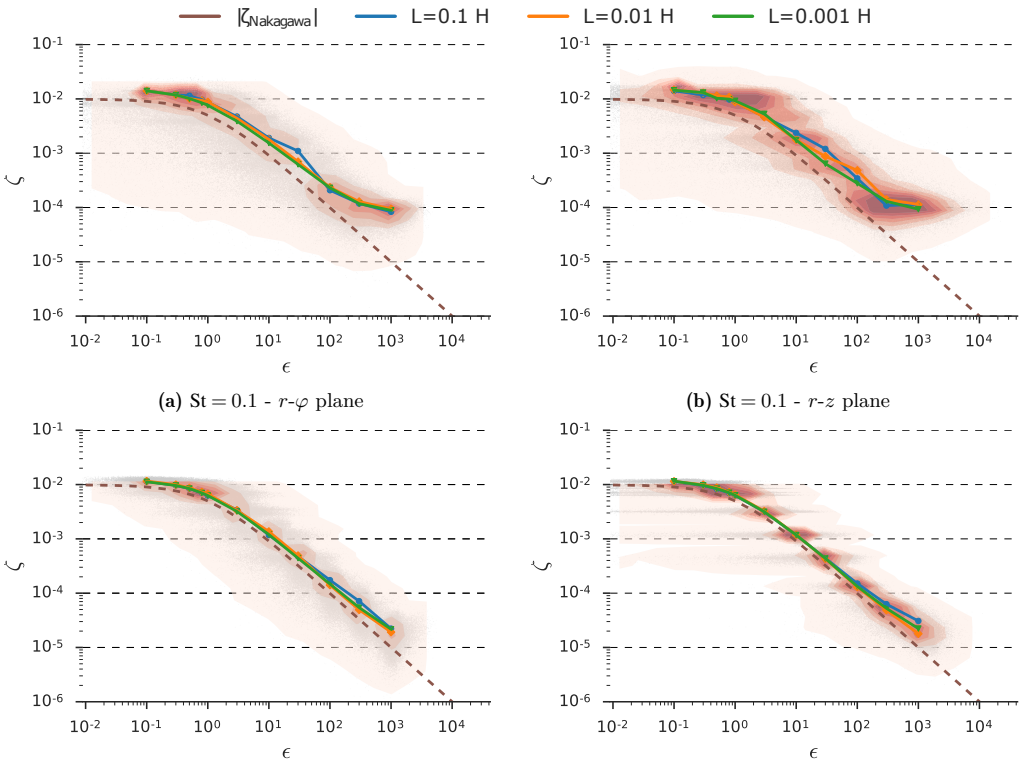

(a) St = 0.1 - r-φ plane

(b) St = 0.1 - r-z plane

(c) St = 0.01 - r-φ plane

(d) St = 0.01 - r-z plane

Figure 5.9: Global drift $\sigma_\circ$ (lines) and local drift $\sigma_\square$ (contour). Blue, orange and green lines show the individual global values. The local, i.e. grid cell wise, values for all simulations combined are shown in shaded contours. As reference in dashed is shown the absolute magnitude of the Nakagawa drift speed from Eq. (2.38). Global and local drift shows perfect agreement, whereas the local dispersion values are always well below the global values. The latter indicates that local particle groups move with similar velocity, but comparing two groups in distinct grid cells they move independently. The similarity in all $\zeta_\circ$ indicates that particles and gas on all scales moves similar relative to each other, following Nagakawa drift prescription. But, clumps $\varepsilon \geq 10^2$ drift faster than actually predicted.

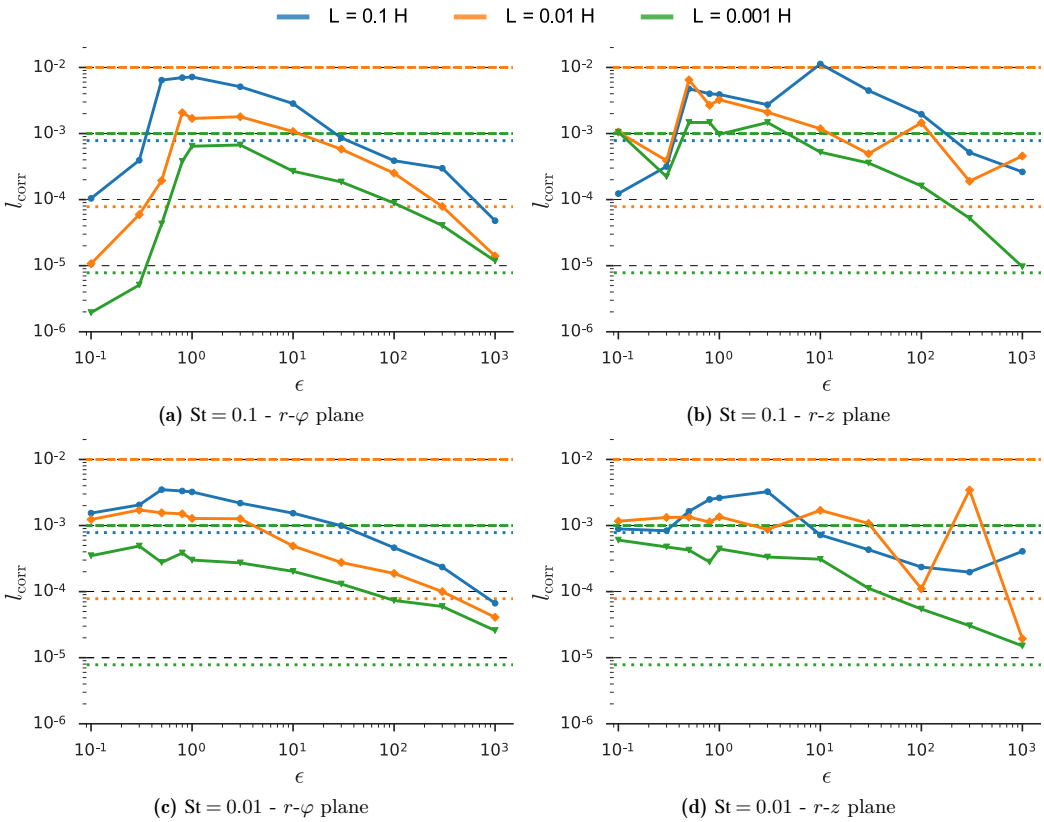

(a) St = 0.1 - r-φ plane

(b) St = 0.1 - r-z plane

(c) St = 0.01 - r-φ plane

(d) St = 0.01 - r-z plane

Figure 5.10: The correlation length resembles the characteristic eddy size in the simulations. In this plot, it is compared with the simulation domain size (dashed) and the grid size (dotted).

clear multi-mode aSI/SI, i.e. $\mathrm{St} = 0.1$, $L = 0.1\,\mathrm{H}$ and $\varepsilon \geq 30$, compare Sec. 5.2.9. Non-aSI/SI-active simulations typically show $\tau_{\mathrm{corr}} = 1.0$. Simulations with decaying aSI/SI-activity show values for the correlation time that are in-between these two values.

For the SI-active simulations with $\mathrm{St} = 0.1$, the found correlation time is $\tau_{\mathrm{corr}} \approx 0.3\Omega^{-1}$. A similar value as found for the aSI with the same Stokes number. The correlation time for both cases is on average flat over ε and only increases, and more strongly varies, once horizontal or vertical modes emerge. For the cases with no active SI, the correlation time increases to $\tau_{\mathrm{corr}} > 1$. The same is true for the simulations at the larger scales in the presence of radial modes.

Correlation length: eddy size

Fig. 5.10 shows the correlatio length for the simulations. The measured l_{corr} is mostly found to be smaller than the domain size and most large than the grid scale. Only for cases with vanishing aSI/SI smaller or larger values are found. All the results from simulations with $l_{\mathrm{corr}} > \mathrm{H}$ or $l_{\mathrm{corr}} < \mathrm{d}x$ should thus be trusted with reservations.

5.2.7 α-value and Schmidt number

The turbulent strength in the gas is measured in terms of α, see Sec. 2.1.4. In the literature, authors often set the turbulence particle diffusion equal to this α-value. This might be true for tightly coupled particles,

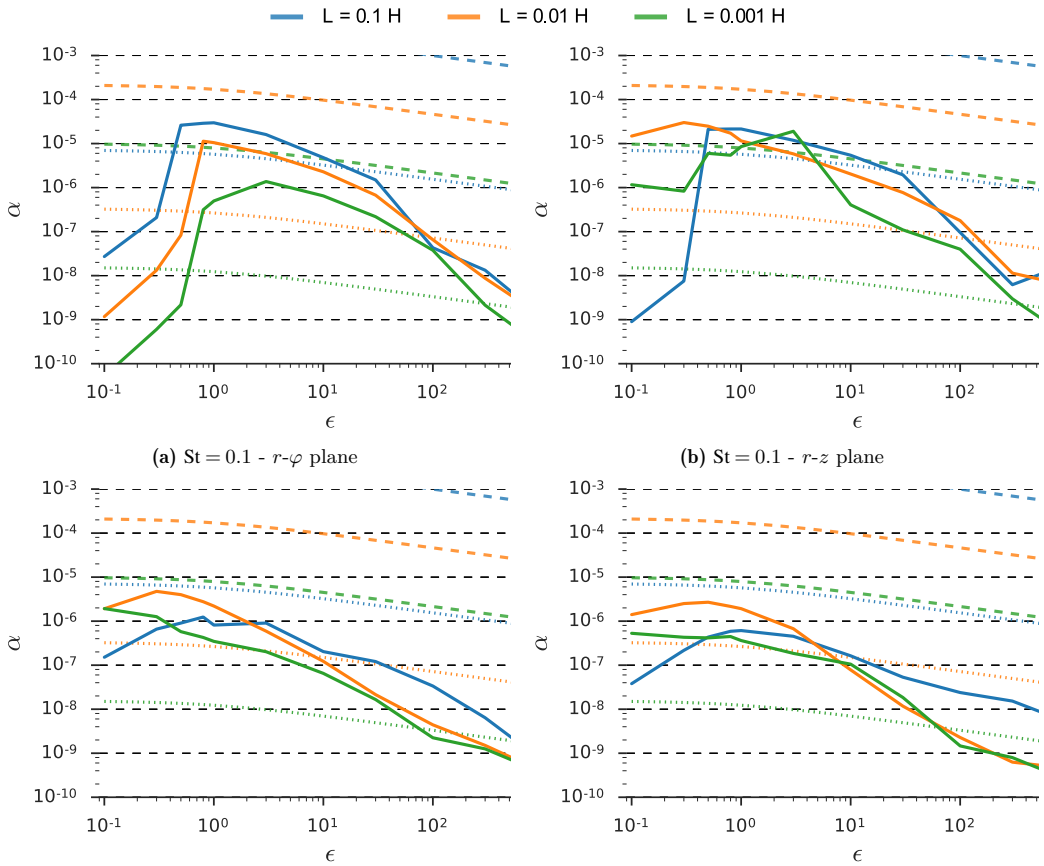

(a) St = 0.1 - r-φ plane

(b) St = 0.1 - r-z plane

(c) St = 0.01 - r-φ plane

(d) St = 0.01 - r-z plane

Figure 5.11: As most investigated quantities for the aSI and SI, the gas α-turbulence shows a steep drop-off once the aSI/SI gets weaker at high dust-to-gas ratios. Plotted as dashed and dotted lines are comparison values that stems from Eq. (3.60). These lines are for comparing the simulations results with an initial $\alpha_0 = 10^{-3}$ turbulence that underwent a turbulent Kolmogorov cascade and energy transfer from a pure gas turbulence into a dust-loaded turbulence. The dashed line represents the upper limit, by having the Kolmogorov cascade to end at the size of the simulation domain, i.e. $l' = L$. The dotted line represents an lower limit, by having the cascade to end at the size of the simulation grid scale, i.e. $l' = \mathrm{d}x$.

but not for $\mathrm{St} > 10^{-2}$. Herein this work, one is in the lucky position to actually measure both quantities. From compare the turbulent gas transport α with particle diffusivity δ, one gains the Schmidt number, see Sec. 5.1.6.

α-turbulence

Fig. 5.11 shows the measured values for the turbulent viscosity, i.e. α-turbulence. Similar to the particle diffusion, the α gas turbulence shows a strong drop-off with SI getting inactive. One finds α to drop towards higher ε-values with the same slope as in the diffusivity measurements. Hence, the measured gas turbulence is correlated with the turbulence in the dust, see also below for the corresponding Schmidt values.

The $\mathrm{St} = 0.1$ runs in r-z show for $\varepsilon < 1$ a significant *alpha* turbulence on the intermediate and on the smallest scales. It stems from the found SI-activity in these runs, hat is not present in the corresponding

aSI case. For $\mathrm{St} = 0.01$, the shape of the measured α-turbulence is quite similar for the aSI and the SI. The for $\mathrm{St} = 0.01$ measured α-values are around one order of magnitude lower than for $\mathrm{St} = 0.1$. But, for the smaller Stokes number simulations, the instability is found to be active for $\varepsilon_0 \leq 1$ and thus providing at these dust-to-gas ratios additional gas turbulence. It is specially strong on the intermediate scales (orange).

It may seem that the measured α-values from the aSI and the SI are much lower than the values known from typical turbulent gas processes in PPDs, like the MRI or the vertical shear instability. But, the α-turbulence stemming from these large scale gas turbulence needs to cascade down via the Kolmogorov cascade, onto the considered scales of $L < 0.1\mathrm{H}$, as explained in Sec. 3.3.3. On these scales, the turbulence will actually be less strong than the turbulence from the aSI/SI. This is especially true, for $\varepsilon \gg 1$, where the momentum of an initially pure gas turbulence needs to be pass over onto a mixture of dust and gas. Thus the turbulent strength should get reduced. This is shown in the form of the dashed and dotted lines in Fig. 5.11, which represent the viscosity estimate ν' from Eq. (3.60). In this comparison, an initial value of $\alpha_0 = 10^{-3}$ is injected on the length scale of $L_0 = \sqrt{\alpha}\mathrm{H} \approx 0.03\mathrm{H}$. The dashed line represents the corresponding turbulent strength that can be expected to be on the scales of the domain size, L, with for each simulation in its respective colour. The dotted line does the same, but on the scales of the respective grid scale $\mathrm{d}x$. One could also do this comparison for the prominent eddy size measured in our simulations via l_{corr}, as calculated below in Sec. 5.2.6. But, in Fig. 5.11 the range of turbulent viscosity that one might expect to find from a turbulent α cascading is shown. These plots show that the expected turbulent viscosity ν' is in a rather broad range of values. The reason is that simulation domain size and grid resolution span a range of two orders of magnitude, hence also the viscosity spans two orders of magnitude. Still, for $\mathrm{St} = 0.1$ the found α by the aSI/SI is well above the best case for the turbulent cascade down onto the scale of $l' = \mathrm{d}x$. Sometimes the measured α-values are even stronger than what is expected for the worst case, i.e. cascade down to only $l' = L$.

This whole discussion does not take all effects into account. How the particles react to the gas turbulence is only mimicked by an energy transfer on a dust loaded eddy. In reality, not a single particle size is present, but a particle distribution of different sizes. Also, the herein this work used Kolmogorov cascade is in reality not present, since it will never be a pure gas turbulent cascade, but instead a dust loaded form that one has to account for. Also, turbulence can only occur as long as the Reynolds criteria is fulfilled. How this criterion behaves on the broad range of scales that are important for planetesimal formation, and in general in the situation of a dust loaded PPDs, remains to be shown. Also, the scales and location where the α_0 turbulence is actually present, i.e. MRI in the upper disk atmosphere, probable is not the same location were aSI/SI is at work or planetesimals form. For example, in a dead zone, the MRI might be active in a layer on top of a dead zone, but the SI could be active within the mid-plane if a sufficient dust-to-gas ratio can be reached. In order to consider those cases, the turbulence not only has to cascade down, but the turbulent velocity needs to be advection towards the mid-plane, i.e. the location of active aSI/SI. Also, a fraction of the turbulent energy that resides in the particles, might get lost earlier in the cascade than in our model, since particle can undergo elastic collisions and by that energy might dissipate more strongly than modelled.

Schmidt number

The found Schmidt numbers are plotted in Fig. 5.12. In this work, the Schmidt value expresses the ratio of turbulent α transport against radial particle diffusion δ_{x}, see Eq. (5.8). This ratio shows a rather flat profile within the aSI/SI-active range. The Schmidt number is found to depend mainly on the size of the simulation domain. Found is also that the particle turbulence is in most of the cases stronger, or at least equality strong, as the gas turbulence. Only on the smallest scales (green) the gas turbulence is slightly stronger within a larger fraction of the aSI/SI-active range. Comparing the r-z runs with the r-φ, one finds that in the simulations that have vertical bands present, i.e. smallest scales and lowest dust-to-gas ratio, the Schmidt number to decrease. This comes from the presence of the vertical bands in the r-z simulations that are strongly diffusing particles in radial direction, though the underlying gas flow is unaltered by them, and hence α-turbulence stays low.

One can conclude that typical Schmidt values for the aSI/SI are of $0.1 < \mathrm{Sc} < 1$. For smaller Stokes number the Schmidt number gets slightly lower. But, this shows that one cannot assume $\delta \approx \alpha$ for the cases of active aSI/SI.

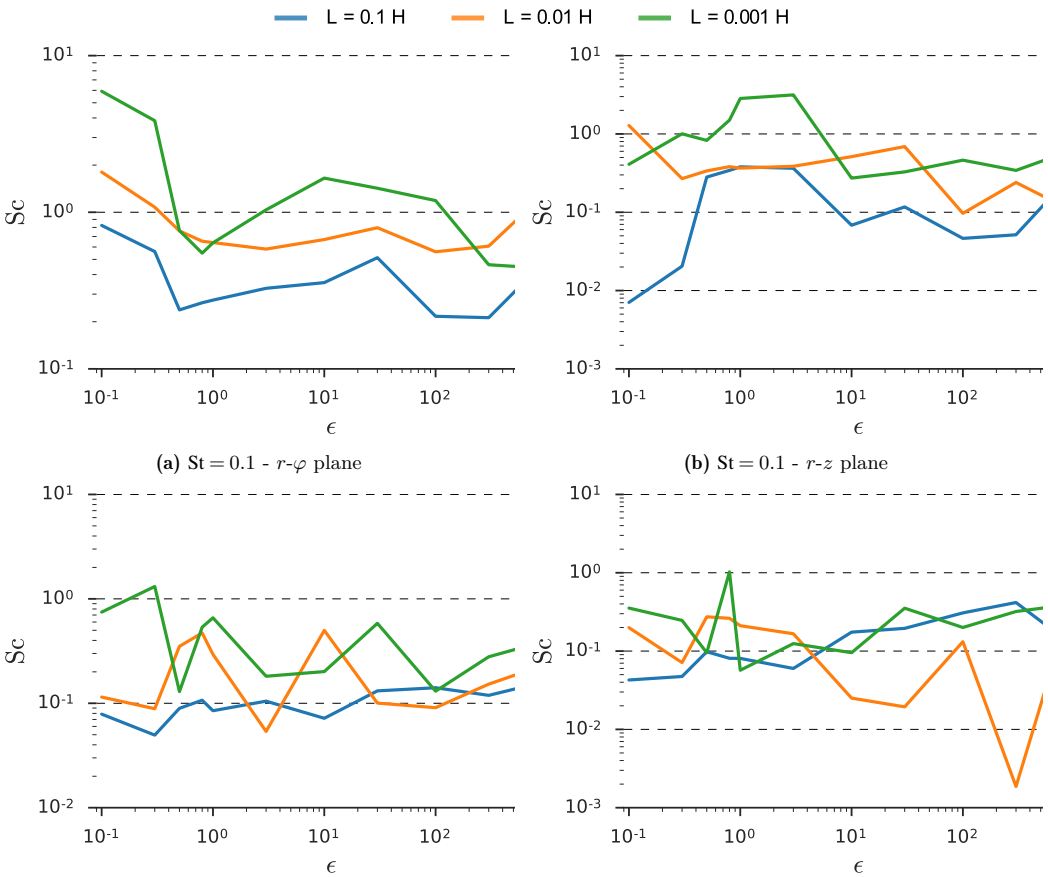

(a) St = 0.1 - r-φ plane

(b) St = 0.1 - r-z plane

(c) St = 0.01 - r-φ plane

(d) St = 0.01 - r-z plane

Figure 5.12: The Schmidt number in the case of active aSI is mostly between $0.1 < \mathrm{Sc} < 1$. This shows that the particle diffusion is in most cases stronger than the gas turbulence. Active zonal flows and active vertical bands, i.e. r-z runs with $\varepsilon_0 < 10$, imprint an increase in Schmidt number.

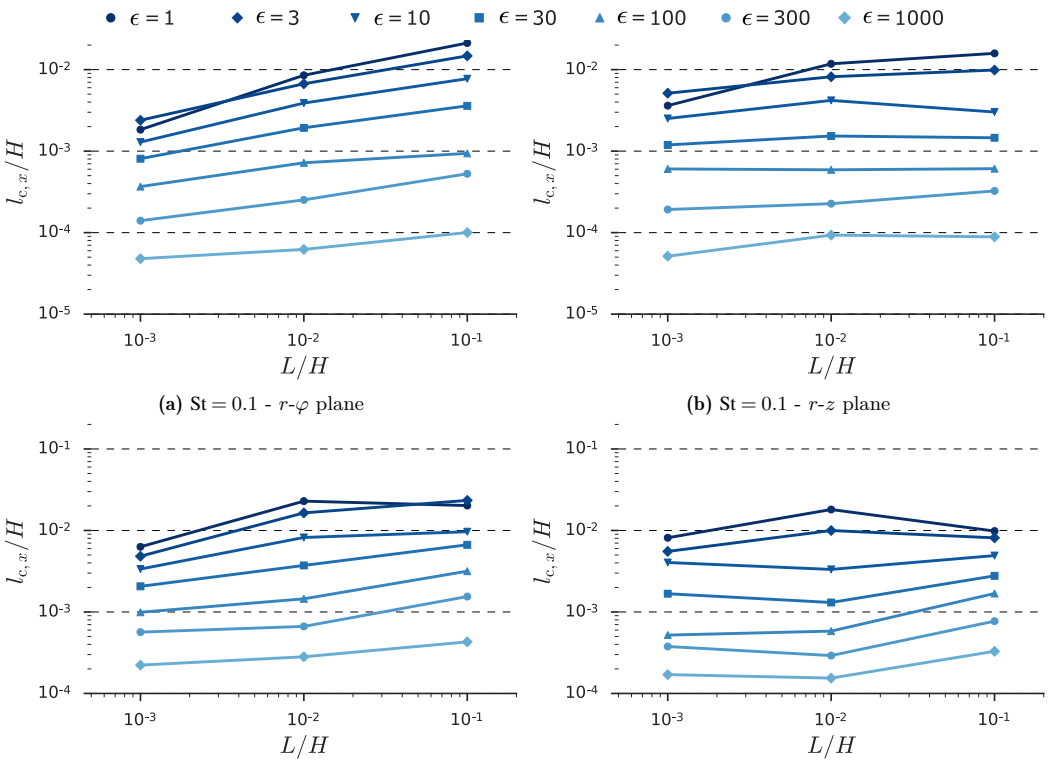

(a) St = 0.1 - r-φ plane

(b) St = 0.1 - r-z plane

(c) St = 0.01 - r-φ plane

(d) St = 0.01 - r-z plane

Figure 5.13: Critical length scales $l_{c,x}$ from aSI and SI radial particle diffusion δ_x measurements, by using Eq. (3.40).

5.2.8 Critical length scales from the (azimuthal) streaming instability

From the measured particle diffusivity one can estimate now the critical length scale that is allowed to collapse, as stated in Sec. 3.3. The values that use the radial diffusivity are shown in Fig. 5.13, and the ones from the vertical diffusivity in Fig. 5.14. As can be seen, mostly the critical length scales that one can expect are around 10^{-3}. The interpretation of these values is difficult, since a cloud that tries to collapse, i.e. that is at Hill density, is not isolated. The turbulent diffusion that is acting on the cloud thus does not solely comes from the turbulence of the aSI/SI that is residing inside the cloud, but also from its surrounding. Since the surrounding should tend to be at a lower dust-to-gas ratio, the modes that get produced are larger and might increase the turbulent strength acting on the cloud. Still, many of the investigated parameters sets show critical length scales that are larger than the corresponding simulation domain size. This indicates that these simulations are prohibited from collapse, as will be shown in Chapter 7. In many of the presented cases, the critical length scale based on the radial diffusion is larger, than the one that is calculated from the vertical particle diffusion. Moreover, as long as the aSI/SI is active, one find that in most cases the critical length scale does only slightly depend on the simulation domain size, but more strongly on the dust-to-gas ratio. Surprisingly, the critical length scales do not strongly depend on the Stokes number, since $l_c \sim \sqrt{\delta/\mathrm{St}}$, and the critical length scales for $\mathrm{St} = 0.01$ particles is only slightly larger than for the bigger particles.

5.2.9 Special cases: zonal flows and vertical band structures

As can be seen in Fig. 5.2, strong horizontal modes, e.g. (r-φ, $\mathrm{St} = 0.1$,$L = 0.1\,\mathrm{H}$, $\varepsilon_0 = 30$), and horizontal bands, e.g. (r-z, $\mathrm{St} = 0.1$,$L = 0.001\,\mathrm{H}$, $\varepsilon_0 = 0.8$), appear in the parameter study. They emerge where the

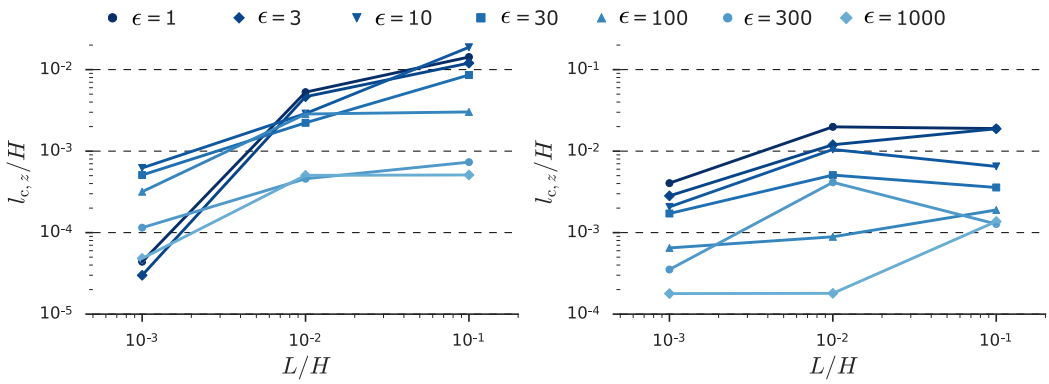

(a) St = 0.1 - r-φ plane **(b)** St = 0.1 - r-z plane

Figure 5.14: Critical length scales $l_{c,z}$ from SI vertical particle diffusion δ_z measurements, by using Eq. (3.40).

aSI/SI modes get to large and only a fraction of the previous modes remain to be resolved. One gets this by comparing the resolved length scales in the simulation with the analytic growth rates for the SI in Fig. 2.8 and Fig. 2.9. Primarily, the band structures appear in the SI simulations, so it could be that in the aSI simulation most of them get destroyed by the Keplerian shear. Since the difference between k_x-k_φ and k_x-k_z modes is that the shear transforms k_x waves numbers into k_φ, by winding them up. Imagine a straight line of points in radial direction in a shearing box frame of reference, this line will tilt by the shear, since the underlying Keplerian shear velocity goes with $v_{\text{shear}} \sim x$. Consequently, strong horizontal bands as they appear in (r-z, $\mathrm{St} = 0.1, L = 0.001\,\mathrm{H}$, $\varepsilon_0 = 0.8$) cannot reside in the r-φ plane.

Looking at the special case of (r-φ, $\mathrm{St} = 0.1, L = 0.1\,\mathrm{H}$, $\varepsilon_0 = 30$), one observes the aSI to saturate in a time between 20 and 30 orbits on a comparable similar maximum dust density fluctuation level of ≈ 10, as it is achieved in most other aSI-active simulations. But, after 30 orbits, the dust further concentrates, reaching maximum dust density fluctuations above $\varepsilon_{\text{max}}/\varepsilon_0 = 100$. This concentration happens in local non-axisymmetric particle heaps residing in zonal gas flows, see Fig. 5.15. They are stable for the rest of the simulation duration and seem to be unaffected by the underlying aSI. These zonal flows are around $0.02\,\mathrm{H}$ to $0.03\,\mathrm{H}$ in width and are limited in azimuthal extend by no more than $0.08\,\mathrm{H}$. Similar structures could not be observed in the smaller r-φ runs with $\varepsilon = 30$, because the zonal flow radial wavenumber is smaller than the smallest wavenumber that is fitting into the next smaller simulation. For the simulations with $\varepsilon \geq 100$ a similar strong phenomenon could also not be observed. One could argue that these bands would disappear if the spatial resolution is increased, therefore a resolution study was performed on the aSI. The results of this study are shown in Sec. 5.3.

One also might expect very strong particle trapping in these modes, as they have ten times higher dust concentrations than the typical value for the aSI, and hence a decrease in particle mobility should be expected, i.e. lower particle diffusivity. But still, averaged over the whole simulation domain, these structures do not significantly affect the measured diffusivity values to a significant degree. For $20 < t < 30 T_{\text{orb}}$, before the zonal flow emerge, the diffusivity is found to be

$$\delta_{\text{x}} = (2.62 \pm 1.35) \cdot 10^{-6},$$

whereas in the case of the fully developed zonal flows the diffusivity is measured to be

$$\delta_{\text{x}} = (3.71 \pm 2.14) \cdot 10^{-6}.$$

The reason for this might be that the mixing time of particles to get into the heap and out again, is comparable short. Because the zonal flows are found to be fully aSI-active, even within the high dust overdensities.

The global particle drift value $\zeta_\circ$ for this zonal flow case is slightly increased, as the particle heaps have a significant higher dust-to-gas ratio and consequently radially drift faster inwards, as seen in the dip in the blue line for $\varepsilon_0 = 30$ in Fig. 5.9a.

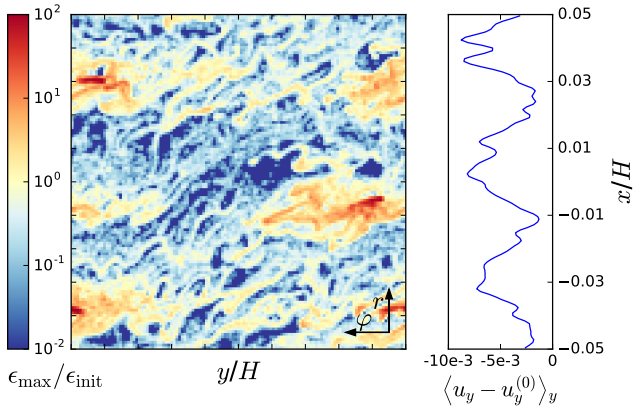

Figure 5.15: St = 0.1 - r-φ plane: The ($L = 0.1\,\mathrm{H}$, $\varepsilon_0 = 30$) run is able to produce three zonal flows with strong particle clustering. Left shows the normalized particle density, right shows the underlying azimuthally averaged gas flow perturbation. The flows emerge after $t = 30 T_{\mathrm{orb}}$ and further concentrate particles up to $\varepsilon = 100$ and do not show up in other simulations. Snapshot is taken at $t = 120 T_{\mathrm{orb}}$.

Similar structures as the zonal flow in (r-φ, $\mathrm{St} = 0.1$,$L = 0.1\,\mathrm{H}$, $\varepsilon_0 = 30$) are found for the r-z simulations with $\mathrm{St} = 0.1$ as vertical or horizontal bands. The vertical bands emerge for (r-z, $\mathrm{St} = 0.1$,$L = 0.1\,\mathrm{H}$, $\varepsilon_0 = 3$) to (r-z, $\mathrm{St} = 0.1$,$L = 0.1\,\mathrm{H}$, $\varepsilon_0 = 100$), and (r-z, $\mathrm{St} = 0.1$,$L = 0.01\,\mathrm{H}$, $\varepsilon_0 = 30$) to (r-z, $\mathrm{St} = 0.1$,$L = 0.01\,\mathrm{H}$, $\varepsilon_0 = 100$). These bands show a repetition with a fixed separation, very similar to the discussed zonal flows in the aSI simulations. It could be that both of this phenomenon are the incarnation of the same physics and a product of the radial wavenumbers of the linear SI to be stronger limited than the vertical wavenumbers, see Fig. 2.8. In the simulations (r-z, $\mathrm{St} = 0.1$,$L = 0.001\,\mathrm{H}$, $\varepsilon_0 = 0.1$) to (r-z, $\mathrm{St} = 0.1$,$L = 0.001\,\mathrm{H}$, $\varepsilon_0 = 3.0$) horizontally extended bands are found that do not show a repetitive pattern in the simulations, as the zonal flows do. It might be that these are the incarnation of larger modes that get unresolved on these small scales. As can be seen in Fig. 2.8 for such small dust-to-gas ratios, the mode activity of the SI is limited to modes with very large extend in radial direction, but all kind of extends in vertical direction are allowed. This is right what is observed in the simulation.

5.2.10 Influence of Hyper-Viscosity and -Diffusivity

An additional remark has to be done on the numerical hyper-diffusivity and -viscosity, see Sec. 4.1. The whole presented parameter study was performed with a resolution dependent but then fixed hyper-viscosity and -diffusivity value of $1.573 \cdot 10^{-19}$, $1.573 \cdot 10^{-24}$ and $1.573 \cdot 10^{-29}$, for the three simulation domain sizes respectively. It has been found later in the post-processing that this is not the lowest stable value for all simulations and by decreasing this value, many of the aSI/SI-inactive simulations could additionally be populated with aSI/SI modes. Still, it is of interest to have the same value of hyper-viscosity and -diffusivity for all simulations of the parameter study, in order to have them consistent and keep the results comparable. To comprehend how this additional parameter influences the results, additional simulations with $\mathrm{St} = 0.1$ particles were performed.

The first run is ($L = 0.1\,\mathrm{H}$, r-φ, $\varepsilon_0 = 100$), where the hyper-diffusivity and -viscosity was increased by one order of magnitude. The result show maximum dust density fluctuations dropped to $\langle \varepsilon_{\max}/\varepsilon_0 \rangle_t \approx 2$, instead of ≈ 10 from the original run. The timeseries of this simulation is shown in Fig. 5.1a, where one can see that the maximum dust density even decreases from the initial maximum value. The particle diffusivity in this case is found to drop from $\delta_x = 1.93 \cdot 10^{-07}$ down to $4.84 \cdot 10^{-08}$. As can be seen, the new diffusivity value is not just zero, but only one order of magnitude smaller. The reason for this effect is not understood yet, and similar diffusivity drops can be observed for the $\mathrm{St} = 0.01$ simulations with the largest domain size.

The second run is ($L = 0.1\,\mathrm{H}$, r-φ, $\varepsilon_0 = 0.5$) with one order of magnitude lower hyper-viscosity and -diffusivity. The previously aSI-dead simulation now was populated with aSI and showed maximum dust

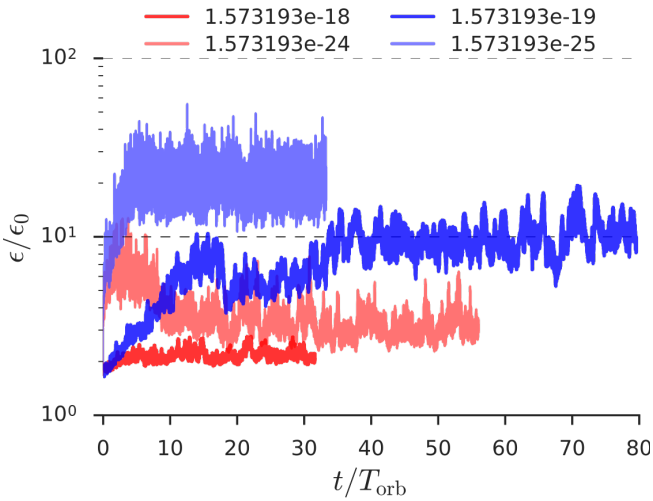

Figure 5.16: Timeseries of maximum dust-to-gas ratio normalized to the initial dust-to-gas ratio for two cases of ($L = 0.1\,\mathrm{H}$, r-φ, $\varepsilon_0 = 100$) and ($L = 0.01\,\mathrm{H}$, r-φ, $\varepsilon_0 = 0.5$). The choice of hyper-viscosity and -diffusivity strength can suppress the aSI since small modes grow the fastest.

density fluctuations up to a value of $\langle \varepsilon_{\max}/\varepsilon_0 \rangle_t \approx 20$, instead of ≈ 3 from the aSI-dead case. The particle diffusivity increased by two orders of magnitude, from $\delta_{\rm x} = 1.09 \cdot 10^{-7}$ to $1.42 \cdot 10^{-5}$.

So from the point of numerical resolution, these two simulations are able to resolve the aSI. But, fastest grow happens on small wavelengths, see Fig. 2.8 that can get suppressed by hyper-viscosity and -diffusion. This then can prevent grow of larger modes as well, since the initial perturbation that the simulations starts with is not strong enough, or because their growth rate is too small, i.e. to small to compete with the Keplerian shear. One sees when looking into a time evolution of the simulations in the form of a video. First, small modes grow, then it takes a while until the larger modes fully develop. Lastly, PencilCode users are recommended to use the mesh based hyper-diffusion and -viscosity, as presented in Yang & Krumholz (2012), to avoid such consideration.

5.3 Resolution study on aSI at $L = 0.1\,\mathrm{H}$ with $\mathrm{St} = 0.1$ particles

The project above found and characterized the *azimuthal Streaming Instability* (aSI). Still, the numerical convergence of these results had to be shown. This was done in a numerical resolution study on the aSI for $\mathrm{St} = 0.1$ particles, which is presented within this section. The simulations of this resolution study were setup with $L = 0.1\,\mathrm{H}$ in the r-φ plane, and are thus basically identical to the simulations from Sec. 5.2. Since the focus lies on aSI-active cases, the initial dust-to-gas ratio was limited to the simulations with $\varepsilon_0 \geq 1$. The used grid resolutions are $N = 128$, $N = 256$, and 1260, where the runs with $N = 128$ are the original runs from the previous section. Hyper-viscosity and -diffusivity were decreased for each resolution step accordingly, in order to resolve the very small length scales. The runs with $N = 1260$ actually state the highest feasible numerical resolution in 2-d, where still the amount of data produced could be handled by the output system of the PencilCode. This project was taking the most effective computational time, all together the simulations ran over 814 days, of course they ran partly in parallel. An overview over the computational effort is stated in Appendix A. An optimized data output scheme is needed if one wants to drive this number to even higher values.

Snapshots of the simulation end-states are shown in Fig. 5.18. In this figure, they are compared with the corresponding original $N = 128$-type simulation. Not all the simulations with $N = 1260$ achieved full saturation, or even if, then not for a longer duration. The reason is that the time stepping gets very small for $L = 0.1\,\mathrm{H}$ and $N = 1260$. Still, no significant change in the investigated quantities is to be expected if

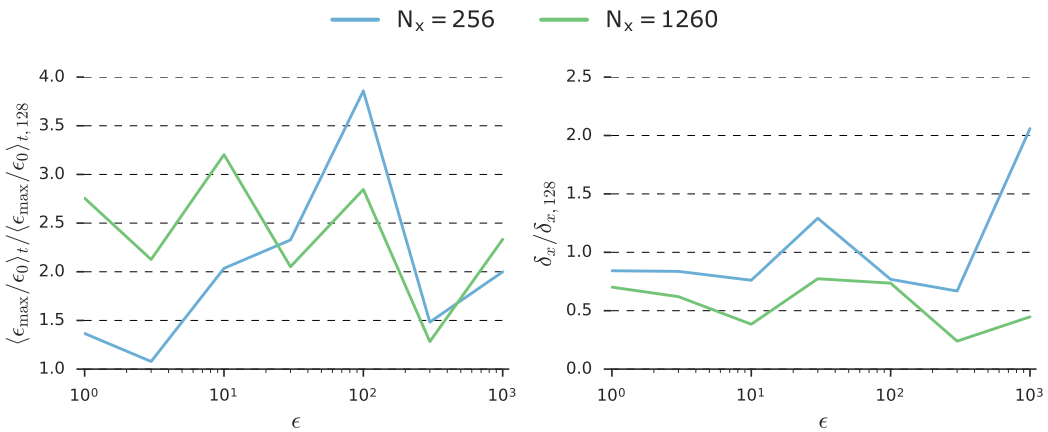

(a) Comparison of maximum dust density concentrations **(b) Comparison of the radial particle diffusion δ_x**

Figure 5.17: Comparison plot for the maximum dust density and radial diffusivity for the resolution study on the aSI, with $\mathrm{St} = 0.1$. The investigated resolutions are $N = 256$ and $N = 1260$ that get compared with the simulations with $N = 128$ from Sec. 5.2. The aSI at the highest resolution is found to be able to increasing the maximum dust-to-gas ratios at lower ε_0 by a factor of 2.5. The $N = 128$ shows only a significant increase for $\varepsilon_0 = 100$, where now zonal flows are found. Also the simulations with $\varepsilon_0 = 30$, i.e. the simulation in which zonal flows appear, is only marginally increasing the maximum dust density by a factor of 2. The radial particle diffusion on the other hand stays roughly constant. Only on very high numerical resolutions the diffusivity drops by a factor of 2.

the simulation were continued for any longer.

Due to the higher resolution, the aSI was able to develop smaller modes than before. These modes are then found to be active even within the larger of the aSI modes. Also, aSI modes are again found to be active inside the emerging zonal flows and particle clumps, see below. The zonal flows found in the (r-φ, $\mathrm{St} = 0.1$,$L = 0.1\,\mathrm{H}$, $\varepsilon_0 = 30$) simulation from the previous chapter, are active in all the simulations with higher resolutions. Thus, the zonal flows in the $N = 128$ simulations are not an effect of a lack in resolution. With increasing resolution, the zonal flows appear to get finer and compacter. Especially in the azimuthal direction the particles cluster into regions of smaller extend. As can be seen in Fig. 5.17a, this refinement of the zonal flows leads to an increase in the maximum occurring dust-to-gas ratio by only a factor of 2 that also equal for both higher resolutions.

For all simulations with higher resolution, only a marginal increase in the maximum dust-to-gas ratio could be found. In the lower end of dust-to-gas ratio range, the simulations with $N = 1260$ produced actually three times stronger maximum dust concentrations, but every other run produced only an average increase in the maximum dust concentration by a factor of two. A surprising peak for this value can be found in the simulation with ($N = 256$, $\varepsilon_0 = 100$). This simulation shows sharp zonal flow features with a high spatial frequency in radial direction, see Fig. 5.18. The herein present structures were unresolved in the equivalent $N = 128$ simulation and thus the simulation now show a sharp increase in the measured maximum dust density. The parameter set of this simulation marks a transition into a realm where the radial aSI wavelengths get too small to be resolved, though from a linear stability analysis they remain present, see Fig. 2.8. If these high dust-to-gas ratios remain of interest in the topic of PPDs and planetesimal formation is doubtful.

As a reminder, the simulation with $\varepsilon_0 = 30$ already showed in the $N = 128$-run a maximum dust concentration enhancement above 100, a ten times higher value than the average. In the herein investigated simulations with higher resolution, this value now peaks at double the value. A factor two in Fig. 5.17a seem small, but the absolute value remains to be a very strong increase in the maximum occurring dust density. Still, for this case, no difference between the $N = 256$ and $N = 1260$ simulations is found. Once can conclude that a higher refined zonal flow is not necessarily increasing the in the found maximum dust-to-gas ratio. Which stays in contradiction to the found increase in Johansen et al. (2015), which clearly not comes from

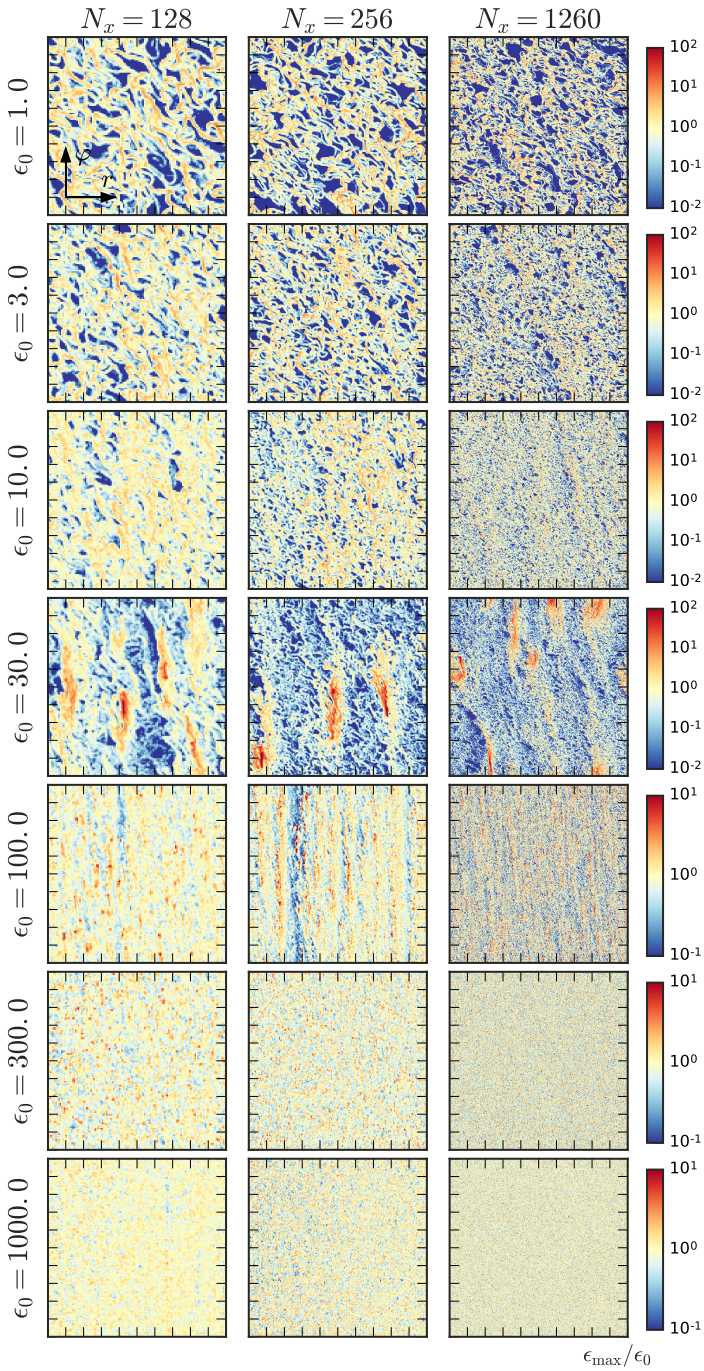

Figure 5.18: St = 0.1 - r-φ plane - $L = 0.1$H: Last snapshots of the dust-to-gas ratio normalized to ε_0 (yellow). Over-densities are coloured in red, particle voids in blue. The aSI mode pattern gets more refined with increasing numerical resolution. The three zonal flows from Sec. 5.2.9 for $\varepsilon_0 = 30$ also emerge at the doubled resolution. At $N = 1260$ found are seven zonal flows with high particle concentration that are smaller in both azimuthal and radial direction than in the runs with coarser resolution. The emerging particle over-densities show aSI activity inside and signs of erosion, i.e. particle flows in radial outward direction at the azimuthal back of the heap.

higher resolving the SI, but by their additional stellar and self-gravity.

Fig. 5.17b now compares the measured radial turbulent diffusivity δ_x with the values measured in the original $N = 128$ simulations. Similar to the comparison of the found maximum dust density fluctuations, one finds the diffusivity to stay also at a constant level. The diffusivity drops at maximum by half its value from the $N = 128$ simulation. This means, the associated critical wavelength gets roughly 70 % smaller. For unknown reasons, the $\varepsilon = 1000$ simulation with $N = 256$ doubles its diffusion value. Since the $N = 1260$ simulation did not show a similar behaviour, this value is considered to be an outlier.

Overall, the simulations with $N = 128$ can be concluded to not be hampered by their coarser resolution. In contrast, the diffusion and maximum dust density values show no significant resolution dependency. One might conclude here on the strongest diffusion to be right injected into the particles by the largest aSI modes. Once these modes are resolved, the measured diffusivity stays fixed for the corresponding value of initial dust-to-gas ratio. The maximum dust density concentrations on the other hand are slightly affected by the resolution. Since with higher resolution smaller aSI modes can be resolved. These smaller modes now can reside within the larger aSI modes and within zonal flows. Since the larger modes already concentrated the dust, the smaller within them can further increase the dust concentration by a factor of 2 to 3. Hence, with smaller resolved modes, slightly higher concentrate of dust are possible. Once the in initial dust-to-gas ratio reaches a level were the aSI shuts down, the dust density fluctuations stay on an identical level for all resolutions. This can be seen in Fig. 5.17a, where the green line drops towards higher values of ε_0 onto a level, where all resolutions have merely the same maximum occurring dust densities. It can be concluded that differently as stated in Johansen et al. (2015), which investigates the SI under the influence of stellar and self-gravity, the pure aSI does not increase its maximum dust-to-gas ratio to arbitrarily high numbers, when the resolution is increased. Probably the same is true for the SI itself.

5.4 Simulations on planetesimal formation within zonal flows

The goal of this thesis is to investigate a model for self-regulated planetesimal formation right at a turbulent diffusion threshold. The threshold is found to be given by the strongest turbulent process in the particles, acting on the scales of planetesimal formation. As seen above, the SI is an excellent candidate to be the driving source of turbulence in the particles. But, two problems gets often stated on this approach. The first comes from the lack of the needed high dust-to-gas ratios in typical PPD models. The found dust density are too low to trigger the SI. A typical approach to overcome this, is by include an additional dynamical process that locally enriches the dust-to-gas ratio up to values where the SI and dust cloud collapse can happen. These particle enhancing processes are typically called particle traps, as explained in Sec. 2.2.6. But, secondly, particle traps are often criticized as being regions of vanishing pressure gradient. Hence, no SI should be active. This section endeavours this claim from the perspective of available literature, and by performing additional simulations of 2-d shearing sheet simulations in radial-azimuthal extent, with an artificially induced zonal flow.

Starting by repeating the main facts on SI. Youdin & Goodman (2004) and Squire & Hopkins (2017) showed the SI to need a velocity difference between dust and gas. In PPDs this comes from the gas pressure gradient and its consequence of gas moving with a sub-Keplerian velocity. See Sec. 2.1.3 on the global gas pressure gradient and Sec. 2.2.4 on the SI. A particle trap now, especially a zonal flow, is characterised by being a region of locally enhanced and/or reduced gas pressure, see Fig. 2.12. In contrast, for a vortex (Barge & Sommeria, 1995; Raettig et al., 2015) as a particle trap, this is only partly true as also the cumulative net forces inside trap particles. Still, a vortex in a PPD is typically anti-cyclonic, i.e. a region of increased pressure. What is claimed, is that these type of particle traps should have no pressure gradient right at their centre, where the particles get trapped. Ergo, no SI should be active inside of particle traps.

Now, many authors showed this to be incorrect, and so do the carried out simulations. The SI actually should be expected to be active within such kind of particle traps, especially in the vicinity of the zero relative velocity point. First, a local pressure bump is typically local and thus its spatial extent is small compared to the disk. Consequently, the increase in gas pressure takes place on a smaller radial extent. Plus, the gas pressure in a trap has to increase by a great amount in order to achieve a zero pressure gradient. The pressure gradient consequently has to be steep in the vicinity of a particle trap, compare with pressure bump model in Taki et al. (2016) and Onishi & Sekiya (2017). Zonal flows additionally often show a second region of depleted gas density, see Dittrich et al. (2013) or Onishi & Sekiya, 2017 with a good visualisation on that.

Hence, the gas pressure gradient becomes steep also in the surrounding of the zonal flow, and the SI more active. Or, to be precise, active already at dust-to-gas ratios below unity. Johansen et al. (2007) for example showed zonal flows that emerge from magnetic coupling of the gas onto an imposed stellar magnetic field. In this work, the SI was indeed shown to be active within the long-lived zonal flow. The SI even managed to increase the dust concentration within the trap by another order of magnitude, and planetesimal formation could be triggered, i.e. in terms of Hill density was reached. A similar approach was done in Raettig et al. (2015), where a vortex was proven to be a good particle trap as well, and were the authors could show aSI activity within it.

Auffinger & Laibe (2017) investigated this situation of SI in a pressure bump analytically. They find the SI to actually have an activity preference inside of zonal flows and go so far to claim SI to only operate inside of a pressure bump. Their finding in increased activity comes from the differential advection of dust and gas into the pressure bump, which gives rise of a higher order variant of the SI. Numerical models of particles inside of a zonal flows tried to argue against this scenario, e.g. Taki et al. (2016) argued that the back reaction of the particles onto the gas will lead to a dispersing zonal flow. But, the timescales of this dispersal are much longer than the typical scales of particle trapping, SI growth time, and cloud collapse. They also did not re-enforce the zonal flow into presence, as done self-consistently in Johansen et al. (2007). A more optimistic approach was presented in Onishi & Sekiya (2017), who also found that pressure bumps are not erased by the particle back reaction. Still, this study lacked an clear indication of active SI, if they even resolve it. Their pressure bumps still reached dust-to-gas ratios well above unity in regions of non-vanishing pressure gradient, where than directly the self-regulated planetesimal formation would start to operate in.

To settle the debate if the within this section newly found aSI can be active within a pressure bump, the PencilCode was extended in a small side project by a pressure bump module. It handles the shape (`pb_shape`) and amplitude (`pb_amplitude`) of a pressure bump, and contains an additional force source acting permanently onto the gas. The shape can be set either as Gaussian or as sine wave function in radial direction, i.e. symmetric in azimuthal and vertical direction. More pressure bump shapes could be added in the future, i.e. one that mimics a vortex, or a non-axisymmetric pressure bump might become useful in the future, as well as vertically correct models of pressure bumps. The radial extend of the pressure bump is set as being the radial domain size. The initial gas velocity has to be set into a grid-wise equilibrium solution with this new pressure force. The equilibrium is thus set by

$$\begin{aligned}\texttt{f(ix,iy,iz,iuy)} = \texttt{f(ix,iy,iz,iuy)} + \\ \texttt{1/(2*Omega)*cs20*beta\_glnrho\_scaled(1)*pb\_profile(ix-l1+1)}.\end{aligned}$$

Where the scaling of the gas pressure gradient $\beta_{\ln(\rho)}$, i.e. the pressure bump shape and amplitude, is contained in the one-dimensional array `pb_profile`. This array basically represents a scale-free pressure bump, as numerically evaluated onto the radial grid space. This then also becomes multiplied with the global acceleration value from the pressure gradient. The pressure bump acts as a force on the radial gas acceleration via

$$df(l1:l2,m,n,(iux-1)+j) = df(l1:l2,m,n,(iux-1)+j) - p\%cs2*beta\_glnrho\_scaled(j)*pb\_profile,$$

and thus the pressure bump is mimicked as being a steady forcing onto the gas. One might compare this with $\beta_{\ln(\rho)}$ from Sec. 4.3.

The module was tested in two different ways in 2-d radial-azimuthal simulations with $N = 256$ grid cells, 10 particles per grid cell and $\mathrm{St} = 0.1$ particles. First, the general ability to trap particles should be showed. Hence, a simulation containing a very strong zonal flow was evaluated. In this run, a pressure bump with sinusoidal shape, and peak amplitude of $\mathrm{PB}_0 = 5$ was tested on an initial dust-to-gas ratio of $\varepsilon_0 = 0.01$. Fig. 5.19a shows the resulting particle density (left) and azimuthal mean gas velocity (right) of the simulation end-state. All the dust is concentrated into a small dense ring with dust-to-gas ratio above 10^2, right at the inner boundary of the zonal flow, where the gas velocity profile is zero. This is the typical trapping location of particles, hence the other point with $u_y = 0$ is unstable to perturbations in the dust particle position. This zonal flow is strong compared with what might be expected in PPDs, compare Onishi & Sekiya (2017) and Taki et al. (2016), and should be seen as a proof of the numerical concept. The strength of the zonal flow actually leads to azimuthal gas velocities between $-0.3c_\mathrm{s} \leq u_y \leq 0.2c_\mathrm{s}$. Were the sub-Keplerian azimuthal gas velocity in the absence of the pressure bump would be $u_y = -0.05c_\mathrm{s}$. The simulation showed that no

particles could escape such a strong trap. In a lower resolution version of this run, the code actually crashed due to high dust density gradients, with this higher resolution the code was stable for several tens of orbits.

Four more simulations where performed, identical to this run, but with a pressure bump amplitude of $\mathrm{PB}_0 = 1$ and variation in the initial dust-to-gas ratio. The pressure bump amplitude is set such the maximum azimuthal gas velocity reaches Keplerian velocity in a single point. These pressure bumps are thus weaker as the in Onishi & Sekiya (2017) and Taki et al. (2016) discussed pressure bumps, but similar in its radial extent. The four simulations start with initial dust-to-gas ratios of $\varepsilon_0 = 0.01$, 0.1, 0.5, and 1.0. The end-states of the dust density distribution is shown in Fig. 5.19b to Fig. 5.19e, together with azimuthal gas velocity profile in the beginning (blue) and in the end-state (green). Particle trapping is found to occur in all cases, but with higher dust load the pressure bump and trapping gets weaker. This comes from the pressure force that now has to stabilize not only the gas, but the gas-dust mixture coupled via friction. It might also be that the dust-density distribution was not initialized in an equilibrium solution, as the dust is initially homogeneously distributed. This could lead to a decrease in gas velocity as regions of the gas profile now have to support higher dust densities. Still, a pressure bump is visible in Fig. 5.19b and Fig. 5.19d. Also found is activity of the aSI once a dust-to-gas ratio above unity is reached. The modes that appear are seem small, but these simulations are much larger in their extent then the simulations from the aSI and SI parameter study above. Still, aSI modes are found to appear everywhere in the simulations, as can be seen by the noisy pattern and tilted line patterns. The maximum dust densities reached are $\max(\rho_\mathrm{d}) \approx 0.15$, 0.5, 2.0, and 7.3. It is unclear if and how strongly the SI is active in (c), but in (d) on can see that the SI indeed is active within the pressure bump. It seems the particle trapping in (b) - (e) is diffuse, i.e. no real trapping but a slow down in the pressure gradient maxima. But this diffuse particle concentration will also come from particle diffusion by the SI, but this needs further investigations.

A last experiment was conducted in a pressure bump that is thought to be similar to the one in Taki et al. (2016) and Onishi & Sekiya (2017), see Fig. 5.19f for the end state. In this run the pressure bump amplitude was increased to $\mathrm{PB}_0 = 2$ and the initial dust-to-gas ratio is set to $\varepsilon_0 = 0.5$. One finds this stronger trap to build up much higher dust density within its pressure gradient maximum, up to a value of $\rho_\mathrm{d} \approx 6$, then the aSI builds up. The aSI manages to further increase the local dust-to-gas ratio in small patches, see Fig. 5.19f, up to values of $\rho_\mathrm{d} \approx 25$. These regions then have dust-to-gas ratios around ≈ 50. The gas density in the runs (b) - (e) increases locally by up to 3 %, whereas in the last run (f) the gas density increases up to 5 %.

This study needs to be continued in the future. Higher resolutions will activate more SI modes within the pressure bump and one might test the diffusion limited collapse in such an simulation. For comparison, the SI study from Sec. 5.2 had a grid resolution of $dx = 7.8125 \cdot 10^{-4}$, whereas the five zonal flow runs here have a one order of magnitude coarser resolution. Also, other schemes in manifesting a pressure bump could be explored, especially the vertical dimension is not resolved in the presented experiments. As one sees, the gas velocity strongly drops once particle load is onto the pressure gradient. The work by Onishi & Sekiya (2017) did not show a strong decrease in the gas velocity profile and hence the applied force in the herein presented experiments might be too weak. Also, these experiments completely lack the vertical extent, and the dust will concentrate only in a small vertical fraction of the gas pressure bump, hence adding a vertical direction will alter the presented results completely. Still, shown has been the activity of aSI in a pressure bump, and maybe one can do better 2-d setups in future that will help to study planetesimal formation in such environments.

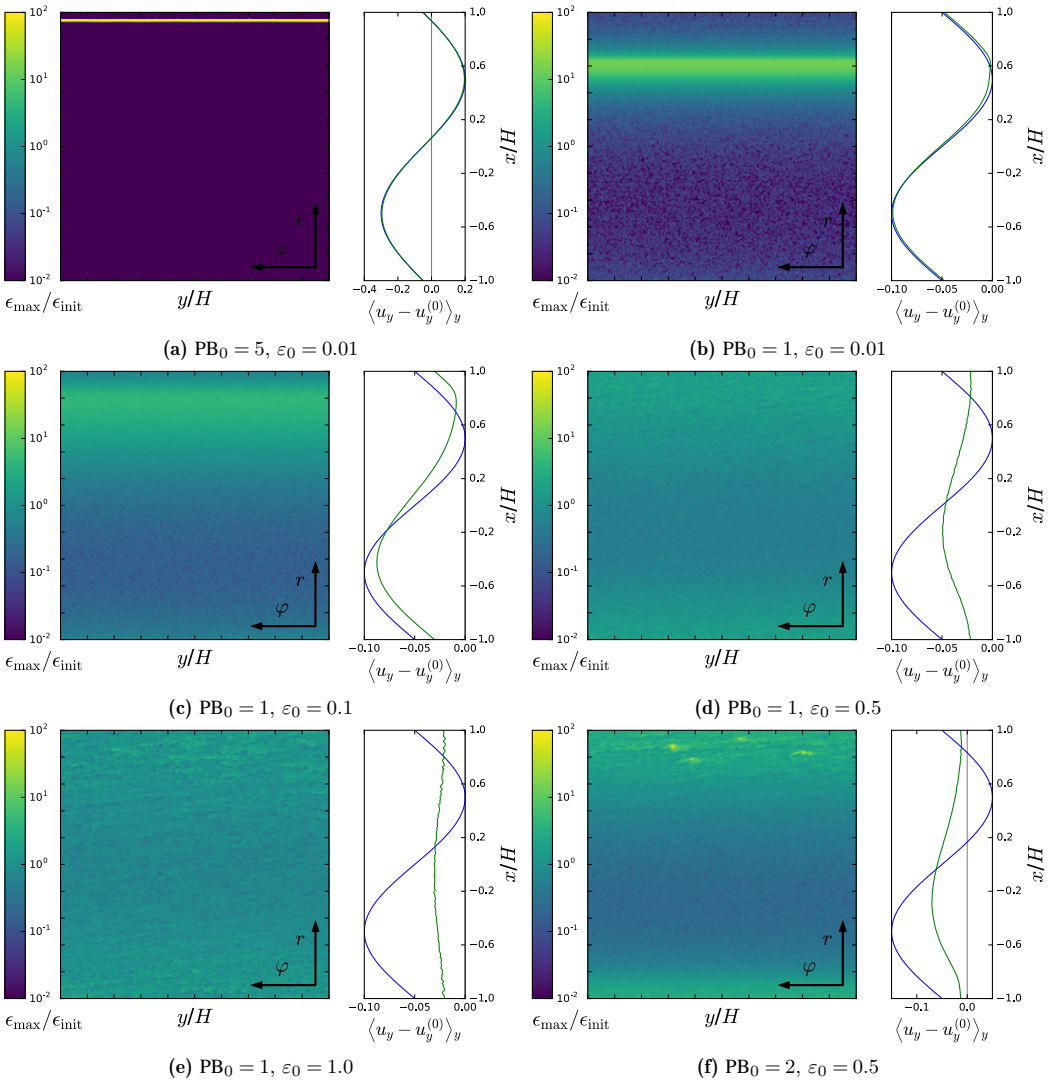

(a) $\mathrm{PB}_0 = 5$, $\varepsilon_0 = 0.01$ **(b)** $\mathrm{PB}_0 = 1$, $\varepsilon_0 = 0.01$

(c) $\mathrm{PB}_0 = 1$, $\varepsilon_0 = 0.1$ **(d)** $\mathrm{PB}_0 = 1$, $\varepsilon_0 = 0.5$

(e) $\mathrm{PB}_0 = 1$, $\varepsilon_0 = 1.0$ **(f)** $\mathrm{PB}_0 = 2$, $\varepsilon_0 = 0.5$

Figure 5.19: End states of particle distribution (left box) and azimuthal mean gas velocity $< u_y - u_y^{(0)} >_y$ (right box) in zonal flow simulations. The azimuthal mean gas velocity is plotted as initialized (blue) and of the end-state (green) that corresponds to the dust density snapshot to the left. (a) resembles a test run with $\mathrm{PB}_0 = 5$ a very high initial pressure bump amplitude, where all particles get trapped into a narrow band in the pressure gradient minimum. Fig. 5.19b has the same initial parameters, but a lower pressure bump amplitude, $\mathrm{PB}_0 = 1$. The amplitude is chosen such that there is a single point where the gas reaches Keplerian velocity. Still, this is sufficient to trap, i.e. slow down, the particle drift and dust density reach values of up to $\varepsilon_{max}/\varepsilon_0 = 16$. The simulations Fig. 5.19c to Fig. 5.19e are identical but have higher dust load ε_0. Maximum enhancements of the dust-to-gas ratio are 5, 5, and 7. It is unclear how much SI is visible in Fig. 5.19c, since by that numbers the maximum occurring dust-to-gas ratio is 0.5 and as shown in Sec. 5.2 this is insufficient to trigger the SI. Starting with run Fig. 5.19d, first signs of the SI are visible, specially also within the pressure bump. The pressure bump itself suffers from the additional dust load, as the azimuthal gas velocity profile deviates from the initial profile (blue). The particles manage to shift the gas velocity profile and reduce the pressure bump amplitude.

5.5 Discussion on the streaming instability in simulations

In the past, only very few works investigated the SI in its pure form, as most of the simulations in literature took sedimentation and self-gravity into account. The main work in the field of numerical SI thus remains to be Johansen & Youdin (2007). In their paper, they study the SI in 2-d and 3-d simulations, but no dedicated investigation in the radial-azimuthal plane was performed. The herein this thesis presented aSI hence remained undiscovered. In order to numerically investigate the relation between SI and aSI, one should perform in future additional simulations. One possibility would be SI simulations in r-z and then slowly superimpose a shear in z direction, until the situations a situation is reached which resembles the aSI, i.e. where the Keplerian shear parameter is $q = 3/2$. Analytically investigating the aSI will be difficult, since the Keplerian shear induces a time dependency that is hard to handle, see Bühler (2016). Wavenumbers in radial direction will get transformed into wavenumbers in azimuthal direction, as the Keplerian shear tilts them over time. As been found by measuring the growth rates, aSI modes show growth also on timescales that are slow compared with a shear timescale. Thus, a good aSI prescription and a verification of its similarity to the SI remains to be a future work.

As said, most recent works on the SI investigated only situations with active gravity. This explains why many works on the SI deal with dust disk surface densities, instead of dust volume densities, e.g. Carrera et al. (2015) or Yang et al. (2016). The work by Carrera et al. (2015) presented a parameter study that targeted for non-transient particle clumping as an indicator for SI-activity. But, one has to be careful with calling this increase of dust concentration to be the effect of the SIsolely. Because, without frictional back reaction of the dust onto the gas, the old picture of Safronov (1972) and Goldreich & Ward (1973) would be correct. It is the turbulent diffusivity of the SI, or the Kelvin Helmholtz instability, see Bai & Stone (2010a) for a comparison of both effects that is actually prohibiting sedimentation and fragmentation. In this picture SI actually prohibits fragmentation. To which degree the measured dust density fluctuations of the aSI/SI contribute to the measured fragmentation on larger scales, remains to be shown. At least the simulations carried out within this chapter showed the SI only to able to concentrate dust up to a factor of ≈ 10. The performed zonal flow simulations then showed only in combination with an assisting zonal flow, total dust-to-gas ratio enhancements can get greater than 10. Where each, the zonal flow and the aSI increased the dust-to-gas ratio by a factor of $\lesssim 10$.

From the study of the aSI and SI within this chapter, one might state a criterion on when the non-linear instability is active, and when not. If the instability is at work, one finds two features. First, the dust concentration rises, and secondly the particles get diffused by the turbulence. Other combinations of these effects to not indicate the non-linear instability to be at work. It can be summarized as in Tab. 5.2.

Latest work by Squire & Hopkins (2017) need to be mentioned, as they found a new way in describing the SI as part of a *Resonant Drag Instability* (RDI). In which instability, dust can get unstable in any suspended media with a relative motion, if this media allows for undamped oscillatory modes. The RDI can be used to separate the SI into two instabilities, one acting at low dust-to-gas ratios and one at high. The RDI also links the SI to the settling instability, where relative motions between dust and gas are induced by settling of the dust to the disk mid-plane and convective motions. But he settling instability has been found to have larger growth rates by an order of magnitude, suggesting the SI to drive the dynamics in collapsing particle clouds. What might be important in the following and upcoming investigations of particle cloud collapse.

ε enhancement	particle diffusion	possible origin
yes	yes	(azimuthal) streaming instability
no	yes	effects of buoyancy / particle not initialized in equilibrium
yes	no	linear streaming instability / traffic jam / zonal flow
no	no	homogeneous disk / no particle feedback

Table 5.2: To find out if the non-linear SI is active, is not always an easy task. Some performed simulations show particle diffusivity, but no dust density enhancements. These show effects of buoyancy by the additional dust load fluctuations, or particles not initialized in perfect local equilibrium. Dust density enhancements without particle diffusion should only exist in the case of a linear SI, or dust trapping, i.e. traffic jam or zonal flows.

6 3-d Streaming Instability at High Dust-to-Gas Ratios and on Small Scales

The numerical project from the previous chapter studied the SI together with the newly found aSI in 2-d simulations. This chapter now takes also the third dimension into account, and investigates the SI in 3-d simulations for $\mathrm{St} = 0.1$ and $\mathrm{St} = 0.01$ particles. The investigated length scales are the same as before, i.e. the simulation domain sizes are altered between $L = 0.1\,\mathrm{H}$, $L = 0.01\,\mathrm{H}$, and $L = 0.001\,\mathrm{H}$, and the numerical resolution is set to $N = 128^3$. Already by these configurations, the computational effort and the storage space needed are extreme, specially since a high temporal resolution is required in order to be able to extract the particle diffusion over time. In total, the in the following presented simulations take up over 23 TB on disk space. Besides high temporal resolution, another reason for this high number in data consumption comes from 128 times higher number of particles, which come from the additional third dimension. As done in the 2-d simulations, each grid cell has to be initialised with 10 particles. Hence, a total number of $N_{\mathrm{par}} = 20\,971\,520$ particles need to be evolved per run, instead of the $N_{\mathrm{par}} = 163\,840$ particles in the 2-d equivalent simlations. See Appendix A for an overview on the data and CPU hour consumption of all the performed projects.

To keep this 3-d project reasonable, the range of investigated dust-to-gas ratios got limited down onto values greater than unity. Most of the analysis from the 2-d study were performed on this 3-d simulations, too. But, the computational afford sets its limits, so mainly the important quantities are investigates, such as fluctuations in the particle density $\varepsilon_{\mathrm{max}}/\varepsilon_0$ and particle diffusivity in radial δ_{x} and vertical δ_{z} direction. The definitions for the presented quantities can be found in the previous chapter and will not be repeated. If one wants to compare the found values, the only comparison found in the literature is still the work of Johansen & Youdin (2007). In their work, they also performed two 3-d simulations with $\mathrm{St} = 0.1$ particles, but on much larger domain sizes of $L = 2\,\mathrm{H}$ and $L = 40\,\mathrm{H}$. Still, they will be used as reference for comparing the herein this thesis found results. Specially for $\mathrm{St} = 0.01$ particles reference values are missing, hence these values get compared with the $\mathrm{St} = 0.1$ run values, too. The performed parameter study represents a corner stone for selecting initial parameters for the 3-d particle cloud collapse simulations in Sec. 7.6.

6.1 Dust density fluctuations

The 3-d SI is found to induce dust density fluctuations with an amplitude very similar to the values of the 2-d aSI/SI, see Fig. 6.1 and compare it with Fig. 5.1. Maximum occurring dust density fluctuations in this 3-d SI simulations with $\mathrm{St} = 0.1$ particles reach the typical values as measured in the 2-d aSI/SI simulations, i.e. the typical value of $\varepsilon_{\mathrm{max}}/\varepsilon_0 \approx 10$ is reached in 3-d, too. In strong contrast, the 3-d SI for $\mathrm{St} = 0.01$ shows only very limited activity. The typical value of $\varepsilon_{\mathrm{max}}/\varepsilon_0 \approx 10$ is only reached in the simulations on the very smallest scales and only for ε_0-values around unity. For increasing dust-to-gas ratio, the 3-d SI with $\mathrm{St} = 0.1$ is found to be almost identical in its ability to locally concentrate dust, as the aSI run with the same Stokes number. For $\mathrm{St} = 0.01$ particles the 3-d SI is only found to be less active and does not compare in activity to the 2-d aSI/SI. Still, 3-d SI-activity has been found.

The simulations with $\mathrm{St} = 0.1$ again show zonal flow features. They appear now not only for $\varepsilon_0 = 30$, but now also for $\varepsilon_0 = 10$, see Fig. 6.3. This figure shows on the left a top view, i.e. slice through the computational domain volume, of the simulation end states, and on the right the corresponding front view. The observed zonal flows are very similar to the ones found in the 2-d simulations, compare with Fig. 5.2a. But, whereas

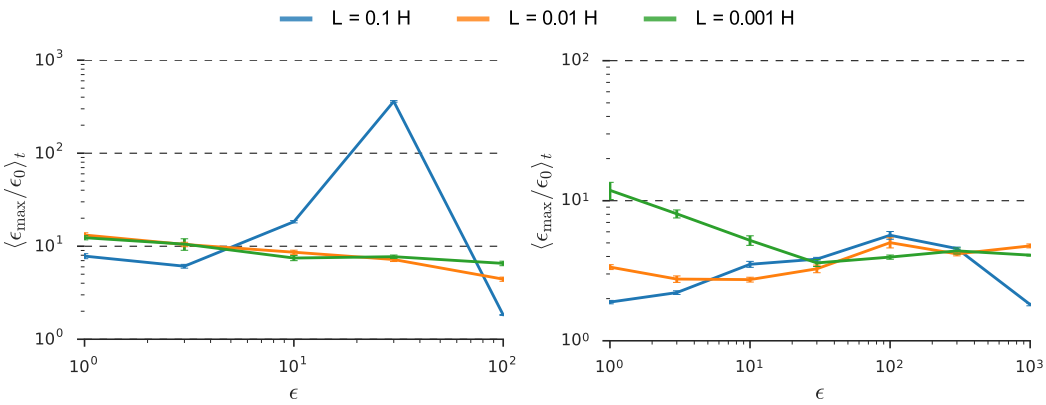

(a) St = 0.1 **(b)** St = 0.01

Figure 6.1: Values of the maximum dust density fluctuations and their standard deviation as error bars. The 3-d SI shows a comparable activity as in the 2-d cases from the previous chapter. For St = 0.1 the 3-d SI basically everywhere produced dust density fluctuations that reach up to dust density values of ≈ 10, so identical to the 2-d case. For this Stokes number again zonal flows appear, but now for $\varepsilon_0 = 10$ and 30. These zonal flows seem to be more efficient in concentrating dust, since values of $\varepsilon_{\max}/\varepsilon_0 \approx 400$ were reached. The picture for St = 0.01 again shows merely no SI-activity. Only on the smallest scales and for the lowest investigated dust-to-gas ratios activity of the SI could be found. The bump at $\varepsilon_0 = 30$ does not come from the SI, see Fig. 6.3 and text on the snapshots below.

in the 2-d case the maximum dust densities were found to be around $\varepsilon = 100$, in the 3-d simulations now the zonal flows were able to concentrate dust up to a value of $\varepsilon = 400$. This might indicate that these modes of the 3-d SI are more efficient in concentrating dust. If the observed behaviour of SI inside of SI induced zonal flows is similar to the situation from Sec. 5.4, where SI was found inside an artificial zonal flow, needs to be investigated. One might further speculate here that planetesimal formation is linked to the appearance of these modes. So far, this could not be proven in any collapse simulation. Specially the collapse simulations from the next chapter have a initial dust-to-gas ratio well below the values for triggering zonal flows.

For the 3-d SI with St = 0.01, the maximum occurring dust densities measured is plotted in Fig. 6.1b. Its values are almost throughout the whole parameter space below $\varepsilon_{\max}/\varepsilon_0 = 10$. As can be seen in Fig. 6.4, only a very small part of the investigated parameter range is actually populated with the 3-d SI. Hence, the bump at $\varepsilon_0 = 100$ in all three curves of Fig. 6.1b does not originate from the SI. Also, if the 3-d SI for St = 0.01 shows activity for initial dust-to-gas ratios below $\varepsilon_0 \leq 1$ needs to be investigated in further studies, as they are out of the scope of this analysis. If the mode activity at low dust-to-gas ratios are of any interest for the final collapse of a particle cloud is doubtful. Still, the rise of the maximum dust-to-gas ratio around unity suggests that SI-activity should be present. Maybe the instability drives turbulent dynamics on the very small scales at dust-to-gas ratios well before planetesimal formation, but how much this influences the overall dust dynamics needs to be studied in future.

6.2 Growth rates

The measured growth rates s are not flat over the initial dust-to-gas ratio, as was it the case in the 2-d simulations. Meaning, now a dependency on the initial dust-to-gas ratio is evident for the 3-d SI. On the largest investigated scale, the simulations with St = 0.1, and initial dust-to-gas ratios of $\varepsilon_0 = 1$ and 3 show a growth rate of around $s \approx 1$. With increasing initial dust-to-gas ratio, the simulations show zonal flows emerging. In these two simulations with $\varepsilon_0 = 10$ and 30 the growth rates decreased by more than one order of magnitude, to values between $s = 10^{-1}$ and $2 \cdot 10^{-2}$.

Actually, on all three domain sizes the growth rate at $\varepsilon_0 = 1$ is $s \approx 1$. But, on the intermediate (orange) and the smallest (green) scales, the growth rate rises with increasing initial dust-to-gas ratio, whereas decreased

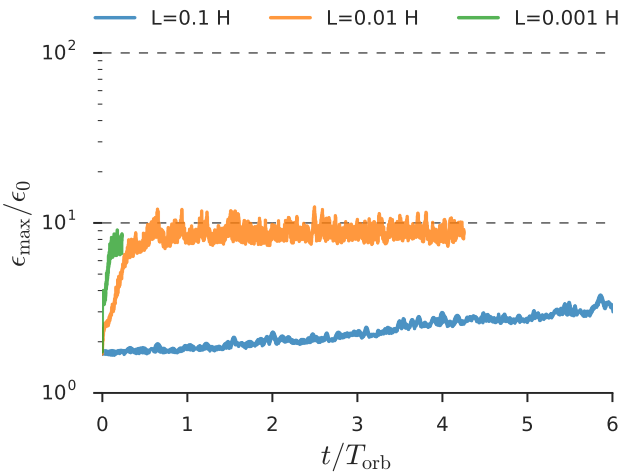

Figure 6.2: Timeseries of the maximum occurring dust-to-gas ratio in the 3-d SI simulations, with $\mathrm{St} = 0.1$ and $\varepsilon_0 = 10$. The time frame in this figure is limited to the growth phase of the instability. In contrast to the 2-d simulations, compare with Fig. 5.4, the growth on the smallest scales (green) is now much faster than on the intermediate scale (orange). On the largest scale, the growth of the SI is very slow. Both, the smaller and the intermediate sizes simulation converge in maximum dust-to-gas ratio to the typical value of $\varepsilon_{\max}/\varepsilon_0 \approx 10$. The continuation of this plot can be found in Appendix C.

on the largest scale. On the intermediate scale, the growth rate is on average $s \approx 1.5$. On the smallest scales the average growth rate is slightly higher with $s \approx 5$. For comparison, in the 2-d aSI/SI simulations the growth rates on the intermediate and smallest scales where merely similar. Now, in 3-d the growth on the smaller scales happens faster. As said, growth rates are also in general higher, maybe because both instabilities, the aSI and the SI, can grow and enhance each other mutually.

An example for the growth of the maximum dust-to-gas ratio is shown in Fig. 6.2 for the simulation with $\varepsilon_0 = 30$. It shows how slowly the modes grow on the largest scale (blue). It also shows the faster growing of modes on the smallest scales (green), compared with the intermediate scale (orange). The full set of all timeseries can be found in Appendix C. They show the zonal flows to emerge after $t = 40\,T_{\rm orb}$ ($\varepsilon_0 = 10$) and after $t = 30\,T_{\rm orb}$ ($\varepsilon_0 = 30$). Thus zonal flows get faster triggered with higher total dust density.

6.3 End-state snapshots

Snapshots of the simulation end-states are shown in Fig. 6.3 and Fig. 6.4. In 3-d simulations found is the best way for visually inspect the 3-d SI mode pattern is in the form of slices in r-φ (left image collection) and r-z (right image collection) direction through the simulation domain. A 3-d volumetric visualisation is picturesque, but not helpful in understanding the dynamics and mode structure. This type of visualization becomes more helpful when if comes to planetesimal formation and will be used in the next chapter on cloud collapse simulations.

The 3-d simulations with $\mathrm{St} = 0.1$ find significant SI activity throughout the parameter space. The only exception is the simulation with $\varepsilon_0 = 100$ on the largest scale, as it shows to be dynamically dead. But for the same initial dust-to-gas ratio is SI remains active on the smaller scales. For $\mathrm{St} = 0.01$ the final picture is different, see Fig. 6.4. It is also different to what was found previously in 2-d simulations, as there remains only a single hot-spot of SI-activity at around $\varepsilon_0 \approx 1$, and this on the very smallest scales. But, every other spot of the parameter space is only weakly SI-active or even dynamically dead.

Comparing the two slice orientations, one sees the $\mathrm{St} = 0.1$ particles clearly the effect of the Keplerian shear, as the modes in r-φ are strongly tilted. From visual inspection, the strength of this tilt seem to be a function of both ε_0 and domain size. The SI mode pattern also seems to have larger modes active in

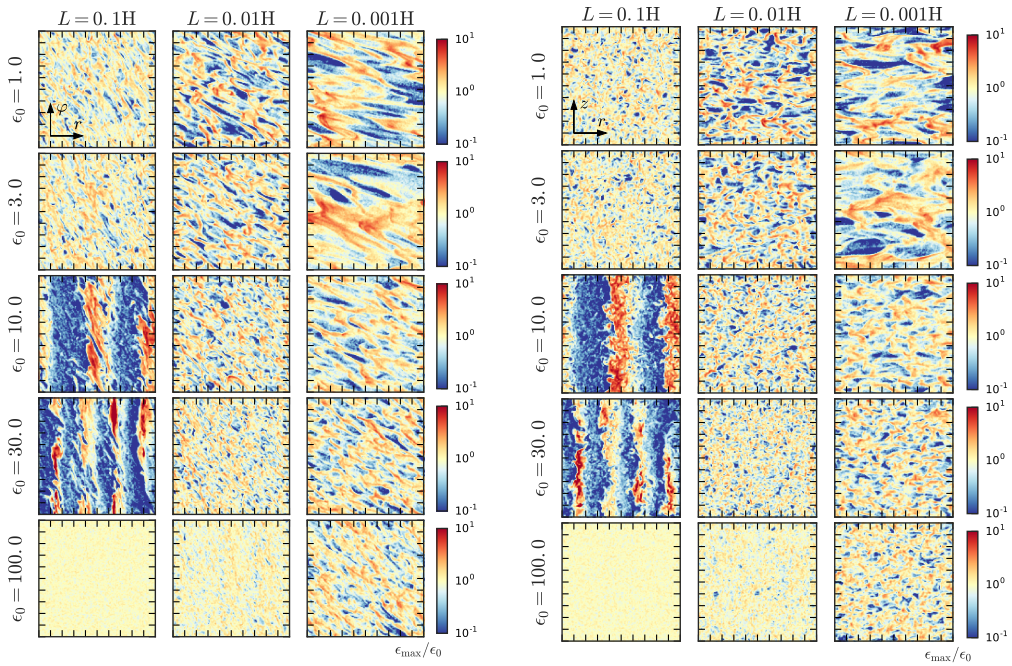

(a) r-φ slice **(b)** r-z slice

Figure 6.3: Slices from the last snapshots of the 3-d SI simulations with $\mathbf{St} = 0.1$. Shown is the dust-to-gas ratio, normalized to ε_0 (yellow). Over-densities are coloured in red, particle voids in blue. The pattern of the SI can be found in almost every simulation of that parameter space. Besides the simulations with the zonal flows, the found particle concentrations are the highest on the intermediate and smallest scales. The zonal flows appear only on the largest scales, but in contrast to the 2-d SI simulations now also for $\varepsilon_0 = 10$. The zonal flows in 3-d also manage to four times higher concentrate the dust into small patches. The zonal flow is a 2-d flow, i.e. a planar flow in vertical-azimuthal direction. This plane has no tilt with respect to the Keplerian shear, but the SI mode pattern itself seems to show a tilt in r-φ plane that angle depends on ε_0 and the simulation domain size. Numerical resolution of all runs is $N = 128^3$, and the simulations start with 10 particles per grid cell.

r-φ, than in r-z. And as similar to the 2-d simulations, the SI mode pattern gets smaller with increasing dust-to-gas ratio.

For $\varepsilon_0 = 10$ and 30, the largest simulations show also the appearing of zonal flows. They are now in 3-d planar in φ-z. Hence, the representation in 3-d seem to be the superposition of the patterns from the aSI and the SI, suggesting the dominant radial wavenumbers in both cases could be identical, compare with Fig. 5.2. The zonal flows appear to not be homogeneous in either the directions, as particle clumps of significant higher density are visible. Also, smaller modes of the SI are found to be active within them. As in 2-d, these zonal flows appear to concentrate particle in azimuthal and vertical patches of very high dust concentration. In contrast to the 2-d simulations, these patches achieve in 3-d four times higher values. The zonal flows in the 3-d simulation with $\varepsilon_0 = 10$ were not present in the 2-d aSI equivalent run, but in the 2-d SI simulation. If the simulation with $\varepsilon_0 = 3$ shows a first sign of a zonal flow is unclear from this analysis, but it would not be surprising since again in 2-d SI a large zonal flow was visible for this configuration.

It might be that the observed zonal flows come from the two allowed regimes of SI to grow in, see Squire & Hopkins (2017) for further reading. As can be seen in Fig. 2.8g, which shows the analytic growth rates for the SI for k_x and k_z at $\varepsilon_0 = 30$, the SI has two major branches were the instability is allowed to grow. The one branch has very low wavenumbers in radial and in vertical direction. These SI modes thus have large wavelengths and might thus be the ones inducing the formation of zonal flows. If this is true, it would

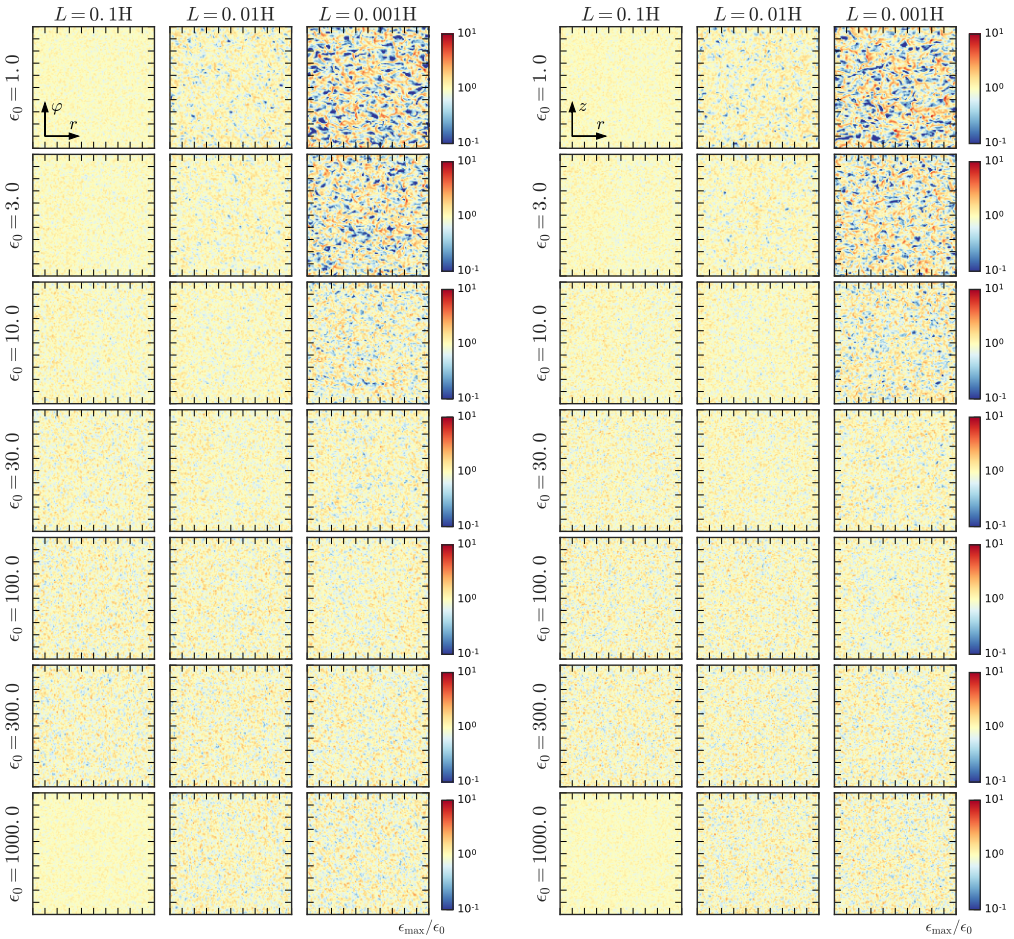

(a) r-φ slice **(b)** r-z slice

Figure 6.4: Slices from the last snapshots of the 3-d SI simulations with $\mathrm{St} = 0.01$. Shown is the dust-to-gas ratio, normalized to ε_0 (yellow). Over-densities are coloured in red, particle voids in blue. The pattern of the SI can only be found in the simulations with low initial dust-to-gas ratio around unity, and only on the small and intermediate scales. Though this is similar to the 2-d simulations, still the 3-d SI at this Stokes number seems to be much less present and if, weaker. Modes that appear in r-φ does not show a strong tilt as the $\mathrm{St} = 0.1$ simulation did. The mode pattern in r-φ and r-z looks very similar, i.e. not spatial preference can be found. The found particle concentrations are the highest in the run with $\varepsilon_0 = 1$ and $L = 0.001\,\mathrm{H}$. The result suggests for this Stokes number an 3-d SIactive range for $\varepsilon_0 < 1$, as in the 2-d equivalent from the previous chapter. Numerical resolution of all runs is $N = 128^3$, and the simulations start with 10 particles per grid cell.

explain why the zonal flows remain populated with smaller SI modes, as the smaller modes remain active even at very high dust-to-gas ratios. Even in situations were one would expect the SI to die out as the particle density strongly dominate over the gas density, the small mode SI can operate, and this is right the one active in the zonal flows from the large scale SI. This would explain why the zonal flows are that regularly spaces, as this resembles the fastest growing mode of the large-scale SI regime. Further, it might be that these modes are identical to the ones producing zonal flows in the 2-d simulations, but since an analytic solution for the 3-d SI is not derived yes, this remains speculation from the obtained data. But, if this is shown to be true, the second branch with small wavelengths, i.e. high wavenumber, state the realm from which the actively turbulent SI modes stem from that are suggested to stall particle cloud collapse.

As said, for the $\mathrm{St} = 0.01$ particles the parameter study shows the 3-d SI to mainly operate on the smallest scales. This result is not too surprising from the previous 2-d experiments. Still, the 3-d SI at $\mathrm{St} = 0.01$ seems to be even weaker than its 2-d equivalent. The peak of activity is reached at dust-to-gas ratios around unity, see the visualisation of the slice data in Fig. 6.4. On the intermediate scale, the SI modes are barely visible. But, they are present, as can be seen in the orange line of Fig. 6.1b and in the particle diffusion, see below. The achieved maximum dust densities on this intermediate scales are low, though, with values of around $\varepsilon_{\mathrm{max}}/\varepsilon_0 \approx 4$. Going to initial dust-to-gas ratios around 100, the maximum dust-to-gas ratios that are measured surprisingly increase again on all scales, but the simulation do not show any signs of SI mode patterns. From manually going through the data it can be said that these high particle concentrations come from very few dense isolated blobs that slowly form, see the timeseries of the simulations in Appendix C. Since this effect is present on all scales, it could be a numerical issue that is observed. A further investigation on the underlying process is recommended, before these values are used in any physical sense.

6.4 Particle diffusion

The particle diffusion is measured by using the prescription from Eq. (2.42). As described in Sec. 2.2.5 this treats the turbulence driven particle movement as a random walk-like process. The diffusion coefficient can be calculated from the spreading of the particle travel distance over time. The measured diffusion strength is expressed in terms of disk units, see Eq. (2.43). Fig. 6.5 presents the particle diffusion strength for both Stokes numbers (columns), and separately for radial and vertical diffusion (rows). The measured values are again compared with the values found by Johansen & Youdin (2007), where there are no values available for $\mathrm{St} = 0.01$ to compare to, hence the same reference values as for $\mathrm{St} = 0.1$ particles are plotted. The diffusion measured in the simulation with $\mathrm{St} = 0.1$, $L = 0.1$ (blue line), and $\varepsilon_0 = 1.0$ is right the value found by Johansen & Youdin (2007), though their simulation domain size is one order of magnitude larger. Hence, the driving 3-d SI modes reside on the scales covered by the large simulation of this parameter study and no stronger turbulent diffusion should be expected.

The diffusion values show the SI-active simulations to have significant particle diffusion in radial and vertical direction. For comparison, the 2-d simulations showed a maximum radial particle diffusion of $\delta_{\mathrm{x}} \approx 10^{-4}$. In the 3-d simulations the maximum radial diffusion is slightly higher than $\delta_{\mathrm{x}} \approx 10^{-5}$. Comparing the maximum dust-density fluctuations for the $\mathrm{St} = 0.01$ simulations on the intermediate and smallest scales, one finds only very small dust-density fluctuations on the intermediate scale. But, the particle diffusivity on the intermediate scale is still one order of magnitude larger than the value on the smallest scale. So, even if no strong SI is visible, the underlying particle diffusion can act stronger than one might expect.

The slopes of the measured particle diffusion are as follows. For $\mathrm{St} = 0.1$, the radial diffusivity drops with a slope of $\delta_{\mathrm{x}} \sim \varepsilon^{0.59} \ldots \varepsilon^{1.25}$, and the vertical diffusivity with $\delta_{\mathrm{z}} \sim \varepsilon^{0.32} \ldots \varepsilon^{0.83}$. The slope in the radial diffusion for the $\mathrm{St} = 0.01$ simulation is $\delta_{\mathrm{x}} \sim \varepsilon^{0.83} \ldots \varepsilon^{0.91}$, and the vertical diffusivity drops with $\delta_{\mathrm{z}} \sim \varepsilon^{0.56} \ldots \varepsilon^{0.91}$. For this estimate, only values from simulations with clear signs of SI were taken into account and outliers are ignored.

Fig. 6.6 now compares the measured radial diffusivity with the azimuthal diffusivity. Interesting to note, the simulations with active 3-d SI have around one order of magnitude larger radial diffusion than in vertical direction. For initial dust-to-gas ratios around unity, the 3-d SI on the smallest scales is even two orders of magnitude larger in radial, then in vertical direction. A consequence arises from that observation for the picture of diffusion limited collapse. The vertical direction will collapse faster than the radial direction, which might lead to interesting phenomena considering cloud collapse in 3-d, see Sec. 7.6. It has to be investigated how much stronger a radial diffusivity has to be, in order to compensate for the vertical collapse. But,

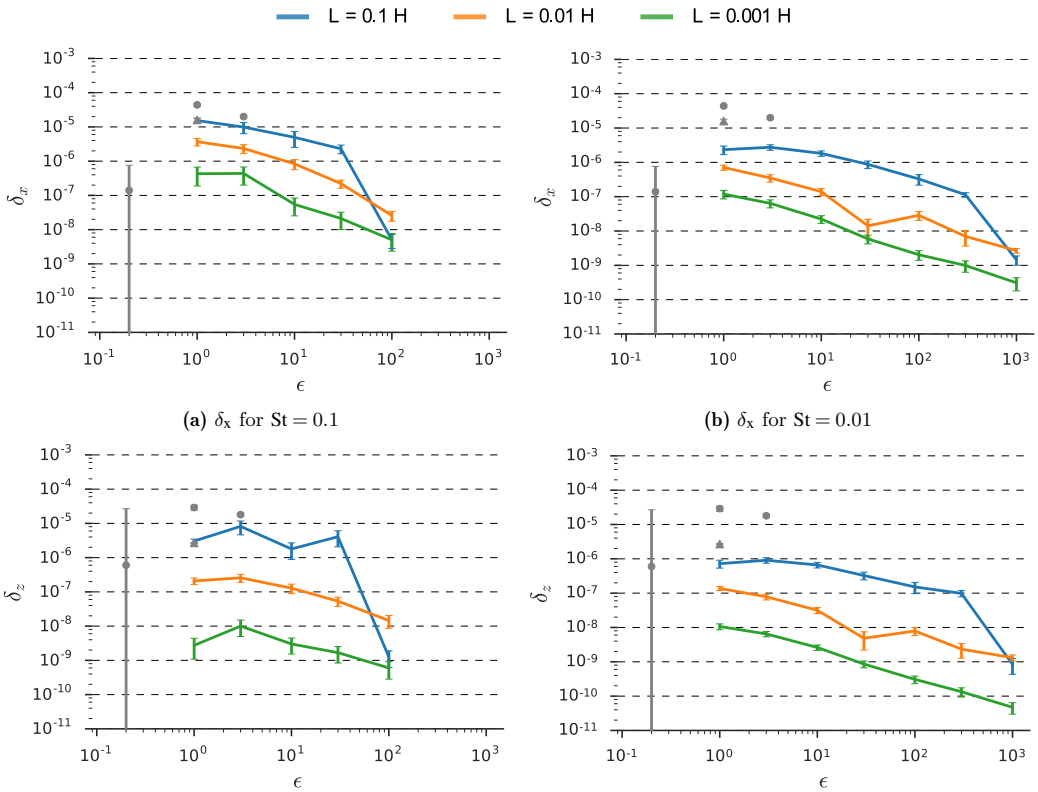

(a) δ_x for $\mathrm{St} = 0.1$

(b) δ_x for $\mathrm{St} = 0.01$

(c) δ_z for $\mathrm{St} = 0.1$

(d) δ_z for $\mathrm{St} = 0.01$

Figure 6.5: Radial (upper row) and vertical (lower row) particle diffusion for the SI with $\mathrm{St} = 0.1$ (left column) and $\mathrm{St} = 0.01$ (right column) particles. For comparison plotted in grey circles (2D) and triangle (3D) are the diffusivities for $\mathrm{St} = 0.1$ particles and $L \geq 2\mathrm{H}$, from JY07 Tab. 3. This is also the case for the right plot, where the grey dots and triangle mark the same comparison values as in the left column, for $\mathrm{St} = 0.1$ particles, since no comparison value for this smaller Stokes number is available in the literature.

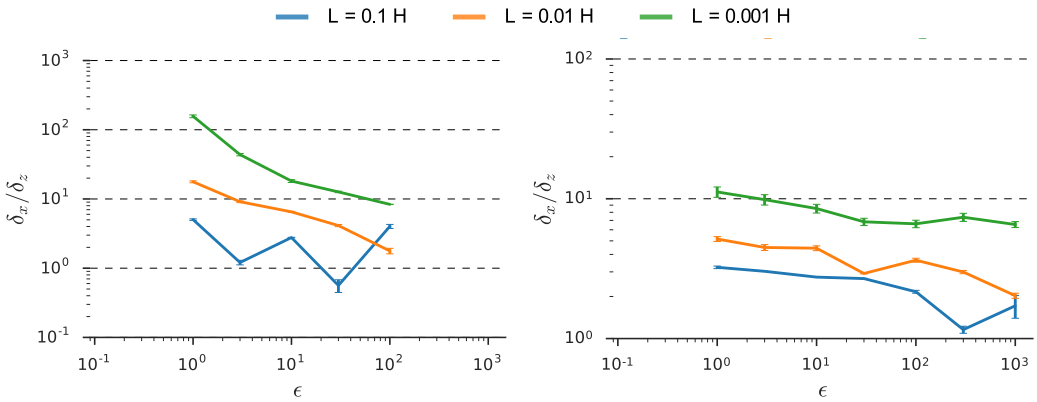

(a) St = 0.1 **(b)** St = 0.01

Figure 6.6: Comparison of radial with vertical particle diffusion from the 3-d SI runs. Left figure shows the comparison for St = 0.1, and right figure the comparison for St = 0.01. From these plots one can clearly see the radial diffusion to be much stronger than the vertical diffusion. Specially when it comes down to the smaller scales, the radial diffusion can be 10 to 100 times higher. The blue curve for the smaller Stokes number particles can be ignored, since in these simulations no SI-activity is found. The homogeneity in the mode pattern of the SI with St = 0.01 particles that could be found visually in Fig. 6.4, does not show up in the comparison of the diffusivity. The radial diffusivity is found around one order of magnitude larger throughout the parameter space.

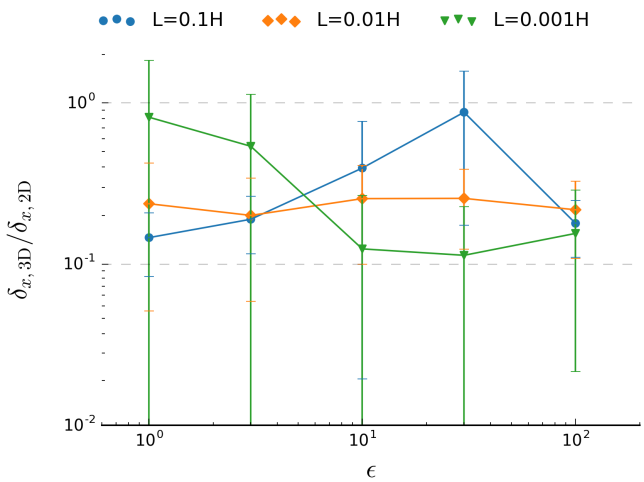

Figure 6.7: Comparison of 3-d SI with 2-d SI radial particle diffusion for St = 0.1 particles. The 2-d data is taken from the aSI simulations. On average, the diffusion is larger in 2-d than in 3-d simulations, by almost one order of magnitude. Still, some of the 3-d SI simulations at the smallest scales (green), and the one with the zonal flows on the largest scales (blue), show almost similar values in the strength of the particle diffusion. From this diagram, one can further find the slope of the decrease in the diffusion on the intermediate scales (orange) are equal in the 2-d and 3-d SI.

this comparison shall not neglect the azimuthal direction. Though in the presented parameter studies the azimuthal diffusion could not be measured, a contribution in this direction is given. The vertical collapse thus needs to actually be faster than the combined radial and azimuthal diffusion. A sophisticated model for cloud collapse is needed that accounts for all effects present at the cloud collapse state.

Lastly, a comparison of the radial particle diffusion strength from the 3-d simulations with the diffusion obtained previously in the 2-d aSI simulations, is presented in Fig. 6.7. One finds the diffusion in 3-d to be almost one order of magnitude smaller than in the 2-d aSI. Only on the smallest scales with initial dust-to-gas ratio around unity, and in the simulations with zonal flows, the diffusion in both simulations is almost equal. Hence, when using the diffusion values to estimate planetesimal sizes, the difference in the planetesimal size in 2-d and 3-d should be a factor of ≈ 2. Which is still okay, since the final planetesimal size also depends on the effectiveness of the collapse, i.e. factor q in Eq. (3.56), which probably will differ in 2-d and 3-d.

6.5 Critical length scales from the 3-d streaming instability

At very last, the diffusion values can be used to derive critical length scales for particle cloud collapse, by using Eq. (3.40). As with the planetesimal size, the critical length scale also scales with $l_c \sim \sqrt{\delta}$ and thus the critical length scale are not much different in 3-d compared with 2-d. Still, only very few parameter sets show to have critical length scales larger than the simulation domain size. This is crucial, as in the following of this thesis collapse simulations shall verify the derived diffusion limited collapse criterion. The scheme to

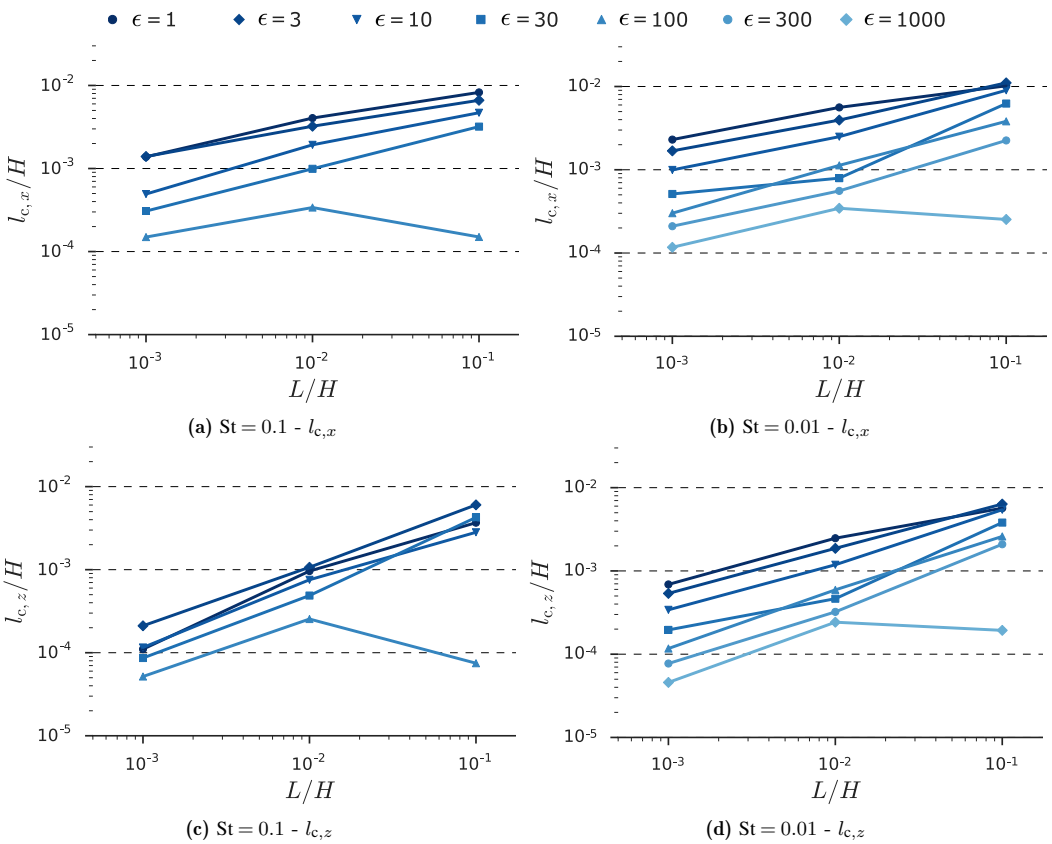

(a) St = 0.1 - $l_{c,x}$ **(b)** St = 0.01 - $l_{c,x}$

(c) St = 0.1 - $l_{c,z}$ **(d)** St = 0.01 - $l_{c,z}$

Figure 6.8: Critical length scales for particle cloud collapse as estimated by using Eq. (3.40) and the measured diffusion values for the 3-d SI.

do so, is by altering the simulation domain size around the critical collapse length scale. Only if the critical length scale is resolved within the simulation domain, collapse is allowed. Hence, the 2-d aSI simulations allowed using initial dust-to-gas ratios of $\varepsilon_0 = 3$. For collapse simulations in 3-d, it is probably saver to start with a lower value as initial dust-to-gas ratio. Later studies then can try to find the limits on the feasible parameters for such an approach.

It is interesting to note the slope of the critical length scale to be rather flat, or not steeper than unity. Hence, when interpreting the simulation domain size L as the particle cloud diameter, then there will allways be a critical size where the cloud becomes smaller than its critical wave length just from the diffusion within it. But, this interpretation is missleading, as such a particle cloud will be embedded in a larger cloud of lower dust-to-gas ratio and thus stronger turbulence. The diffusion felt by the particles in such an embedded cloud is not investigated herein, but the presented values state a minimum critical length scale.

With this, the project on investigating the SI at dust-to-gas ratios well above unity is completed and one can go over to collapse simulations that incorporate these findings.

7 Simulations on Diffusion Limited Collapse

The efforts made throughout this thesis converge in the following chapter. This chapter investigates the diffusion limited collapse criterion from Eq. (3.40) in 2-d r-φ and 3-d simulations. The way of testing the diffusion limited particle cloud collapse criterion is very similar to what has been done to validate the Jeans criterion for star formation, see the approaches in Bodenheimer (1994) and Truelove et al. (1997). In their work, they vary the simulation domain size around the critical Jeans length scale. A derivation of this length criterion can be found in Sec. 3.1.1. By altering the domain size, one alters the effective gas cloud size. The prediction on the simulatoin is thus, that the Jeans criterion predicts collapse to happen once the critical length scale is resolved within the simulation domain. Hence, one should find collapse to occur once the simulation domain size exceeds the critical Jeans scale, i.e. once the critical length scales is resolved. Smaller simulations should not show any kind of fragmentation.

The herein this project used scheme to verify the diffusion limited critical length scale l_c for particle cloud collapse is identical. One starts with choosing a computational feasible initial parameter set of particle Stokes number and initial dust-to-gas ratio. The previously performed parameter study from Chapter 5 showed which of these showed the critical length scale to be resolvable in the simulation domain. The chosen parameter set should also allow the simulation to be computed within a reasonable time frame, i.e. it is suggestive that the domain size should not undergo a size of $L \geq 0.001$. From this parameter set, a series of simulations is set up with domain sizes around the predicted value for l_c, estimated from the diffusion values from Sec. 5.2. These simulations than have to run into SI saturation, in order to have the turbulent particle diffusion and the maximum density fluctuations fully developed. Then, particle self-gravity can be switched on, with a value at Hill density, i.e. of $f = 1$. Since, the cloud density in code units is expressed via $\hat{G}$, one has to alter the gravitational code constant to a value that represents Hill density, see Eq. (4.7). Now, gravity can compete with turbulent diffusion from the SI and collapse should occur as stated by the prediction, if done right. Note that in the following the term SI is also used as a synonym for aSI. The following work is based on Klahr & Schreiber (2015) and Klahr et al. (2018) (in prep.), but extended and reworked to the presented form.

7.1 Small or large clump? The proper regime for gravitational collapse

Two different Stokes numbers are separately investigated in this collapse study project: $\mathrm{St} = 0.1$ and 0.01. These are values that are expected to be the largest sizes of grains occurring in PPDs (Birnstiel et al., 2010) and values were the turbulent diffusion strength is known from Sec. 5. As $\mathrm{St} < 1$ particles couple comparable fast onto the gas, one might ask, if in the situation of a collapsing particle cloud with dust-to-gas ratio well above unity would not drag along the underlying gas. If so, one should investigate a suspension of dust and gas that is collapsing and not treat dust as particles. In the estimate for the collapse time in Sec. 3.2 the gas is assumed to be static and hence particle in a suspension with the gas would not follow the collapse length prediction. This could further be underlined by the fact of contraction time of $\mathrm{St} = 0.01$ particles cloud is significantly larger than for $\mathrm{St} = 0.1$ particles:

$$\tau_\mathrm{c}(\mathrm{St} = 0.01) \approx 11.71\Omega^{-1} \approx 1.86 T_\mathrm{orb}$$
$$\tau_\mathrm{c}(\mathrm{St} = 0.1) \approx 1.75\Omega^{-1} \approx 0.28 T_\mathrm{orb}$$

Shi & Chiang (2013) discusses a gravitational instability criterion for such small particles that are tightly embedded into the gas. They find two cases. One, in which the sound crossing time across a self-gravitating particle cloud is longer than the stopping time ($\tau_{\rm sound} > \tau_{\rm s}$) between particles and gas, and a second case in which it is shorter. In the first case, the mixture behaves like a suspension and the clump gets stabilised by the gas cloud internal pressure gradient as the cloud is getting compressed. In this case, one has to consider the stability of the gas-dust mixture, see also Cuzzi et al. (2008). In the other extreme case, dubbed as 'small clump' regime, when the stopping time is longer than the sound crossing time ($\tau_{\rm sound} < \tau_{\rm s}$), one can neglect the effect of the gas, as its not getting compressed.

Now, considering particles with a Stokes number of $St = 0.1$ and typical dust-to-gas ratios of $\varepsilon = 3 - 100$, then for collapse the sound crossing distance can be evaluated via

$$\lambda = H \frac{St}{\sqrt{\varepsilon}} > 10^{-2} H \,,$$

see Eq. (39) in Shi & Chiang (2013). This distance is much larger than the clumps consider in the following project, as the clumps are found to have $l_{\rm c} \approx 4 \cdot 10^{-3}\,{\rm H}$, see below. Consequently, the gas can be treated as incompressible in the following considerations. In the case for the smaller particles ($St = 0.01$), one actually enters the *large clump* regime, see further analysis on the simulations in Sec. 7.4.2, as in this case the gas is found to get slightly compressed during the collapse of the particle cloud. Nevertheless, it will be shown that the diffusion limited collapse criterion still holds, though it is derived only for the 'small clump' regime.

7.2 Numerical model

The numerical model is very similar to the model used in the parameter study of the aSI/SI in Chapter 5. The difference is that now gravity is allowed, but only self-gravity. This is justified, since the stellar gravity only is a tenth of the strength of the self-gravity of a dust layer at Hill density, revisit Sec. 4.4.1. As a numerical feasible, and physically speaking not completely off value, the initial dust-to-gas ratio is chosen to be $\varepsilon_0 = 3$. The gravitational constant right at Hill density, one gets from Eq. (4.7) in code units as $\hat{G} = 0.2387$. The collapse study is performed in 2-d simulations with $\mathsf{St} = 0.1$ and 0.01, as described above. In the thereafter presented 3-d simulations use $\mathsf{St} = 0.1$ particles. In the 3-d study, not the simulation domain size but the gravitational constant was altered, as this also alters the critical length scale. The details are described in Sec. 7.6.

7.3 Effects of particle collisions during the collapse

The whole project is performed without particle-particle collisions. Firstly, this project shall show the basic principle of the critical length scale criterion to be valid. Secondly, taking collisions into account would state a need on specifying the exact particle size, and this would restrict the results onto a certain distance from the central star only. Lastly, the initial chosen parameters, e.g. ε_0, where taken from the aSI/SI parameter study from Chapter 5 which also neglected collisions. Hence, taking now collisions into account would not only undermine the goal to be achieved, but also would change the resulting particle diffusion and the collapse simulations would not be comparable to that previous result.

Still, if this decision to neglect particle collisions is justified, can be verified by estimating the collisional timescale $\tau_{\rm coll}$ and compare it to the collapse timescale from Sec. 3.2. If the collapse is fast enough, collisions will not play a driving roll. The collision time per particle is given by the particle its mean-free-path and the particle bulk rms-velocity via

$$\tau_{\rm coll} = \frac{\lambda_{\rm free}}{v_{\rm rms}} \,.$$

The mean-free-path is a function of particle number density n, of the particle size a and of their combined cross section $\sigma = 4\pi a^2$. From this, the mean-free-path can be expressed as

$$\lambda_{\rm free} = \frac{1}{4\pi n a^2} \,.$$

The particle number density n has to be calculated from the particle mass density, which is $\rho_\mathrm{d} = f\rho_\mathrm{Hill}$. The particle mass density herein gets again expressed in multiples f of the Hill density. With this, the number density becomes

$$n = \frac{f\rho_\mathrm{Hill}}{\frac{4}{3}\pi a^3 \rho_0},$$

and thus the mean-free-path is expressed by

$$\lambda_\mathrm{free} = \frac{a}{3f}\frac{\rho_0}{\rho_\mathrm{Hill}}.$$

This could be explicitly calculated if only the actual particle size would be known. As explained in the derivation of the Stokes number, this is only possible if one would define all the physical parameters entering the relation between Stokes number and particle size, i.e. stellar mass, distance to the star, density and gas temperature and lastly the porosity of the dust (Krijt et al., 2014). But, as one knows that the particle mass density equals the Hill density, or multiples f of it, plus the particle Stokes number was set to be $\mathrm{St} = 0.1$, one can further simplify things. Starting with the equation for friction in the Epstein regime, see Eq. (2.34), of

$$\mathrm{St} = \tau_\mathrm{s}\Omega = \frac{a\rho_\bullet\Omega}{\rho_\mathrm{g} c_\mathrm{s}},$$

this directly gives a particle size

$$a = \frac{H\mathrm{St}\rho_\mathrm{Hill}}{\rho_\mathrm{int}\varepsilon}.$$

Where the gas density is expressed in terms of Hill density per dust-to-gas ratio ε. Combining both expressions results in:

$$\boxed{\lambda_\mathrm{free} = \frac{H\mathrm{St}}{3f\varepsilon}} \tag{7.1}$$

With the chosen run parameters of $\varepsilon = 3$ and $\mathrm{St} = 0.1$, this relates to

$$\lambda_\mathrm{free} = \frac{0.01}{f}H. \tag{7.2}$$

Consequently, for all simulations, inside their initial homogeneous particle distribution, the mean-free-path is larger than the smallest expected critical length of $l_\mathrm{c} \simeq 0.004H$. Within late stage particle overdensities with $f \geq 10$ this now changes to $\lambda_\mathrm{free} \geq 0.001H$. Still, the length scale of the overdensity with size $l \approx 0.0001H$ is smaller.

One can conclude, for all clumps found in the following simulations the mean-free-path is equal to or larger than the clump size itself. Once the mean-free-path gets comparable to the clump size, and demanding the particle rms-speed to stay lower than the collapse velocity of the clump, than the collision timescale will still be longer as the collapse timescale.

It is therefore safe to neglect collisions in the present work. In follow up studies, one will have to treat them correctly in order to get a better understanding of the collision processes on the final outcome of planetesimals. Collisions could be responsible for e.g. multiplicity, which is the fraction of bound multi-planetesimal systems, or the spin rate, or the dust grain size structure of the final planetesimal. This derivation here is equivalent to the discussion by Youdin & Lithwick (2007).

7.4 Collapse simulations in 2-d

In two studies of 2-d simulations, the collapse of a particle cloud to a planetesimal is investigates and compared with the critical collapse length scale l_c from Eq. (3.40). The particle cloud size is equivalent

Name	L[H]	$d_{x,y}$[H]	η	$T_{max,orb}$
Ae3L002	0.02	7.81e−5	0.05	2.82
Ae3L001	0.01	3.91e−5	0.05	3.67
Ae3L0005	0.005	1.95e−5	0.05	4.24
Ae3L0005lp	0.005	1.95e−5	0.025	13.06
Ae3L0005hp	0.005	1.95e−5	0.1	32.78
Ae3L0003	0.003	1.17e−5	0.05	10.03
Ae3L0003lp	0.003	1.17e−5	0.025	14.47
Ae3L0002	0.002	7.81e−6	0.05	3.83
Ae3L0001	0.001	3.91e−6	0.05	3.50

(a) $\mathrm{St} = 0.1$ **simulations - A-runs**

Name	L[H]	$d_{x,y}$[H]	η	$T_{max,orb}$
Be3L005	0.05	1.95e−4	0.05	12.57
Be3L003	0.03	1.17e−4	0.05	26.22
Be3L002	0.02	7.81e−5	0.05	50.93
Be3L001	0.01	3.91e−5	0.05	31.83
Be3L0005	0.005	1.95e−5	0.05	16.84
Be3L0003	0.003	1.17e−5	0.05	11.58

(b) $\mathrm{St} = 0.01$ **simulations - B-runs**

Table 7.1: Initial parameters for the 2-d collapse simulations: Domain size L, grid spacing $d_{x,y}$, gas sub-Keplerianess η and maximum simulation runtime in orbits. All simulations have the same numerical resolution of 256^2 grid cells and same initial dust-to-gas ratio of $\varepsilon_0 = 3$. The physical domain size L is altered around the predicted critical length scale l_c. Self gravity is enabled at $T = 1.59 T_{orb}$ (A-run) or $T = 4.77 T_{orb}$ (B run). Additional simulations where performed with variation in the pressure gradient η, by a factor of 2 (hp = high pressure) or by a factor ½ (lp = low pressure).

by the simulation domain size, and hence simulations with domain sizes L larger than l_c are expected to collapse. This study is performed in 2-d shearing sheet simulations, similar to the ones of the previous parameter study from Chapter 5. Each simulation uses 16 CPUs in x- and 8 CPUs in y- and 1 CPU in z-direction. They evaluate a numerical grid out of 256×256×1 grid cells, and the particles therein. The runs are initiated with 10 super-particles per grid cell, thus having 655,360 particles per run. Two particles sizes, in terms of Stokes number, are used, each comes with its own set of simulations. The simulation with $\mathrm{St} = 0.1$ particles are the A-runs, and the B-runs have $\mathrm{St} = 0.01$ particles, see Tab. 7.1 for an overview over the simulation setups. The particles are initially randomly distributed, but such they match an initial average dust-to-gas ratio of $\varepsilon_0 = 3$. Both, gas and dust particle velocities are initiated in Nakagawa drag force equilibrium, see Sec. 2.2.2. As the simulation domain represents a dust particle cloud of size L, the domain size is varied around l_c, see Tab. 7.1, and simulations with domain size larger than l_c are expected to show collapse. The results confirm the l_c collapse criterion to be valid in these 2-d simulations. From reducing the problem onto two dimensions, no contradiction arises in the collapse time. As was shown in Eq. (3.33), the collapse time of a homogeneous cylinder is equal to the one of a homogeneous sphere.

All simulations start initially with gravity switched off. This ensures the SI to be saturated once gravity is turned on, i.e. the maximum turbulent strength is present before collapse is allowed. This is done by activating self-gravity after $t = 1.59$ orbits in the A-runs, and $t = 4.77$ orbits B-runs. A longer time in the B-runswas actually not needed, as the aSI grows faster at $\mathrm{St} = 0.01$, see Sec. 5.1. The gravitational constant is set such that the density in the simulation domain represents Hill density, as derived in Sec. 4.4.1.

Additionally, the impact of variations in pressure gradient η on the stability criterion is investigated. This is done in three A-run simulations with $\mathrm{St} = 0.1$ particles that are set up around $l_c \approx L$ with $2 \cdot \eta$ (hp) and $0.5 \cdot \eta$ (lp), see Tab. 7.1a.

7.4.1 Simulation results

The radial diffusivity δ_x is needed to estimate the critical length scale. The diffusion is thus measured when the SI is saturated, but before gravity is switched on, see Fig. 7.7. Fig. 7.1 shows the measured diffusivities. These measurements show an increase in diffusivity with increasing simulation domain size L. This confirms the findings from Sec. 5.2, as larger SI modes stronger diffuse the particles. Or differently, the larger SI modes get suppressed with decreasing simulation domain size. The blue lines in Fig. 7.1 are linear fits to the values simulations without a variation in the pressure gradient (circles). The measured slope p in these fits are sallow, with $p_A = 6.04 \cdot 10^{-4}$ and $p_B = 4.98 \cdot 10^{-4}$. The triangle pointing up indicates the run with double the pressure gradient (hp), triangles pointing down indicate runs with half the pressure gradient (lp).

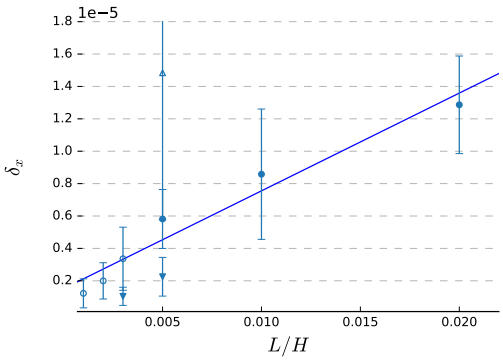

(a) $\mathrm{St} = 0.1$ **simulations - A-run**

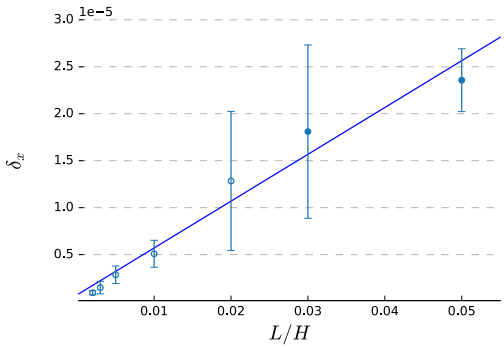

(b) $\mathrm{St} = 0.01$ **simulations - B-run**

Figure 7.1: Radial particle diffusion plotted over simulation domain size. Circles indicate unaltered runs, in terms of pressure gradient (A-run). If a symbol is filled, it marks a run in which collapse occurred. The straight line is a fit to the diffusion values of the unaltered simulations, i.e. circles. Slopes of these fits are sallow with $p_\mathrm{A} = 6.04 \cdot 10^{-4}$ and $p_\mathrm{B} = 4.98 \cdot 10^{-4}$. The triangle pointing up indicates the run with double the pressure gradient (hp), triangles pointing down indicate runs with half the pressure gradient (lp).

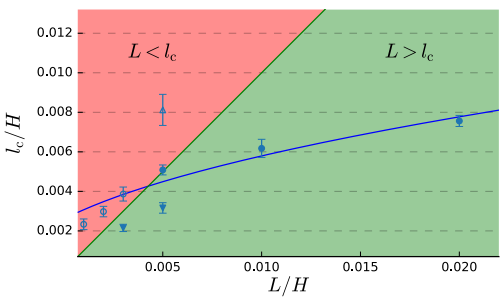

(a) A-runs with St = 0.1

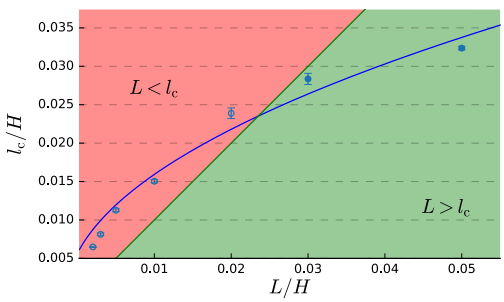

(b) B-runs with St = 0.01

Figure 7.2: Numerical results compared with the analytical predicted diffusion limited collapse criterion. With domain size L on the x-axis plotted are the individual critical length scale l_c for each simulation. This scale is determined by measuring the particle diffusivity of the SI before switching on self-gravity. The red region indicates $L < l_\mathrm{c}$ where no collapse should be possible whereas in the green region $L > l_\mathrm{c}$ collapse should occur. It has been found for $\mathrm{St} = 0.1$ and 0.01 a very good agreement between the prediction and the simulation results. Meaning, all simulations with filled symbols did collapse and lie in the green region, all the ones with open symbols did not collapse and lie in the red region. Added to this study are three additional runs right at the boarder of stability, in which the radial pressure gradient is altered. The triangle pointing upward indicates a model that was collapsing beforehand, but did not do so if the pressure gradient is doubled, the reason is the therefore induced stronger turbulence. Reversely, the downward pointing triangles indicate models with a reduced pressure gradient by a factor of two, which both collapsed.

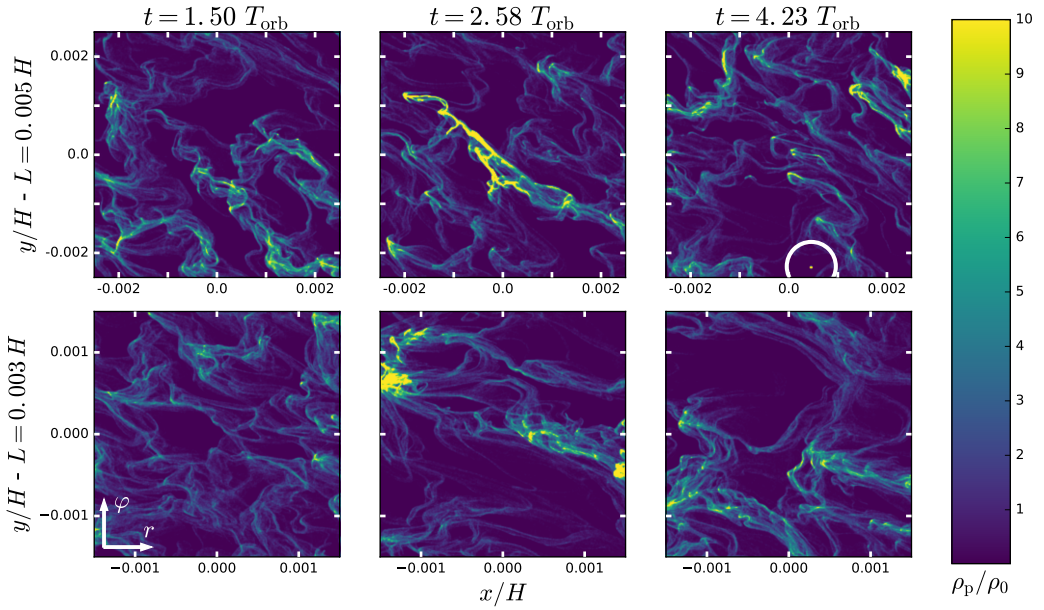

Figure 7.3: $\mathrm{St} = 0.1$**:** Particle distribution for the two simulations closest to the boarder of stability. In the two rows compared are two simulations with only slightly different box-sizes of $L = 0.005\,\mathrm{H}$ and $0.003\,\mathrm{H}$. The three columns show different time steps. From left to right, the gravity free SI in its saturation phase, the formation of a self-gravitating filament one orbit after self-gravity is switched on. The upper right picture shows the planetesimal (white cricle) that formed from the collapse of the filament (middle column), the lower instead shows the situation where the self-gravitating cloud did not collapse but dissipated. This simulation is in a steady gravitoturbulent state. The larger simulation (upper) covers the critical collapse length scale, with $L \approx 1.02 \cdot l_{\rm c}$, see Fig. 7.2a, i.e. the critical length scale is resolved. This $l_{\rm c}$ is given by the underlying turbulent diffusion as described in Sec. 3.3. Hence, the particles in the simulation are allowed to undergo gravitational collapse by self-gravity. The smaller simulation (lower) has a box size of $L \approx 1.29 \cdot l_{\rm c}$ and is consequently not allowed to collapse by the formulated critical length scale criterion. In the middle column, both simulations had an equally strong maximum in their dust density fluctuations, see Fig. 7.7 , but only the large cloud could collapse. The simulations are performed at Hill density, i.e. $f = 1$ in Eq. (4.7).

Fig. 7.2 shows the corresponding critical length scales. They are derived from the measured particle diffusivity. The blue line stems from the linear function fitted onto the diffusion data points and translated into a critical length scale. In this diagram, the unfilled symbols indicate simulations that did not collapse, the filled symbols indicate collapsed simulations. The red region marks the area, where the critical length scale is larger than the simulation domain size, where, following the $l_{\rm c}$ criterion, collapse is not allowed. The green are marks the opposite, where the critical length scales is resolved and collapse is allowed. The data points are filled symbols if the particular simulation collapsed, and unfilled if not. As can be seen, the filled symbols (collapse) all lie in the green area, whereas the unfilled symbols (no collapse) all lie in the red area. This shows for the investigated cases the diffusion limited collapse criterion to perfectly hold for both Stokes number particles.

Herein this study, the error in particle diffusivity $\Delta\delta$ is estimated by calculating the standard deviation of the diffusivity timeseries $D(t)$, see Eq. (2.43). From this, one also gets the error in the critical length scale via error propagation. The error in $l_{\rm c}$ can be calculated via

$$\Delta l_{\rm c} = \frac{2}{6} \Delta\delta \cdot \delta^{-\frac{1}{2}}\,, \tag{7.3}$$

and plotted in Fig. 7.2.

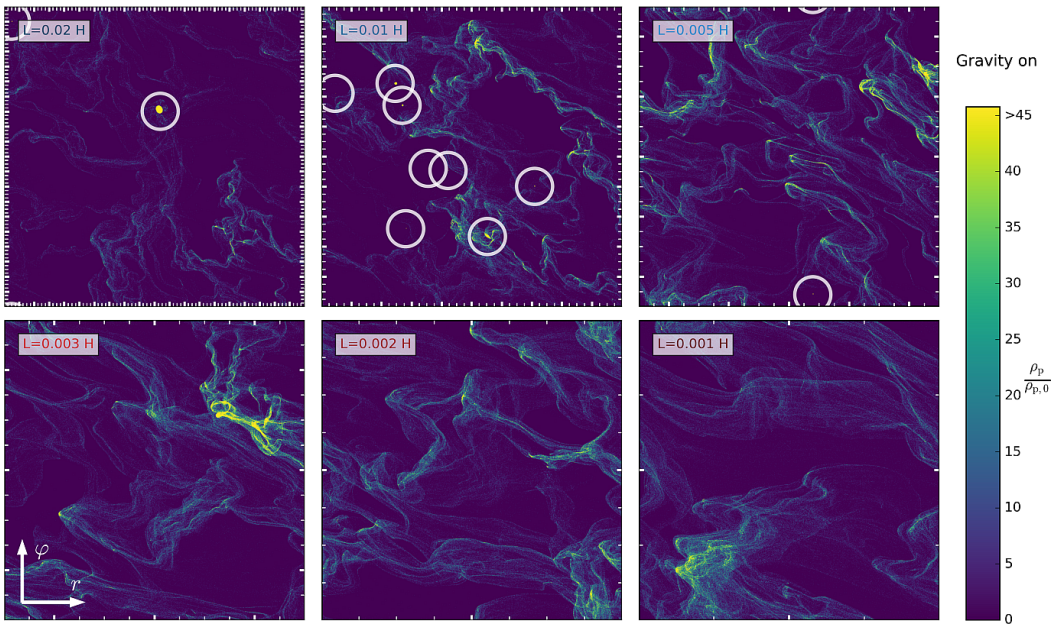

Figure 7.4: St = 0.1: Final particle concentration for all runs with fixed pressure gradient, see Tab. 7.1. In white circles highlighted are all planetesimals formed, i.e. areas with a particle concentration several hundred times higher than the mean value. Only the runs with blue-colored labels (upper row) produced planetesimals as predicted by the critical length scale criterion. In these simulations the formed planetesimals are particle clumps which stay bound together after its formation. Since each simulation is set at its critical Hill density, one would expect all runs to completely collapse to a single object. In contrast, the simulations show for clouds (i.e. simulation domain) much larger than its corresponding l_c the formation of more than one object. The runs with sizes less than its l_c (lower row) do not collapse due to the diffusion from the underlying SI. For all images the tick spacing is kept equal. The simulation with $L = 0.01\,\mathrm{H}$ produced even 8 bound objects. Also two binary objects are formed.

Results of the `A`-runs

The simulations `Ae3L0003`, `Ae3L0002`, and `Ae3L0001` are the ones not collapsing from the `A`-run parameter set. In contrast, the simulations with larger domain size `Ae3L0005`, `Ae3L001`, and `Ae3L002` did collapse. This is right as predicted by the diffusion limited collapse criterion in Sec. 3.3. The run `Ae3L0003` did not even collapse after more than 8 orbits, though it is close to the boarder of stability. Fig. 7.7a shows the timeseries of the maximum dust-to-gas ratio for all these runs. The grey area on the left marks the time range where gravity was switched off. The largest two simulations immediately collapsed after gravity was turned on. The `Ae3L0005` simulation did only collapse one orbit after self-gravity was switched on.

Hence, the collapse criterion cannot be seen as a sharp criterion, but rather as a collapse likelihood. Particle clouds close or above the critical length scale have a higher tendency to collapse. This becomes clear once one considers dust density fluctuations within the particle cloud. If the density fluctuations exceed the value stated by the criterion, they can indeed trigger collapse. With a higher likelihood in producing strong density fluctuations comes thus a higher likelihood for collapse. But, this collapse is only successful if not diffusion acts faster. This could be seen in the `Ae3L0005` run, where after the first planetesimal formed, another cloud tried unsuccessfully to collapse. The cloud is visualized under the name `e_e3L0005H_1` in the two-page planetesimal overview graphic on page 138. If one looks closely on this object, one actually finds it to have a long tail at its back and two particle outflows starting from its head. The latter come from erosion by gas ram pressure, see Fig. 7.9.

From these results, one can conclude for the considered scales the particle diffusion to act faster than

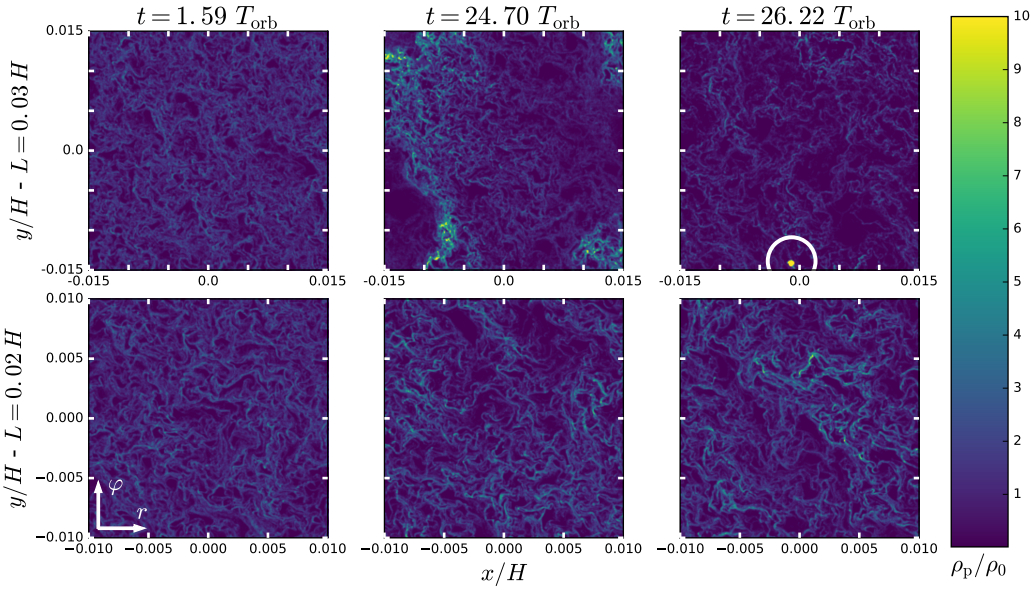

Figure 7.5: St = 0.01**:** Particle distribution for the two simulations closest to the boarder of stability. In the two rows compared are two simulations with only slightly different box-sizes of $L = 0.03\mathbf{H}$ and $0.02\mathbf{H}$. The three columns show different time steps. From left to right, the gravity free SI in its saturation phase, the formation of a self-gravitating filament one orbit after self-gravity is switched on. The upper right picture shows the planetesimal (white cricle) that formed from the collapse of the filament (middle column), the lower instead shows the situation where the self-gravitating cloud did not collapse but dissipated. This simulation is in a steady gravitoturbulent state. The larger simulation (upper) covers the critical collapse length scale, with $L \approx 1.06 \cdot l_{\rm c}$, see Fig. 7.2a, i.e. the critical length scale is resolved. This $l_{\rm c}$ is given by the underlying turbulent diffusion as described in Sec. 3.3. Hence, the particles in the simulation are allowed to undergo gravitational collapse by self-gravity. The smaller simulation (lower) has a box size of $L \approx 0.84 \cdot l_{\rm c}$ and is consequently not allowed to collapse by the formulated critical length scale criterion. All simulations of the `B`-run did not produce a clear filament, which is in contrast to the `A`-runs. The simulations are performed at Hill density, i.e. $f = 1$ in Eq. (4.7).

cloud collapse from self-gravity. Whereas in the three simulations with scales larger than $L \geq 0.005H$ 15 planetesimals formed, see section below and Tab. 7.2, the simulations with smaller domain did not produce a single one, even after many orbits with gravity switched on. The run `Ae3L0005` is found to be the smallest simulation still capable of producing a planetesimal. It is found to be right on the boarder of stability, see Fig. 7.2a. Moreover, in this run there is only one planetesimal forming, a second gets disrupted in its making. For the next larger simulation (`Ae3L001`) one can count 8 bound objects of different size, see the discussion on planetsimals below in Sec. 7.5. Four of these planetesimals are actually found to be bound in a binary system, which should get compared with the results from numerical N-body simulations in the future, such as presented in Nesvorny et al. (2010). The `Ae3L002` simulation was special, as it produced first several smaller collapsing clouds, which then collided and merged into one single object. A second planetesimal is formed in this run at later time, so in the end two planetesimals get produced of which one is extremely heavy.

Fig. 7.3 shows in two rows the time evolution of the dust density in three snapshots. The two simulations shown are the ones that are right at the boarder of stability, i.e. `Ae3L0005` (upper) and `Ae3L0003` (lower). The first column shows the SI saturated state before gravity is switched on. The measured particle diffusion is in the `Ae3L0005` simulation 1.7 times stronger, though the visual inspection shows not much of a difference in the aSI mode pattern. Also, the maximum dust-density concentrations reach identical values in both runs at a similar time, see Fig. 7.7a. The middle column of this plot shows the gravitoturbulent state of these

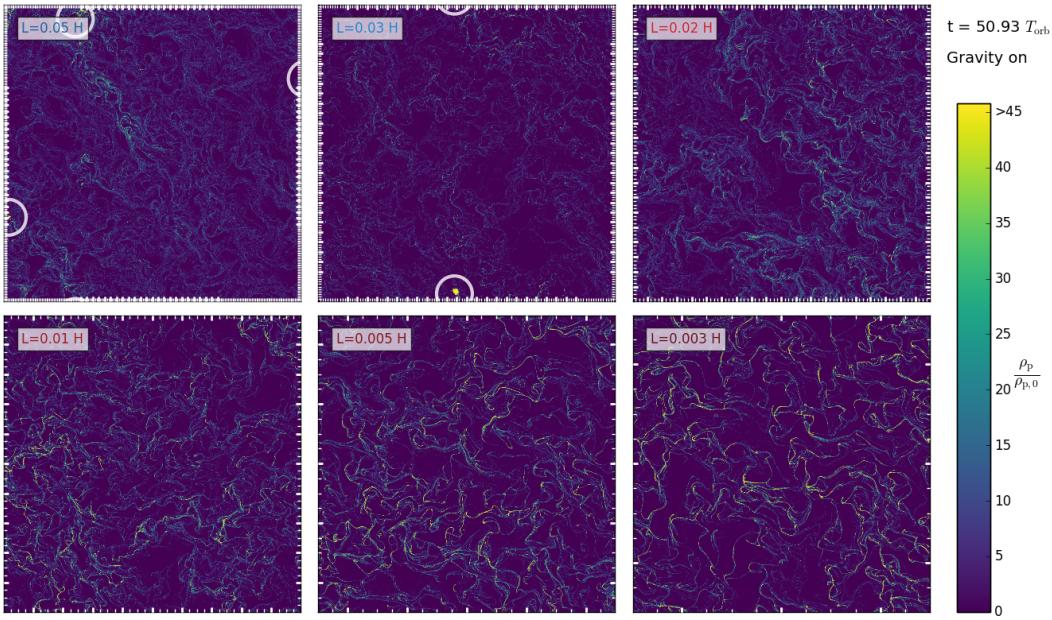

Figure 7.6: St = 0.01**:** Final particle concentration for all runs with fixed pressure gradient, see Tab. 7.1. In white circles highlighted are all planetesimals formed, i.e. areas with a particle concentration several hundred times higher than the mean value. Only the runs with blue-colored labels (upper row) produced planetesimals as predicted by the critical length scale criterion. In these simulations the formed planetesimals are particle clumps which stay bound together after its formation. Since each simulation is set at its critical Hill density, one would expect all runs to completely collapse to a single object. In contrast, the simulations show for clouds (i.e. simulation domain) much larger than its corresponding $l_{\rm c}$ the formation of more than one object. The runs with sizes less than its $l_{\rm c}$ (lower row) do not collapse due to the diffusion from the underlying SI. For all images the tick spacing is kept equal. The simulation with $L = 0.05\,\mathrm{H}$ produced 2 bound objects.

two simulations, right before the filament in the larger simulation collapses into a planetesimal. As said, in this snapshot, both simulation have an identical over density of $\varepsilon_{\rm max}/\varepsilon_0 \approx 200$, but only the larger fragment collapses. The larger simulations shows a very impressive view on the actual collapsing dust filament. In this filament reside 38.7 % of all the available particles as they try to collapse to a planetesimal. In the end, only 9.1 % of the filamentary mass gets incorporated into the final planetesimal, which is named `e_e3L0005H_0` in the following. This planetesimal then has 3.5 % of the total available mass of the simulation in it. This seems to represent only a small fraction of the total mass, but since the final planetesimal radius scales with $\sim m^{1/3}$, the radius is still around 80 km for typical solar system parameters, see the planetesimal analysis blow. The last column in this figure shows the end-state of both simulation. The larger simulation produced a single planetesimal (white circle), whereas the smaller did not.

The end-states of all simulations are compared in Fig. 7.4. From the top left to bottom right, the simulation domain size decreases. Simulation with blue title show collapse, the ones with red title do not. Already from this plot, one sees the one planetesimal in `Ae3L002` that is extremely large. This object is the combination of many fragments that formed in the dust cloud immediately after self-gravity is switched on. In contrast, the `Ae3L001` run shows a cloud of planetesimals, where also two binary systems are formed, see the intersecting white circles. The `Ae3L0005` run only produced a single planetesimal. As stated, a second collapse actually occurred but is not successful. The second collapsing cloud has only 17.7 % of the mass of the filament that in the end formed `e_e3L0005H_0`, and thus was simply to low in mass. It also shows a rather spherical shape and is thus different to the larger elongated filament. The cloud got disrupted from a combination of turbulent diffusion, a high intrinsic rms-velocity, and gas ram pressure which comes from a high radially inward drift velocity.

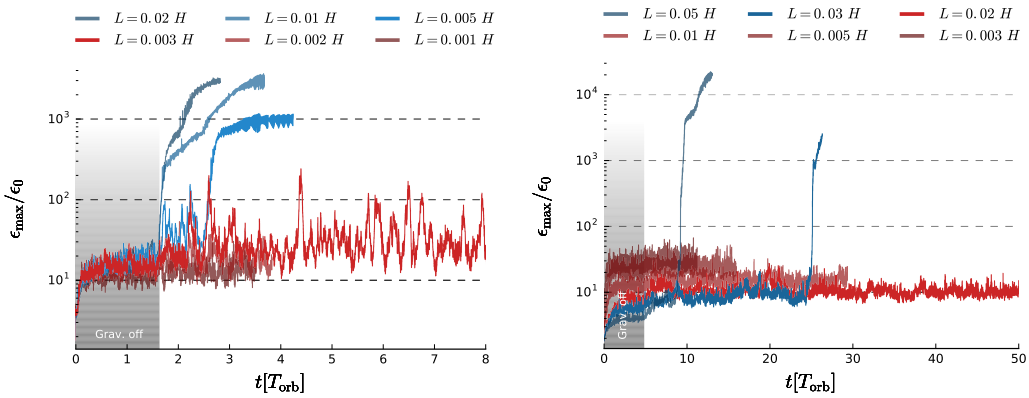

(a) A-runs with $\mathrm{St} = 0.1$ **(b)** B-runs with $\mathrm{St} = 0.01$

Figure 7.7: Time evolution of maximum dust-to-gas ratio. Simulations with $L > l_c$ are colored in blue, smaller simulations with $L < l_c$ in red. Particles self-gravity is turned on at $t = 1.59 T_{orb}$ (A-runs) and $t = 4.8 T_{orb}$ (B-runs). As a smaller Stokes number means longer collapse time (see Sec. 3.2) the simulations with $\mathrm{St} = 0.01$ takes longer to collapse. The border cases just below the instability criterion (bright red) have been running the longest to show the validity of this criterion. Additionally to the collapse, this is when the ε_{max} increases by orders of magnitude within a short time, one sees post-formation growth and merging events of this fragmented objects. The B-runs show an additional increase in maximum solid concentration due to the SI but still our criterion holds.

The simulations with an increased or decreased pressure gradient are discussed separately below in Sec. 7.4.2.

Results of the B-runs

The B-runs with $\mathrm{St} = 0.01$ particles also find agreement with the critical length scale prediction, see Fig. 7.2b. From the maximum particle density timeseries in Fig. 7.7b, one finds an overall increase in the maximum particle concentration with decreasing domain size. Interestingly, this is not sufficient to trigger cloud collapse. Hence, the collapse is determined only by resolving the critical length scale. In the B-runs, only the largest two simulation did collapse, see Fig. 7.6. The simulation right on the boarder of stability forms only a single planetesimal, though with very high mass. The largest simulation is well in the collapse regime and hence overshoots in planetesimal formation by producing two planetesimals. See the discussion on the formed planetesimals in Sec. 7.5.

Fig. 7.5 compares the time evolution of the two runs that are closest to the boarder of stability. The lower row shows the simulation with the smaller domain size that is not showing cloud collapse, the upper is the larger simulation with one planetesimal formed by collapse. The gravity-free situation in the left column now seems to be very identical in both simulations, as the mode pattern is almost indistinguishable. Comparing the situation right before collapse, middle column, the collapsing filament in the B run is now much larger and fills the whole simulation domain, which itself is also now six times larger than in the A-run. This filament then collapses again only into a single planetesimal. As the smaller simulation does not collapse, this states the diffusion limited collapse criterion to be valid for $\mathrm{St} = 0.01$ particles, too. How much these simulations benefit from being periodic in azimuthal direction and thus axisymmetric collapse is beneficial needs to be investigated in a future project. Having simulation domains with a higher aspect ratio could lead to smaller minimal planetesimal sizes as this makes axisymmetric collapse less efficient.

The final end-state of the two collapsing and four non-collapsing simulations is shown in Fig. 7.6. The simulation in the non-stable realm, i.e. Be3L005 and Be3L003, show three planetesimals to be formed in total. The simulations with domain size below the critical length scale, i.e. with $L \leq 0.02$, surprised with an increasing values in the maximum achieved dust densities, see Fig. 7.7b, but still, these enhancements do not promote collapse to a planetesimal.

Name	$N_{\rm p.}$	$\delta_{\rm x}$	$\Delta\delta_{\rm x}$	$l_{\rm c}$	$u_{\rm rms}$	$u_{\rm rms,x}$	$v_{\rm rms}$	$v_{\rm rms,x}$
Ae3L002	2	1.23e−5	4.80e−8	7.40e−3	5.77e−3	6.93e−3	4.02e−3	5.02e−3
Ae3L001	8	8.34e−6	6.94e−8	6.09e−3	4.24e−3	6.78e−3	3.05e−3	4.88e−3
Ae3L0005	1	5.86e−6	2.95e−8	5.10e−3	3.55e−3	4.39e−3	2.74e−3	3.22e−3
Ae3L0005lp	3	2.25e−6	1.19e−6	3.16e−3	2.27e−3	2.60e−3	1.79e−3	2.00e−3
Ae3L0005hp	0	1.48e−5	9.09e−6	8.12e−3	6.20e−3	8.08e−3	4.76e−3	6.44e−3
Ae3L0003	0	3.35e−6	1.95e−6	3.86e−3	2.55e−3	4.20e−3	1.71e−3	2.96e−3
Ae3L0003lp	1	1.04e−6	5.61e−7	2.15e−3	1.59e−3	2.52e−3	1.23e−3	2.07e−3
Ae3L0002	0	2.00e−6	1.58e−8	2.98e−3	1.62e−3	2.61e−3	1.34e−3	1.82e−3
Ae3L0001	0	1.31e−6	8.04e−9	2.41e−3	1.79e−3	4.56e−3	0.88e−3	2.84e−3
Be3L005	2	2.36e−5	8.25e−6	3.24e−2	5.68e−3	6.81e−3	5.53e−3	6.61e−3
Be3L003	1	1.81e−5	9.23e−6	2.84e−2	4.27e−3	5.05e−3	4.07e−3	4.83e−3
Be3L002	0	1.28e−5	7.40e−6	2.39e−2	3.97e−3	4.91e−3	3.75e−3	4.67e−3
Be3L001	0	5.09e−6	1.44e−6	1.50e−2	3.44e−3	3.54e−3	3.22e−3	3.32e−3
Be3L0005	0	2.85e−6	9.35e−7	1.13e−2	3.54e−3	3.09e−3	2.40e−3	2.88e−3
Be3L0003	0	1.49e−6	6.58e−7	8.13e−3	3.36e−3	2.77e−3	2.56e−3	2.46e−3

Table 7.2: Simulation results A-runs with $\mathrm{St} = 0.1$ particles and B-runs $\mathrm{St} = 0.01$. Diffusivities and velocities are measured by tracking the radial position of 10^4 particles for several orbits and treating it similar to a turbulence driven random walk. Diffusivity and rms-velocities are measured in the non-gravitating fully turbulent situation. The number of planetesimals $N_{\rm p}$ is the number of objects we find in our final snapshots.

Conclusions

Combining both series of simulations, one can conclude that there is not much variation allowed in the steepness of the $l_{\rm c}$ criterion in Fig. 7.2. One could for example assume the observed formation threshold to be the result of shear timescale being faster than the collapse timescale. This means that shear is the mechanism that disrupts the collapsing filaments and not diffusion. One can evaluate this by setting the diffusion timescale equal the shear timescale. The result would be a criterion like $l_{\rm c}^* = \sqrt{8/3}\sqrt{\delta}H$ that is not corre and which would also be much steeper. Hence, this is not in agreement with the observed collapse threshold.

Tab. 7.2 gives an overview over all simulation results: number of planetesimals formed $N_{\rm p}$, measured particle diffusion $\delta_{\rm x}$, the corresponding error in the diffusivity $\Delta\delta_{\rm x}$, the therefrom calculated critical length scale $l_{\rm c}$, and the rms-velocities of gas and dust. The rms-velocities are respectively given for the radial component and in the form of the absolute value. All the given rms-velocities, and the particle diffusivity, are measured before gravity was turned on and in a simulation snapshot that is fully SI turbulent. The gas rms-velocities are measured by using the grid data, particle rms-velocities by using the full particle data set. Diffusivities are calculated by tracking a set of 10^4 particles and estimating the spreading of the travel distance, see Eq. (2.42).

A further conclusion can be drawn by looking at the reached dust densities. The maximum dust densities in the fully gravitoturbulent state of the SI are well above the Hill density, see Fig. 7.7, as $\varepsilon_{\rm max} = 3$ is set by $\hat{G}$ to represent Hill density. Consequently, reaching Hill density is not sufficient for cloud collapse. Most authors in the literature use the Hill, or Roche, density, but the underlying turbulent physics in the particles were falsely neglected. One should at least take particle rms-velocities into account, see Sec. 5.2.5, if the underlying diffusion is unknown or unresolved. As long as diffusion by turbulence is faster than the collapse timescale, collapse gets unlikely.

This also stages the situation of planetesimal formation in a particle trap. A trap will slowly get filled with dust coming from the outer radii and the planetesimal will be formed right at the boarder of stability. They thus will produced one by one and probably all with a similar initial size. Hence, simulations like the one from Johansen et al. (2015) or Simon et al. (2016) do produce an overshooting in planetesimal formation, i.e. an outburst in planetesimal formation. What they thus need to do, is repeat their simulation but slowly increase the dust density until a single planetesimal forms. It is the prediction from this study that this single planetesimal then will have a size of around 100 km, if the turbulence driving length scales are resolved.

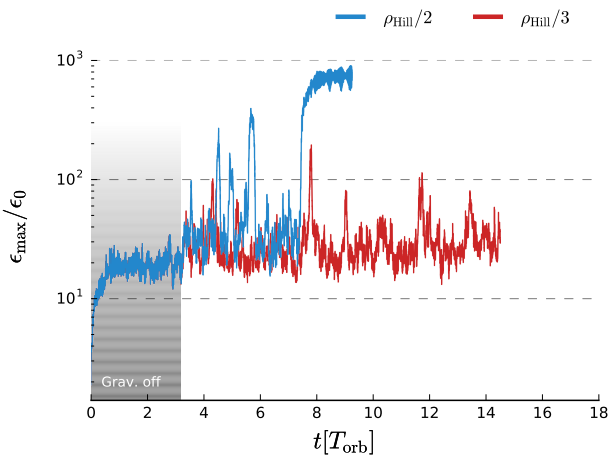

Figure 7.8: Timeseries of the maximum dust enrichment for the two runs that base on the `Ae3L001`-run, but with half (blue) and a third (red) of Hill density. The initial `Ae3L001`-run did collapse immediately when self-gravity is switched on and eight planetesimals were formed in total. Now, the run with half the Hill density does still collapse, but it takes two more orbits to collapse for the first time, though high overdensities did form already at earlier times that not finally collapsed. The run with a third of Hill density did produce over-density spikes but non of them collapsed within the 12 orbits runtime with gravity on.

Similar overshooting in dust mass and outbursts in planetesimal formation are seen in the runs `Ae3L002`, `Ae3L001`, `Be3L005`, and `Ae3L0005lp`, which one might compare these results with.

7.4.2 Further effects on planetesimal formation

Many other effects can influence the shown planetesimal formation process. Some of them are discussed in the following. One should keep in mind how new this diffusion limited collapse scenario to the community is. Many of the simulation performed in the literature simply lack the needed resolution in order to resolve l_{c}. One could thus think of a sub-grid model that includes the unresolved particle dynamics. The following discusses some more ideas that came up working with the stability criterion. Hopefully, they lead to new ideas that will further refine the presented diffusion limited collapse criterion.

Assuming critical density lies below Hill density

In Eq. (3.39) an additional degree of freedom f is added to scale the critical density for shear stability, i.e. scaling in terms of Hill density. From this followed Eq. (3.40), showing how the critical length scale is scaling with this underlying density via f. To narrow down this parameter f, two simulations with $f = 0.5$ and $f = 0.33$ where performed, based on the setup of the `Ae3L001`-run. This original run is 'super-critical', i.e. meaning in this run not one, but eight planetesimals were formed. The first collapse also occurred immediately after gravity is switched on.

The new run with $f = 0.5$ showed a delayed collapse, which took four orbits until it occurred, see Fig. 7.8. Further reducing the density scaling parameter to a factor of $f = 0.3$ leads to no collapse within 15 orbits, after which the simulation was stopped.

Going for the values for the critical length scales for that specific runs, and comparing it with the simulation domain size of $L = 0.01$, one finds for the different f values:

$$l_{\mathrm{c}}\,(f = 0.5) = 8.6 \cdot 10^{-3} < L_x \qquad \text{and} \qquad l_{\mathrm{c}}\,(f = 0.3) = 1.1 \cdot 10^{-2} > L_x\,. \tag{7.4}$$

Hence, the observed result is in very good agreement with the presented critical length scale criterion under

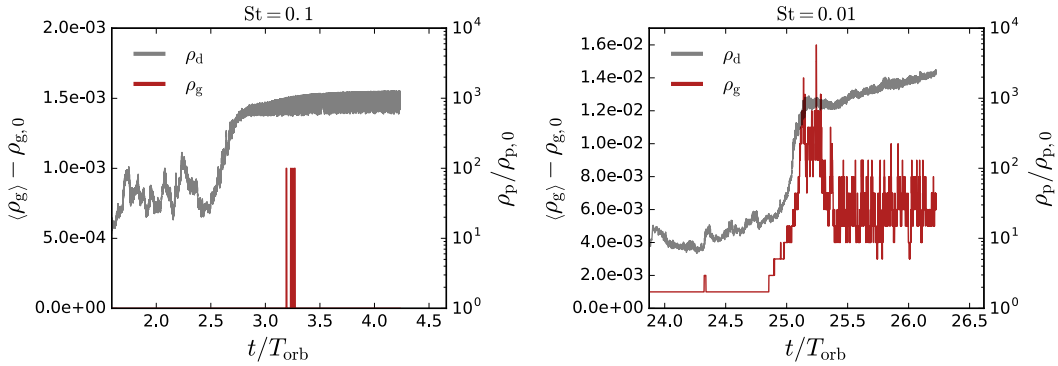

Figure 7.9: Change in gas density (red) during the collapse phase of the dust cloud (grey) for both investigated Stokes numbers. Gas density is equal to gas pressure, hence this represents a measure of how much the collapsing dust cloud is able to drag along the gas. In these figures, the last orbits of the collapse are shown. Only for $\mathrm{St} = 0.01$ a small change in gas density can be found, as the one in the run with $\mathrm{St} = 0.1$ does not correlate with the cloud collapse, but with the formation of a second cloud that radially drifts inwards and gets stripped of particles by ram pressure. From this timeseries, no hints on a strongly delayed collapse by oscillations can be found. They may remain unresolved or could be stronger present in the case of higher initial dust-to-gas ratios.

scaling with the f parameter. Moreover, whereas the `Ae3L001`-run produced 8 planetesimals, for $f = 0.5$ only a single planetesimal is formed. Still, this result is surprising, since $f < 1$ should state a non-shear stable density and no collapse should occur in any cases. The explanation for this is not final, but one it could be the density fluctuations in the simulation domain reach values which are still shear stable, i.e. $f = 0.5$ combined with the maximum dust-to-gas ratio of $\varepsilon_\mathrm{max}/\varepsilon_0 \gtrsim 10$, gives still a density higher than Hill density in certain parts of the simulation domain. Another possibility is an axisymmetric collapse that is triggered from the short azimuthal extent of the simulation domain. This would undermine the presented results and thus should be investigated in upcoming studies.

Variations in pressure gradient

Another verification of the presented numerical results was performed by doing additional simulations of the `A`-runswith variations in the pressure gradient. These simulations are marked in Tab. 7.1a with `lp` and `hp` suffix in the name, standing for *lower pressure gradient* and *higher pressure gradient* respectively. If not proven elsewise by these additional simulations, one could actually argue that the smaller simulations did not undergo collapse because the spatial resolution was simply smaller, as the number of grid cells throughout the whole study is fixed. Or, because the weaker SI is leading to lower dust density fluctuations. Both might potentially inhibit fragmentation.

Therefore, the largest non-collapsing setup (`Ae3L0003`) was taken and the pressure gradient was reduced by a factor 1/2. This led to a weaker SI and consequently weaker diffusivity, see left downward triangle in Fig. 7.1a. As result, the critical length l_c is reduced as well, now fitting again into the simulation domain, see Fig. 7.2a. The l_c prediction then expected collapse to occur, which is right what happened in the performed numerical experiment, see Fig. 7.10. This result is in good agreement with Bai & Stone (2010b), where they showed that a small pressure gradient results in a smaller particle disk scale height H_p, as the SI gets weaker in its ability to diffuse particles. The same is true here, where the now weaker radial SI turbulence can no longer prohibit the collapse.

Vice versa, increasing the pressure gradient of a collapsing case (`Ae3L0005`) does strengthen the turbulent diffusivity. Found in the simulations is collapse to become indeed stalled by diffusion. This is another confirmation for the collapse criterion, as it tests the physical effects of the particle diffusion and one does not get fooled by numerical artefacts or Keplerian shear being responsible for preventing collapse.

Furthermore, decreasing the pressure gradient in `Ae3L0005` leads again to a weaker SI turbulent strength.

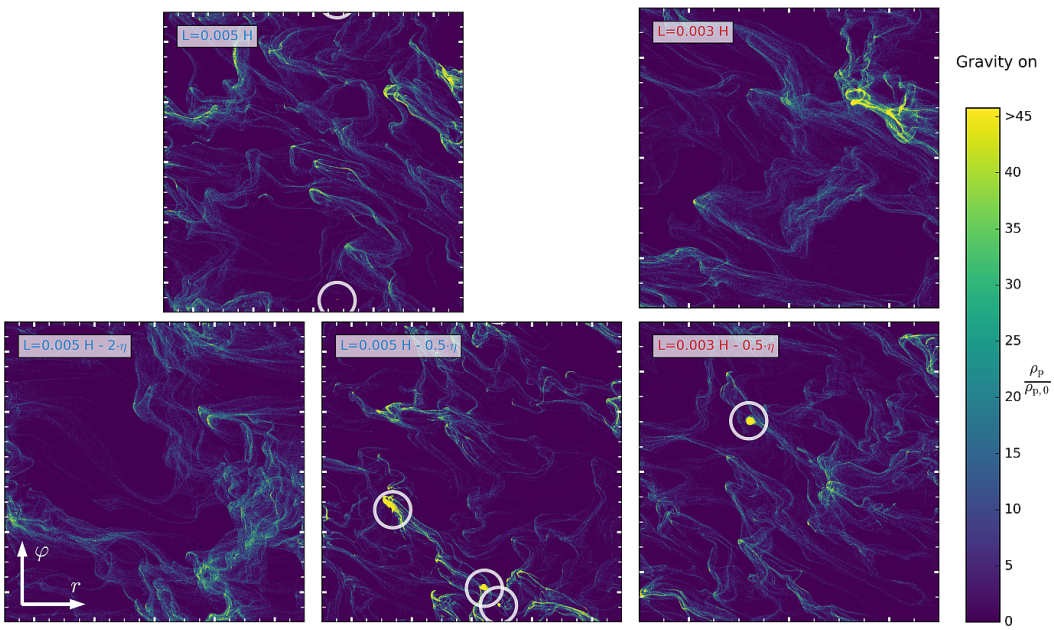

Figure 7.10: Comparison of final particle concentration for the simulations with variation in the pressure gradient strength. The upper row shows the original comparing `A`-run simulations with default pressure gradient. The lower row the two simulations with half the pressure gradient (middle and right) and the one with double the pressure gradient (left). A lower pressure gradient results in a less diffusive SI. Hence, the run $L = 0.003H$ is able to collapse. In contrast, when the pressure gradient is increased in the $L = 0.005H$ run, no collapse is found to occur anymore. This demonstrates the diffusion of the SI to be the cause of a stalled collapse and not the Keplerian shear! Hence, the criterion of being close to collapse at Hill density holds in absence of additional introduced diffusion. Moreover, for a decreasing diffusivity in the $L = 0.005H$ run found, is an increasing planetesimal formation rate, i.e. at the end of runtime this run produced three instead of only a single planetesimal. In all images the tick spacing is kept equal.

Observed for this case os collapse to occur faster, and not one, but three planetesimals were produced, see Fig. 7.10.

Building up of local gas pressure by the dust cloud collapse

The gas pressure inside the collapsing cloud might increase during the collapse phase due particle friction, dragging the gas along while collapsing. The reason is that the collapse phase is a situation of high dust concentration, meaning momentum of the dust is large, and Stokes number is lower than unity. Hence, the dust motion remains well coupled onto the gas, and the gas has to relax faster than it gets compressed by the collapsing particle cloud. Shariff, Karim and Cuzzi, Jeffrey N. (2015) describes this effect in numerical 1-d models. They claim it can lead to oscillations in cloud dust density and the forming cloud core itself. In their study, they find the oscillations to delay the collapse for a certain parameter range of initial dust-to-gas ratios from $\varepsilon = 10$ to 100.

In the herein presented simulations, the gas pressure is equal to the gas density, since the calculations are in the ideal gas limit and thus $P = c_s^2 \rho_g$. The simulations are consequently investigated for an increase in gas density that correlates with particle cloud collapse. Fig. 7.9 shows the timeseries of gas and dust density for the critical collapsing cases for both investigates Stokes numbers, i.e. the runs `Ae3L0005` and `Be3L003`. For $\mathrm{St} = 0.1$ basically no change in gas density could be observed and the strongest change in gas density is happening far after the planetesimal has formed. This increase in dust density has been found to correlate with the formation of a second unsuccessfully collapsing particle cloud that feels gas ram pressure as it rapidly drifts inwards, see section below. For $\mathrm{St} = 0.01$ found is indeed a correlated increasing in gas pressure, being slowly build up while the dust cloud is collapsing. But, the change in pressure is with $\Delta p \approx 0.01$ rather small. Consequently, one can assume to not be in the suspension regime. If the increase in gas pressure might has an influence at unresolved scales should be subject to further studies with higher resolution. Still, the found oscillations of the bound particle cloud probably will not prevent a final collapse and the found results in the planetesimals holds.

7.5 Properties of the formed planetesimals

Within the 15 presented 2-d simulations, seven of them produced planetesimals, here leaving out the simulations with altered density parameter f as no diagnostics has been performed in them, yet. In total, 18 planetesimals of different sizes were formed and analysed. Part of the analysis, the visualization tool *UnShear* and some of the plots are from the co-author paper Müller et al., 2018. By planetesimal meant in the following is a gravitationally bound, mostly spherical particle cloud that stays bound for the rest of the simulation duration. It is not necessarily a planetesimal in the actual sense, since the numerical resolution does not allow for following the further evolution of the bound particle sphere. In the simulations, these planetesimals come in very different shapes and sizes, see the large overview graphic on page 138f. The overview graphic shows not the clouds to scale, as they appear in the simulations, but scaled to their final planetesimal size, as calculated below. This size is basically proportional to the square root of the total number of particles bound to it. If one would scale the clouds by their actual diameter as one would get them from the simulations, see Tab. 7.3, the largest object would be 10^4 times larger than the smallest one. As the further compactification of these objects is unresolved, they mark a perfect start for further analysis in smooth particle hydrodynamics and N-body simulations.

The overview graphic shows the variety of shapes of the found planetesimals. Some are rather isotropic, some show clear spirals, and substructures, i.e. up-winded structures that steam from the SI mode pattern in the collapse phase. These structure indicate a slow collapse in which the cloud internal pattern remains throughout the collapse, whereas other planetesimals clearly got homogenized. The largest planetesimal are found specially for the $\mathrm{St} = 0.01$ particle simulations (`B`-runs), but also one is found in the `Ae3L002` run, which marks the largest simulations with $\mathrm{St} = 0.1$ particles. The smallest planetesimal are found for the simulations that are right at the boarder of criticality, see Sec. 3.3.1.

Tab. 7.3 gives an overview of all produced planetesimals. It shows the width of the particle cloud which has been identified as being the planetesimal. The particles that belong to a planetesimal are marked by hand in the specially for this simulations developed tool UnShear[6] (Müller et al., 2018). Therefore, particles

[6] Thank you, Thomas Müller, for developing this unique tool!

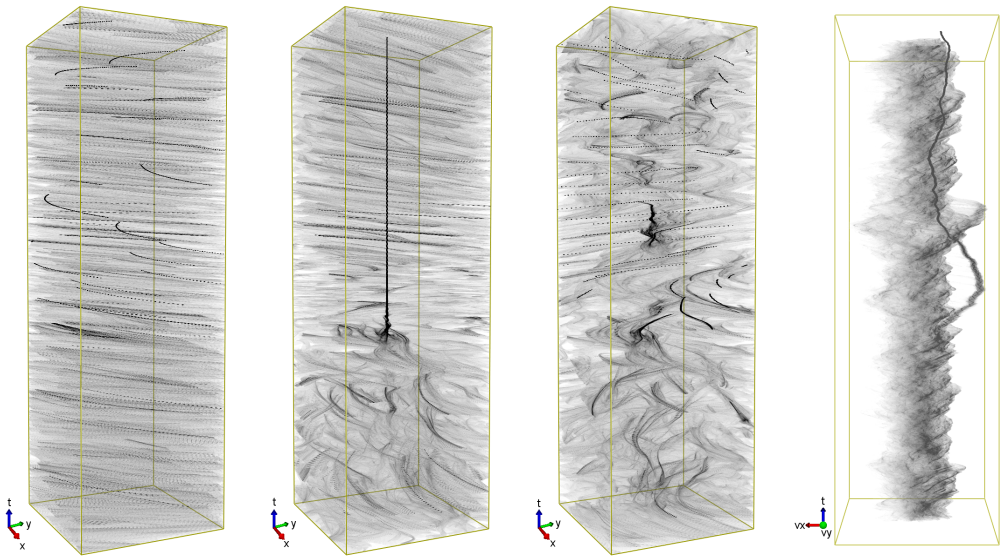

(a) standard view **(b)** centered around p1 **(c)** centered around p2 **(d)** velocity

Figure 7.11: Maximum intensity projection rendering of space-time stacks for the simulation `e3L0005H`, the bottom of this view marks the time where gravity is switched on. (a) The standard view on the domain does not show clear the structures of the forming planetesimal, nor the particle cloud collapse. (b) The view is centred around the main planetesimal `e_e3L0005H_0` now clearly shows the formation process. (c) Centred view around a particle of a second collapsing cloud that does not succeed in staying bound, `e_e3L0005H_1`, see planetesimal overview graphic. (d) Stacked view of the sheer-free particle velocities. Here, the main planetesimal clearly separates from the aSI turbulent particle ensemble, and undergoes radial inward migration. This migration slows down with time and the planetesimal enters a circular orbit. It reaches nearly Keplerian orbital velocity and by that lies ahead of the underlying particles cloud in the velocity digram. The non-collapsing particle cloud can be seen as a finger-shaped filament in the velocity-time stack. From this one sees that the rms-velocity is much higher than it was in the successfully collapsing cloud before. This explains why collapse is not possible. *Thanks to Thomas Müller for the support with this work.* (Müller et al., 2018)

where selected by being closely packed in the velocity space and bound over time in the position space. In order to measure the final planetesimal shape, a 2-d Gaussian is fitted by means of two standard deviations. The longer side, gives the planetesimal width, as shown in Tab. 7.3 together with its its aspect ratio. This value can then be compared to the numerical grid resolution $\mathrm{d}x$, which is additionally shown in the table. Note that the particle cloud width is measured in the simulation end-state for all planetesimal, and their size might already shrank over time, as they loose spin due to friction with the gas. By counting the number of bound particles within the planetesimal and dividing it by the total number of particles, the dust mass fraction κ incorporated into the planetesimal is estimated. This mass fraction κ is not equal to the collapse efficiency q from Eq. (3.56), which compares the mass of the planetesimal with the mass of its original cloud.

The spin l is a measure of the specific angular momentum of a planetesimal. It is calculated via

$$l = \sum_i \left(r_{y,i} v_{x,i} - r_{x,i} v_{y,i}\right) ,$$

which then is directly used to calculate the rotational frequency ω via

$$\omega = \frac{l}{r_i^2} .$$

Here, r_i is the absolute distance from the planetesimal center-of-mass to its particle i, with its velocity $\vec{v}_i$.

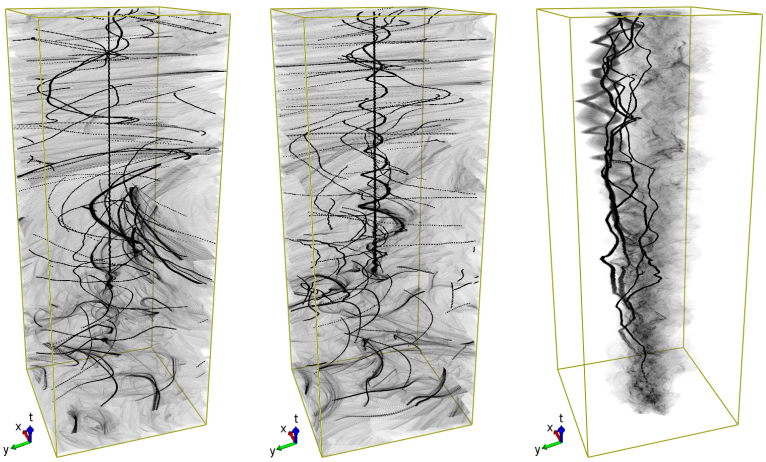

(a) Single planetesimal **(b)** Binary system **(c)** velocity

Figure 7.12: Maximum intensity projection rendered space-time stacks centred around different planetesimals from simulation `Ae3L001H`. (a) a planetesimal and (b) a different planetesimal that is bound in a binary system, see spiral black line around the central line of the planetesimal in focus. (c) shows the velocity of all particles. Specially prominent are the eight black lines of produced the planetesimals. The shown timesteps range from the activation time of gravity at $N = 1000$ up to $N = 2307$. *Thanks to Thomas Müller for the support with this work.* (Müller et al., 2018)

Note again that the spin is measured for all planetesimals in the final snapshot of the simulation and by that time they already might have lost some angular momentum via friction with the underlying gas.

The final planetesimal size a_c is an estimate that relies on assumptions on the PPD it is forming in. By that it depends on the parameters of the central star. It is derived from the mass fraction inside of the planetesimal $\kappa = m_c/M_{tot}$, by assuming the final planetesimal to be a sphere of density $\rho_\bullet$ and set the total mass equal to the planetesimal mass from the simulation:

$$\frac{4}{3}\pi a_c^3 \rho_\bullet = \kappa \rho_{Hill} \cdot L_x L_y L_z = \kappa \rho_{Hill} L^3 .$$

Where the total mass within the simulation domain has been used, as $\rho_{Hill} L^3$. Solving this equation for the planetesimal diameter yields

$$a_c = \sqrt[3]{\frac{9\rho_\odot}{4\pi\rho_\bullet}} R_\odot \sqrt[3]{\kappa} \frac{L}{R},$$

where the ratio of L/H indirectly expresses the H/R ratio together with the simulation domain size.

These final planetesimal sizes are of major interest, as they directly can be compared with the observations of planetesimals in our solar system and they can directly be used in planetesimal models in protoplanetary disk simulations and planet synthesize codes. Hence, Fig. 7.14 gives an overview over the formed planetesimals in four histograms that highlight different formation scenarios. In these diagrams, the grey bars in the background resemble the total of all 18 planetesimals, binned by size. Subplot 7.14a shows the planetesimals that formed in `e_e3L001H`, which is a run that produced more than one planetesimal. It thus can be compared to Johansen et al. (2015) and Simon et al. (2016), in which also an outburst of planetesimals was recorded. Though, the for this work interesting simulations are the ones right at the boarder of stability, shown in subplot 7.14b. They now can be compared with observation data, if one accaptes the fact that the main belt asteroids and KBOs stem from a process that produced them right at the cloud stability threshold of planetesimal formation. The work by Delbo et al. (2017) actually found the main belt asteroids to initially have had a Gaussian distribution in their size, with a characteristic size of 80 to 85 km and a Gaussian width

name	width in H	dx in H	w/h	κ	spin	ω	binary	a_c in km
b_e3L003_0	54.93e−5	11.72e−5	0.91	43.3 %	8.3e−1	85.3	-	1005.9
b_e3L005_0	13.39e−5	19.53e−5	0.66	0.5 %	−2.25e−5	−2311.2	-	366.5
b_e3L005_1	29.38e−5	19.53e−5	0.73	3.4 %	−7.47e−3	−42.7	-	716.7
e_e3L0005H_0	0.66e−5	1.95e−5	0.87	3.5 %	−1.30e−7	58.0	-	72.5
e_e3L001H_0	1.39e−5	3.91e−5	0.91	2.9 %	−1.18e−6	48.1	-	136.2
e_e3L001H_1	0.31e−5	3.91e−5	0.36	1.5 %	2.94e−7	−691.8	2	110.4
e_e3L001H_2	3.98e−5	3.91e−5	0.78	7.3 %	−2.42e−4	−43.2	1	185.8
e_e3L001H_3	0.42e−5	3.91e−5	0.78	2.0 %	7.41e−7	177.5	-	119.6
e_e3L001H_4	6.47e−5	3.91e−5	0.86	14.3 %	−1.50e−5	12.1	5	231.6
e_e3L001H_5	0.58e−5	3.91e−5	0.73	2.4 %	2.29e−6	−547.7	4	127.9
e_e3L001H_6	0.19e−5	3.91e−5	0.20	1.2 %	7.95e−9	3882.9	-	102.5
e_e3L001H_7	10.16e−5	3.91e−5	0.56	4.4 %	4.56e−4	23.5	-	156.5
e_e3L002H_0	49.79e−5	7.81e−5	0.64	66.6 %	−6.47e−1	−78.5	-	774.0
e_e3L002H_1	3.62e−5	7.81e−5	0.63	2.8 %	2.87e−5	661.4	-	270.4
lp_e3L0003H_0	6.17e−5	1.17e−5	0.91	17.3 %	6.64e−4	28.1	-	74.0
lp_e3L0005H_0	8.93e−5	1.95e−5	0.76	8.6 %	−4.84e−4	−31.3	1	97.9
lp_e3L0005H_1	4.12e−5	1.95e−5	0.70	1.8 %	1.31e−5	8.2	0	58.3
lp_e3L0005H_2	24.10e−5	1.95e−5	0.41	4.9 %	9.88e−4	−0.5	-	81.3

Table 7.3: Overview of planetesimal properties from the 2-d simulations, measured in the simulation end-state. The particle that belong to a planetesimal are marked by hand in the UnShear tool, developed by Thomas Müller. The numbering of the planetesimals does not indicate the birth order. The planetesimal width is estimated by fitting a 2-d Gaussian to the particle point cloud and taking its semi-major axes. In order to compare this value with the numerical resolution of the respective run, the grid scale dx is listed, too. The planetesimal aspect ratio w/h indicates if the object has a spherical shape. Most of them are spherical to a good degree, though the simulation runtime is too short to guarantee this to be the final value. The mass fraction κ indicates the percentage of all the available mass that ended into the object. The spin gives the specific angular momentum. When the object is in a bound binary system, the partner is written by its number in that column. The planetesimal size is calculated as derived in the text, and the value is based on typical parameters for the early solar system.

of 45 km. This falls in very good engagement with the resulting planetesimal sizes for the $\mathrm{St} = 0.1$ particle simulations, though many of the produced planetesimals are still larger than what is found for the initial main belt asteroids. This is not too surprising, since the presented simulations are 2-d and have parameters that are not right what can be expected for the solar nebular, i.e. dust-to-gas ratio will not have been $\varepsilon = 3$.

In the info graphic on page 138 shown is also `e_e3L0005_1`, which is not a planetesimal, but a collapsing cloud with a short time stability. It can also be seen in the stacked view plot in Fig. 7.11c, and as a *finger* in the stacked view on the particle velocity in Fig. 7.11d. This self-gravitating clump desolves quickly by gas ram pressure, as can be seen in a time-correlated increase in gas density in Fig. 7.9.

The planetesimals from the `A`-runs were taken for a deeper analysis in their simulation domain. A problem that arises is the shearing sheet domain, in which the formation of the planetesimal cannot easily be followed up, as it multiple times crosses the shearing sheet boundary. This induces a time depended offset and a shift in the relative velocity, so that a coordinate transformation into the planetesimal frame of reference was wishful, as well as into a global frame of reference. This side-project was carried out with the support of the intern-student *Patrick Quicker* and the visualization assistant *Thomas Müller*. Fig. 7.11 shows the simulation `e_e3L0005_0` once in the shearing sheet frame (a), in the frame of reference of the forming planetesimal (b), in the frame of reference of the short time existing second self-gravitation clump, and in (d) the shear-substracted velocity field. The time evolution of the collapsing filament from Fig. 7.3 can now be followed up in this still image. The filament has been found to only partly collapse, explaining why only $\approx 10\,\%$ of the filament mass ends in the planetesimal. The environment of the collapse is still highly turbulent and second, the moment the planetesimal is born it starts to radially drift inwards, and accelerate in azimuthal direction, see (d) of this figure. Hence, the planetesimal moves out of the collapsing

Figure 7.13: Drift trajectory of the planetesimal `e_e3L002H_0` after its birth in radial (x) and azimuthal (y) direction. The planetesimal is followed over many simulation domain length, as it drifts radially inward. In the PencilCode, when the planetesimal is jumping over the radial domain boundary, the planetesimal enters the domain again on the opposite side, but shifted by the shear length and corrected in velocity. In this picture now the planetesimal is followed over the boundary by now shifting the simulation domain by the respective distance such that it looks like the planetesimal can leave the simulation domain and enter the radially next one. Counting the number of simulation domains that the planetesimal is traveling through, one ends with a travel distance of 3.5 simulation domains. Since each simulation domain is $0.02\,\mathrm{H}$ in size, this translates into an radial drift of $0.07\,\mathrm{H}$. For a disk with aspect ratio $h = 0.04$, this translates into a drift distance of 0.3 % of its birth radius. This figure is not necessarily the ground truth, but suggest that further analysis of the drift distance after birth is needed.

filament and stalls the mass supply by the filament. The second clump that finally not collapses, shows in subplot 7.11c its short appearance. The collapsing filament shows to be smaller and short-lived, explaining the low mass in this clump. This clump than also immediately starts to drift inwards. This is seen in (d) in the form of the upper finger to the right (radially inward). This velocity plot also shows a significant larger rms-velocity within this clump, i.e. the finger that resembles this clump in velocity space is comparable more extent. But it is also the gas ram pressure, compare with Fig. 7.9, disrupting the clump. This can be seen in the overview from page 138 as a long tail to the back and two tails starting from the head of the clump. Since only 3 % of the total mass was incorporated into the planetesimal `e_e3L0005_0`, it is understandable for the simulation to undergo collapse again. From the stability criterion perspective, it is not too uprising to find this second collapse to not be successful. If not over a longer time a second planetesimal could actually form, needs to be shown in future work.

One might see `e_e3L0005_0` as an archetype of a planetesimal, as it formed not only right on the stability threshold, but also resembles a planetesimal size that is expected for asteroid main belt objects to be their initial size. Hence, the planetesimal is followed in its first few orbits in Fig. 7.15. The figure shows the rms-velocity in the clump (top left), the rotational period ω, the velocity of the centre of mass in radial (vx) and azimuthal direction (vy), the squared distance from the centre of mass `sigmax`, and a quantity that resembles the flatness of the object, which is `sigmax/vrms`. The plot of `sigmax` shows the planetesimal to be initially spread out over $2 \cdot 10^{-3}\,\mathrm{H}$, but than the collapse starts at $t = 1500$ and the planetesimal forms as an object with lower than $10^{-5}\,\mathrm{H}$ in size. The planetesimal is found to radially migrate inwards during the collapse phase and its first orbits of existence. During this period the planetesimal increases its azimuthal velocity until it reaches Keplerian velocity. The diagram of the azimuthal velocity shows many smaller jumps which come from the velocity correction when passing over the radial shearing sheet boundary condition. The particle rms-velocity is found to approach zero, i.e. the particles that resemble this object gain an ordered rotational motion around the centre of mass. With this rotation the planetesimal rotates 50 times per orbital revolution around its rotational axis.

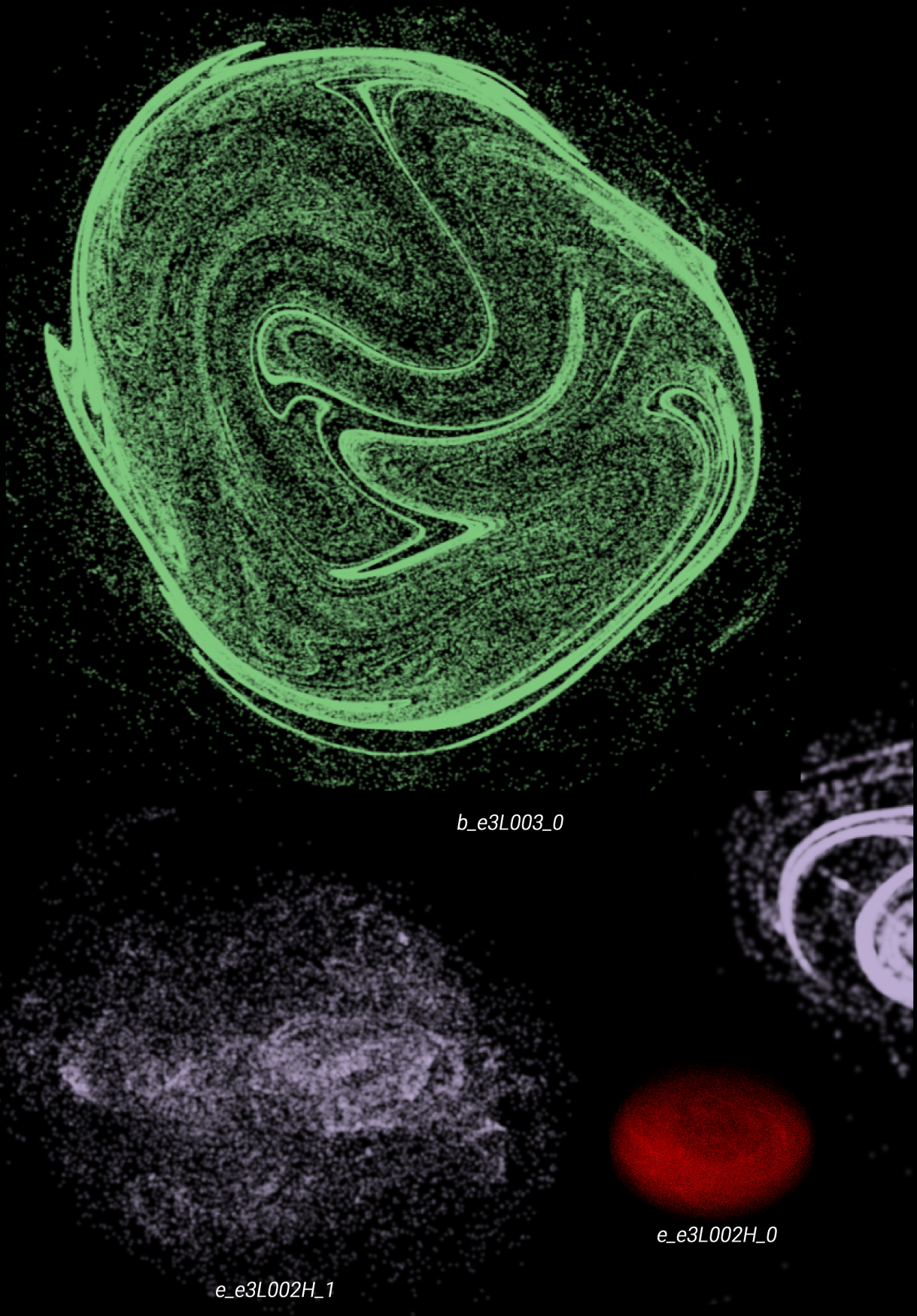
b_e3L003_0
e_e3L002H_0
e_e3L002H_1

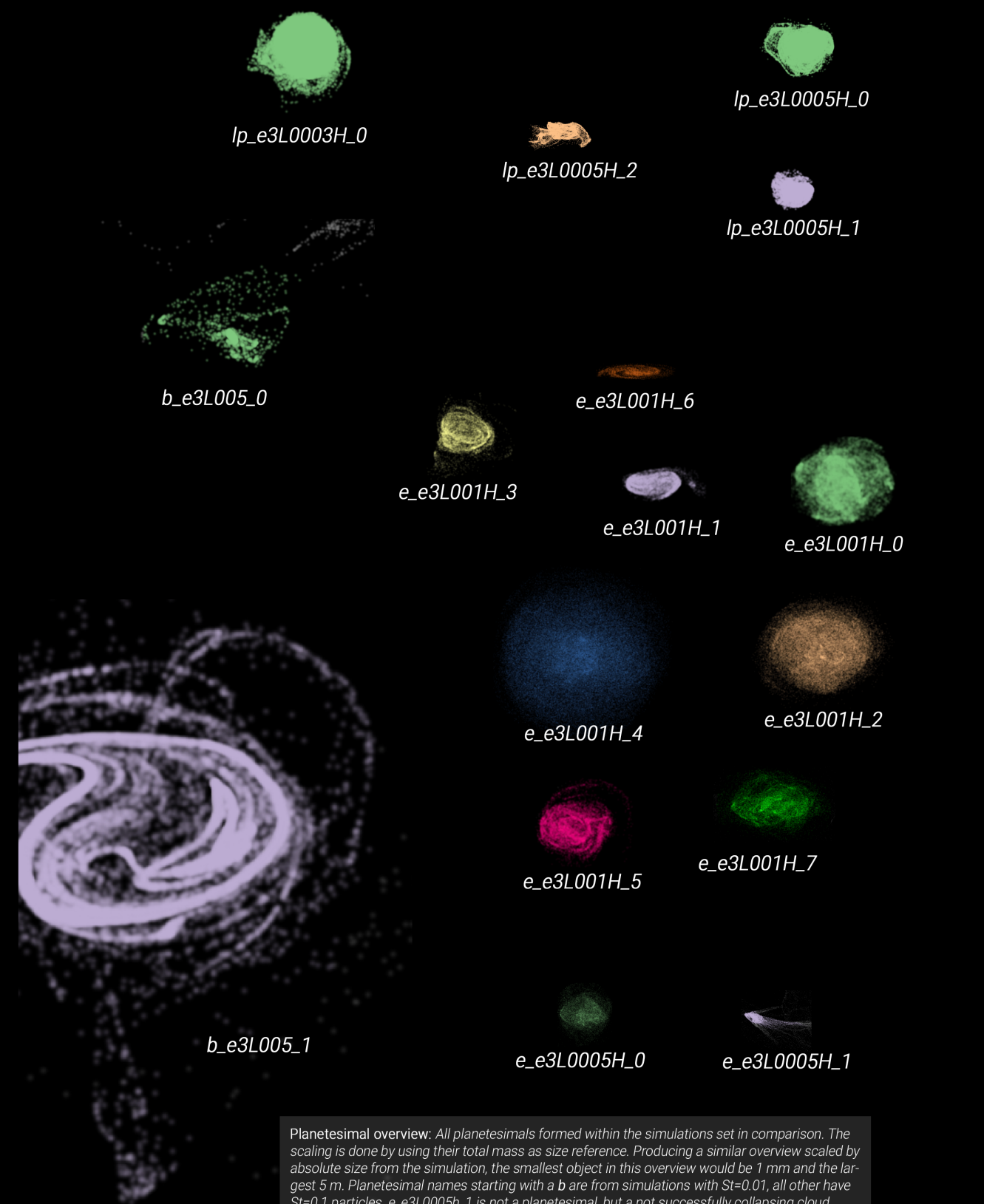

Planetesimal overview: *All planetesimals formed within the simulations set in comparison. The scaling is done by using their total mass as size reference. Producing a similar overview scaled by absolute size from the simulation, the smallest object in this overview would be 1 mm and the largest 5 m. Planetesimal names starting with a* ***b*** *are from simulations with St=0.01, all other have St=0.1 particles. e_e3L0005h_1 is not a planetesimal, but a not successfully collapsing cloud.*

As found in the previous section, the simulation `Ae3L001H` has the largest outburst in planetesimal formation with 8 planetesimals formed in total. Fig. 7.12 shows centered views on two of these planetesimals. In Fig. 7.12a one sees that is hard to entangle the dynamics of these objects, still the formation in a small filament can be identified and a lot of planetesimals that pass by and interact gravitationally. In the top left of this image two curly lines can be found that resemble a binary system of planetesimals. Changing into this binary system give Fig. 7.12b, where one can find the binary system to not come from a capturing event, but from a single collapsing filament. Which is something very hard to spot in a simple video analysis. The velocity diagram in Fig. 7.12c reveals that all planetesimals initially drift inwards, but the mutual interaction deflects them so their trajectory is hard to follow. This diagram shows a lot of kinks the come right from these gravitational interactions. Still, all the planetesimals try to take the velocity space volume with very low inward drift velocity and Keplerian azimuthal velocity. The variety in the formed planetesimals is astonishing, as they all have different sizes, but only one would be larger than 200 km in our solar nebula. Still, some of them rotate very fast, i.e. `e_e3L001_6` with an additionally weirdly low aspect ratio, small size, and hence small spin. This simulation also is special, as it produced two binary systems.

The run `Ae3L002H` was further used to study the initial planetesimal behaviour. This run produced the objects, `e_e3L002_0` a very massive planetesimal which is a merger product of many clumps that formed during the collapse. And `e_e3L002_1` is comparable to the planetesimals from the smaller simulations sizes. `e_e3L002_0` was followed during its formation and lifetime in a global reference view. This is shown in Fig. 7.13 in a diagram with radial (x) and azimuthal y direction, where once the target jumps of a boundary, the simulation domain was shifted and distorted accordingly to the Keplerian shear as if the planetesimal could leave the simulation domain and as if one could follow its path through the PPD. The formation of this object happened in an extended cloud in the top right corner. The simulation domain size is still visible in the quadratic boxes within this plot, and since the box size is 0.02 H, one can conclude the collapsing cloud in this simulation to be larger than 0.01 H. But one also sees this cloud to collapse into many objects that then merge into what is called planetesimal `e_e3L002_0`. The formed planetesimal then quickly leaves its formation cloud and drifts inwards over a time. The drift distance here is around four simulation domain sizes, hence $\approx 0.08\,\mathrm{H}$. Then the planetesimal has readjusted to the Keplerian velocity and the planetesimal starts to orbit the central star.

Discussion on the initial mass function

These results now give a new impression on the simulations that have been performed by Johansen et al. (2015) and Simon et al. (2016). In their work they derived an initial mass and size distribution for planetesimals as being a power spectrum, with lower end close to 100 km. From the interpretation of overshooting planetesimal formation in this work, their simulation results are not too surprising. One, they still lack the needed resolution for diffusion limited collapse, and two, their simulation are brought to fast into a high dust-to-gas ratio regime. Due to the too high dust load they observe the collapse not to happen at the boarder of stability, but well in the unstable regime. The presented work finds already by a slight overshooting in dust mass the formation of a cluster of planetesimals or very massive planetesimals. It is thus highly recommended repeating the simulations from Johansen et al. (2015) and Simon et al. (2016), but with a much slower increase in dust-to-gas ratio. Then the collapse should only happen at the boarder of stability and the resulting planetesimal sizes can get directly compared to the analytic prediction from the diffusion limited collapse criterion. Hence, it is the prediction from this work that the initial size function is not a power law (Hopkins, 2016), but a narrow Gaussian around a mean size of 80 km in diameter.

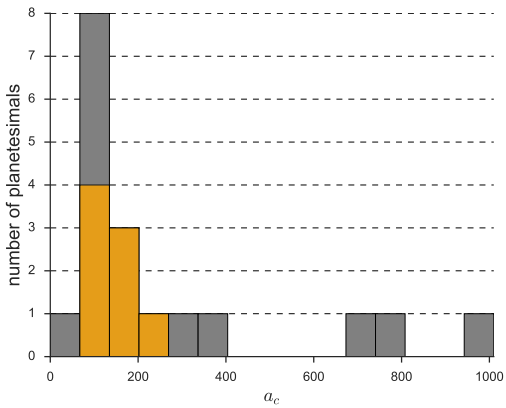

(a) Planetesimals formed within `e_e3L001H` This is the simulations with a 'burst' of planetesimal formation.

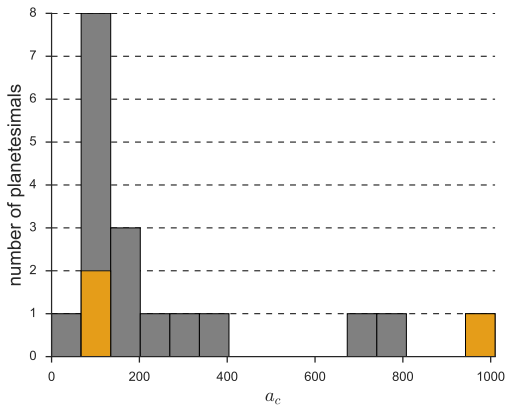

(b) The three planetsimals that formed in the three simulations right at the boarder of stability: `e_e3L0005H_0`, `lp_e3L0003H_0`, and `b_e3L005_1`.

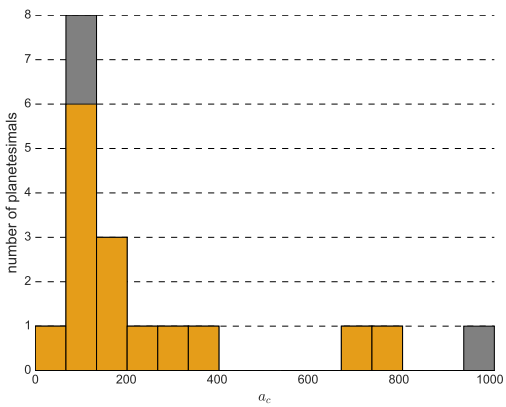

(c) Planetesimals from the four simulations that lie well in the collapsing realm. They represent overshooting cases, where collapse is granted: `Ae3L002`,`Ae3L001`, `Ae3L0005lp`, and `Be3L005`.

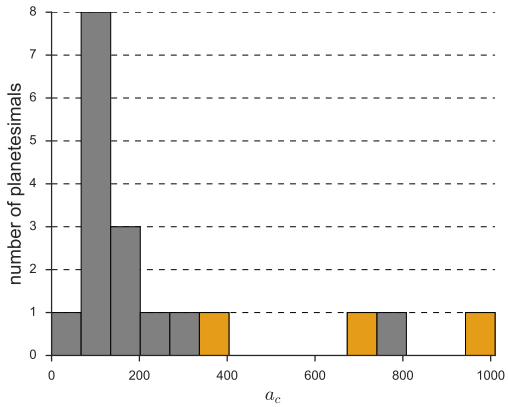

(d) Planetesimals that are formed in simulations with $\mathrm{St} = 0.01$ particles tend to be much more massive.

Figure 7.14: Histograms of the planetesimals diameters a_c that formed in all the 2-d collapse simulations. Grey are all the planetesimals for reference, orange are from a selected group, as described in the caption below each plot. The planetesimal size is estimated by counting the number of particles that are bound into the objects and by multiplying this with the mass represented by each particle. Most of the planetesimals are found to be around 100 km in size. Which is right the value where the cumulative size distribution in pristine solar system objects has a knee (Sheppard & Trujillo, 2010). Specially, for $\mathrm{St} = 0.1$ the planetesimals formed right at the boarder of stability are 72.5 and 74.0 km in size. The planetesimal diameter can be calculated, since it is found to be to first order independent from the radial distance from the star, see Sec. 3.3.3.

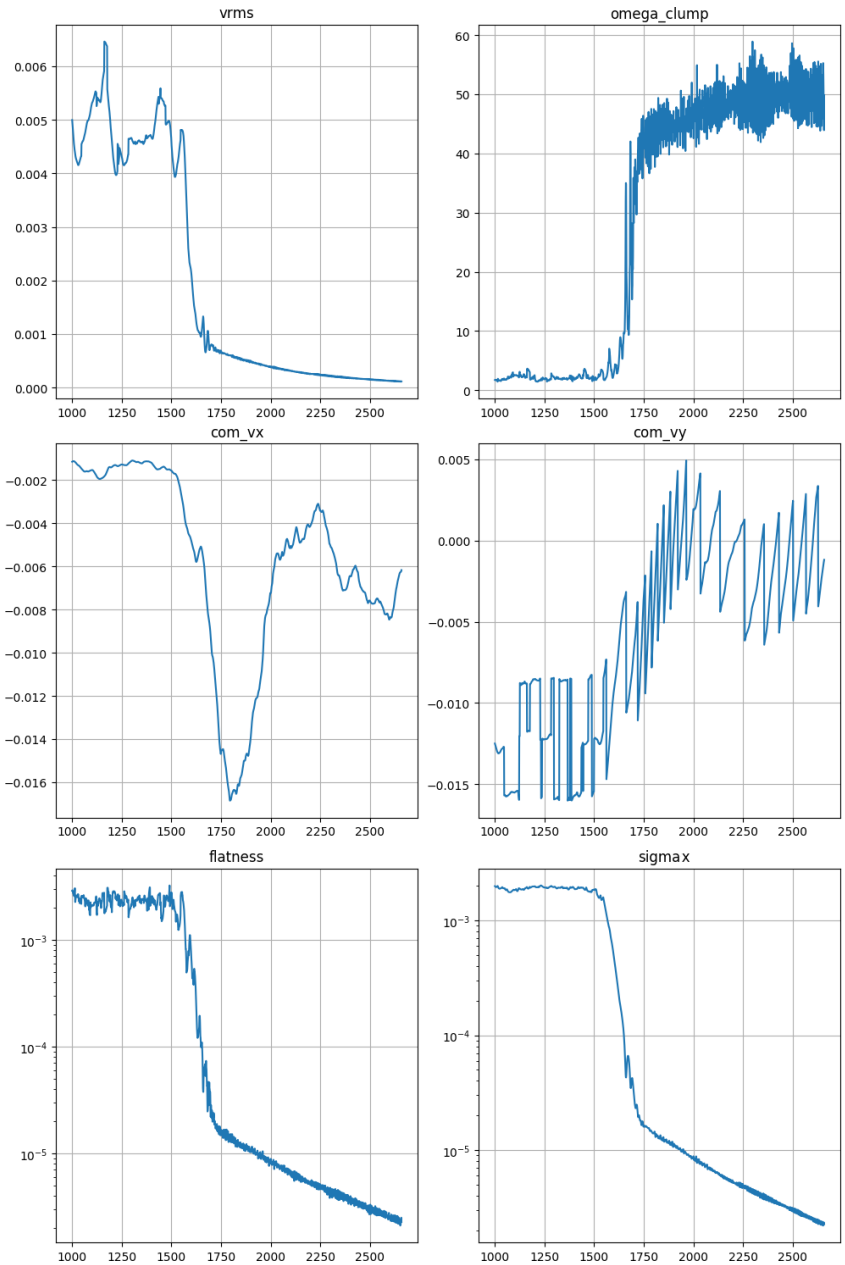

Figure 7.15: Physical parameters of the planetesimal `e_e3L0005H_0`. Measured are, from top left to bottom right: Particle rms-velocity, rotation frequency of the planetesimal Ω_c, radial and azimuthal velocity of its centre of mass, flatness `sigmax`/vrms, and squared particle distance from the centre of mass, here named `sigmax`. *Thanks to Thomas Müller for the support with this work.*

7.6 Collapse simulations in 3-d

In this project, a first step into analysing the presented diffusion limited collapse criterion in 3-d has been made. A simulation with domain size $L_x = L_y = L_Z = 0.001\,\mathrm{H}$, $\mathrm{St} = 0.1$ particles, pressure gradient of $\beta_{\ln(\rho)} = -0.1$ and initial dust-to-gas ratio $\varepsilon_0 = 1$ has been carried out. This simulation is thus similar to one of the investigated gravity-free 3-d SI simulations, see their diffusion values in Fig. 6.5. The runtime of such a simulation is quite long, as it took 22 days of effective runtime to bring the simulation into a state with saturated SI, i.e. before gravity could be switched on. Hence, any further tests were performed with this single simulation as its basis. This initial run was set up at Hill density with $f = 1$, i.e. $\hat{G} = 0.71$, see Eq. (3.40). The timeseries of the maximum dust-to-gas ratio is shown in Fig. 7.17 (blue). The vertical grey bar indicates when self-gravity is switched on. The particle diffusivity is measured in the saturated SI state in radial and vertical direction before gravity was switched on. Measured are the diffusivities as:

$$\delta_\mathrm{x} = (1.90 \pm 1.22) \cdot 10^{-6} \qquad \text{and} \qquad \delta_\mathrm{z} = (7.25 \pm 2.20) \cdot 10^{-9}.$$

Hence, the radial diffusivity was found to be more than two orders of magnitude larger than the vertical diffusion. These values translate into critical length scales of

$$l_{\mathrm{c},x} = (2.90 \pm 0.30) \cdot 10^{-3}\mathrm{H} \quad \approx 2.9 L_x\,,$$

and

$$l_{\mathrm{c},z} = (0.18 \pm 0.01) \cdot 10^{-3}\mathrm{H} \quad \approx 0.2 L_z\,.$$

As the critical length scale in vertical direction is a factor of ten smaller, the question is if the strong radial diffusivity is enough to prevent collapse. Surprisingly, no collapse happened in the run with $f = 1$.

As can already be expected from these values together with no planetesimal formation, the simulation found the particles to undergo a collapse into a dust layer. This dust layer is not the disk mid-plane, as there is

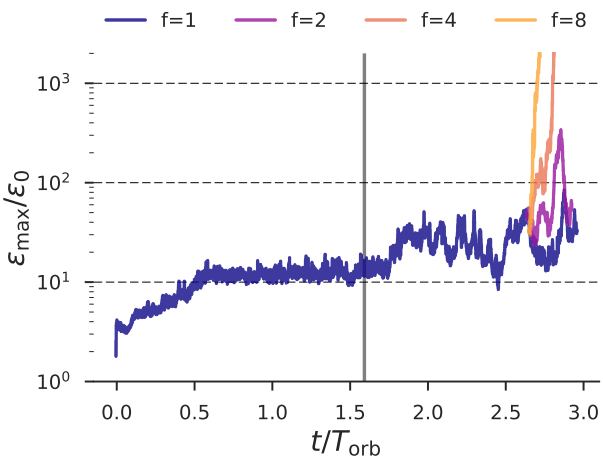

Figure 7.16: Timeseries of the maximum dust-to-gas ratio occurring in the 3-d collapse simulation with $\mathrm{St} = 0.1$ particles. Grey vertical line marks the time, where self-gravity is turned on. The initial gravity parameter is set to $\hat{G} = 0.71$, which represents Hill density (blue). The measured critical length scales predicted that vertical collapse is allowed, but radial collapse is not. Since the result was no collapse, as predicted, the gravity parameter was increased (other coloured lines), starting from a gravitoturbulent snapshot. The simulation with eight times higher gravity collapsed immediately (yellow). The one with four times higher gravity took longer, but collapsed after a quarter of an orbit (orange). The run with two times higher gravity did not collapse (purple).

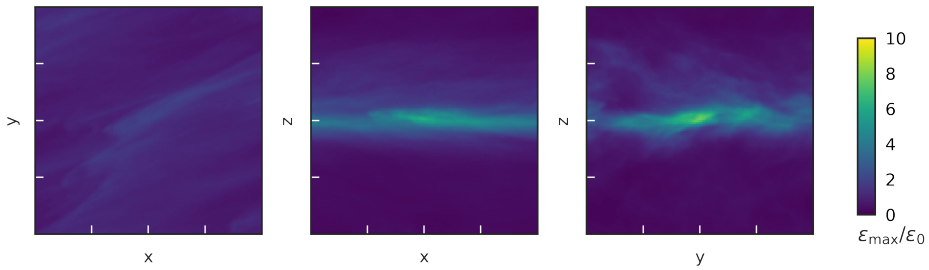

(a) $f = 1$ - $t = 2.94\,\Omega$

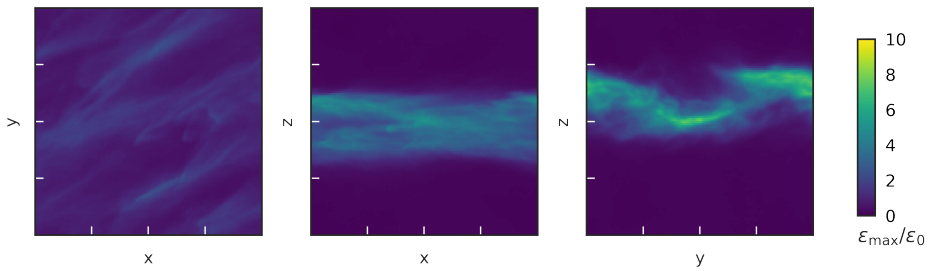

(b) $f = 2$ - $t = 2.89\,\Omega$

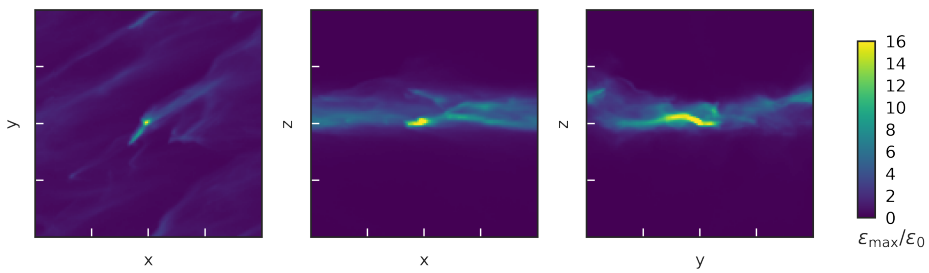

(c) $f = 4$ - $t = 2.79\,\Omega$

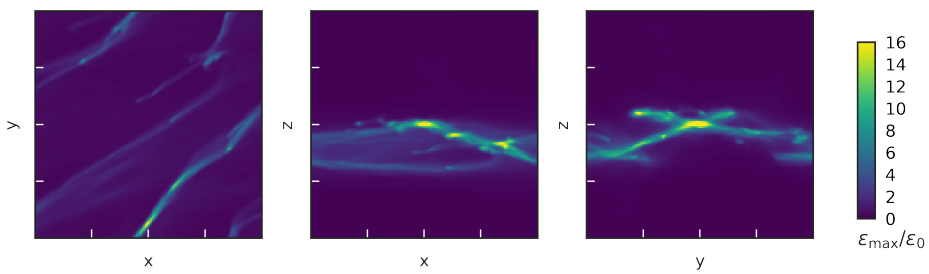

(d) $f = 8$ - $t = 2.69\,\Omega$

Figure 7.17: Simulation end-states of the 3-d collapse study. The views present projects along the vertical (left), azimuthal (middle), and radial (right) axis. Thus, the colorbar shows the column dust-to-gas ratio along the projection axis. All four simulations have the same set of parameters, only the internal density, i.e. total mass that gets scales via $\hat{G}$, is altered by the f parameter. Simulations with $f \leq 2$ show no fragments, but $f = 1$ shows a single prominent large self-gravitating cloud, and $f = 2$ two distinct clouds (see right view). The two simulations with higher total mass collapsed each into a single planetesimal, though the run with $f = 8$ shows some additional overdensities which are unclear if the collapse, or merge with other over-densities.

not stellar gravity inside these simulations. The observed dynamics are better described as self-sedimentation to the maximum in the vertical dust density. Such thin dust layers can trigger other instabilities, as the known Kelvin Helmholtz instability (Johansen et al., 2006a). Moreover, Bai & Stone (2010a) suggest the SI might change its behaviour. As found in their work, the SI can sustain a vertical dust layer to a greater amount than what is thought. This happens due to an increase in turbulent strength when sedimenting to the disk mid-plane. If in this is the case in the presented simulations has to be shown.

Thus, the vertical dust layer is investigated. It is found to have a Gaussian shape. Hence, the dust layer has a scale height, which can be measured via the standard deviation. With $s = 1.31 \cdot 10^{-4}$ the vertical dust scale height was found to be a tenth of the simulation domain size. From this, one can try to estimate the underlying turbulent strength δ'_z be setting the collapse timescale equal to the diffusion timescale. This approach is similar to Birnstiel et al. (2010), where they used settling timescale and stirring timescale. Using the vertical gravitational force g_z from a dense mid-plane at Hill density with vertical height s, which shall now represent a dense particle layer, i.e. compare with Eq. (4.4.1), the gravitational force is given by

$$g_z = 4\pi L_z \rho_{\text{Hill}} G \,.$$

This is a constant force, independent from the height over the dust layer. Thus, Eq. (37) from Johansen et al. (2006a) could not be used to determine the turbulent strength as their gravitational acceleration is a function of height.

The particle layer is stable only if the collapse time $\tau_{\text{coll}} = s/v$ is equal to the diffusion timescale, which is again $\tau_{\text{D}} = s^2/D'$. With D' the diffusion constant and v the collapse velocity. This collapse velocity can be again set to be the terminal velocity of a dust grain with a certain Stokes number. The terminal velocity is thus expressed by

$$v = \tau_{\text{s}} g_z = 4\pi \tau_{\text{s}} L_z \rho_{\text{Hill}} G \,.$$

Setting collapse timescale and diffusion timescale equal asks for an equilibrium solution between turbulent diffusion and vertical settling, which is basically the observed state in the simulation. Solving this equilibrium for the needed vertical diffusion coefficient δ'_z, i.e. D' is herein expressed in code units, gives

$$\boxed{\delta'_z = 9 \tfrac{s}{L} \text{St} \left(\tfrac{L}{\text{H}}\right)^2 \,.} \tag{7.5}$$

With this formula, the vertical diffusivity in the simulation could be estimated to be

$$\delta'_z \approx 1.18 \cdot 10^{-7} \quad \approx 16 \cdot \delta_z \,.$$

A critical length scale from this diffusivity might not be fully conclusive, but interestingly is with

$$l'_{c,z} \approx 1.63 L_z$$

larger than the simulation domain.

As this project turned out to be computational expensive, it was not repeated with different domain sizes, as done in the 2-d collapse experiments from Sec. 7.4. Instead, the total mass was altered to values larger than Hill density, which similar to altering the box size as this reduces l_c/L, too. By using the scaling in density f from Eq. (3.40), one can estimate that a simulation with $f = 2$ should still not collapse, see below, but $f = 4$ and higher should do. Three new simulation were setup up such that they start already with the self-sedimented dust layer, but with higher f parameter. The corresponding critical scale length for collapse should be

$$\begin{aligned} f = 2: &\qquad l'_{c,z} \approx 1.15 L_z \\ f = 4: &\qquad l'_{c,z} \approx 0.81 L_z \\ f = 8: &\qquad l'_{c,z} \approx 0.58 L_z \end{aligned}$$

The maximum dust-to-gas ratio timeseries in Fig. 7.16 shows from where the snapshot was taken and the time evolution for this three additional simulations, with $f = 2$ (purple), 4 (orange), and 8 (yellow). Surprisingly, the $l'_{c,z}$ criterion was giving a good hint on the result of these experiments, as the simulation with $f = 2$ remained stable, too, and the simulation with $f = 4$ was taking longer to collapse as the simulation with $f = 8$.

The radial particle diffusion was found to also change within the emerging of the self-gravitating dust layer. In contrast to the vertical diffusion value, the new radial diffusion value δ'_x can be measured with the default method of tracking the particle travel distance over time, see Eq. (3.40). The new value for the radial particle diffusion is

$$\delta_x = (2.38 \pm 1.38) \cdot 10^{-5} .$$

Hence, the radial diffusion strength was in the dust-layer ten times higher than in the ideal SI situations before gravity was switched on.

It remains an open question if the vertical collapse observed with $f \geq 4$ could happen in a situation with outflow boundaries, where the collapsing dust cloud could spread in the x-y plane while collapsing in z. The radial particle transport by diffusion might be faster than the collapse and hence prohibit the collapse of the particle cloud. If this is true should be analysed in a future project. This will than answer if still the higher radial diffusivity states the final collapse criterion on planetesimal formation in PPDs.

Fig. 7.17 shows the end-states of all four simulations. The simulation with $f = 1$ finds a particle layer with a single self-gravitating cloud in it, see Fig. 7.17a. But this cloud is continuously dispersing and reforms again. The simulation with double the density, see Fig. 7.17b, finds two of such self-gravitating clouds. The height of the particle layer also reduced to half the size of the $f = 1$ simulation, which is right what one expects from the estimate of δ'_z above. Going to even higher densities, the run with $f = 4$ slowly collapses, forming a single planetesimal. The run with $f = 8$ directly collapses to a more massive filament, and the resulting planetesimal number is unclear by this shown state. For comparison, the radial diffusion is much stronger and would in a similar approach actually require a increase in total density by a factor of $f \approx 8$, but only under the assumption that the radial diffusivity remains unaltered once the particle layer forms, which is not what is observed.

One might conclude here that the diffusion limited collapse criterion holds in 3-d only roughly. Still, already this set of simulations shows that diffusion can prevent the collapse of a particle cloud. Thus, the general scheme of diffusion limited collapse holds. But, with outflow boundary conditions it is a good guess that none of the simulations would have collapse as radial diffusion is too strong. Only by allowing the mass inside the cloud to remain within it, vertical collapse could proceed.

The properties of the planetesimals were tried to estimate, though the particle cloud that states the planetesimal was not clearly to be identified and the following values should be taken with caution. In the simulation with $f = 4$, the mass efficiency, see Sec. 7.5, is $\kappa \approx 0.036$. In the run with $f = 8$ the mass efficiency of the largest particle clump is $\kappa \approx 0.015$. Hence, the planetesimal have a size of 58.8 km in the $f = 4$-case and 86.5 km in the $f = 8$-case.

8 Discussion and Outlook

Understanding the formation of planetesimals is crucial for explaining the solar system as we observe it today. But still, the transformation of µm-sized dust into km-sized planetesimals states a missing link in our understanding of the formation of planets and moons, and all the variety of objects tat are observable with current techniques. Such as the strange visitor *Oumuamua* (Raymond et al., 2017) that could be a planetesimal remnant from an extra-solar nebula. Observations of extra-solar systems revealed planets to be highly abundant[7], debris disks to be common (MacGregor et al., 2017), and even comets are now found in extra-solar systems (Rappaport et al., 2018)k an explanation of their formation, too. This missing link further prevents us from deriving a self-consistent picture of a planetary system in its making. Furthermore, when it comes to deriving the abundance of certain elements in the early solar system, a final explanation for the observed elementary abundances in our solar system today cannot be made without a formation mechanism of the initial planetary building material at hand.

A diffusion criterion on planetesimal formation

This work is a big step towards closing this missing link of planet formation. It was the endeavour of this thesis to derive a criterion on the formation of a planetesimal from an initial dust cloud via gravitational self-collapse (Chapter 3), and to verify this criterion on numerical experiments (Chapter 7). The instability criterion has been derived for the first time by H. Klahr during this work was carried out and afterwards further refined by myself. It was published in Klahr & Schreiber (2015). A second publication including the herein presented results on the collapse simulations is in preparation. The collapse criterion is derived by comparing the turbulent diffusion timescale τ_D with the collapse timescale τ_{coll} of a self-gravitating particle cloud. A mechanism that was not foreseen to be at work in the original works of Safronov (1972) and Goldreich & Ward (1973). The herein used collapse timescale takes the friction of the particles with the gas into account. It was found to be inversely proportional to the Stokes number.

The collapse is assumed to start with a Hill stable particle cloud, as this states stability against Keplerian shear and tidal forces. This can be seen as a minimum density condition $\rho_c > \rho_{Hill}$ for a collapsing particle cloud in a PPD, and is regularly used in other works as a boarder of gravitational stability. The in this thesis identified turbulent processes are found to undermine this minimal density criterion. Thus, it had to be replaced by the presented dynamical criterion which incorporates the Hill stability, but is based on the particle dynamics during the collapse. A future project should determine if the assumption of Hill density being the critical density is justified for cloud collapse inside of a PPD, as friction with the gas is dragging on the particles. The critical density, herein this work expressed via the f parameter, cold thus be found to be a function of Stokes number and local sub-Keplerianess.

The new *diffusion limited collapse criterion* states the condition on a particle cloud to be larger than a critical size $L \geq l_c$ in order to collapse faster than turbulent diffusion can dissolve it, see Sec. 3.3.1. This expression can be understood as a critical length for planetesimal formation, similar to the Jeans length in star formation. Regions of less than the critical density and of diameter less than l_c cannot collapse. But, larger or more massive regions can do. The diffusion timescale for this criterion is determined by the

[7] See www.exoplanet.eu

strongest particle diffusion process right on the scales of particle cloud collapse. Since the collapse has to happen at Hill density, one can expect the dust-to-gas ratio $\varepsilon > 1$. The process that is diffusing the particles has thus to be specially strong in the realm of such high dust-to-gas ratios.

A turbulent process that is active right in suchlike particle dense regions has already been found in the work by Youdin & Goodman (2004), Youdin & Johansen (2007) and Johansen & Youdin (2007), as they discovered the *Streaming Instability* (SI) in PPDs. In most works that followed, the SI has been thought of as a mechanism to enhance the dust density locally, though Johansen & Youdin (2007) already measured a significant turbulent strength in the non-linear instability phase. The turbulence found in their work yet went unnoticed in its consequences till today, and has mainly been discussed in literature by its ability to concentrate particles. An exception to be noted is Bai & Stone (2010a), who found the particle turbulent from the SI to vertically limit the dust scale height, a very similar process to cloud collapse.

Combining the diffusion values from Johansen & Youdin (2007) with the derived diffusion limited collapse criterion leads to critical length scales that are of the order of $l_c \approx 8 \cdot 10^{-3}\,\mathrm{H}$. This is a reasonable value for cloud collapse in a PPD. Consequently, turbulent particle diffusion has to be taken into account when it comes to particle cloud collapse. The resulting critical length scale is found to depend on the underlying dust density via $\sqrt{f}$. But, in the size estimate for the resulting planetesimals it arises via $f^{1/6}$ and hence the planetesimal size has only a very weak dependency on the precise collapse density. Moreover, cloud collapse will always set in once this newly found boarder of stability is reached. Thus, larger or more massive clouds are unlikely to form in the first place. Only if a lot of mass is provided on a short timescale, as done in Johansen et al. (2015) and Simon et al. (2016), this boarder of criticality can be surpassed. If so, it can come to an outburst in planetesimal formation, producing more and larger objects at once. In contrast, the herein found mode of diffusion limited planetesimal formation predicts them all to be formed around a characteristic size and is thus by all means different from other initial planetesimal mass functions that have been derived, e.g. by Hopkins (2016), Johansen et al. (2015), and Simon et al. (2016).

In conclusion, the typical mass of planetesimals is given as being proportional to the Hill density ρ_{Hill} times the cubed value of the critical length scale l_c. But, whereas the Hill density decreases with distance from the star, the cubed critical length scale increases at the same rate, leading to constant initial planetesimal masses at all distances. Moreover, in Sec. 3.3.2 a similar expression to Eq. (3.40) could be derived from solving the dispersion relation for the SGI under the additional influence of turbulent diffusion. The derived length scales for the linear phase are a factor of three times larger than from the timescale based estimation. The carried out numerical verification of the diffusion limited collapse criterion showed clearly the timescale criterion to be the right one, see the results of Chapter 7.

Planetesimal formation moderated by the streaming instability

As already noted in Cuzzi et al. (2008) and Shariff & Cuzzi (2014), the processes that can stall a particle cloud collapse can be divided into internal and external processes. From the picture posed in this thesis, it is the turbulent diffusion from inside and outside the collapsing cloud that can bring collapse to a stall. Hence, the SI strength from outside the clump needs to be taken into account, too. This is foremost neglected with this work, but needs to be kept in mind for future research. The described collapse is observed in all but one performed numerical simulation, which is the simulation `Ae3L0005`. In this case, a second particle cloud tries to collapse after already a planetesimal formed, but is not successful. After its formation, the cloud is observed to rapidly drift inwards. Correlated with this drift is a measured increase in the maximum gas density, indicating this cloud to actually get disrupted by gas ram pressure, as suggested to happen by Cuzzi et al. (2008). Still, it is found to be the turbulent strength that is responsible for limiting the cloud collapse in all other investigated cases and the criterion holds in all investigated cases. Also, in some performed simulations the collapse happens on scales smaller than the simulation domain size. It is already in those cases not only internal turbulence limiting collapse, but also cloud external turbulence.

Now, with this new stability criterion at hand, one needs to know what turbulent diffusion strength can be expected within a collapsing particle cloud, and also its surrounding. As the surrounding can be expected to be particle dense too, this could actually state another driving source of turbulence. Hence, an intense

parameter study in 2-d, 2.5-d (Chapter 5), and 3-d simulations (Chapter 6) was carried out in a total of 225 simulations over the past four years. They covered a parameter space of dust-to-gas ratios from $\varepsilon_0 = 0.1$ to 1000, had domain sizes varied from $0.1\,\mathrm{H}$ to $0.001\,\mathrm{H}$, particle Stokes numbers of $\mathrm{St} = 0.01$ and 0.1, and resolutions from $N = 128$ to 1260 grid cells per direction. Some of these simulations took months to perform. This parameter study helped in classifying not only the turbulent strength of the SI, but also found a new turbulent instability. This new instability was found to operate in the r-φ plane and hence named *azimuthal Streaming Instability* (aSI).

This new aSI shows very similar properties as the 2-d SI. Both, when fully active, manage to induce fluctuations in the maximum dust-to-gas ratio by a factor of $\varepsilon_{\mathrm{max}}/\varepsilon_0 \approx 10$. Both also show similar growth rates and similar activity levels at the same initial parameters, and both drop similar in strength when going from $\mathrm{St} = 0.1$ particles to 0.01 particles. Hence, one might state, the two instabilities have the same origin. This also shows the Keplerian shear to not be able to suppress aSI modes in the r-φ plane. The performed 2-d and 3-d simulations both found the strongest diffusion to be in radial direction. The radial diffusion is found to differ from the vertical diffusion by up to two orders of magnitude. As seen in the collapse simulations from Chapter 7, this might result in non-spherical collapse. This states directly an opportunity for a future project, in which this observation is to be classified and one improves the analytical diffusion limited collapse criterion into a form that takes non-isotropic turbulent diffusion into account. For $\mathrm{St} = 0.01$ only very little aSI/SI-activity was found, but the calculations of linear growth rates suggest that they might be operating on even smaller wavelength than what was investigated in this thesis.

The presented work neglects any influence that might arise from external gas turbulence, see for example Turner et al. (2014) on possible origins thereof. One can argue that especially at large dust-to-gas ratios and on small scales the SI should dominate the particle dynamics. Still, if a disk is on large scales sufficiently turbulent in the gas, this could cascade down onto the considered small scales of planetesimal formation. But, even if the gas turbulence dominates the particle diffusion, then the diffusion that enters the critical length scale would have to be replaced by this stronger external driven turbulent diffusion. The argument over the role of diffusion to set a critical length scale for planetesimal formation still holds, as it is a fundamental process. Strong external turbulence might therefore have the possibility to lead to even larger initial planetesimals, as more mass would be needed to overcome the turbulent diffusion threshold. In the numerical experiment from Johansen et al. (2007) and Johansen et al. (2011), they did show the SI to operate in simulations were a global turbulence was induced with a value of up to $\alpha = 3 \cdot 10^{-3}$. But still, they showed SI remained active on the small scales. Therefore, one can safely assume the SI to define the birth size of planetesimals and not the global turbulence. Only if for some reason no turbulence is active, or a disk patch suddenly has too much mass, then the resulting planetesimals will deviate from the predicted size.

Large scale turbulence is also found to form particle traps, such as zonal flows and vortices. They were found to concentrate particles sufficiently to trigger the SI (Dittrich et al., 2013; Raettig et al., 2015; Auffinger & Laibe, 2017). The numerical experiments conducted in Johansen et al. (2007) and Johansen et al. (2011) already showed 3-d SI to be active within zonal flows, and the work from Raettig et al. (2015) showed SI-activity in a particle trapping vortex Barge & Sommeria (1995); Raettig et al. (2015). Still, often this is unclear to the scientific community, as a zonal flow has a point where the pressure gradient is zero and hence SI should be inactive. Sec. 5.4 goes through some of these arguments and numerically showed the newly discovered aSI to be active right within a zonal flow. In combination, this confirms the findings of Auffinger & Laibe (2017), who analytically found SI-activity within zonal flows. A future continuation of the zonal flow experiments should add a vertical extend and dust settling to a disk mid-plane. By that, the back reaction of the particles gets focused onto the disk mid-plane, whereas in the herein performed experiments the back reaction is distributed over the whole disk column. Then, the upper gas disk atmospheres can replenish the pressure bump, see Onishi & Sekiya (2017). This project should also investigate a correct initial condition for particles to be fed into the simulation, as they were herein this work homogeneously distributed, similar to the project Onishi & Sekiya (2017). It might be even better to seed the dust into the simulation domain at the outer boundary condition, and have them outflow again at the inner boundary. Finally, self-gravity should be included in these simulations, which rises hope to find the proclaimed diffusion limited planetesimal formation at work within the zonal flow. This would give insight in the minimum dust mass flux needed for a zonal flow to form planetesimals and the zonal flow dust trapping efficiency. Also,

the local pressure gradient varies in the vicinity of a dust trap and thus the value for the diffusivity may be different then in the performed estimates within this work.

It is interesting to note that the SI might have a dual role in the process of planetesimal formation, both being contrary to each other. On large scales, the SI helps to form planetesimals by concentrating dust locally into dense filaments. Yet, on the small scales, it prevents the formation of arbitrarily small planetesimals by diffusing collapsing clumps faster than they could potentially collapse.

Verification of the derived diffusion limited collapse criterion

The derived diffusion limited collapse criterion states a sharp criterion on when collapse can occur and when not. Hence, it had to be testable in simulations that isolate the case onto situations which clearly state if collapse should occur or not. In Chapter 7 this was carried out in a series of 2-d and 3-d experiments that simulate the collapse of an isolated particle cloud. In this project, the simulation domain itself mimicked the particle cloud in its size. Hence, a simulation domain smaller than the critical length scale should not be able to collapse. A scheme already used to verify the Jeans criterion (Truelove et al., 1997). The critical length scales derived in Chapter 5 and Chapter 6 where used to determine a set of numerical parameters that allowed for such a scheme to be performed on, i.e. at one point the critical length scale had to be larger than the corresponding simulation domain size.

In this project, shearing box simulations with fully developed SI for $\mathrm{St} = 0.1$ and $\mathrm{St} = 0.01$ particles got induced with dust self-gravity right at the Hill density. By varying the simulation domain size L around l_c, the correctness of the critical length scale could be proven, as only simulations within the allowed realm collapsed, see Fig. 7.2. In contrast to previous works of Johansen et al. (2015) and Simon et al. (2016), the critical length scale l_c was resolved in this project by 128 grid cells. Some simulations were successfully adjusted to be right at the boarder of stability. Each of these critical runs formed only a single planetesimal, further underlining the correctness of the diffusion limited collapse criterion. Going to higher total masses in the simulations resulted in an outburst of up to eight planetesimals being formed, or in the formation of extremely large objects. In these out-bursting simulations, it would be interesting to study the order in which the planetesimals form and to check if in these cases the larger planetesimals formed first. If such overshooting situations exist in real PPDs has to be understood in future research. Larger initial planetesimals would allow a quicker start of pebble accretion if they exceed several 100 km and thus faster planet formation Weidenschilling & Cuzzi (1993); Kobayashi et al. (2016); Ormel (2017). A consequence is that planetesimal formation in numerical simulations demands patience, as inducing too much mass, or a too high metallicity, will produce larger objects than what the critical value would give.

Future studies will have to show how turbulent diffusion from the SI depends on the present particle size distribution. Such studies could help to explain the observed variations in the typical masses and colours of the different object families. The results of this thesis thus have the implication to be tested against the continuously improving observational data. For example, the compositional mapping of the asteroid belt objects (DeMeo & Carry, 2014), or the colour range of binaries, which is surprisingly indistinguishable from the larger population of single trans-Neptunian objects (Benecchi et al., 2009). Whatever mechanism produced the colours of apparently single TNOs acted equally on binary systems. Hence, the most likely explanation is that the colours of trans-Neptunian objects and binaries alike are primordial and indicative of their origin in a locally homogeneous, globally heterogeneous PPD but common formation mechanism. As found in the performed 2-d simulations, two binary system could be produced from in the overshooting parameter set. This confirms the high tendency of gravitational collapse to produce binary systems. The further evolution of a binary planetesimal, e.g. by dissipation of orbital energy via tidal forces, can result in a slowly merging binary. This merged binary then becomes a *contact binary*, for example as seen in the comet *Tschurjumow-Gerassimenko* (Rickman et al., 2015).

For comparison, it is in the nature of planetesimal formation via fluffy dust growth to demand at each given time a continuous size distribution of objects from small to large. This is in contradiction to the recent findings of an initial Gaussian size distribution for the asteroid belt by Delbo et al. (2017). From the maximum dust density timeseries of the simulations performed, see Fig. 7.4, one finds with decreasing

domain size it takes longer to form a planetesimal, until planetesimal formation is finally forbidden. This can be understood as the collapse criterion is in reality not a razor-sharp criterion, but rather gives a collapse likelihood around the boarder of stability. A result from this could be right a Gaussian planetesimals size distribution which then could be compared with the initial size distribution of the asteroid belt from Delbo et al. (2017). A first impression of such a size distribution gives the size histogram in Fig. 7.14. It not only shows most of the planetesimals of this study to have a size around 100 km, but also that only very few larger planetesimal were produced and even less smaller planetesimals. The higher number in larger objects comes specially from the simulations that have too much mass and are initialized as overcritical, in terms of the ability to gravitationally collapse. Taking only simulations around the boarder of stability shows a rather Gaussian distribution, though this is low number statistics. This states another future project, in which as many planetesimals as possible get produced right at the boarder of stability, leading to a size distribution that directly can be compared with finding of Delbo et al. (2017). Today, the power-law in the asteroids size distribution is then the outcome of planetesimal collisions and particle accretion (Johansen et al., 2015). In fact, Tsirvoulis et al. (2016) published recent observational evidence for the initial size distribution of asteroids to have been much shallower than presumed. This could be reproduced indeed by a Gaussian initial size distribution centred around $80-85\,\mathrm{km}$ (Delbo et al., 2017). The diffusion limited gravitational collapse of a particle cloud in a dust trap is so far the only prediction for a narrow initial size-distribution of planetesimals instead of a power law distribution. Nevertheless, the process of collisional growth in a turbulent disk (Kobayashi et al., 2016) is of major importance to understand the further evolution of the initial planetesimals to planetary cores as well as to the size distribution among asteroids and other minor bodies observed today.

Of course not all possible influences on planetesimal formation were investigated in the conducted numerical experiments, as it was designed to be a dedicated verification of the derived stability criterion. One might argue that the planetesimal sizes found in the 2-d simulations are different to what should be expected in 3-d. What can be said is that spherical collapse and cylindrical collapse were found to have identical collapse timescales. Moreover, the critical length scales does scale with $l_\mathrm{c} \sim \sqrt{\delta}$, and hence a one order of magnitude lower diffusion, see comparison of 3-d and 2-d diffusion coefficients in Fig. 6.7, should only change the critical length scale by a factor of ≈ 3. The same is true for the found planetesimal size prediction. But, how this incorporates into the collapse efficiency parameter q, see Eq. (3.56), needs to be studied in a future project. So far, the collapse efficiency tends to be around $q \approx 0.1$.

As a consequence from this work, one should be careful with the term *streaming instability assisted planetesimal formation* in the future, as this is actually misleading. As already found in Bai & Stone (2010a), it is the turbulent diffusion of the SI that stalls collapse, in their work it stalls the collapse of the dust dense mid-plane. Instead, the SI should not be understood as a process producing the planetesimals, but as a process controlling it. This process shall be called *diffusion limited planetesimal formation*.

Lastly, 3-d collapse simulation were performed for one parameter set that showed the diffusion limited collapse criterion to hold in 3-d, too. Instead of altering the simulation domain size, the total mass in these simulations was increased stepwise. The increase was induced in a situation where a dense particle layer had already been fully developed and thus might not reflect spherical collapse. In these two simulations, the collapse was stalled by vertical diffusion. This is a surprise, as vertical diffusion was lower than the radial diffusion and hence collapse should be allowed. By measuring the vertical dust layer height, the turbulent strength could be derived that supported the dust layer. The vertical diffusion was found to have increased in its value and this new value stated the collapse criterion to hold again. A prediction on how much the total mass had to be increased in order to trigger collapse was fulfilled once the f parameter was altered. Here, the increase in the total mass via f is similar to increasing the physical simulation domain size, but this way the underlying turbulent diffusion strengths were kept at a fixed value. From the 3-d experiments, one cannot conclude that a lack in vertical diffusion will ultimately trigger cloud collapse in PPDs. As the simulations were set up with periodic boundaries, the radial were not able to diffuse away the cloud mass and hence could not compete with the vertical collapse. The same is true for the azimuthal diffusion, which has not been considered so far as shear dominates that direction. The reason is the mass does re-entered the simulations over the (shear) periodic boundary. Hence, the mass of the dust layer was maintained. In a real situation, the mass would have been transported away from the cloud, as diffusion acts in the direction

of the negative concentration gradient. Then, collapse would have been possible only if the vertical collapse is faster than the radial and azimuthal turbulent transport of the dust. A future projects on 3-d dust cloud collapse will have to deal with non-isotropic diffusion strength and maybe the periodic boundary condition should be changed to an outflow boundary once gravity is switched on.

In either way this project develops in the future, both 3-d and high-resolution 2-d studies become very extensive in computational demands. Not only time-stepping becomes slow from the high physical resolution, particles in the PencilCode tend to produce large amounts of data that need a better handling strategy. 2-d simulations are found to be easier for understanding the underlying physics, diagnostics can be done faster, as file sizes and numbers are drastically lower than in 3-d and also the critical length scales needed to be resolved are slightly larger. 3-d simulations are more realistic and might give a more precise picture that can be compared with reality. Still, how the process of diffusion limited planetesimal formation operates in such setups is only at its beginning to be understood. As diffusion is measured via the particle travel distance, this measurement sets an upper limit on the temporal output rate. Future studies should consider additional post-processing schemes which collect the data produced from the simulations in efficient `hdf5`-files. These will give easier and faster access to the data and hopefully allows progressing in understanding the formation of planetesimals by supporting the methodology of this research.

On planetesimal formation in protoplanetary disks and our solar system

The idea of planetesimals were born big was postulated in Morbidelli et al. (2009). Their finding of all main belt asteroids should have started at a nearly identical size, was lately confirmed by Delbo et al. (2017). This thesis now analytically and numerically supports their observation, by stating that turbulent diffusion prevents smaller planetesimals from being formed and larger planetesimals will not form as their birth cloud should have already collapsed earlier. Surprisingly, the predicted sizes for this initial planetesimals and the planetesimals found within the carried out numerical experiments, both were found to be right at the characteristic size suggested by the observations. This characteristic size is not only found in observations of the asteroid belt (Bottke et al., 2005), but also the Kuiper belt (Nesvorny et al., 2010; Nesvorný et al., 2011; Parker & New Horizons Science Team, 2015), the Jupiter Trojans (Jewitt et al., 2000; Emery et al., 2015), and lately the Neptune Trojans (Sheppard & Trujillo, 2010), see Fig. 1.3. But, even with this work, the missing link of dust growing into km-sized planetary building blocks is not completely closed. Still, the exact mechanisms to form gravitationally unstable dust over-density at different times and in different locations of a PPD, has to be understood. Suggested are a variety of particle traps and dust instabilities that could drive this mechanism, but which of them was actually at work in which particular situations remains unclear. It is a hope for the future of the diffusion limited collapse criterion to give hints back on the underlying dust trapping mechanism.

Another situation discussed lately, i.e. in Carrera et al. (2017), are high metallicity disks that might occur towards the end of the gas disk lifetime. As this is clearly too late for planet formation, obviously for gas giants, this could be the point in time where leftover material gets transformed into smaller comets. It would be an interesting project to study if the presented diffusion limited collapse criterion also holds in high metallicity, low mass disks, and if this can produce objects of comet sizes. Due to the high metallicity the late phase could be an ideal situation for triggering the SI. Roche density would then be reached at higher dust-to-gas ratios, thus lower diffusivity. Consequently, the formed planetesimal sizes are smaller than in the gaseous disk phase. Enough material should still be available as the dust mass reservoir in the outer disk is often found to be significantly large (Birnstiel et al., 2012), as the steady radial gas outflow transported small dust grains outwards. Comets have the benefit to be observed regularly, many of them are found to be pristine, i.e. unprocessed, and they come from far away of the inner solar system. Hence, they could provide a good test bed for the presented collapse criterion. See Fernández & Sosa (2012) and Meech et al. (2000) for further reading on comet size statistics.

The planetesimal sizes obtained in this work mainly come from 2-d simulations, and only two planetesimals were found in the 3-d study. Still, it can be expected for a higher number of 3-d collapse simulation to find a very similar planetesimal statistic. If so, this is giving initial planetesimal distributions in good agreement with observations from the solar system. As the found planetesimal sizes fit extremely well to what is

observed in the solar system and as the diffusion limited collapse criterion is only weakly depending on the distance from the star, it is hard to believe there is a different mechanism at work with an identical outcome. But, if diffusion limited planetesimal formation is the driving mode for planetesimal formation in the early solar system, and also in all other PPD, has to be proven in the future. One should stay open for other convincing formation mechanisms that are not covered by this work, e.g. fluffy growth and the lucky-one scenario, as so often in nature a combination of all possible pathways is the key.

From the presented derivation of a critical length scale, one finds that basically all planetesimals will be, to first order, proportional to H/R. This is in typical disk models relatively constant with radius (Bell et al., 1997; D'Alessio et al., 1998). This explains why all asteroids and classical Kuiper Belt objects were initially roughly of the same size, see Sheppard & Trujillo (2010). Maybe at earlier times, with stronger SI the resulting planetesimals were larger, but they cannot be found any more today, or at the very late times with little gas left in the nebula the SI was so weak to allow for the formation of smaller planetesimals, which may be the cause of the more like 10 km sized comets. Further research will have to clarify this. In this paradigm, larger asteroids up to giant planet cores are the result of secondary growth processes like particle accretion (Ormel & Klahr, 2010; Johansen et al., 2015) and collisions (Kobayashi et al., 2016). Smaller objects are then the outcome of a collisional fragmentation cascade (Morbidelli et al., 2009). These evolution processes explain the currently observed power laws above and below initial planetesimal size. Hence, it can be said that the characteristic size observed today in the solar system, is an imprint of their initial size.

From this thesis, one can conclude the critical length criterion l_c to be a fundamental concept that has to be applied on the planetesimal formation process in future research. Hopefully, one will be able to make predictions for the solar system from the diffusion limited collapse criterion which verify this path of planetesimal formation to be the one that shaped the solar system as we see it today.

A Appendix

A Disk space and CPU consumption of the presented projects

Project name	St	Cluster	Num. files	Total size	Comp. time in days	Core hours ·1000
2-d SI resolution study	0.1	ISAAC	1115147	1.9 TB	31.0	1118.1
3-d collapse study	0.1	ISAAC	344347	274 GB	58.7	1441.9
3-d SI	0.01	ISAAC	10022804	15.2 TB	165.0	2027.1
2-d SI	0.1	ISAAC	2949998	3.0 TB	109.3	108.5
2-d aSI	0.1	ISAAC	2680051	3.1 TB	69.1	66.4
2-d aSI	0.01	ISAAC	1999408	3.1 TB	70.5	77.9
2-d SI	0.01	ISAAC	1478634	1.9 TB	90.2	86.6
3-d SI	0.1	HYDRA	1335648	2.2 TB	1262.0	14792.1
2-d collapse	0.1	HYDRA	10273905	4.5 TB	132.9	406.7
2-d collapse	0.01	HYDRA	38177295	19.0 TB	157.9	490.9
TOTAL			70377237	46.7 TB	2146.5	20616.0

Table A.1: Statistic over the performed numerical projects from within this thesis. Many other studies were performed that could not find their place within this thesis. The statistic also only takes the work performed on `ISAAC` and `HYDRA` into account, not the work on `JUQUEEN`, `DRACO`, and `THEO`

.

B Timeseries from the 2-d streaming instability parameter study

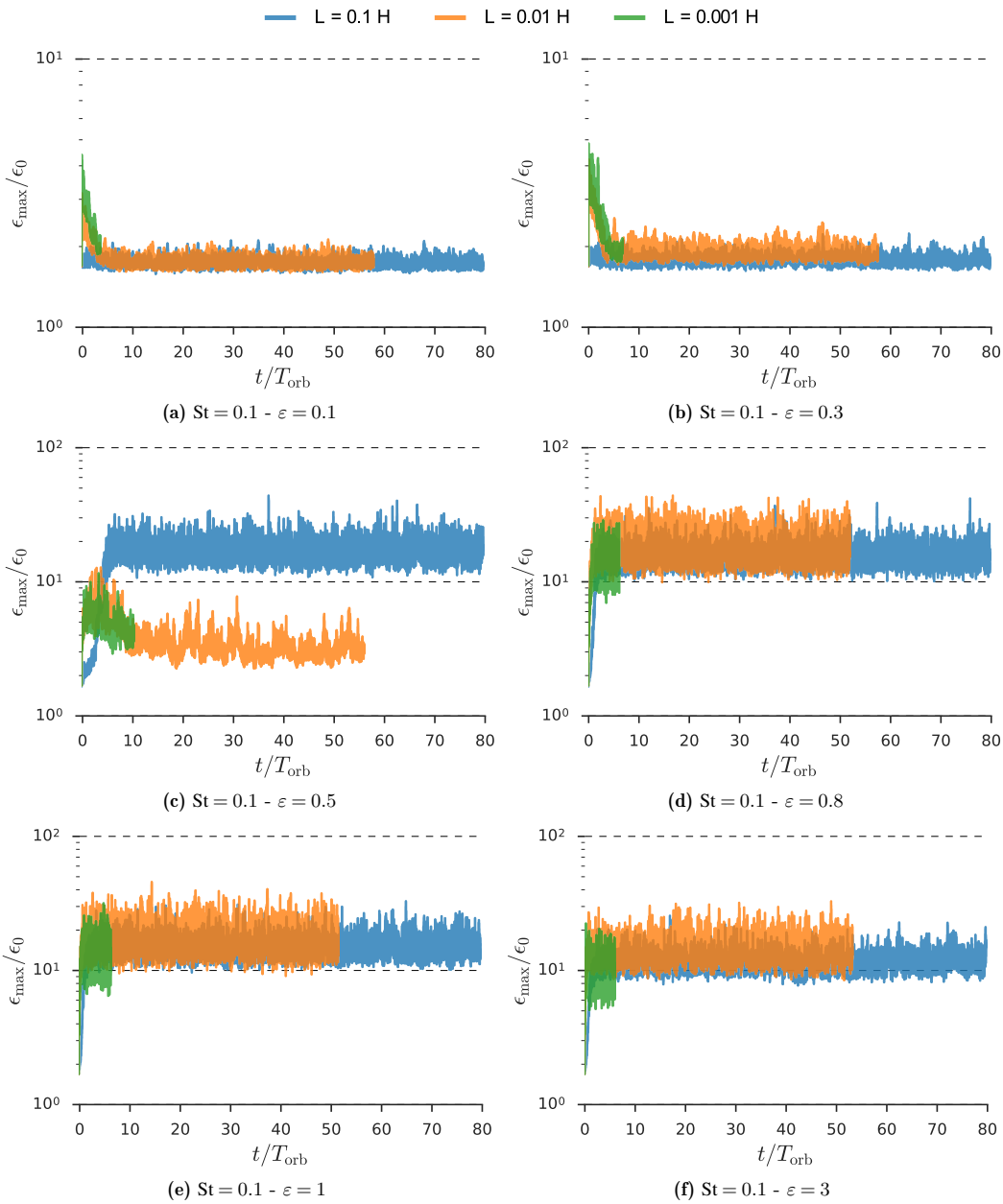

(a) St = 0.1 - $\varepsilon = 0.1$ **(b)** St = 0.1 - $\varepsilon = 0.3$

(c) St = 0.1 - $\varepsilon = 0.5$ **(d)** St = 0.1 - $\varepsilon = 0.8$

(e) St = 0.1 - $\varepsilon = 1$ **(f)** St = 0.1 - $\varepsilon = 3$

Figure B.1: Timeseries of the maximum dust-to-gas ratio for the r-φ plane simulations with St = 0.1. Time range on the x-axisis not equal in all figure.

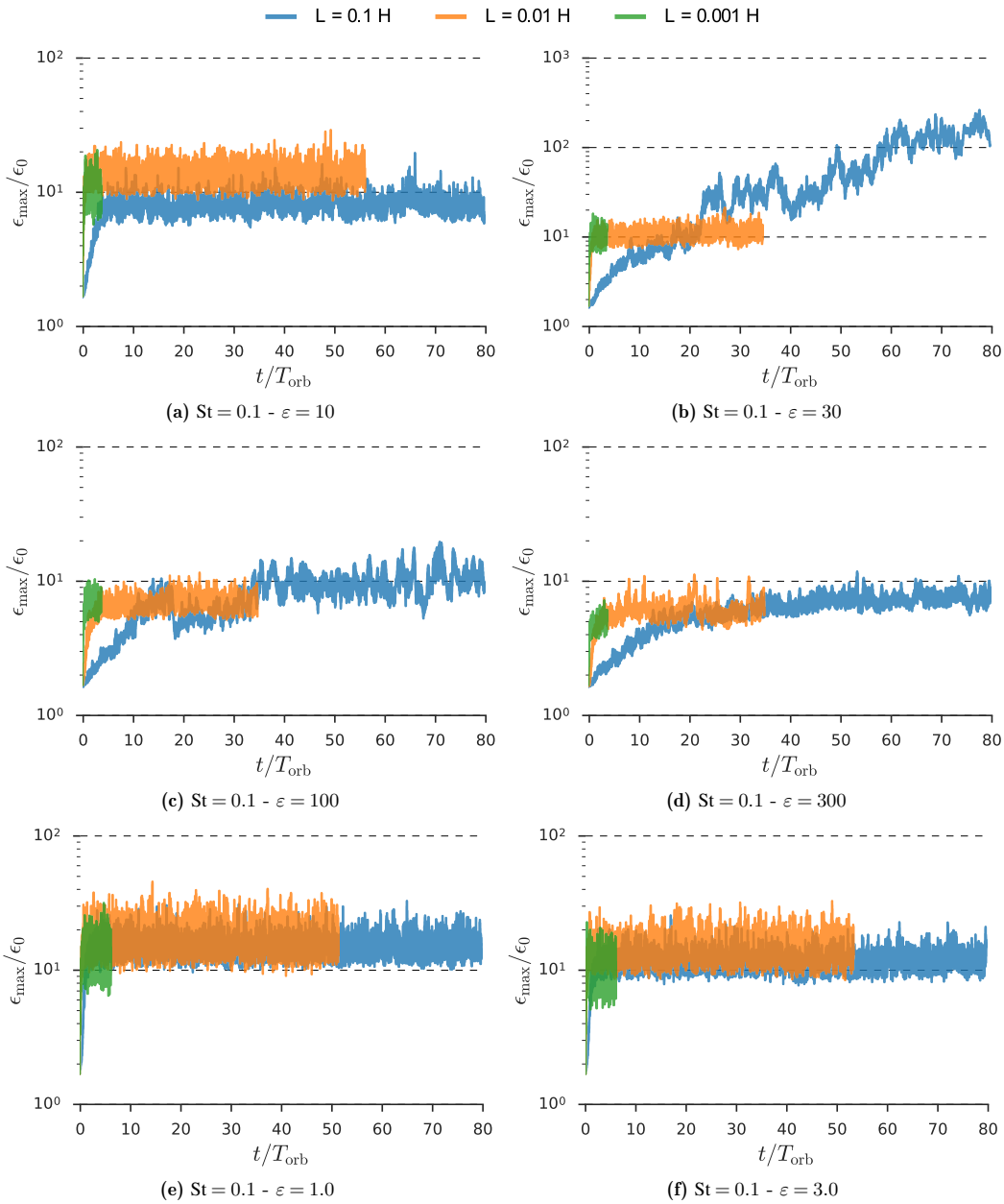

(a) St = 0.1 - $\varepsilon = 10$ **(b)** St = 0.1 - $\varepsilon = 30$

(c) St = 0.1 - $\varepsilon = 100$ **(d)** St = 0.1 - $\varepsilon = 300$

(e) St = 0.1 - $\varepsilon = 1.0$ **(f)** St = 0.1 - $\varepsilon = 3.0$

Figure B.2: Timeseries of the maximum dust-to-gas ratio for the r-φ plane simulations with St = 0.1. Time range on the x-axisis not equal in all figure.

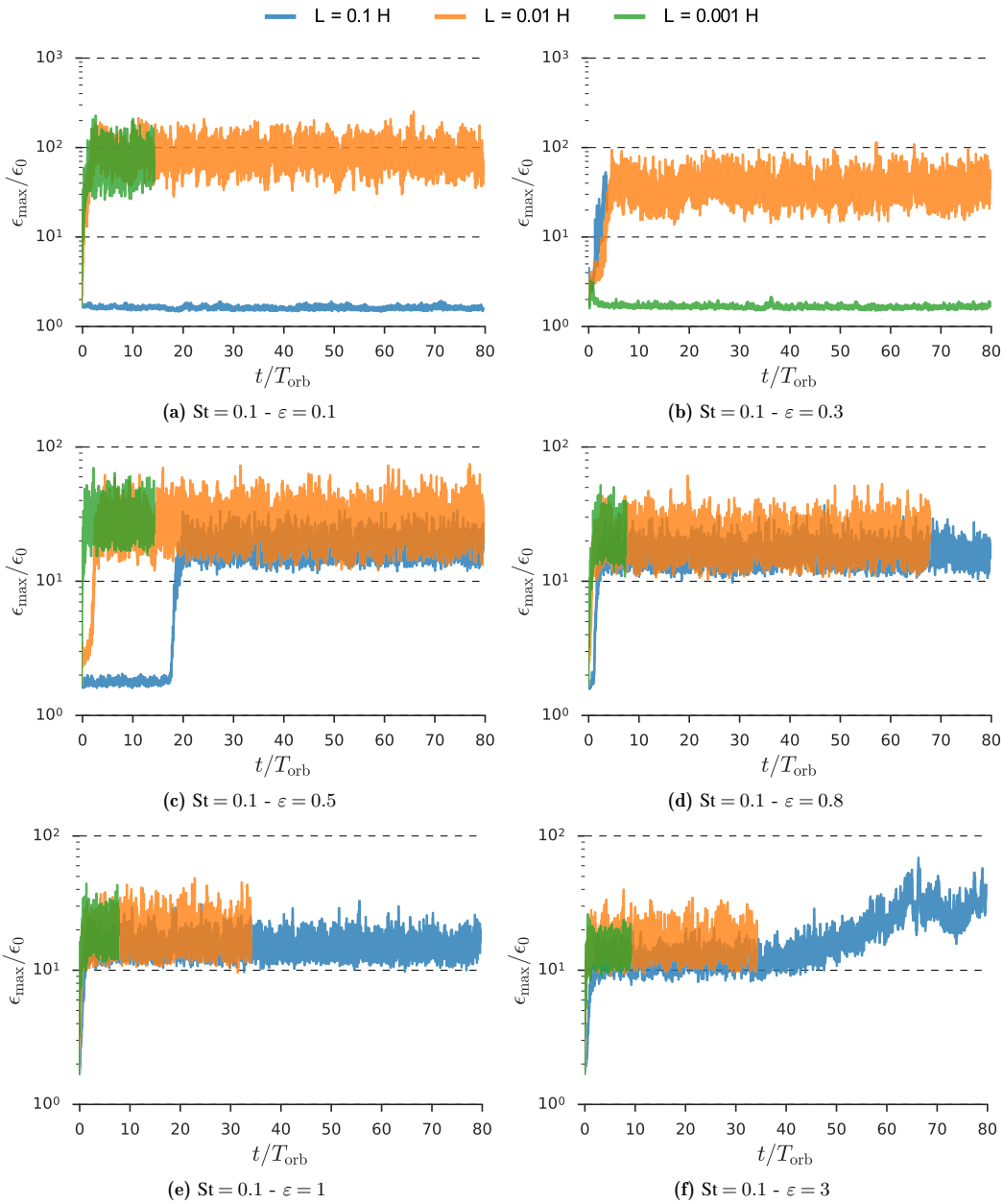

(a) St = 0.1 - $\varepsilon = 0.1$

(b) St = 0.1 - $\varepsilon = 0.3$

(c) St = 0.1 - $\varepsilon = 0.5$

(d) St = 0.1 - $\varepsilon = 0.8$

(e) St = 0.1 - $\varepsilon = 1$

(f) St = 0.1 - $\varepsilon = 3$

Figure B.3: Timeseries of the maximum dust-to-gas ratio for the r-z plane simulations with St = 0.1. Time range on the x-axisis not equal in all figure.

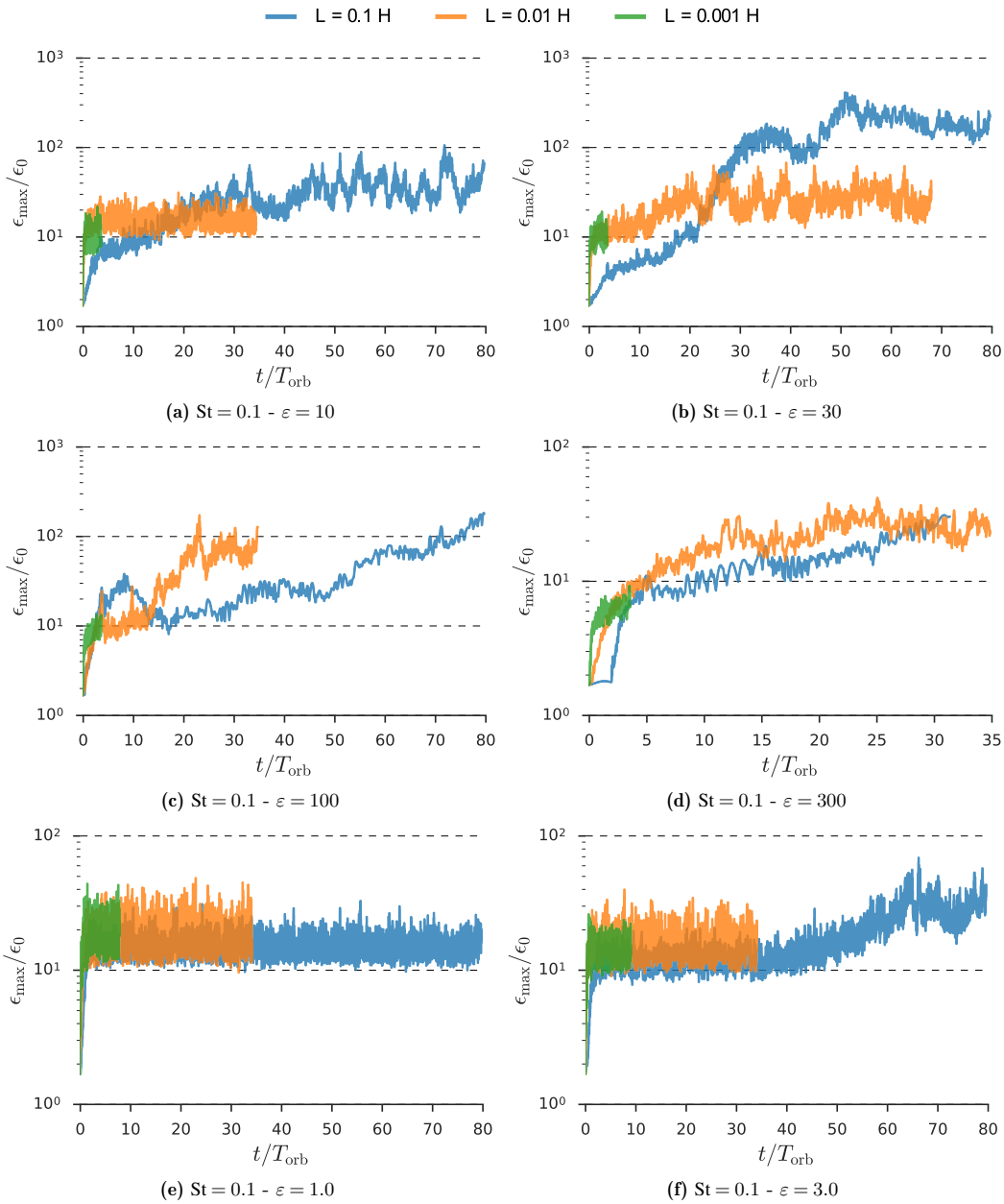

(a) St = 0.1 - $\varepsilon = 10$ **(b)** St = 0.1 - $\varepsilon = 30$

(c) St = 0.1 - $\varepsilon = 100$ **(d)** St = 0.1 - $\varepsilon = 300$

(e) St = 0.1 - $\varepsilon = 1.0$ **(f)** St = 0.1 - $\varepsilon = 3.0$

Figure B.4: Timeseries of the maximum dust-to-gas ratio for the *r*-*z* plane simulations with St = 0.1. Time range on the x-axisis not equal in all figure.

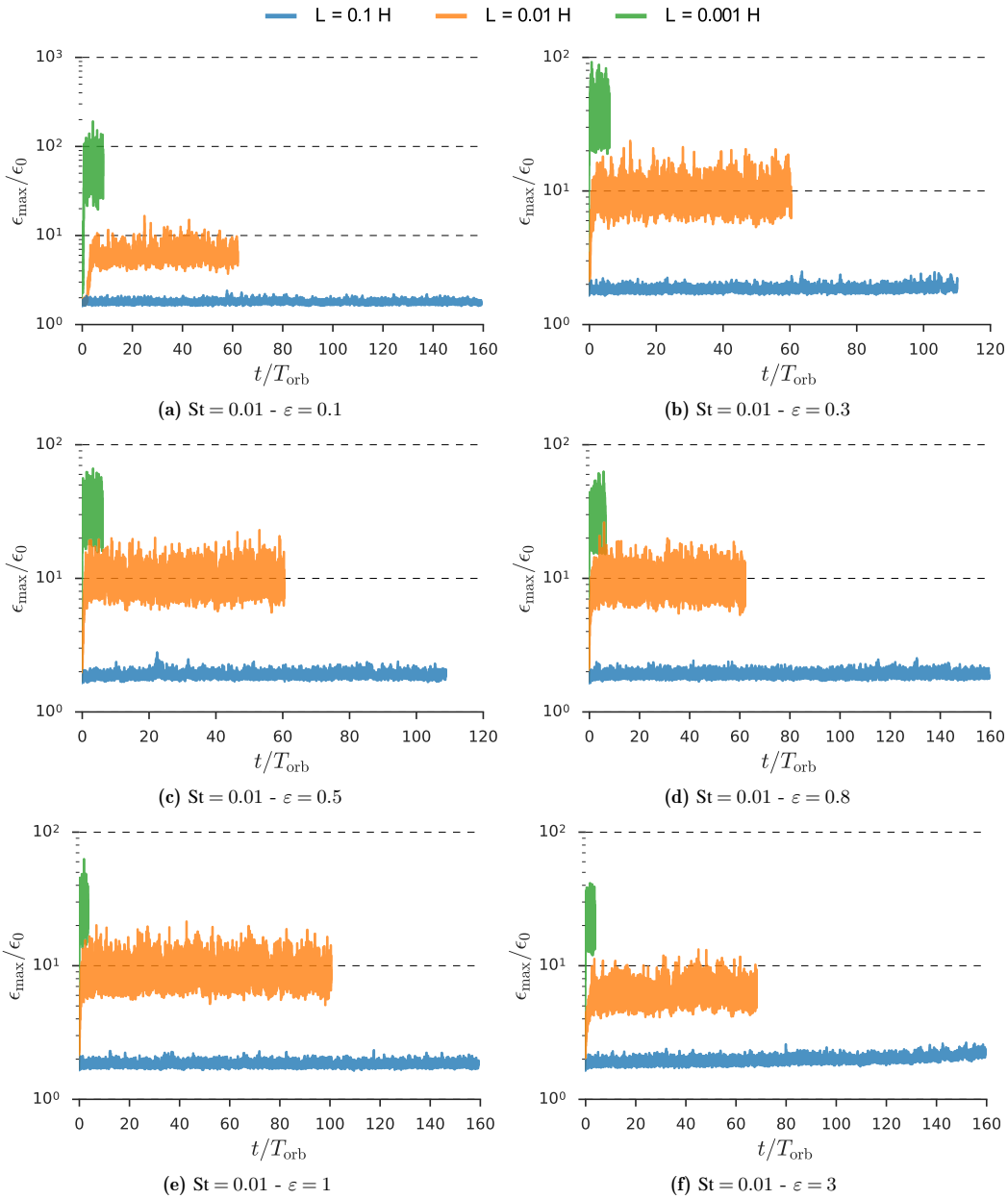

(a) St = 0.01 - $\varepsilon = 0.1$

(b) St = 0.01 - $\varepsilon = 0.3$

(c) St = 0.01 - $\varepsilon = 0.5$

(d) St = 0.01 - $\varepsilon = 0.8$

(e) St = 0.01 - $\varepsilon = 1$

(f) St = 0.01 - $\varepsilon = 3$

Figure B.5: Timeseries of the maximum dust-to-gas ratio for the r-φ plane simulations with St = 0.01. Time range on the x-axisis not equal in all figure.

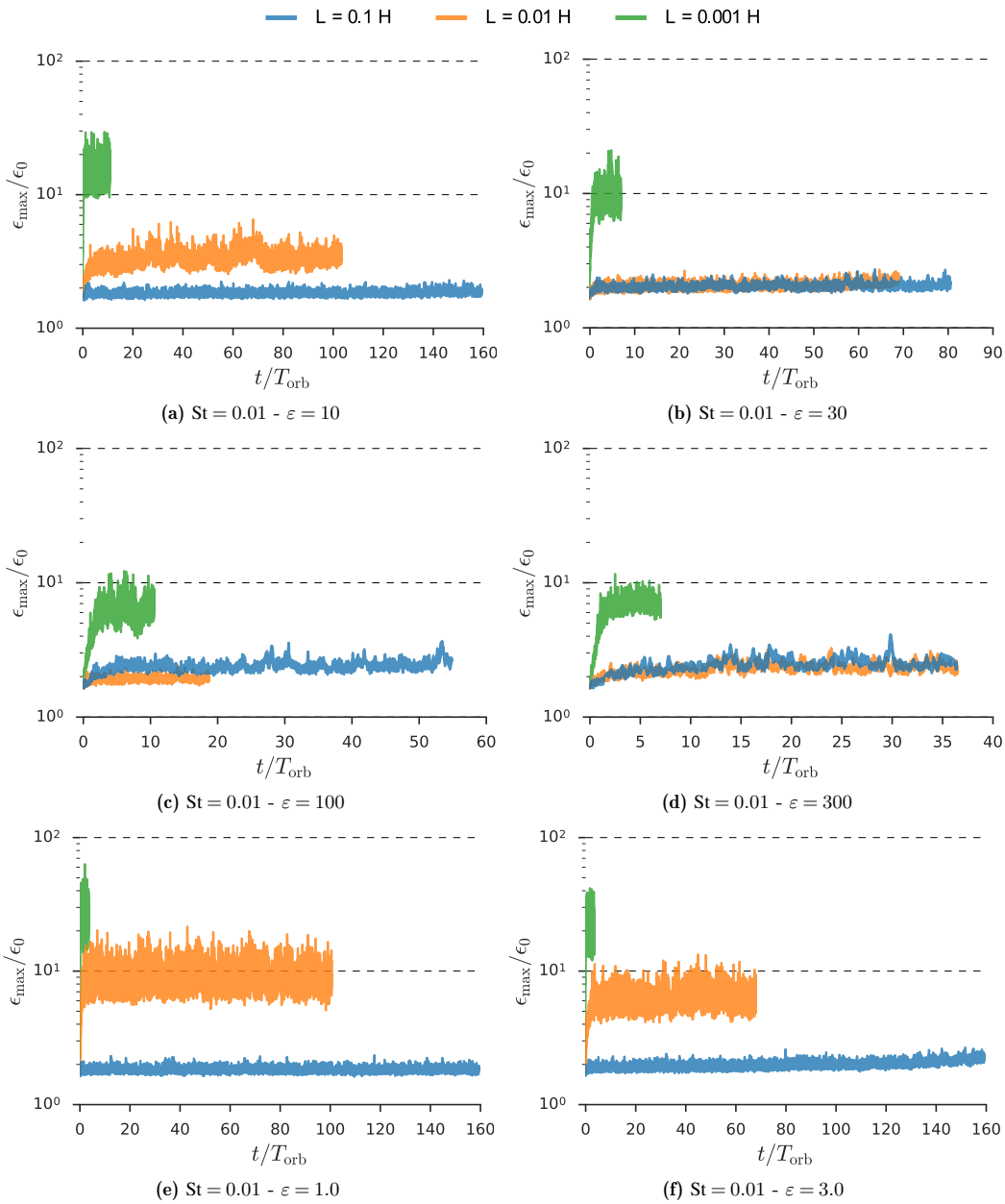

(a) St = 0.01 - $\varepsilon = 10$ **(b)** St = 0.01 - $\varepsilon = 30$

(c) St = 0.01 - $\varepsilon = 100$ **(d)** St = 0.01 - $\varepsilon = 300$

(e) St = 0.01 - $\varepsilon = 1.0$ **(f)** St = 0.01 - $\varepsilon = 3.0$

Figure B.6: Timeseries of the maximum dust-to-gas ratio for the r-φ plane simulations with St = 0.01. Time range on the x-axisis not equal in all figure.

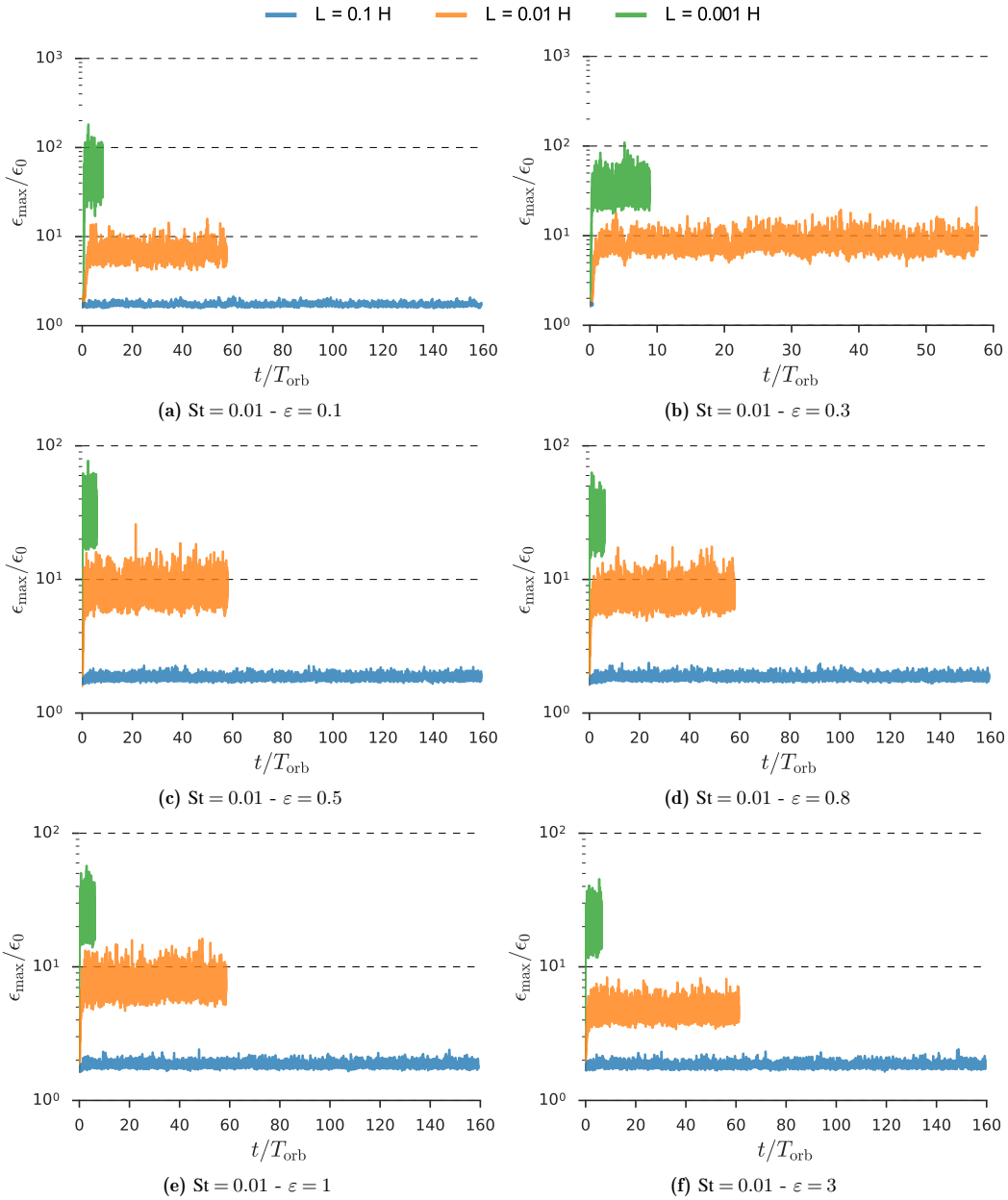

(a) St = 0.01 - $\varepsilon = 0.1$

(b) St = 0.01 - $\varepsilon = 0.3$

(c) St = 0.01 - $\varepsilon = 0.5$

(d) St = 0.01 - $\varepsilon = 0.8$

(e) St = 0.01 - $\varepsilon = 1$

(f) St = 0.01 - $\varepsilon = 3$

Figure B.7: Timeseries of the maximum dust-to-gas ratio for the r-z plane simulations with St = 0.01. Time range on the x-axisis not equal in all figure.

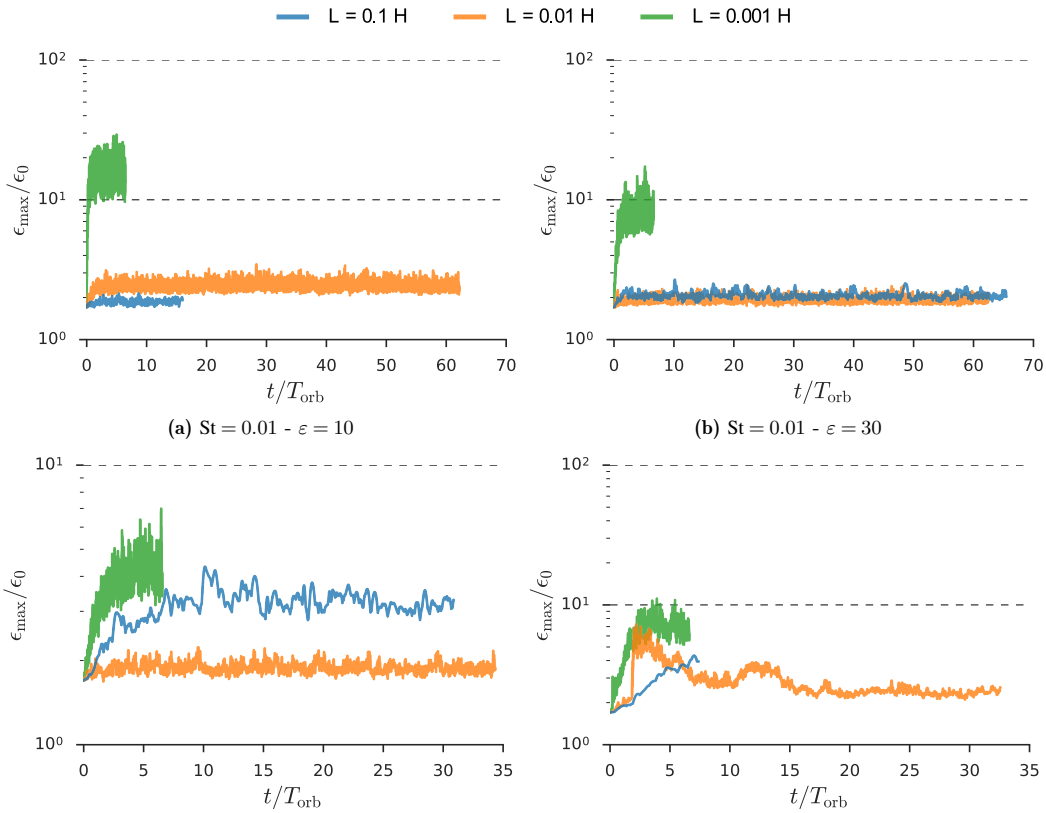

(a) St = 0.01 - $\varepsilon = 10$

(b) St = 0.01 - $\varepsilon = 30$

(c) St = 0.01 - $\varepsilon = 100$

(d) St = 0.01 - $\varepsilon = 300$

Figure B.8: Timeseries of the maximum dust-to-gas ratio for the r-z plane simulations with St = 0.01. Time range on the x-axisis not equal in all figure.

C Timeseries from the 3-d streaming instability parameter study

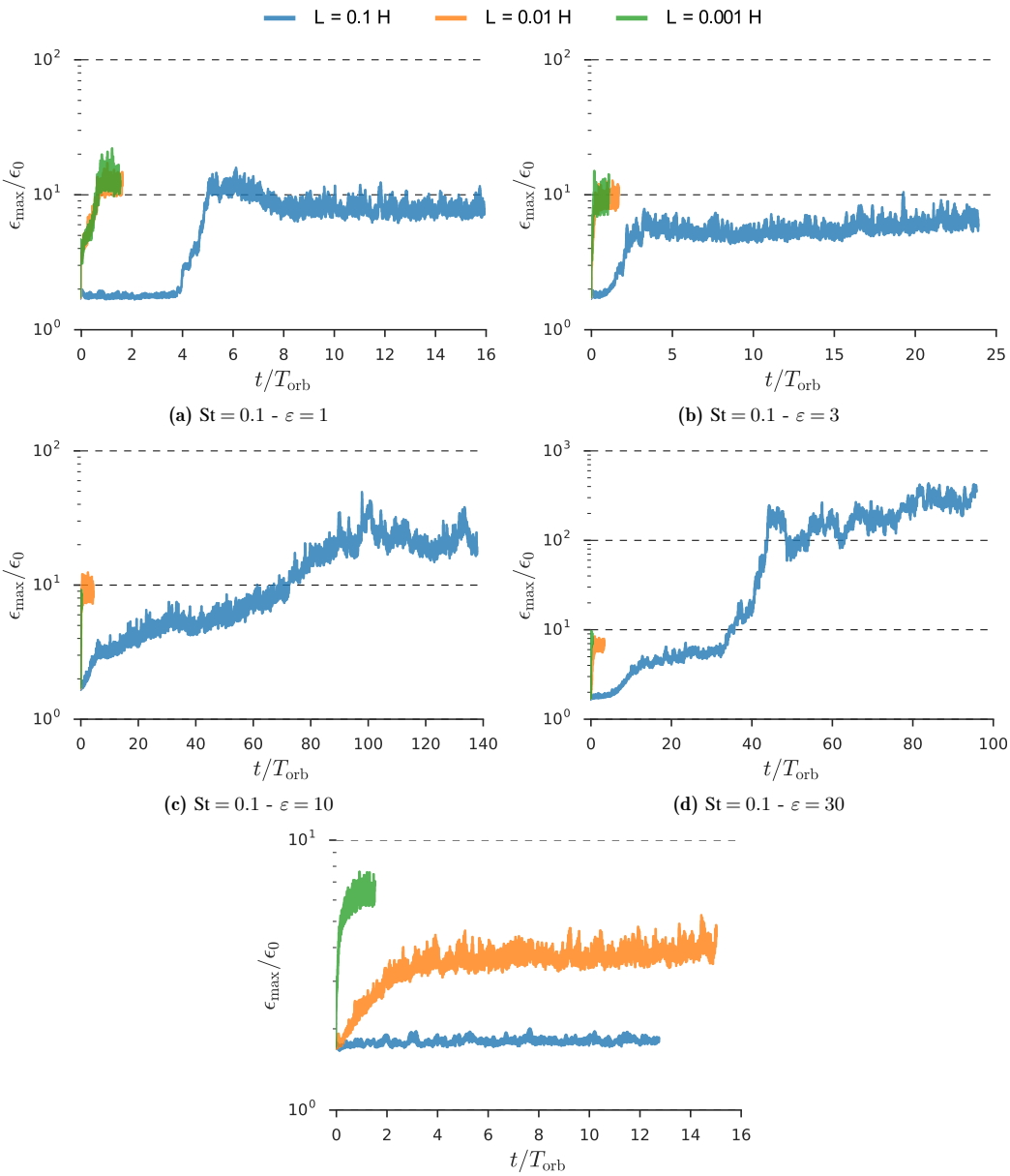

(a) $\mathrm{St} = 0.1$ - $\varepsilon = 1$

(b) $\mathrm{St} = 0.1$ - $\varepsilon = 3$

(c) $\mathrm{St} = 0.1$ - $\varepsilon = 10$

(d) $\mathrm{St} = 0.1$ - $\varepsilon = 30$

(e) $\mathrm{St} = 0.1$ - $\varepsilon = 100$

Figure C.9: Timeseries of the maximum dust-to-gas ratio for the 3-d SI simulations with $\mathrm{St} = 0.1$. Time range on the x-axisis not equal in all figure.

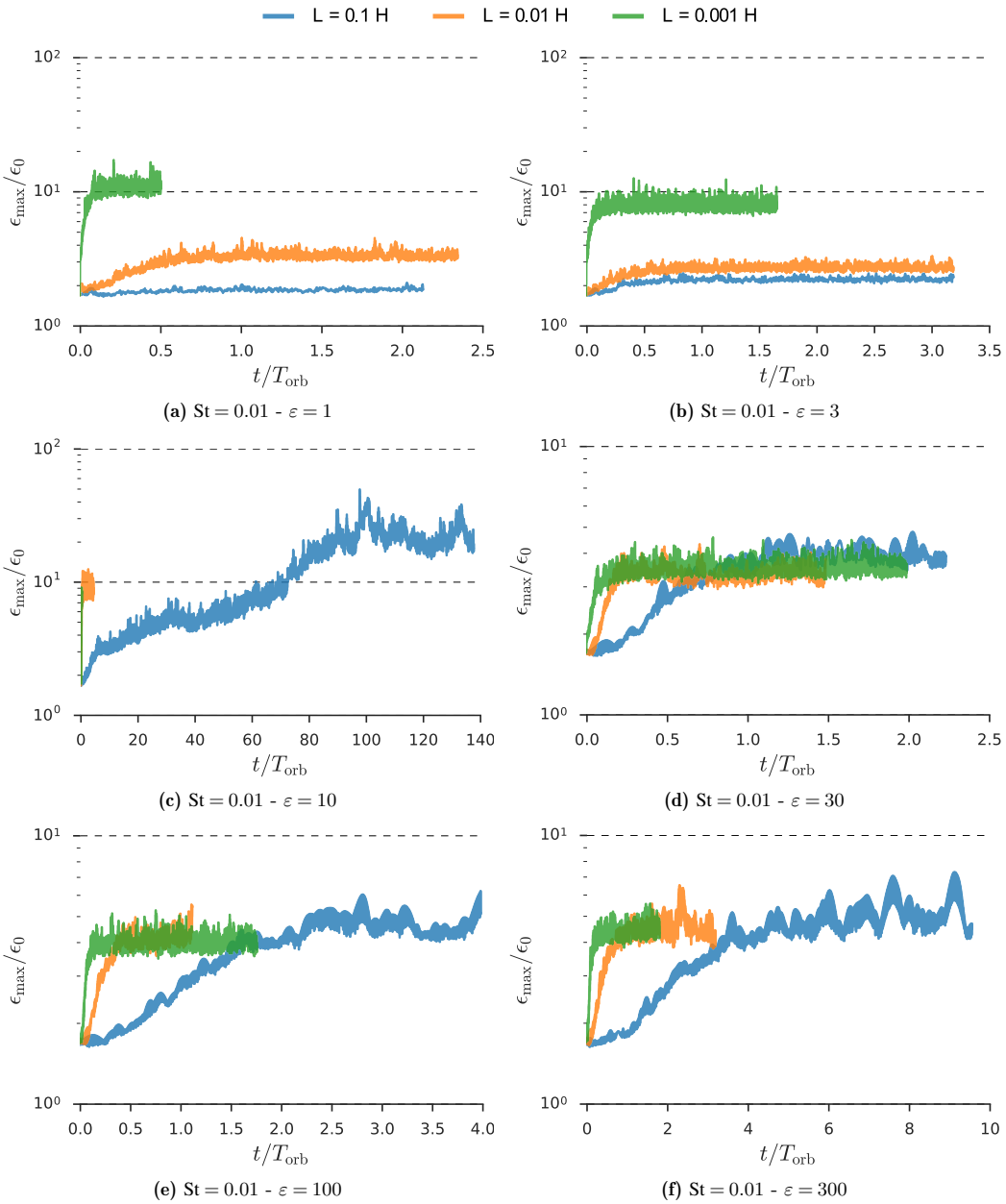

(a) St = 0.01 - $\varepsilon = 1$ **(b)** St = 0.01 - $\varepsilon = 3$

(c) St = 0.01 - $\varepsilon = 10$ **(d)** St = 0.01 - $\varepsilon = 30$

(e) St = 0.01 - $\varepsilon = 100$ **(f)** St = 0.01 - $\varepsilon = 300$

Figure C.10: Timeseries of the maximum dust-to-gas ratio for the 3-d SI simulations with St = 0.01. Time range on the x-axisis not equal in all figure.

D Detailed lists of simulation results

D.1 Simulation results I: aSI for St=0.1

Name	$T_{\max}\,[2\pi\Omega]$	$\alpha \pm \Delta\alpha$	$\delta_x \pm \Delta\delta_x$	$\sigma_\circ$	$u_{\rm rms} \pm \Delta u_{\rm rms}$	$\zeta_\circ$	$l_{\rm corr}$	$\tau_{\rm corr}$	Sc
01_01H_e0	79.58	$(2.5 \pm 0.022) \cdot 10^{-8}$	$(3.3 \pm 0.9) \cdot 10^{-8}$	3.13e−4	4.55e−2	1.41e−2	1.04e−4	3.33e−1	7.76e−1
01_01H_e0	79.58	$(2.1 \pm 0.0095) \cdot 10^{-7}$	$(3.8 \pm 0.96) \cdot 10^{-7}$	9.60e−4	3.86e−2	1.18e−2	3.94e−4	4.10e−1	5.55e−1
01_01H_e0	79.58	$(2.8 \pm 0.02) \cdot 10^{-5}$	$(1.1 \pm 0.41) \cdot 10^{-4}$	1.68e−2	3.95e−2	1.14e−2	6.43e−3	3.84e−1	2.60e−1
01_01H_e0	79.58	$(3.8 \pm 0.019) \cdot 10^{-5}$	$(1.1 \pm 0.36) \cdot 10^{-4}$	1.56e−2	3.45e−2	9.69e−3	7.01e−3	4.50e−1	3.52e−1
01_01H_e1	79.58	$(2.6 \pm 0.018) \cdot 10^{-5}$	$(1.0 \pm 0.29) \cdot 10^{-4}$	1.41e−2	3.22e−2	8.67e−3	7.17e−3	5.08e−1	2.62e−1
01_01H_e3	79.58	$(1.4 \pm 0.0068) \cdot 10^{-5}$	$(4.9 \pm 1.2) \cdot 10^{-5}$	9.57e−3	1.92e−2	4.74e−3	5.11e−3	5.34e−1	2.83e−1
01_01H_e10	79.58	$(3.7 \pm 0.008) \cdot 10^{-6}$	$(1.3 \pm 0.4) \cdot 10^{-5}$	4.74e−3	8.53e−3	1.91e−3	2.84e−3	5.99e−1	2.76e−1
01_01H_e30	79.58	$(1.4 \pm 0.0018) \cdot 10^{-6}$	$(2.9 \pm 1.4) \cdot 10^{-6}$	3.38e−3	6.41e−3	1.10e−3	8.61e−4	2.55e−1	4.96e−1
01_01H_e100	79.58	$(4.3 \pm 0.0062) \cdot 10^{-8}$	$(1.9 \pm 0.4) \cdot 10^{-7}$	5.10e−4	8.96e−4	2.08e−4	3.78e−4	7.41e−1	2.24e−1
01_01H_e300	79.58	$(1.3 \pm 0.0006) \cdot 10^{-8}$	$(6.3 \pm 1.5) \cdot 10^{-8}$	2.10e−4	4.11e−4	1.19e−4	2.98e−4	1.42	2.12e−1
01_01H_e1000	79.58	$(1.1 \pm 0.00067) \cdot 10^{-9}$	$(2.3 \pm 0.87) \cdot 10^{-9}$	4.73e−5	1.58e−4	8.33e−5	4.79e−5	1.01	5.01e−1
01_001H_e0	57.82	$(9.7 \pm 2.3) \cdot 10^{-10}$	$(6.3 \pm 2.8) \cdot 10^{-10}$	5.99e−5	4.55e−2	1.41e−2	1.05e−5	1.75e−1	1.55
01_001H_e0	57.4	$(9.0 \pm 0.92) \cdot 10^{-9}$	$(1.2 \pm 0.53) \cdot 10^{-8}$	2.08e−4	3.86e−2	1.18e−2	5.94e−5	2.85e−1	7.27e−1
01_001H_e0	55.97	$(6.2 \pm 0.067) \cdot 10^{-8}$	$(1.1 \pm 0.39) \cdot 10^{-7}$	5.61e−4	3.34e−2	1.02e−2	1.94e−4	3.45e−1	5.69e−1
01_001H_e0	51.82	$(5.0 \pm 0.075) \cdot 10^{-6}$	$(1.7 \pm 1.1) \cdot 10^{-5}$	8.35e−3	3.05e−2	9.37e−3	2.07e−3	2.48e−1	2.91e−1
01_001H_e1	51.26	$(8.6 \pm 0.24) \cdot 10^{-6}$	$(1.6 \pm 0.93) \cdot 10^{-5}$	9.66e−3	2.79e−2	8.82e−3	1.69e−3	1.75e−1	5.26e−1
01_001H_e3	53.18	$(4.4 \pm 0.028) \cdot 10^{-6}$	$(1.0 \pm 0.46) \cdot 10^{-5}$	5.63e−3	1.58e−2	4.40e−3	1.80e−3	3.19e−1	4.34e−1
01_001H_e10	55.99	$(2.0 \pm 0.0031) \cdot 10^{-6}$	$(3.4 \pm 1.1) \cdot 10^{-6}$	3.18e−3	7.30e−3	1.80e−3	1.07e−3	3.37e−1	5.94e−1
01_001H_e30	34.34	$(5.1 \pm 0.016) \cdot 10^{-7}$	$(8.4 \pm 2.2) \cdot 10^{-7}$	1.45e−3	3.22e−3	6.99e−4	5.80e−4	4.00e−1	6.07e−1
01_001H_e100	34.59	$(5.6 \pm 0.002) \cdot 10^{-8}$	$(1.2 \pm 0.2) \cdot 10^{-7}$	4.64e−4	9.61e−4	2.35e−4	2.51e−4	5.41e−1	4.83e−1
01_001H_e300	34.66	$(1.1 \pm 0.00081) \cdot 10^{-8}$	$(1.4 \pm 0.22) \cdot 10^{-8}$	1.82e−4	3.86e−4	1.29e−4	7.87e−5	4.33e−1	7.42e−1
01_001H_e1000	34.68	$(1.1 \pm 0.00034) \cdot 10^{-9}$	$(8.7 \pm 2.4) \cdot 10^{-10}$	6.21e−5	1.73e−4	9.45e−5	1.40e−5	2.26e−1	1.31
01_0001H_e0	3.37	$(-1.9 \pm 0.22) \cdot 10^{-9}$	$(1.9 \pm 2.5) \cdot 10^{-11}$	9.88e−6	4.55e−2	1.41e−2	1.95e−6	1.97e−1	−9.92e1
01_0001H_e0	6.66	$(4.4 \pm 0.75) \cdot 10^{-9}$	$(1.5 \pm 1.2) \cdot 10^{-10}$	2.96e−5	3.86e−2	1.18e−2	5.10e−6	1.72e−1	2.95e1
01_0001H_e0	10.01	$(-1.9 \pm 0.96) \cdot 10^{-9}$	$(2.9 \pm 2.0) \cdot 10^{-9}$	6.65e−5	3.34e−2	1.01e−2	4.29e−5	6.44e−1	−6.60e−1
01_0001H_e0	6.09	$(7.4 \pm 0.031) \cdot 10^{-7}$	$(5.6 \pm 3.9) \cdot 10^{-7}$	1.47e−3	2.80e−2	8.47e−3	3.79e−4	2.58e−1	1.33
01_0001H_e1	6.01	$(4.8 \pm 0.03) \cdot 10^{-7}$	$(7.6 \pm 7.0) \cdot 10^{-7}$	1.18e−3	2.51e−2	7.62e−3	6.43e−4	5.46e−1	6.38e−1
01_0001H_e3	5.86	$(8.4 \pm 0.21) \cdot 10^{-7}$	$(1.3 \pm 1.2) \cdot 10^{-6}$	1.92e−3	1.34e−2	3.89e−3	6.71e−4	3.49e−1	6.48e−1
01_0001H_e10	3.45	$(8.2 \pm 0.035) \cdot 10^{-7}$	$(3.7 \pm 1.5) \cdot 10^{-7}$	1.39e−3	5.62e−3	1.54e−3	2.69e−4	1.93e−1	2.20
01_0001H_e30	3.46	$(2.9 \pm 0.0076) \cdot 10^{-7}$	$(1.8 \pm 0.61) \cdot 10^{-7}$	7.92e−4	2.54e−3	6.22e−4	2.33e−4	2.94e−1	1.59
01_0001H_e100	3.48	$(6.7 \pm 0.032) \cdot 10^{-8}$	$(3.0 \pm 0.9) \cdot 10^{-8}$	3.43e−4	8.67e−4	2.30e−4	8.85e−5	2.58e−1	2.20
01_0001H_e300	3.48	$(2.3 \pm 0.0056) \cdot 10^{-9}$	$(4.4 \pm 1.2) \cdot 10^{-9}$	1.09e−4	2.69e−4	1.18e−4	4.06e−5	3.73e−1	5.19e−1
01_0001H_e1000	3.49	$(2.9 \pm 0.0015) \cdot 10^{-10}$	$(5.2 \pm 2.4) \cdot 10^{-10}$	4.38e−5	1.38e−4	8.85e−5	1.18e−5	2.69e−1	5.63e−1

Table D.2: 2-d simulations in r-φ extent. Simulation name is constructed from **St** number, domain size $L_{x,y}$ and dust-to-gas ratio ε_0.

D.2 Simulation results II: aSI for St=0.01

Name	$T_{\max}\,[2\pi\Omega]$	$\alpha \pm \Delta\alpha$	$\delta_x \pm \Delta\delta_x$	$\sigma_\circ$	$u_{\rm rms} \pm \Delta u_{\rm rms}$	$\zeta_\circ$	$l_{\rm corr}$	$\tau_{\rm corr}$	Sc
001_01H_e0	159.15	$(1.7 \pm 0.0029) \cdot 10^{-7}$	$(2.1 \pm 0.48) \cdot 10^{-6}$	1.39e−3	4.55e−2	1.14e−2	1.54e−3	1.11	7.87e−2
001_01H_e0	110.04	$(4.0 \pm 0.37) \cdot 10^{-7}$	$(8.0 \pm 1.9) \cdot 10^{-6}$	3.91e−3	3.87e−2	9.67e−3	2.05e−3	5.24e−1	4.96e−2
001_01H_e0	108.62	$(1.3 \pm 0.009) \cdot 10^{-6}$	$(1.4 \pm 0.38) \cdot 10^{-5}$	4.05e−3	3.37e−2	8.42e−3	3.49e−3	8.61e−1	8.95e−2
001_01H_e0	159.15	$(2.0 \pm 0.0057) \cdot 10^{-6}$	$(1.9 \pm 0.55) \cdot 10^{-5}$	5.59e−3	2.83e−2	7.07e−3	3.33e−3	5.95e−1	1.07e−1
001_01H_e1	159.15	$(7.8 \pm 0.023) \cdot 10^{-7}$	$(9.2 \pm 2.0) \cdot 10^{-6}$	2.85e−3	2.51e−2	6.28e−3	3.22e−3	1.13	8.48e−2
001_01H_e3	159.15	$(1.3 \pm 0.0018) \cdot 10^{-6}$	$(1.2 \pm 0.38) \cdot 10^{-5}$	5.63e−3	1.37e−2	3.41e−3	2.18e−3	3.88e−1	1.05e−1
001_01H_e10	159.15	$(1.5 \pm 0.011) \cdot 10^{-7}$	$(2.1 \pm 0.41) \cdot 10^{-6}$	1.36e−3	4.77e−3	1.18e−3	1.54e−3	1.13	7.18e−2
001_01H_e30	80.4	$(1.3 \pm 0.00081) \cdot 10^{-7}$	$(1.0 \pm 0.16) \cdot 10^{-6}$	1.01e−3	2.03e−3	4.76e−4	9.95e−4	9.89e−1	1.31e−1
001_01H_e100	54.86	$(3.2 \pm 0.00063) \cdot 10^{-8}$	$(2.3 \pm 0.32) \cdot 10^{-7}$	4.88e−4	8.01e−4	1.74e−4	4.62e−4	9.46e−1	1.41e−1
001_01H_e300	36.3	$(6.4 \pm 0.0015) \cdot 10^{-9}$	$(5.4 \pm 0.76) \cdot 10^{-8}$	2.28e−4	3.55e−4	7.13e−5	2.35e−4	1.03	1.19e−1
001_01H_e1000	55.1	$(6.8 \pm 0.0025) \cdot 10^{-10}$	$(4.2 \pm 0.65) \cdot 10^{-9}$	6.22e−5	1.02e−4	2.22e−5	6.67e−5	1.07	1.63e−1
001_001H_e0	61.74	$(1e+01 \pm 0.54) \cdot 10^{-7}$	$(8.7 \pm 4.8) \cdot 10^{-6}$	7.07e−3	4.60e−2	1.16e−2	1.23e−3	1.75e−1	1.15e−1
001_001H_e0	60.31	$(-1.4 \pm 0.077) \cdot 10^{-6}$	$(1.6 \pm 1.1) \cdot 10^{-5}$	9.35e−3	3.97e−2	9.96e−3	1.72e−3	1.84e−1	−8.87e−2
001_001H_e0	60.27	$(5.1 \pm 0.028) \cdot 10^{-6}$	$(1.4 \pm 0.93) \cdot 10^{-5}$	9.29e−3	3.47e−2	8.67e−3	1.56e−3	1.68e−1	3.51e−1
001_001H_e0	61.82	$(-6.3 \pm 0.016) \cdot 10^{-6}$	$(1.3 \pm 0.77) \cdot 10^{-5}$	8.95e−3	2.93e−2	7.30e−3	1.50e−3	1.68e−1	−4.71e−1
001_001H_e1	100.41	$(3.5 \pm 0.028) \cdot 10^{-6}$	$(1.2 \pm 0.77) \cdot 10^{-5}$	9.22e−3	2.67e−2	6.71e−3	1.28e−3	1.39e−1	2.94e−1
001_001H_e3	67.88	$(3.3 \pm 0.0076) \cdot 10^{-7}$	$(6.1 \pm 3.2) \cdot 10^{-6}$	4.80e−3	1.35e−2	3.36e−3	1.27e−3	2.64e−1	5.38e−2
001_001H_e10	103.12	$(7.5 \pm 0.0041) \cdot 10^{-7}$	$(1.3 \pm 0.52) \cdot 10^{-6}$	3.09e−3	5.57e−3	1.37e−3	4.08e−4	1.32e−1	5.99e−1
001_001H_e30	68.87	$(3.1 \pm 0.034) \cdot 10^{-8}$	$(3.1 \pm 0.91) \cdot 10^{-7}$	1.13e−3	1.97e−3	4.92e−4	2.76e−4	2.44e−1	1.00e−1
001_001H_e100	18.62	$(4.3 \pm 0.0056) \cdot 10^{-9}$	$(4.7 \pm 0.79) \cdot 10^{-8}$	2.51e−4	5.75e−4	1.40e−4	1.88e−4	7.50e−1	9.07e−2
001_001H_e300	36.45	$(1.5 \pm 0.00013) \cdot 10^{-9}$	$(1e+01 \pm 1.6) \cdot 10^{-9}$	9.95e−5	2.13e−4	4.95e−5	1.00e−4	1.01	1.52e−1
001_001H_e1000	17.78	$(4.2 \pm 0.00062) \cdot 10^{-10}$	$(1.8 \pm 0.3) \cdot 10^{-9}$	4.37e−5	8.13e−5	1.92e−5	4.07e−5	9.33e−1	2.39e−1
001_0001H_e0	8.28	$(1.7 \pm 0.071) \cdot 10^{-6}$	$(2.3 \pm 2.5) \cdot 10^{-6}$	6.59e−3	4.59e−2	1.13e−2	3.49e−4	5.30e−2	7.47e−1
001_0001H_e0	5.93	$(2.8 \pm 0.033) \cdot 10^{-6}$	$(2.1 \pm 1.9) \cdot 10^{-6}$	4.32e−3	3.89e−2	9.62e−3	4.90e−4	1.13e−1	1.31
001_0001H_e0	6.03	$(1.3 \pm 0.14) \cdot 10^{-7}$	$(1.0 \pm 1.0) \cdot 10^{-6}$	3.74e−3	3.36e−2	8.45e−3	2.76e−4	7.37e−2	1.29e−1
001_0001H_e0	6.17	$(7.2 \pm 0.15) \cdot 10^{-7}$	$(1.3 \pm 1.3) \cdot 10^{-6}$	3.48e−3	2.80e−2	7.02e−3	3.84e−4	1.11e−1	5.36e−1
001_0001H_e1	3.4	$(5.9 \pm 0.33) \cdot 10^{-7}$	$(8.9 \pm 6.0) \cdot 10^{-7}$	2.98e−3	2.53e−2	6.29e−3	3.01e−4	1.01e−1	6.58e−1
001_0001H_e3	3.43	$(9.5 \pm 0.22) \cdot 10^{-8}$	$(5.2 \pm 2.2) \cdot 10^{-7}$	1.93e−3	1.29e−2	3.20e−3	2.72e−4	1.41e−1	1.81e−1
001_0001H_e10	10.64	$(5.1 \pm 0.13) \cdot 10^{-8}$	$(2.5 \pm 1.0) \cdot 10^{-7}$	1.26e−3	4.99e−3	1.20e−3	2.03e−4	1.61e−1	2.01e−1
001_0001H_e30	6.95	$(5.6 \pm 0.011) \cdot 10^{-8}$	$(9.6 \pm 3.0) \cdot 10^{-8}$	7.35e−4	1.81e−3	4.42e−4	1.30e−4	1.77e−1	5.83e−1
001_0001H_e100	10.45	$(2.9 \pm 0.012) \cdot 10^{-9}$	$(2.1 \pm 0.96) \cdot 10^{-8}$	3.01e−4	5.95e−4	1.47e−4	6.99e−5	2.32e−1	1.37e−1
001_0001H_e300	6.97	$(2.0 \pm 0.0006) \cdot 10^{-9}$	$(7.2 \pm 1.6) \cdot 10^{-9}$	1.21e−4	2.20e−4	5.43e−5	5.96e−5	4.93e−1	2.79e−1
001_0001H_e1000	10.46	$(4.4 \pm 0.0015) \cdot 10^{-10}$	$(8.5 \pm 2.5) \cdot 10^{-10}$	4.34e−5	8.41e−5	2.17e−5	1.96e−5	4.52e−1	5.23e−1

Table D.3: 2-d simulations in r-φ extent. Simulation name is constructed from St number, domain size $L_{x,y}$ and dust-to-gas ratio ε_0.

D.3 Simulation results III: SI for St=0.1

Name	α	$\delta_x \pm \Delta\delta_x$	$\delta_z \pm \Delta\delta_z$	$\sigma_\circ$	$u_{\rm rms} \pm \Delta u_{\rm rms}$	$\zeta_\circ$	$l_{\rm corr}$	$\tau_{\rm corr}$	Sc
01_01H_e0	−1.9e−9	$(1.4 \pm 2.6) \cdot 10^{-7}$	$(3.0 \pm 3.8e+01) \cdot 10^{-8}$	1.03e−3	4.55e−2	1.41e−2	1.35e−4	1.31e−1	−1.33e−2
01_01H_e0	1.4e−8	$(3.7 \pm 1.5) \cdot 10^{-7}$	$(7.9 \pm 2.9e+01) \cdot 10^{-8}$	1.17e−3	3.86e−2	1.18e−2	3.17e−4	2.72e−1	3.72e−2
01_01H_e0	1.9e−5	$(7.5 \pm 2.4) \cdot 10^{-5}$	$(4.9 \pm 1.6) \cdot 10^{-5}$	1.58e−2	3.92e−2	1.14e−2	4.75e−3	3.01e−1	2.59e−1
01_01H_e0	2.5e−5	$(6.3 \pm 1.5) \cdot 10^{-5}$	$(4.4 \pm 1.3) \cdot 10^{-5}$	1.57e−2	3.42e−2	9.78e−3	4.00e−3	2.55e−1	4.03e−1
01_01H_e1	2.0e−5	$(5.6 \pm 1.4) \cdot 10^{-5}$	$(4.6 \pm 1.3) \cdot 10^{-5}$	1.45e−2	3.20e−2	8.79e−3	3.90e−3	2.69e−1	3.55e−1
01_01H_e3	1.5e−5	$(2.2 \pm 0.55) \cdot 10^{-5}$	$(3.3 \pm 1.0) \cdot 10^{-5}$	1.19e−2	2.60e−2	4.69e−3	1.85e−3	1.55e−1	6.99e−1
01_01H_e10	1.0e−5	$(2.1 \pm 1.4) \cdot 10^{-6}$	$(7.9 \pm 4.0) \cdot 10^{-5}$	7.05e−3	1.67e−2	2.37e−3	2.91e−4	4.13e−2	5.10
01_01H_e30	4.3e−6	$(4.8 \pm 4.7) \cdot 10^{-7}$	$(1.7 \pm 0.62) \cdot 10^{-5}$	3.72e−3	1.33e−2	1.20e−3	1.29e−4	3.46e−2	8.94
01_01H_e100	2.9e−7	$(8.4 \pm 2.6) \cdot 10^{-8}$	$(2.1 \pm 1.1) \cdot 10^{-6}$	1.05e−3	2.35e−3	3.43e−4	7.94e−5	7.54e−2	3.42
01_01H_e300	6.2e−9	$(2.4 \pm 1.4) \cdot 10^{-8}$	$(1.2 \pm 0.53) \cdot 10^{-7}$	2.34e−4	4.56e−4	1.08e−4	1.02e−4	4.35e−1	2.62e−1
01_01H_e1000	1.9e−8	$(1.8 \pm 0.73) \cdot 10^{-9}$	$(5.8 \pm 3.7) \cdot 10^{-8}$	2.23e−4	5.67e−4	1.15e−4	7.96e−6	3.58e−2	1.08e1
01_001H_e0	−1.6e−6	$(1.2 \pm 1.0) \cdot 10^{-5}$	$(7.1 \pm 1.9e+01) \cdot 10^{-7}$	1.10e−2	5.13e−2	1.47e−2	1.05e−3	9.60e−2	−1.35e−1
01_001H_e0	4.7e−9	$(6.8 \pm 3.9) \cdot 10^{-8}$	$(1.3 \pm 0.32) \cdot 10^{-9}$	1.74e−4	3.86e−2	1.18e−2	3.89e−4	2.23	6.98e−2
01_001H_e0	2.1e−5	$(7.3 \pm 5.8) \cdot 10^{-5}$	$(3.9 \pm 3.1) \cdot 10^{-6}$	1.13e−2	3.68e−2	1.15e−2	6.48e−3	5.73e−1	2.83e−1
01_001H_e0	7.4e−5	$(4.5 \pm 4.4) \cdot 10^{-5}$	$(5.1 \pm 3.3) \cdot 10^{-6}$	1.68e−2	3.83e−2	1.08e−2	2.68e−3	1.60e−1	1.64
01_001H_e1	5.6e−6	$(3.1 \pm 2.4) \cdot 10^{-5}$	$(6.3 \pm 3.5) \cdot 10^{-6}$	9.61e−3	2.78e−2	8.74e−3	3.25e−3	3.39e−1	1.80e−1
01_001H_e3	8.3e−6	$(1.5 \pm 0.95) \cdot 10^{-5}$	$(4.9 \pm 2.2) \cdot 10^{-6}$	7.17e−3	1.66e−2	4.61e−3	2.10e−3	2.93e−1	5.50e−1
01_001H_e10	2.3e−6	$(4.0 \pm 1.2) \cdot 10^{-6}$	$(1.9 \pm 0.67) \cdot 10^{-6}$	3.35e−3	7.89e−3	1.76e−3	1.18e−3	3.53e−1	5.72e−1
01_001H_e30	1.1e−6	$(5.3 \pm 4.3) \cdot 10^{-7}$	$(1.1 \pm 0.43) \cdot 10^{-6}$	2.26e−3	4.98e−3	8.76e−4	2.34e−4	1.03e−1	2.12
01_001H_e100	5.0e−7	$(7.8 \pm 5.6) \cdot 10^{-8}$	$(1.8 \pm 0.99) \cdot 10^{-6}$	1.26e−3	3.65e−3	4.83e−4	6.21e−5	4.93e−2	6.40
01_001H_e300	1.4e−8	$(1.2 \pm 0.25) \cdot 10^{-8}$	$(4.7 \pm 0.89) \cdot 10^{-8}$	2.49e−4	5.33e−4	1.41e−4	4.64e−5	1.86e−1	1.18
01_001H_e1000	7.7e−9	$(2.0 \pm 0.66) \cdot 10^{-9}$	$(5.7 \pm 2.1) \cdot 10^{-8}$	1.25e−4	3.67e−4	1.14e−4	1.56e−5	1.25e−1	3.93
01_0001H_e0	2.0e−8	$(2.1 \pm 1.7) \cdot 10^{-6}$	$(4.2 \pm 2e+01) \cdot 10^{-9}$	1.95e−3	4.68e−2	1.45e−2	1.05e−3	5.39e−1	9.79e−3
01_0001H_e0	1.1e−6	$(7.9 \pm 1.8e+01) \cdot 10^{-7}$	$(1.8 \pm 7.1) \cdot 10^{-9}$	3.54e−3	4.18e−2	1.31e−2	2.23e−4	6.29e−2	1.40
01_0001H_e0	9.6e−6	$(3.8 \pm 1.1) \cdot 10^{-6}$	$(3.1 \pm 9.9e+01) \cdot 10^{-10}$	2.60e−3	4.66e−2	1.03e−2	1.47e−3	5.65e−1	2.50
01_0001H_e0	7.5e−6	$(3.5 \pm 1.2) \cdot 10^{-6}$	$(3.4 \pm 8.8e+01) \cdot 10^{-10}$	2.41e−3	3.52e−2	9.92e−3	1.47e−3	6.09e−1	2.12
01_0001H_e1	6.6e−6	$(2.9 \pm 0.88) \cdot 10^{-6}$	$(4.4 \pm 8.3e+01) \cdot 10^{-10}$	3.02e−3	3.31e−2	9.22e−3	9.74e−4	3.22e−1	2.26
01_0001H_e3	1.8e−5	$(5.9 \pm 1.2) \cdot 10^{-6}$	$(2.0 \pm 1.4e+01) \cdot 10^{-10}$	4.04e−3	3.01e−2	5.31e−3	1.47e−3	3.64e−1	3.07
01_0001H_e10	1.6e−6	$(1.4 \pm 1.7) \cdot 10^{-6}$	$(1.2 \pm 0.56) \cdot 10^{-7}$	2.72e−3	6.08e−3	1.75e−3	5.22e−4	1.92e−1	1.14
01_0001H_e30	9.0e−8	$(3.2 \pm 1.8) \cdot 10^{-7}$	$(5.8 \pm 1.8) \cdot 10^{-8}$	8.92e−4	2.46e−3	6.42e−4	3.58e−4	4.01e−1	2.80e−1
01_0001H_e100	7.6e−8	$(8.2 \pm 3.5) \cdot 10^{-8}$	$(2.3 \pm 0.93) \cdot 10^{-8}$	5.10e−4	1.25e−3	2.79e−4	1.61e−4	3.16e−1	9.24e−1
01_0001H_e300	6.1e−9	$(8.3 \pm 1.8) \cdot 10^{-9}$	$(3.0 \pm 0.92) \cdot 10^{-9}$	1.59e−4	3.64e−4	1.30e−4	5.23e−5	3.30e−1	7.38e−1
01_0001H_e1000	4.9e−10	$(5.9 \pm 2.8) \cdot 10^{-10}$	$(4.1 \pm 1.5) \cdot 10^{-10}$	6.16e−5	1.59e−4	9.29e−5	9.65e−6	1.57e−1	8.28e−1

Table D.4: 2-d simulations in r-z extent. Simulation name is constructed from St number, domain size $L_{x,z}$ and dust-to-gas ratio ε_0.

D.4 Simulation results IV: SI for St=0.01

Name	α	$\delta_x \pm \Delta\delta_x$	$\delta_z \pm \Delta\delta_z$	$\sigma_\circ$	$u_{\rm rms} \pm \Delta u_{\rm rms}$	$\zeta_\circ$	$l_{\rm corr}$	$\tau_{\rm corr}$	Sc
001_01H_e0	4.2e−8	$(6.4 \pm 1.2) \cdot 10^{-7}$	$(9.9 \pm 2.4) \cdot 10^{-7}$	1.12e−3	4.55e−2	1.14e−2	5.74e−4	5.14e−1	6.61e−2
001_01H_e0	2.2e−7	$(1.5 \pm 0.36) \cdot 10^{-6}$	$(5.0 \pm 3.9) \cdot 10^{-8}$	1.99e−3	3.85e−2	9.63e−3	7.63e−4	3.83e−1	1.43e−1
001_01H_e0	4.2e−7	$(1.9 \pm 0.51) \cdot 10^{-6}$	$(4.3 \pm 1.2) \cdot 10^{-6}$	2.61e−3	3.34e−2	8.35e−3	7.36e−4	2.82e−1	2.18e−1
001_01H_e0	6.3e−7	$(2.2 \pm 0.65) \cdot 10^{-6}$	$(7.8 \pm 2.2) \cdot 10^{-6}$	3.16e−3	2.80e−2	6.97e−3	6.95e−4	2.20e−1	2.89e−1
001_01H_e1	6.5e−7	$(2.2 \pm 0.66) \cdot 10^{-6}$	$(8.1 \pm 2.1) \cdot 10^{-6}$	3.07e−3	2.52e−2	6.28e−3	7.07e−4	2.30e−1	2.99e−1
001_01H_e3	4.8e−7	$(1.5 \pm 0.43) \cdot 10^{-6}$	$(8.0 \pm 2.8) \cdot 10^{-6}$	2.44e−3	1.28e−2	3.16e−3	6.06e−4	2.48e−1	3.22e−1
001_01H_e10	1.7e−7	$(5.4 \pm 1.0) \cdot 10^{-7}$	$(9.5 \pm 1.5) \cdot 10^{-7}$	1.32e−3	4.84e−3	1.17e−3	4.13e−4	3.14e−1	3.04e−1
001_01H_e30	5.6e−8	$(1.7 \pm 0.28) \cdot 10^{-7}$	$(2.9 \pm 0.47) \cdot 10^{-7}$	6.69e−4	1.90e−3	4.40e−4	2.59e−4	3.87e−1	3.25e−1
001_01H_e100	2.5e−8	$(6.4 \pm 1.2) \cdot 10^{-8}$	$(8.1 \pm 1.3) \cdot 10^{-8}$	3.44e−4	7.74e−4	1.50e−4	1.86e−4	5.40e−1	3.89e−1
001_01H_e300	1.5e−8	$(1.3 \pm 0.39) \cdot 10^{-8}$	$(3.7 \pm 1.3) \cdot 10^{-8}$	1.86e−4	4.47e−4	6.27e−5	7.20e−5	3.87e−1	1.14
001_01H_e1000	4.8e−9	$(2.4 \pm 0.87) \cdot 10^{-9}$	$(4.2 \pm 2.1) \cdot 10^{-8}$	1.04e−4	2.35e−4	3.08e−5	2.35e−5	2.26e−1	1.99
001_001H_e0	1.4e−6	$(7.1 \pm 5.7) \cdot 10^{-6}$	$(7.1 \pm 7.3) \cdot 10^{-6}$	6.14e−3	4.60e−2	1.15e−2	1.16e−3	1.89e−1	1.99e−1
001_001H_e0	−1.0e−6	$(1.1 \pm 0.8) \cdot 10^{-5}$	$(1.4 \pm 1.3) \cdot 10^{-5}$	1.09e−2	4.03e−2	9.95e−3	9.81e−4	9.01e−2	−9.62e−2
001_001H_e0	3.8e−6	$(1.1 \pm 0.71) \cdot 10^{-5}$	$(1.4 \pm 1.3) \cdot 10^{-5}$	1.04e−2	3.52e−2	8.76e−3	1.01e−3	9.66e−2	3.64e−1
001_001H_e0	2.2e−6	$(8.1 \pm 3.8) \cdot 10^{-6}$	$(8.5 \pm 5.6) \cdot 10^{-6}$	7.54e−3	2.89e−2	7.24e−3	1.07e−3	1.41e−1	2.78e−1
001_001H_e1	1.9e−6	$(7.3 \pm 3.3) \cdot 10^{-6}$	$(8.9 \pm 5.1) \cdot 10^{-6}$	6.54e−3	2.61e−2	6.49e−3	1.12e−3	1.72e−1	2.54e−1
001_001H_e3	5.4e−7	$(2.2 \pm 0.72) \cdot 10^{-6}$	$(3.2 \pm 1.2) \cdot 10^{-6}$	3.69e−3	1.31e−2	3.24e−3	6.07e−4	1.64e−1	2.39e−1
001_001H_e10	6.2e−8	$(2.5 \pm 0.69) \cdot 10^{-7}$	$(2.5 \pm 0.88) \cdot 10^{-6}$	1.46e−3	4.77e−3	1.18e−3	1.71e−4	1.18e−1	2.49e−1
001_001H_e30	1.1e−8	$(3.8 \pm 0.81) \cdot 10^{-8}$	$(5.8 \pm 1.9) \cdot 10^{-7}$	5.39e−4	1.74e−3	4.30e−4	7.12e−5	1.32e−1	2.93e−1
001_001H_e100	2.3e−9	$(7.6 \pm 1.1) \cdot 10^{-9}$	$(1.8 \pm 0.31) \cdot 10^{-8}$	1.61e−4	5.40e−4	1.30e−4	4.74e−5	2.95e−1	3.07e−1
001_001H_e300	7.2e−10	$(1.9 \pm 1.0) \cdot 10^{-9}$	$(3.9 \pm 1.9) \cdot 10^{-7}$	1.12e−4	2.19e−4	4.87e−5	1.71e−5	1.52e−1	3.77e−1
001_001H_e1000	3.9e−10	$(5.4 \pm 1.4) \cdot 10^{-10}$	$(7.3 \pm 2.4) \cdot 10^{-10}$	3.76e−5	8.61e−5	1.79e−5	1.43e−5	3.79e−1	7.26e−1
001_0001H_e0	1.1e−6	$(3.1 \pm 4.5) \cdot 10^{-6}$	$(8.2 \pm 1e+01) \cdot 10^{-7}$	5.20e−3	4.58e−2	1.15e−2	6.02e−4	1.16e−1	3.54e−1
001_0001H_e0	4.8e−7	$(2.0 \pm 2.1) \cdot 10^{-6}$	$(6.4 \pm 5.3) \cdot 10^{-7}$	4.14e−3	3.87e−2	9.72e−3	4.75e−4	1.15e−1	2.46e−1
001_0001H_e0	1.5e−7	$(1.6 \pm 1.7) \cdot 10^{-6}$	$(4.6 \pm 3.6) \cdot 10^{-7}$	3.68e−3	3.36e−2	8.43e−3	4.25e−4	1.16e−1	9.51e−2
001_0001H_e0	1.4e−6	$(1.3 \pm 1.2) \cdot 10^{-6}$	$(3.2 \pm 1.8) \cdot 10^{-7}$	4.81e−3	2.83e−2	7.09e−3	2.80e−4	5.83e−2	1.03
001_0001H_e1	8.5e−8	$(1.5 \pm 2.3) \cdot 10^{-6}$	$(3.7 \pm 2.2) \cdot 10^{-7}$	3.36e−3	2.52e−2	6.35e−3	4.43e−4	1.32e−1	5.69e−2
001_0001H_e3	8.6e−8	$(6.9 \pm 5.0) \cdot 10^{-7}$	$(1.8 \pm 0.83) \cdot 10^{-7}$	2.06e−3	1.27e−2	3.16e−3	3.34e−4	1.62e−1	1.25e−1
001_0001H_e10	3.5e−8	$(3.7 \pm 2.2) \cdot 10^{-7}$	$(9.6 \pm 4.5) \cdot 10^{-8}$	1.19e−3	4.79e−3	1.18e−3	3.09e−4	2.60e−1	9.53e−2
001_0001H_e30	2.3e−8	$(6.3 \pm 2.1) \cdot 10^{-8}$	$(6.6 \pm 3.3) \cdot 10^{-8}$	5.90e−4	1.80e−3	4.35e−4	1.07e−4	1.81e−1	3.71e−1
001_0001H_e100	1.9e−9	$(6.1 \pm 1.6) \cdot 10^{-9}$	$(9.5 \pm 2.2) \cdot 10^{-9}$	1.74e−4	5.38e−4	1.33e−4	3.50e−5	2.01e−1	3.11e−1
001_0001H_e300	1.0e−9	$(3.2 \pm 0.42) \cdot 10^{-9}$	$(2.8 \pm 0.56) \cdot 10^{-9}$	1.05e−4	2.16e−4	5.25e−5	3.05e−5	2.91e−1	3.20e−1
001_0001H_e1000	2.9e−10	$(6.5 \pm 1.3) \cdot 10^{-10}$	$(7.2 \pm 1.8) \cdot 10^{-10}$	4.76e−5	9.09e−5	2.23e−5	1.37e−5	2.88e−1	4.39e−1

Table D.5: 2-d simulations in r-z extent. Simulation name is constructed from **St** number, domain size $L_{x,z}$ and dust-to-gas ratio ε_0.

E List of own publications

These scientific publications have been submitted and published during my studies, or are in preparation for a publication with this year. The following articles are partially or fully presented within this thesis:

1. **Schreiber, A.** & Klahr, H. 2018,
   Azimuthal and Vertical Streaming Instability at High Dust-to-gas Ratios and on the Scales of Planetesimal Formation,
   submitted to ApJ, under review

2. Klahr, H., **Schreiber, A.** & Johansen, A. 2018,
   Turbulent Diffusion Determines the Initial Size of Planetesimals,
   in prep.

3. Müller, T., **A. Schreiber**, H. Klahr & F. Sadlo 2018,
   Tracking Planetesimals Formation in Protoplanetary Disks,
   in prep.

4. **Schreiber, A.** & Klahr, H. 2018,
   The Azimuthal Streaming Instability Regulates the Planetsimal Formation in Zonal Flows,
   in prep.

5. **Schreiber, A.** & Klahr, H. 2018,
   Diffusion Limited Planetesimal Formation in 3-D Simulations,
   in prep.

6. Klahr, H., & **Schreiber, A.** 2016,
   Linking the Origin of Asteroids to Planetesimal Formation in the Solar Nebula,
   Asteroids: New Observations, New Models, 318, 1

7. Klahr, H. H., Birnsitel, T., **Schreiber, A.**, & Lenz, C. 2015,
   Linking the Origin of Asteroids to Planetesimal formation in the Solar Nebula,
   IAU General Assembly, 22, 2255939

Additional publications addressed the public domain and outreach:

8. **Schreiber, A.** & Obermeier, C. 2016,
   Planetenforscher im Datenreichtum,
   Sterne und Weltraum 11|2018

9. Klahr, H. & **Schreiber, A.** 2015,
   The formation of planetesimals: building bricks for planetary systems,
   NIC Symposium 2016

10. **Schreiber, A.** & Klahr, H. 2015,
    Gravoturbulent Planetesimal Formation,
    GCS Press release

Bibliography

Adachi, I., Hayashi, C., & Nakazawa, K. 1976, Progress of Theoretical Physics, 56, 1756 20

ALMA Partnership, Brogan, C. L., Pérez, L. M., et al. 2015, ApJ, 808, L3 13

Amelin, Y., Krot, A. N., Hutcheon, I. D., & Ulyanov, A. A. 2002, Science (New York, N.Y.), 297, 1678 12

Andrews, S. M., Rosenfeld, K. A., Kraus, A. L., & Wilner, D. J. 2013, Astrophysical Journal, 771, 1305.5262 18

Andrews, S. M., Wilner, D. J., Hughes, A. M., Qi, C., & Dullemond, C. P. 2010, Astrophysical Journal, 723, 1241 20

Ansdell, M., Williams, J. P., van der Marel, N., et al. 2016, ApJ, 828, 46 17

Armitage, P. J. 2015, 128 20

Asphaug, E., & Benz, W. 1996, Icarus, 121, 225 45

Auffinger, J., & Laibe, G. 2017, MNRAS, 11, 1 75, 101, 151

Baehr, H., & Klahr, H. 2015, ApJ, 814, 155 49

Bai, X.-N., & Stone, J. M. 2010a, The Astrophysical Journal, 722, 25 34, 104, 145, 150, 153

Bai, X. N., & Stone, J. M. 2010b, Astrophysical Journal Letters, 722, 10 131

Balbus, S. A., & Hawley, J. F. 1991, ApJ, 376, 214 22

Balbus, S. A., & Hawley, J. F. 1992, The Astrophysical Journal, 400, 610 68

Barge, P., & Sommeria, J. 1995, A&A, 295, L1 41, 100, 151

Bell, Cassen, P. M., Klahr, H., & Henning, T. 1997, Astrophysical Journal v.486, 486, 372 62, 155

Benecchi, S. D., Noll, K. S., Grundy, W. M., et al. 2009, Icarus, 200, 292 152

Bühler, R. 2016, Bachelor's Thesis, Streaming-instability in protoplanetary discs 104

Binney, J., Tremaine, S., & Freeman, K. 2009, Physics Today, 62, 56 60

Birnstiel, T., Dullemond, C. P., & Brauer. 2010, Astronomy and Astrophysics, 513, 79 119, 145

Birnstiel, T., Dullemond, C. P., & Brauer, F. 2009, Astronomy and Astrophysics, 503, L5 32

Birnstiel, T., Fang, M., & Johansen, A. 2016, Space Science Reviews, 205, 41 32

Birnstiel, T., Klahr, H., & Ercolano, B. 2012, A&A, 539, A148 32, 33, 62, 154

Bodenheimer, P. 1994, Three-dimensional fragmentation calculations of protostar collapse (Numerical Simulations in Astrophysics) 119

Bottke, W. F., Durda, D. D., Nesvorný, D., et al. 2005, Icarus, 179, 63 11, 62, 154

Brandenburg, A. 2001, Advances in Non-linear Dynamos, 269 67

Brandenburg, A. 2005, Astronomische Nachrichten, 326, 787 67

Brandenburg, A., & Dobler, W. 2002, Computer Physics Communications, 147, 471 67

Brandenburg, A., Nordlund, A., Stein, R. F., & Torkelsson, U. 1995, Dynamo-generated Turbulence and Large-Scale Magnetic Fields in a Keplerian Shear Flow, doi:10.1086/175831 68

Brauer, F., Dullemond, C. P., & Henning, T. 2008, Astronomy & Astrophysics, 480, 859 32

Carrera, D., Gorti, U., Johansen, A., & Davies, M. B. 2017, The Astrophysical Journal, 839, 16 41, 154

Carrera, D., Johansen, A., & Davies, M. B. 2015, Astronomy & Astrophysics, 579, A43 34, 41, 104

Chiang, E. I., & Youdin, a. N. 2010, Forming Planetesimals in Solar and Extrasolar Nebulae, Vol. 38, 493, arXiv:0909.2652 50

Coradini, A., Magni, G., & Federico, C. 1981, A&A, 98, 173 60

Cuzzi, J. N., Hogan, R. C., Paque, J. M., & Dobrovolskis, A. R. 2001, ApJ, 546, 496 21, 22, 42, 62, 63

Cuzzi, J. N., Hogan, R. C., & Shariff, K. 2008, The Astrophysical Journal, 687, 1432 12, 42, 53, 120, 150

D'Alessio, P., Canto, J., Calvet, N., & Lizano, S. 1998, The Astrophysical Journal, 500, 411 18, 62, 155

Delbo, M., Walsh, K., Bolin, B., Avdellidou, C., & Morbidelli, A. 2017, Science, 357, 1026 62, 135, 152, 153, 154

DeMeo, F. E., & Carry, B. 2014, Nature, 505, 629 152

Dittrich, K., Klahr, H., & Johansen, A. 2013, Astrophysical Journal, 763, 18 41, 100, 151

Dominik, C., & Tielens, a. G. G. M. 1997, The Astrophysical Journal, 480, 647 27

Drążkowska, J., Windmark, F., & Dullemond, C. P. 2013, A&A, 556, A37 42

Einstein, A. 1905, Annalen der Physik, 322, 549 58

Emery, J. P., Marzari, F., Morbidelli, A., French, L. M., & Grav, T. 2015, in Asteroids IV No. June 2015, 277–326 50, 62, 154

Epstein, P. S. 1924, Physical Review, 23, 710 28

Fernández, J. A., & Sosa, A. 2012, Monthly Notices of the Royal Astronomical Society, 423, 1674 154

Flaherty, K. M., Hughes, A. M., Andrews, S. M., et al. 2016, ApJ, 818, 97 22

Flaherty, K. M., Hughes, A. M., Rose, S. C., et al. 2017, ApJ, 843, 150 22

Flock, M., Nelson, R. P., Turner, N. J., et al. 2017, The Astrophysical Journal, 850, 131 22

Fromang, S., & Nelson, R. P. 2005, Monthly Notices of the Royal Astronomical Society: Letters, 364, L81 41

Fuentes, C. I., & Holman, M. J. 2008, Astronomical Journal, 136, 83 11

Gammie, C. F. 1996, ApJ, 457, 355 50

Goldreich, P., & Lynden-Bell, D. 1965, Monthly Notices of the Royal Astronomical Society, 130, 125 59, 68

Goldreich, P., & Ward, W. R. 1973, The Astrophysical Journal, 183, 1051 12, 59, 104, 149

Gundlach, B., & Blum, J. 2015, Astrophysical Journal, 798, arXiv:1410.7199 31

Güttler, C., Blum, J., Zsom, A., Ormel, C. W., & Dullemond, C. P. 2010, A&A, 513, A56 14, 31

Haghighipour, N., & Boss, A. P. 2003, The Astrophysical Journal, 583, 996 41

Hayashi, C. 1981, Progress of Theoretical Physics Supplement, 70, 35 19

Hopkins, P. F. 2016, Monthly Notices of the Royal Astronomical Society, 456, 2383 140, 150

Jacquet, E., Balbus, S. A., & Latter, H. 2011, Monthly Notices of the Royal Astronomical Society, 415, 3591 33

Jansson, K. W., Johansen, A., Wahlberg Jansson, K., et al. 2014, Astronomy & Astrophysics, 570, A47 42

Jeans, J. H. 1902, Philosophical Transactions of the Royal Society A: Mathematical, Physical and Engineering Sciences, 199, 1 46

Jedicke, R., Larsen, J., & Spahr, T. 2002, Asteroids III, 71 11

Jewitt, D. C., Trujillo, C. A., & Luu, J. X. 2000, The Astronomical Journal, 120, 1140 11, 62, 154

Johansen, A., Blum, J., Tanaka, H., et al. 2014, Protostars and Planets VI, 547 13, 42

Johansen, A., Henning, T., & Klahr, H. 2006a, The Astrophysical Journal, 643, 1219 145

Johansen, A., Klahr, H., & Henning, T. 2011, Astronomy & Astrophysics, 529, A62 151

Johansen, A., Klahr, H., & Mee, a. J. 2006b, Monthly Notices of the Royal Astronomical Society: Letters, 370, arXiv:0603765 76

Johansen, A., Klahr, H. H., & Henning, T. 2006c, The Astrophysical Journal, 636, 1121 12

Johansen, A., Low, M.-m. M., Lacerda, P., & Bizzarro, M. 2015, Science Advances, 1 33, 41, 98, 100, 129, 135, 140, 150, 152, 153, 155

Johansen, A., Oishi, J. S., Low, M.-M. M., et al. 2007, Nature, 448, 1022 12, 41, 59, 71, 75, 101, 151

Johansen, A., & Youdin, A. N. 2007, The Astrophysical Journal, arXiv:0702626v1 26, 33, 34, 40, 41, 62, 70, 75, 78, 83, 104, 107, 112, 150

Johansen, A., Youdin, A. N., & Klahr, H. 2009, The Astrophysical Journal, 697, 1269 41

Kant, I. 1755, Allgemeine Naturgeschichte und Theorie des Himmels, oder Versuch von der Verfassung und dem mechanischen Ursprunge des ganzen Weltgebäudes nach Newtonischen Grundsätzen abgehandelt (Petersen) 12

Kataoka, A., Tanaka, H., Okuzumi, S., & Wada, K. 2013, Astronomy & Astrophysics, 557, L4 14, 41

Kato, M. T., Nakamura, K., Tandokoro, R., Fujimoto, M., & Ida, S. 2009, ApJ, 691, 1697 42

Klahr, H. 2004, Astrophysical Journal, 606, 1070 41

Klahr, H., & Bodenheimer, P. 2003, ApJ, 582, 869 22, 41, 77

Klahr, H., & Henning, T. 1997, \Icarus, 128, 213 41

Klahr, H., & Hubbard, A. 2014, ApJ, 788, 21 22, 41

Klahr, H., & Lin, D. 2000, in Astronomical Society of the Pacific Conference Series, Vol. 219, Disks, Planetesimals, and Planets, ed. G. Garzón, C. Eiroa, D. de Winter, & T. J. Mahoney, 375 41

Klahr, H., & Schreiber, A. 2015, Proceedings of the International Astronomical Union, 10, 1 46, 59, 119, 149

Klahr, H., Schreiber, A., & Johansen, A. 2018, in prep. 46, 119

Kobayashi, H., Tanaka, H., & Okuzumi, S. 2016, The Astrophysical Journal, 817, 105 152, 153, 155

Kolmogorov, A. N. 1991, Proceedings of the Royal Society A: Mathematical, Physical and Engineering Sciences, 434, 15 22, 64

Krijt, S., Ormel, C. W., Dominik, C., & Tielens, A. G. G. M. 2014, 16 41, 121

—. 2015, A&A, 13 41

Kuiper, G. P. 1951, Proceedings of the National Academy of Science, 37, 1 49

Laplace, P. S., & Young, T. 1821, Elementary Illustrations of the Celestial Mechanics of Laplace (J. Murray) 12

Latter, H. N., & Rosca, R. 2016, Mon. Not. R. Astron. Soc, 000, 0 50

Lin, D. N. C., & Papaloizou, J. 1980, MNRAS, 191, 37 21

Lorek, S., Gundlach, B., Lacerda, P., & Blum, J. 2016, A&A, 128, 14 31

Lucas, G., & Ackbar, G. 1983, It's A Trap! 41

Lyra, W. 2014, The Astrophysical Journal, 789, 77 41

Lyra, W., Johansen, A., Klahr, H., & Piskunov, N. 2008, Astronomy and Astrophysics, 491, L41 42

Lyra, W., Johansen, A., Klahr, H., & Piskunov, N. 2009, A&A, 493, 1125 42

Lyra, W., & Klahr, H. 2010, arXiv, astro-ph.E, arXiv:1011.0497 22

MacGregor, M. A., Matrà, L., Kalas, P., et al. 2017, ApJ, 842, 8 149

Meech, K. J., Hainaut, O. R., & Marsden, B. G. 2000, Minor Bodies in the Outer Solar System, ed. Fitzsimmons, Jewitt, & West (Springer), 75, 1 154

Müller, T., Schreiber, A., Klahr, H., & Sadlo, F. 2018, in prep. 133, 134, 135

Morbidelli, A., Bottke, W. F., Nesvorný, D., & Levison, H. F. 2009, Icarus, 204, 558 11, 12, 62, 154, 155

Morbidelli, A., Bottke Jr., W. F., Froeschlé, C., & Michel, P. 2002, in Asteroids III, 409–422 10

Musiolik, G., Teiser, J., Jankowski, T., & Wurm, G. 2016, The Astrophysical Journal, 827, 1 31

Nakagawa, Y., Sekiya, M., & Hayashi, C. 1986, Icarus, 67, 375 17, 28, 30, 87

Nelson, R. P., Gressel, O., & Umurhan, O. M. 2013, Monthly Notices of the Royal Astronomical Society, 435, 2610 22

Nesvorný, D., Vokrouhlický, D., Bottke, W. F., Noll, K. S., & Levison, H. F. 2011, The Astronomical Journal, 141, 159 62, 154

Nesvorny, D., Youdin, A. N., Richardson, D. C., et al. 2010, The Astronomical Journal, 3, 1 126, 154

Okuzumi, S., Tanaka, H., Kobayashi, H., & Wada, K. 2012, The Astrophysical Journal, 752, 106 28, 41

Onishi, I. K., & Sekiya, M. 2017, Earth, Planets and Space, 69, 1 42, 100, 101, 102, 151

Ormel, C. W. 2017, in Astrophysics and Space Science Library, Vol. 445, Astrophysics and Space Science Library, ed. M. Pessah & O. Gressel, 197 14, 152

Ormel, C. W., & Klahr, H. 2010, Astronomy and Astrophysics, 520, A43 155

Parker, A., & New Horizons Science Team. 2015, New Horizons Press Conference at the 47th Annual AAS/Division for Planetary Science Meeting in Washington, D.C on Nov. 9, 2015, 547 62, 154

Paszun, D., & Dominik, C. 2009, A&A, 507, 1023 27

Pringle, J. E. 1981, Annual Review of Astronomy and Astrophysics, 19, 137 21

Raettig, N., Klahr, H., & Lyra, W. 2015, Astrophysical Journal, 804, 1 34, 41, 75, 78, 100, 101, 151

Raettig, N., Lyra, W., & Klahr, H. 2013, ApJ, 765, 115 22

Rappaport, S., Vanderburg, A., Jacobs, T., et al. 2018, MNRAS, 474, 1453 149

Raymond, S. N., Armitage, P. J., Veras, D., Quintana, E. V., & Barclay, T. 2017, ArXiv e-prints, arXiv:1711.09599 149

Rickman, H., Marchi, S., A'Hearn, M., et al. 2015, Astronomy & Astrophysics, 583, A44 152

Safronov, V. 1972, Israel Program for Scientific Translations, Jerusalem, 11 12, 13, 14, 59, 104, 149

Schoonenberg, D., & Ormel, C. W. 2017, A&A, 21, arXiv:1702.02151 42

Schreiber, A., & Klahr, H. 2018, Apj, submitted 75

Seizinger, A., & Kley, W. 2013, A&A, 551, A65 27

Seizinger, A., Krijt, S., & Kley, W. 2013, A&A, 560, A45 27

Sekiya, M. 1983, Progress of Theoretical Physics, 69, 1116 52

Shakura, N. I., & Sunyaev, R. a. 1973, Astronomy and Astrophysics, 24, 337 21

Shariff, K., & Cuzzi, J. N. 2011, ApJ, 738, 73 60

Shariff, K., & Cuzzi, J. N. 2014, The Astrophysical Journal, 805, 42 150

Shariff, Karim and Cuzzi, Jeffrey N. 2015, Astrophysical Journal, 805, arXiv:1409.2541 46, 59, 133

Sheppard, S. S., & Trujillo, C. A. 2010, Astrophysical Journal Letters, 723, 233 11, 62, 141, 154, 155

Shi, J.-M., & Chiang, E. 2013, The Astrophysical Journal, 764, 20 120

Simon, J. B., Armitage, P. J., Li, R., & Youdin, A. N. 2016, The Astrophysical Journal, 822, 55 33, 129, 135, 140, 150, 152

Squire, J., & Hopkins, P. F. 2017, ArXiv e-prints, arXiv:1711.03975 34, 36, 37, 100, 104, 110

Squire, J., & Hopkins, P. F. 2017, MNRAS, arXiv:1706.05020 34

Stammler, S. M., Birnstiel, T., Panić, O., Dullemond, C. P., & Dominik, C. 2017, A&A, 140, arXiv:1701.02385 42

Stokes, G. G. 1851, Mathematical and Physical Papers, 1 28

Takahashi, S. Z., & Inutsuka, S.-i. 2014, The Astrophysical Journal, 794, 55 50

Takeuchi, T., & Ida, S. 2012, ApJ, 749, 89 50

Taki, T., Fujimoto, M., & Ida, S. 2016, A&A, 1 100, 101, 102

Teague, R., Guilloteau, S., Semenov, D., et al. 2016, A&A, 592, A49 22

Truelove, J. K., Klein, R. I., McKee, C. F., et al. 1997, ApJ, 489, L179 119, 152

Tsirvoulis, G., Morbidelli, A., Delbo, M., & Tsiganis, K. 2016, Icarus, 0, 1 153

Turner, N. J., & Drake, J. F. 2009, ApJ, 703, 2152 50

Turner, N. J., Fromang, S., Gammie, C., et al. 2014, eprint arXiv, 1401, 7306 63, 151

van der Marel, N., van Dishoeck, E. F., Bruderer, S., et al. 2013, Science, 340, 1199 42

VonNeumann, J., & Richtmyer, R. D. 1950, Journal of Applied Physics, 21, 232 68

Wada, K., Tanaka, H., Okuzumi, S., et al. 2013, Astronomy & Astrophysics, 559, A62 27

Ward, W. R. 1976, in Frontiers of Astrophysics, ed. E. H. Avrett, 1–40 60

Ward, W. R. 2000, On Planetesimal Formation: The Role of Collective Particle Behavior, ed. R. M. Canup, K. Righter, & et al., 75–84 59, 60

Weidenschilling, S. J. 1977, Astrophysics and Space Science, 51, 153 19

Weidenschilling, S. J., & Cuzzi, J. N. 1993, Protostars and planets III 13, 152

Weidenschilling, S. J., & Davis, D. R. 1985, Icarus, 62, 16 20

Weidenschilling, Stuart J. 1987, MNRAS, 1 28, 30

Weizsäcker, C. 1946, Naturwissenschaften, 8 12

Whipple, F. 1972, From Plasma to Planet, 211 32, 41, 42

Whipple, F. L. 1964, Proceedings of the National Academy of Science, 52, 565 12, 41

Windmark, F., Birnstiel, T., & Güttler, C. 2012, arXiv preprint arXiv: ..., 73, 1 31

Windmark, F., Birnstiel, T., Ormel, C. W., & Dullemond, C. P. 2012, A&A, 544, L16 14, 41

Yang, C.-C., Johansen, A., & Carrera, D. 2016, 1 34, 41, 104

Yang, C.-C., & Krumholz, M. 2012, The Astrophysical Journal, 758, 48 97

Yarkovsky, I. 1901, The density of luminiferous ether and the resistance it offers to motion 10

Youdin, A. N. 2005, ArXiv Astrophysics e-prints, astro-ph/0508659 60

Youdin, A. N. 2011, The Astrophysical Journal, 731, 99 50

Youdin, A. N., & Goodman, J. 2004, The Astrophysical Journal, 620, 1 26, 33, 34, 75, 78, 100, 150

Youdin, A. N., & Johansen, A. 2007, The Astrophysical Journal, 662, 613 26, 33, 67, 68, 78, 150

Youdin, A. N., & Kenyon, S. J. 2013, Planets, 1 13

Youdin, A. N., & Lithwick, Y. 2007, Icarus, 192, 588 121

Zsom, A.; Ormel, C. W.; Güttler, C.; Blum, J.; Dullemond, C. P. 2010, arXiv preprint arXiv: ..., arXiv:arXiv:1001.0488v1 32

Danksagung

„If I have seen further it is by standing on the sholders of Giants.“
- Sir Isaac Newton

First, I would like to thank my supervisor Hubert Klahr for the four years of support and teaching. Without you, this whole project would not have been a success. I am very grateful for the opportunity to spend my PhD years on such a ground breaking astrophysical project and for the confidence you put in me. These years in your group was an endeavour, I will look back to and be very thankful. I hope we will be proven right with our origin for the planetesimals! What a joyful time we had. Thanks for the beer!

I want to thank my many supporters from our scientific community: Chao-Chin Yang, who I could always ask on my Pencil Code problems. Jono Squire, who supported my efforts for deriving the linear growth rates for the streaming instability. Anders Johansen, for providing this awesome particle module. Til Birnstiel, Kees Dullemond, Willy Kley, Andrew Youdin, Alessandro Morbidelli, Akimasa Kataoka, Wlad Lyra, Chris Ormel and many more, for the fruitful discussion and support with the idea of a diffusion limited collapse criterion. And of course, the whole Pencil Code community, specially Simon Candelaresi who develops together with me a new Python based diagnostic tool kit for the pencil code.

I have very big gratitude for my beloved Vivien, my lovely family and my friends, Alexander Adam and Marcel Langer, as they never stopped supporting me. Especially, in the last weeks of writing, the support I got from you, Vivien, kept me on track. I want to thank my mother and my brother who backed me up in these very hard times of ours. Dad, we miss you. This thesis is for you, who always saw in me what great think I could achieve. I wish you could see..

Furthermore, I want to thank all the nice people I met during the past years. Starting with the Elsässer crew, I thank you for this wonderful office and the time we spend. These are Adriana Pohl, Paul Molliere, Christian Lenz. Big thanks also goes to the rest of our awesome PSF theory group! Special thanks to Hans Baehr and Adriana Pohl, for teaching skiing to Vivien and me. Another special thanks goes to the thesis proofreaders: Vivien, Christian and Adriana.

I also want to thank the friends I made in the past years for sharing endurance and all the fun activities we had. This list is long, so if I do not mention you by name, since you read this, yes its you! Thanks! :-) A big greeting goes to all the people from the MPIA! Specially I want to thank: Paul Mollière, for spreading his passion for science. Christian Obermeier, who encouraged me to start using my camera. Matthias Samland, all the nice food we had. Matthäus Schulik, who proved one can do science in metal-style. Christoph Mordasini, for the drunken time. Yuri Fujii and Masanobu Kunitomo, for their warmly welcoming in Japan. Many thanks to the students that spend their time with me on these projects: Fabian Krautgasser, Tunde Aluko, Patrick Quicker and Robin Bühler. Big gratitude also goes towards Thomas Mueller, who helped me a lot with the analysis of the planetesimal formation simulations and visualising them.

Lastly, I also want to thank my thesis committee, Hubert, Kees, Eva Grebel, and Mario Trieloff, who kindly agreed to referee this work.

Declaration of Originality

Declaration of Originality

I hereby declare that this thesis is my own work and
that I have used no other than the stated sources and aids.

Declaration

Ich versichere, dass ich diese Arbeit selbstständig verfasst habe und
keine anderen als die angegebenen Quellen und Hilfsmittel benutzt habe.

Heidelberg, der 20. März 2018

(Andreas Schreiber)

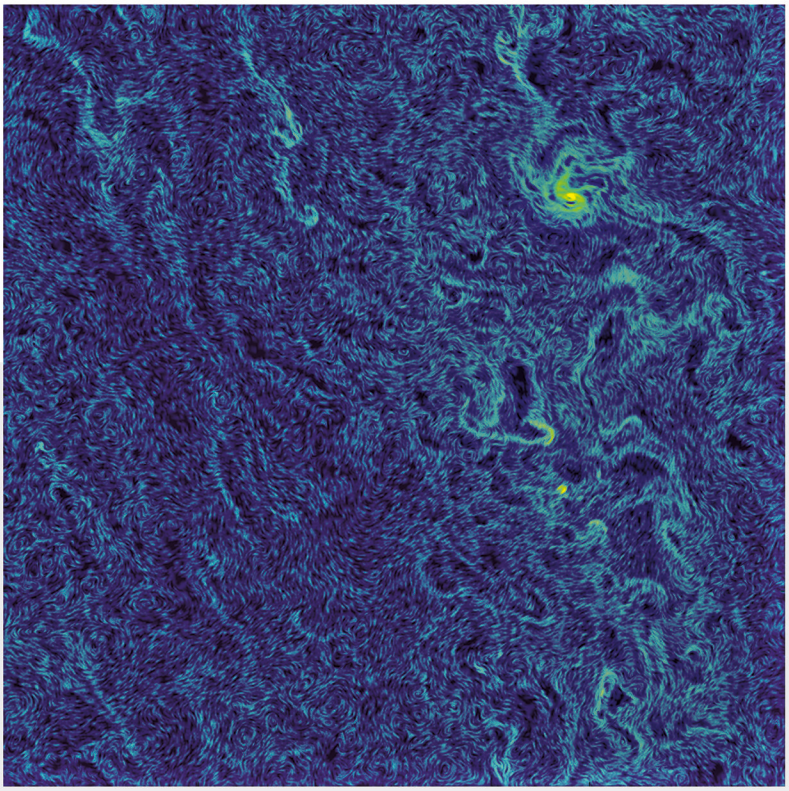

How asteroids were born: Dust flow pattern of a collapsing particle cloud to a planetesimal. The underlying turbulent diffusion is found to state a size limitaion on the final outcome. This gives an impression on how asteroids and Kuiper-belt objects were formed.

Max-Planck-Institut für Astronomie Heidelberg
Max Planck Institute for Astronomy Heidelberg